International Journal of Photoenergy

# Solar PV/Thermal Research

Guest Editors: Xudong Zhao, Clito Afonso, and Jie Ji

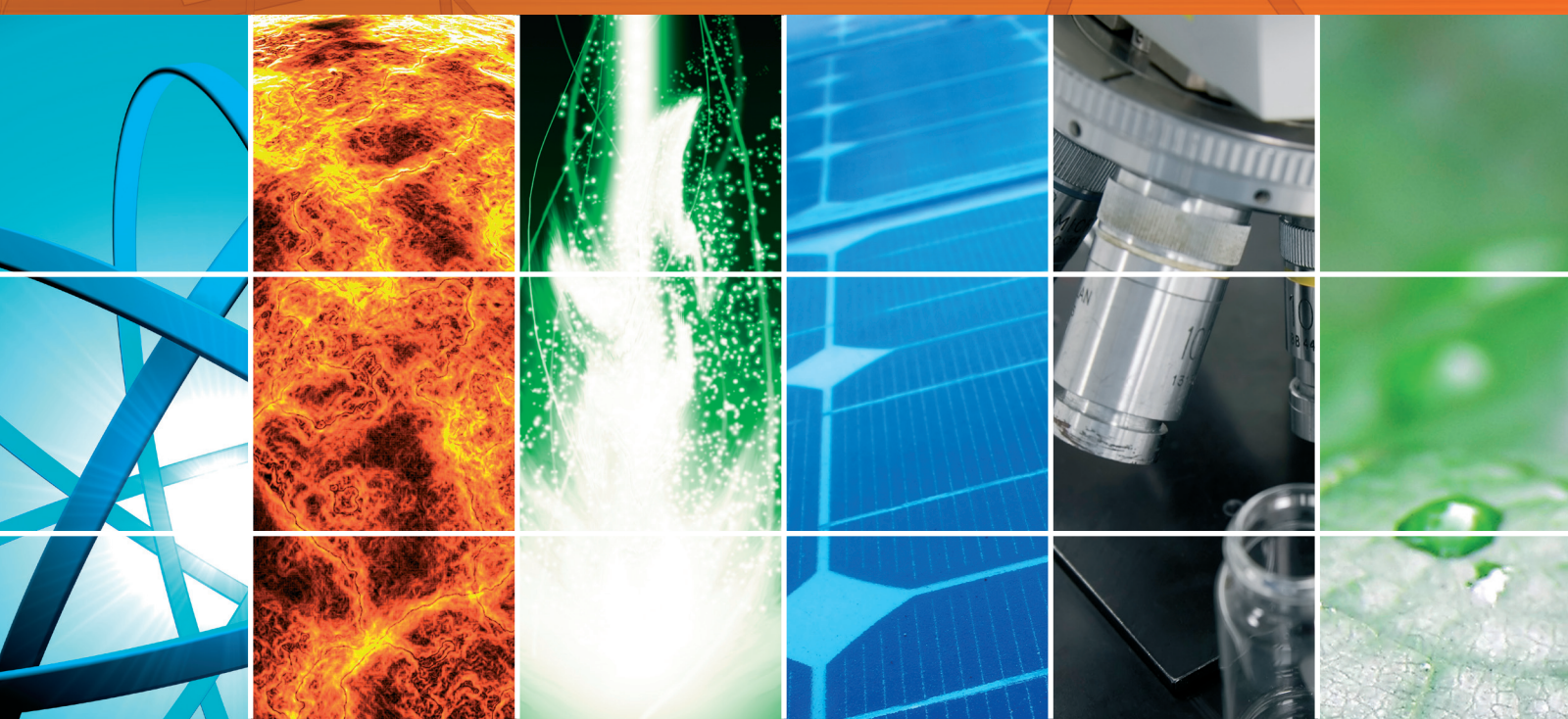

# Solar PV/Thermal Research

International Journal of Photoenergy

# Solar PV/Thermal Research

Guest Editors: Xudong Zhao, Clito Afonso, and Jie Ji

# Editorial Board

# Contents

Hindawi Publishing Corporation
International Journal of Photoenergy
Volume 2016, Article ID 2396973, 1 page
http://dx.doi.org/10.1155/2016/2396973

# *Editorial*
# Solar PV/Thermal Research

**Xudong Zhao,[1] Clito Afonso,[2] and Jie Ji[3]**

[1]*School of Engineering, Faculty of Science and Engineering, University of Hull, Yorkshire, UK*
[2]*Centre of Innovation on New and Renewable Energies, Institute of Mechanical Engineering and Industrial Management, University of Porto, Rua Dr. Roberto Frias, 4200-465 Porto, Portugal*
[3]*School of Engineering and Science, University of Science and Technology of China, Hefei, China*

Correspondence should be addressed to Xudong Zhao; xudong.zhao@hull.ac.uk

Received 26 January 2016; Accepted 2 February 2016



This special issue is now ready for publication under the joint effort of the editorial board of this journal and the above-named special editors. The special issue contains the original research articles and review articles in relation to solar PV, solar thermal, and combined PV/thermal, addressing various aspects of the topics including theory, methodology and computer simulation, innovative materials, system configurations, energy, and socioeconomic performance analysis, as well as application case studies. We received a total of 30 manuscripts, of which 15 were selected for publication through the strict experts' peer reviews. The papers to be published in the special issue are "Application of a Noncarboxylated Dye Compound in a Dye-Sensitized Solar Cell Containing a Cyclodextrin Layer"; "Method to Calculate the Electricity Generated by a Photovoltaic Cell, Based on Its Mathematical Model Simulations in MATLAB"; "Study on Concentrating Characteristics of a Solar Parabolic Dish Concentrator within High Radiation Flux"; "Electrical and Thermal Performance Analysis for a Highly Concentrating Photovoltaic/Thermal System"; "Sensitive Analysis for the Efficiency of a Parabolic Trough Solar Collector Based on Orthogonal Experiment"; "Competitiveness Level of Photovoltaic Solar Systems in Ouagadougou (Burkina Faso): Study Based on the Domestic Electric Meters Calibration"; "Safety Analysis of Solar Module under Partial Shading"; "Design and Implementation of Automatic Wheat Mower Based on Smart Sensor Fed by a Photovoltaic"; "Price-Efficiency Relationship for Photovoltaic Systems on a Global Basis"; "Technique for Outdoor Test on Concentrating Photovoltaic Cells"; "Behavior of Photovoltaic System during Solar Eclipse in Prague"; "PID Testing Method Suitable for Process Control of Solar Cells Mass Production"; "Glazed PVT Collector with Polysiloxane Encapsulation of PV Cells: Performance and Economic Analysis"; "Experimental Investigation of the Effects of Partial Shading on Photovoltaic Cells' Electrical Parameters"; "Solar Thermal System Evaluation in China."

We believe the issue can showcase the latest technology development and excellent academic standard in this uprising subject, which has enormous market perspectives in the next decades. We would like to take this opportunity to thank all the authors who are interested in publishing their articles in this special issue. Our specific thanks will be to the editorial board members of this journal; without their help and contribution, this issue will never be concluded in such a short duration.

*Xudong Zhao*
*Clito Afonso*
*Jie Ji*

Hindawi Publishing Corporation
International Journal of Photoenergy
Volume 2016, Article ID 2653560, 6 pages
http://dx.doi.org/10.1155/2016/2653560

*Research Article*

# Behavior of Photovoltaic System during Solar Eclipse in Prague

**Martin Libra, Pavel Kouřím, and Vladislav Poulek**

*Czech University of Life Sciences Prague, Kamycka 129, 16521 Prague 6, Czech Republic*

Correspondence should be addressed to Martin Libra; libra@tf.czu.cz

Received 4 September 2015; Revised 6 January 2016; Accepted 6 January 2016

Academic Editor: Clito Afonso



PV power plants have been recently installed in very large scale. So the effects of the solar eclipse are of big importance especially for grid connected photovoltaic (PV) systems. There was a partial solar eclipse in Prague on 20th March 2015. We have evaluated the data from our facility in order to monitor the impact of this natural phenomenon on the behavior of PV system, and these results are presented in the paper. The behavior of PV system corresponds with the theoretical assumption. The power decrease of the PV array corresponds with the relative size of the solar eclipse. *I-V* characteristics of the PV panel correspond to the theoretical model presented in our previous work.

## 1. Introduction

We have developed and tested a number of PV systems of various structures especially with one ax tracking stand at Faculty of Engineering, the Czech University of Life Sciences Prague. The results were published, for example, in reports [1–3]. We have developed a new generation of PV panels particularly suited to areas with extreme climatic conditions [4]. They are the existing PV systems with two-ax tracking stand; they are described, for example, in the report [5].

On 20th March 2015, there was a partial solar eclipse in Prague, which amounted to a maximum of 68% coverage of the surface of the solar disc. There was very favorable weather during two consecutive very sunny days. We have had the opportunity to measure and evaluate data on the behavior of PV system during this unique natural phenomenon. These data are presented and discussed below in this paper. Similar data are not found in the literature, so we believe that they are unique. But the behavior of PV systems in artificial shading was tested in some works, for example, [6–9]. There are other models of the partial shading effect in [10, 11]. The effect of the solar eclipse on grid connected PV power plants was investigated in [12].

In our previous work [13], we have examined the theoretical model of the behavior of *I-V* characteristics in terms of the theory of semiconductors. The results of our measurement of relevant variables during the solar eclipse presented below confirmed a good agreement of theory and experiment.

## 2. Experimental

The PV system used for the measurement of the time series of instantaneous output power and amount of generated electric energy is shown in Figure 1. Three mono-Si PV panels MOTECH with a nominal power of 170 $W_p$ are connected in series. The total nominal output power of PV system is therefore 510 $W_p$. The PV system is oriented to the south at an angle of 45°. The PV panels are connected to the SMA Sunny Boy SB 700 inverter and the output alternating current is connected directly into the public grid. The data are saved automatically.

The radiation intensity and the temperature of PV panels and of the air were measured by the SMA Sunny Sensor Box. Thermometers were based on thermistors. The height and azimuth of the Sun were deduced from the ephemeris and the angle of incidence was calculated as the deviation of the vector directed toward the Sun and of the vector perpendicular to the plane of PV panels. We defined Cartesian coordinates: $x$: horizontal from west to east, $y$: vertical from down to up, $z$: horizontal from north to south. The vector $a = (0, 1, 1)$ is perpendicular to the PV panels, and the vector $\vec{b}$ directed toward the Sun depends on the actual height and azimuth.

Figure 1: Our PV system used for data monitoring during the solar eclipse.

Table 1: Selected values of important variables during the solar eclipse on March 20, 2015.

| Eclipse phase | Time (h) | Solar disk coverage (%) | Sun height (°) | Sun azimuth (°) | Angle of incidence of sun rays on PV panels (°) |
|---|---|---|---|---|---|
| Start | 9:37 | 0 | 30 | 134 | 39 |
| Maximum | 10:46 | 68 | 37 | 154 | 21 |
| Finish | 11:58 | 0 | 40 | 176 | 5 |

The following equation $\vec{a} \cdot \vec{b} = |\vec{a}| \cdot |\vec{b}| \cdot \cos\alpha$ is valid for the scalar product. We calculated the deviation $\alpha$ from this equation.

The Yingli 230 $W_p$ poly-Si PV panel was used for $I$-$V$ characteristics measurement. The orientation to the south and the angle were identical with the above-mentioned monocrystalline PV panels MOTECH. Characteristics were measured by the semiautomatic device Prova 210 during the eclipse.

## 3. Results and Discussion

Figure 2 shows the Sun at the stage of maximum eclipse, as seen from our university campus. Selected values of important parameters during the solar eclipse are summarized in Tables 1 and 2. The intensity of the incident solar radiation was measured on a horizontal plane. These values were later recalculated on the values corresponding with the plane perpendicular to the sun rays and with the plane of PV panels surface. The recalculation was done by projection of the plane to the plane perpendicular to the sun rays.

Figure 3(a) is a plot of instantaneous power at the time and the amount of electricity produced during two sunny days 19th to 20th March 2015. It is seen that the maximum decrease of the instantaneous power during the eclipse was −69% in comparison with the value from the previous day. It excellently corresponds with the coverage area of the solar disc 68% with regard to the minor differences of

Figure 2: Sun in the maximum phase of the eclipse visible from our university campus in Prague.

measurement conditions in two consecutive sunny days. The amount of generated electric energy corresponds with the area under the graph curve. It is lower by about 13.5% in the eclipse day.

Figure 3(b) shows the corresponding dependences of the solar radiation intensity incident on a horizontal plane. However, the graphs in Figure 3 cannot be accurately compared, because the angle of incidence of sun rays on horizontal plane varies with the time a bit differently compared to the angle of incidence on the surface of the PV panels with an inclination towards south (see Table 2).

Table 2: Selected values of important variables during the solar eclipse on March 20, 2015.

| Eclipse phase | Time (h) | Solar radiation intensity on horizontal plane ($W \cdot m^{-2}$) | Solar radiation intensity on perpendicular plane ($W \cdot m^{-2}$) | Solar radiation intensity on PV panels ($W \cdot m^{-2}$) | Temperature of PV panels (°C) | Instantaneous output power (W) |
|---|---|---|---|---|---|---|
| Start | 9:37 | 437 | 874 | 679 | 31 | 340 |
| Maximum | 10:46 | 155 | 258 | 241 | 14 | 124 |
| Finish | 11:58 | 612 | 952 | 948 | 43 | 415 |

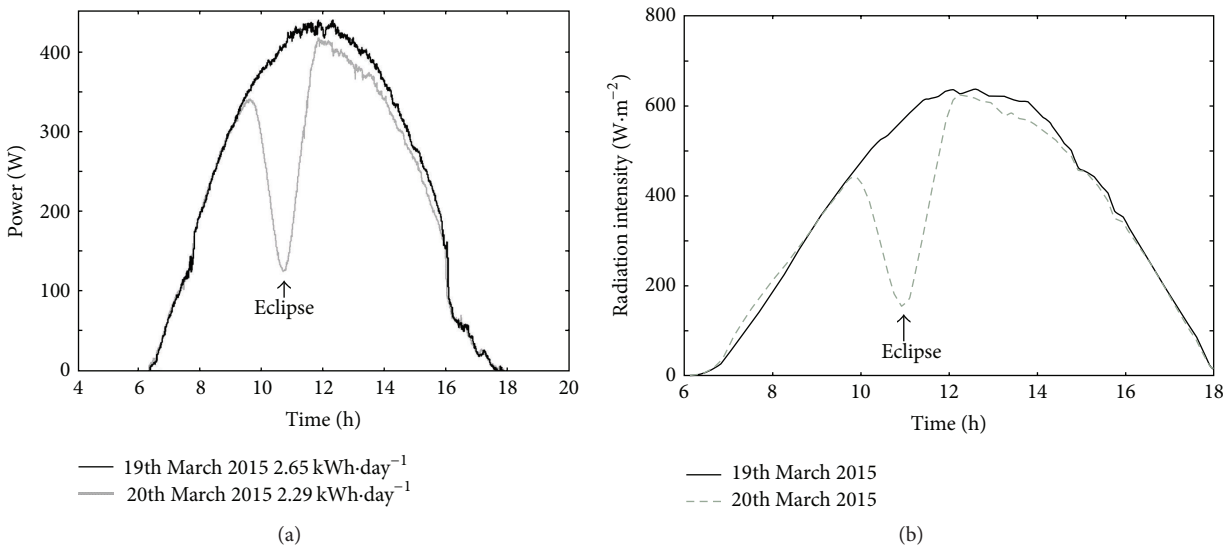


Figure 3: (a) Time series of instantaneous output power and the amount of generated electric energy and (b) time series of solar radiation intensity incident on a horizontal plane, during two sunny days (19th to 20th March 2015).

Figure 4 shows dependences of PV panels temperature, air temperature, and wind speed on the time during both monitored days. The decrease of the air temperature and of the PV panels temperature during a solar eclipse is seen, which is related to the decrease in the intensity of radiation (see Table 2). Moreover, on 19th March 2015 noon, mild local minimum of temperature related to the higher wind speed and thus to more intense cooling of the PV panels is seen (see Figure 4(b)). Conversely, on 20th March 2015 around noon, after the solar eclipse, the air temperature and PV panels temperature showed maximum, because the wind speed was lower than at noon the previous day. On 20th March 2015, the wind speed was increased after the 13th hour and then also the temperature of PV panels began to decrease.

Figure 5 shows the *I-V* characteristics of the PV panel measured at different stages of the eclipse. It is obvious that their behavior accurately corresponds to theoretical model published in [13] and/or for instance [14, 15]. The open circuit voltage is reduced at higher temperature of PV panel. It is associated with a shift of the Fermi energy level $E_F$ toward the center of the forbidden gap in a band diagram of energy levels in the semiconductor (see Figure 6). This leads to a reduction in potential barrier of the PN junction. The higher radiation intensity causes higher short-circuit current due to higher generation of free electrons and holes. It coincides well with the theory of semiconductors.

Solar eclipse is then reflected in the energy sector on a wider scale. Total eclipse has on the Earth's surface the area of a circle with a diameter of about 200 km and it is moving. The entire eclipse process takes about 2.5 h from the beginning to the end. On a much larger area, there is a partial eclipse. On an area corresponding to the total eclipse, in some countries (especially in Europe, including Germany, Czech Republic, etc.), the installed nominal power of PV power plants is in the range $\approx$1000 $MW_p$. The installed nominal output power is even much higher on the area of partial eclipse. Figure 3(a) shows that the absolute value of the maximum derivative of the power curve by the time is corresponding to a decrease (and later increase) in the instantaneous power of about 0.1 $W \cdot s^{-1}$. For PV system with a nominal output of 510 $W_p$, it represents 0.02%$\cdot s^{-1}$. Thus, if PV power plants with the nominal output power of 1,000 $MW_p$ are installed on the said area, on a sunny day, there would be maximum power decrease rate (and later increase rate) 0.2 $MW \cdot s^{-1}$ in the local grid during the total eclipse.

## 4. Conclusion

Thanks to the favorable weather on 19th to 20th March 2015, we were able to observe the behavior of PV system during the solar eclipse. Monitoring of the data during two

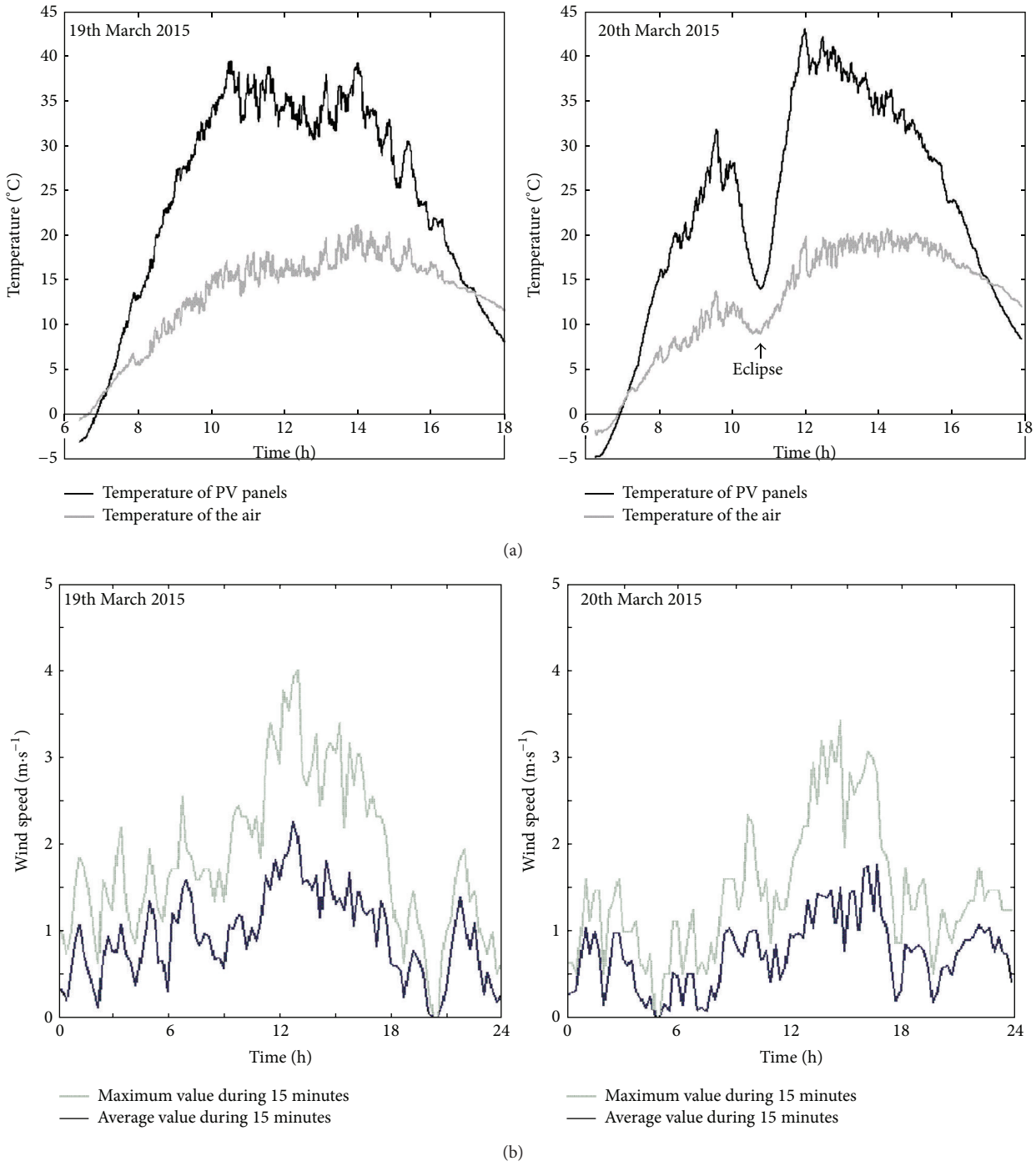


Figure 4: (a) Time series of PV panels temperature and air temperature and (b) time series of wind speed, during two sunny days (19th to 20th March 2015).

consecutive sunny days, including the solar eclipse, shows excellent agreement of theory and experiment.

(i) Decrease of the instantaneous output power of the PV system during the solar eclipse corresponds with the relative shading of the solar disc and with decrease of the intensity of solar radiation.

(ii) A lower value of instantaneous output power after the eclipse may be associated with the condensation of water vapor in atmosphere due to the decrease of

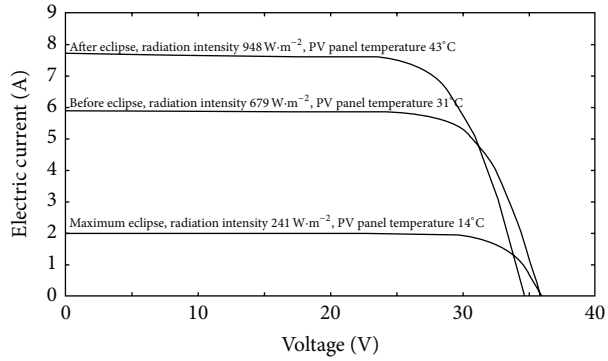


FIGURE 5: $I$-$V$ characteristics of the Yingli 230 $W_p$ poly-Si PV panel in various stages of eclipse.

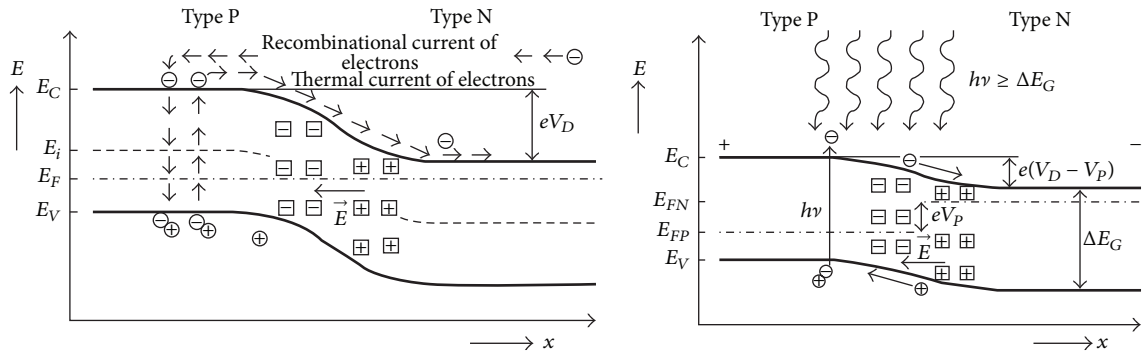


FIGURE 6: Band diagram of energy levels of the PN junction: (a) not illuminated, (b) illuminated ($E_F$: Fermi energy level, $E_i$: center of the forbidden gap, $E_V$: valence band edge, $E_C$: conduction band edge, $\Delta E_G$: energy forbidden gap, $V_D$: diffusion voltage, $V_P$: photovoltaic voltage, $\vec{E}$: electric field intensity, $\nu$: frequency, $h$: Planck constant, and $x$: coordinate perpendicular to the PN junction).

air temperature during eclipse and with the higher absorption in the near infrared region of the spectrum.

(iii) Temperature of PV panels corresponds mainly with the radiation intensity, but it is also influenced by the wind speed and therefore by natural cooling.

(iv) Behavior of $I$-$V$ characteristics of PV panel corresponds with the theoretical model based on the theory of semiconductors.

(v) Solar eclipse has a significant impact on the energy sector of some countries focused on renewable energy sources. The drop in performance PV power plants have to be balanced and covered from other sources.

## Conflict of Interests

The authors declare that there is no conflict of interests regarding the publication of this paper.

## Acknowledgment

The work was supported by Internal Research Project, Faculty of Engineering, Czech University of Life Sciences.

## References

[1] V. Poulek and M. Libra, "New solar tracker," *Solar Energy Materials and Solar Cells*, vol. 51, no. 2, pp. 113–120, 1998.

[2] V. Poulek and M. Libra, "A new low-cost tracking ridge concentrator," *Solar Energy Materials and Solar Cells*, vol. 61, no. 2, pp. 199–202, 2000.

[3] M. Libra, P. Sedláček, J. Mareš, and V. Poulek, "Porovnání PV systémů s pevným a proměnným sklonem PV panelů," *Jemná Mechanika a Optika*, vol. 55, no. 10, pp. 270–271, 2010 (Czech).

[4] V. Poulek, D. S. Strebkov, I. S. Persic, and M. Libra, "Towards 50 years lifetime of PV panels laminated with silicone gel technology," *Solar Energy*, vol. 86, no. 10, pp. 3103–3108, 2012.

[5] R. Gregor, Y. Takase, J. Rodas, L. Carreras, D. Gregor, and A. López, "Biaxial solar tracking system based on the MPPT approach integrating ICTs for photovoltaic applications," *International Journal of Photoenergy*, vol. 2015, Article ID 202986, 10 pages, 2015.

[6] I. Reda, "Solar eclipse monitoring for solar energy applications," *Solar Energy*, vol. 112, pp. 339–350, 2015.

[7] P. Kofinas, A. I. Dounis, G. Papadakis, and M. N. Assimakopoulos, "An Intelligent MPPT controller based on direct neural control for partially shaded PV system," *Energy and Buildings*, vol. 90, pp. 51–64, 2015.

[8] E. Karatepe, M. Boztepe, and M. Çolak, "Development of a suitable model for characterizing photovoltaic arrays with shaded solar cells," *Solar Energy*, vol. 81, no. 8, pp. 977–992, 2007.

[9] J.-C. Wang, Y.-L. Su, K.-C. Kuo, J.-C. Shieh, and J.-A. Jiang, "Toward multiple maximum power point estimation of photovoltaic systems based on semiconductor theory," *Progress in Photovoltaics: Research and Applications*, vol. 23, no. 7, pp. 847–861, 2014.

[10] Y. J. Wang and R. L. Sheu, "Probabilistic modeling of partial shading of photovoltaic arrays," *International Journal of Photoenergy*, vol. 2015, Article ID 863637, 10 pages, 2015.

[11] W. He, F. Liu, J. Ji, S. Zhang, and H. Chen, "Safety analysis of solar module under partial shading," *International Journal of Photoenergy*, vol. 2015, Article ID 907282, 8 pages, 2015.

[12] C. Köhler, H. Ruf, A. Steiner, D. Lee, J. Thieler, and M. Casel, "Nutzung Numerischer Wettervorhersagen in der Simulation von Verteilnetzen: Die Effekte einer Sonnenfinsternis auf netzgekoppelte PV-Anlagen und Netztransformatoren," in *30th Symposium Photovoltaische Solarenergie*, Bad Staffelstein, Germany, March 2015, https://www.researchgate.net/publication/273143752_Nutzung_Numerischer_Wettervorhersagen_in_der_Simulation_von_Verteilnetzen_Die_Effekte_einer_Sonnenfinsternis_auf_netzgekoppelte_PV-Anlagen_und_Netztransformatoren.

[13] V. Poulek and M. Libra, *Photovoltaics*, ILSA, Prague, Czech Republic, 2010.

[14] M. Barukčić, Ž. Hederić, and Ž. Špoljarić, "The estimation of I–V curves of PV panel using manufacturers' I–V curves and evolutionary strategy," *Energy Conversion and Management*, vol. 88, pp. 447–458, 2014.

[15] C. Carrero, D. Ramírez, J. Rodríguez, and C. A. Platero, "Accurate and fast convergence method for parameter estimation of PV generators based on three main points of the *I-V* curve," *Renewable Energy*, vol. 36, no. 11, pp. 2972–2977, 2011.

Hindawi Publishing Corporation
International Journal of Photoenergy
Volume 2016, Article ID 9698070, 10 pages
http://dx.doi.org/10.1155/2016/9698070

*Research Article*

# Competitiveness Level of Photovoltaic Solar Systems in Ouagadougou (Burkina Faso): Study Based on the Domestic Electric Meters Calibration

**Konan Lambert Amani,[1] Raguilignaba Sam,[2] and François Zougmoré[1]**

[1] *University of Ouagadougou, 03 BP 7021, Ouagadougou 03, Burkina Faso*
[2] *Polytechnic University of Bobo-Dioulasso, 01 BP 1091, Bobo-Dioulasso 01, Burkina Faso*

Correspondence should be addressed to Konan Lambert Amani; amani_konan@hotmail.fr

Received 23 July 2015; Accepted 1 December 2015

Academic Editor: Xudong Zhao



The mean cost price of electricity in Burkina Faso at the end of the last quarter of 2012 was 158 FCFA/kWh for a country where more than 46% of the population lives below the national poverty threshold. To look for solution to that problem, the resort to photovoltaic solar energy is justified for that country. The purpose of this study is to promote the integration of both technical and economical surveys in solar energy preliminary projects in Ouagadougou. To reach that, investigations were carried out in some households and attention was paid from the calibration of the domestic electric meters. Energy demands collected within each household allow us to design a corresponding solar kit through optimization rules. An estimate was edited and financial viability study for each household was also carried out thereafter. In this study, only households using the national electricity network calibration meter on their disadvantage favorably answered to all financial indicators and appear as the only one that could profit from such project. This work is helpful to note that photovoltaic solar energy still stays at a primitive level of competitiveness compared to conventional energy resources for small systems in Ouagadougou.

## 1. Introduction

The crisis of the energy which has led all Africa for several years does not save Burkina Faso. The country's dependence on oil of which most of the electric production depends does not help the things. The country is in an energetic context where 67.2% of the consumed electricity is from the local thermal source, 15.7% is from the hydroelectric source, and 17.1% is from the imports. According to the World Bank Group (http://data.worldbank.org/ on October 23, 2013.), only 14.6% of the population has access to that resource. The report of SONABEL (Société Nationale d'Electricité du Burkina Faso), the national electricity company, estimates, at the last quarter of 2012, at 158 FCFA/kWh (African Financial Community Franc with 1 Euro = 655.96 FCFA (XOF) by the converter from Euro to Western African FCFA with rates of exchange of October 23, 2013, http://fr.coinmill.com/EUR_XOF.html#EUR=1)the average national cost of consumed electricity. This cost remains relatively high for the majority of the population in a country where 46.4% of the population lived below the national poverty line (Population below national poverty line is the percentage of the population living below the national poverty line, which is the poverty line deemed appropriate for a country by its authorities. National estimates are based on population-weighted subgroup estimates from household surveys.) [1] over the period 2000–2009.

Among the ECOWAS (Economic Community of the of West Africa States) countries, except electricity consumptions higher than 300 kilowatt-hours per month where it is preceded by Benin, Burkina Faso is the country where populations pay for the electricity from the national network expensively (from Climate Change Knowledge Portal for Development Practioners and Policy Makers database on December 15, 2012: http://donnees.banquemondiale.org/pays/burkina-faso). This high cost finds its first explanation in the

lack of a real knowledge on behalf of the national electricity subscribers during the calibration of their domestic electric meters. Those are not enough informed on this cause; some of them use electric meters overgauged for their electricity consumption, which inevitably increase the final cost of their electricity invoice. Taking into account this high cost, 110 million households at low income in Africa spend more than 4 billion dollars per year for lighting based on kerosene, an expensive, ineffective, and dangerous product for safety and health [2]. According to UNDP [1], 82.4% of the population of Burkina Faso lives without modern sources of energy. That entrains significant carbon dioxide ($CO_2$) emissions (Refer to the quantity of greenhouse gas converted into equivalent $CO_2$.), essential gas in the global warming estimated in 2010 at 1.441 million Mt (https://www.cia.gov/library/publications/the-world-factbook/geos/uv.html).

CCI-BF [3] estimates that the majority of Burkinabe lives far from the electrical supply network with only 3% as national electrification rate at December 31, 2009. In Burkina Faso, 73.5% of the total population lives in rural areas [1]. For these rural communities, it is technically too complex to extend the network towards them or because the cost of an electric connection is not justified compared to other existing solutions. However, it is often essential to have access to electricity in order to ensure some basic services such as lighting, production of cold, and operation of radio or television stations sets (http://www.planete-burkina.com/economie_burkina.php.).

Paradoxically, Burkina Faso belongs to the sunniest areas of the earth, with a potential of average solar irradiation of approximately 5-6 kWh/m$^2$/day. That could justify the alternative to feed these isolated sites in electricity by photovoltaic (PV) solar energy. The importance of this solar resource and the real reduction of the PV technology costs [4, 5] result in very significant contributions in PV systems mainly for rural populations in Burkina Faso.

The objective of this study is to show the households in which electric consumption can be ensured by a PV system focusing on the calibration of the domestic electric meters of the national electricity supply. To succeed, we review a broad and recent literature in order to highlight the key drivers and uncertainties of PV systems costs, prices, and potential regarding economic indicators.

## 2. Material and Methods

*2.1. Field Site Location.* Burkina Faso is a landlocked country, located at the heart of west Africa, between the 9° and 15° of Northern latitude, the 2°30′ of eastern longitude, and the 5°30′ of western longitude. It covers a surface of 274 000 km$^2$ and is limited by six countries: Niger in the east; Mali in the north and the west; and Ivory Coast, Ghana, Togo, and Benin in the south. The total population is 17 million inhabitants in 2011 with an average annual growth simulated to be 3% over the period 2010–2015 [1]. Ouagadougou, the experimental site, is the capital of Burkina Faso located at the center of the country (Figure 1).


Figure 1: Location of the experimental site. Source: modified from CIA (from Central Intelligence Agency: https://www.cia.gov/library/publications/the-world-factbook/geos/uv.html).

*2.2. Households Energy Needs Survey.* Before the electrification of a site, it is compulsory to well know the energy demand of that site's inhabitants in order to adapt to the expected system's productivity. For this study, the data are acquired by campaigns carried out within a sample of five (5) households in Ouagadougou. There is one household in the district of Wemtenga, one in the district of Zogona, and three households in the district of Dassasgho. At Wemtenga and Dassasgho 01 where inhabitants pay for their electricity consumption by cash-power, daily electricity consumption measurements are carried out from 2012/11/09 to 2013/01/15. At Dassasgho 02, Dassasgho 03, and Zogona where inhabitants pay monthly for their electricity by bills, seven bills have been considered. As all the households' appliances work in alternative current (AC), the power of each household appliance is collected in order to well design the solar inverter power. Each average energetic need found is set constant during the year and is calculated by the following:

$$E_{ch,j} = \sum_{i=1}^{n} \left(P_i \times \Delta t_i\right). \quad (1)$$

$E_{ch,j}$ is the daily energy consumption [Wh/day], $i$ is the electric appliance, $n$ is the total number of electric appliances, $P_i$ is the nominal power of the electric appliance [W], and $\Delta t_i$ is the average daily duration of the operating appliance [h/day].

These households are thereafter divided into two classes according to their domestic meters calibration (3A (Amp) and 5A) and the effective cost of energy paid from SONABEL following the tariff grid of that company was calculated.

*2.3. Technical Considerations.* For a given household, technical aspects include the solar database and the design of

the size of the main components of the PV system such as modules, batteries, inverter, and regulator. The system positioning and other technical considerations are also taken into account.

*2.3.1. Solar Data Acquisition.* Before any design of system PV, it is important to know the solar resource at the site of study because the weather data influence the productivity of system PV a lot. All databases used for solar data acquisition are tools for decision-makers and investors especially during the analysis of the financial resources during the projects of rural electrification [6, 7]. For this study, we used the database RETScreen previously used by Leng et al. [8], RNCan [9], RNCan [10], Suri et al. [6], Gifford et al. [11], Mermoud [12], and Mermoud and Lejeune [13].

*2.3.2. Design of Modules Nominal Power.* The PV module performance is highly affected by the solar irradiance and the PV module temperature. In this paper, a simplified equation is used to estimate the PV module nominal power [14]:

$$P_{\mathrm{PV}} = \frac{E_{ch,j}}{\mathrm{PR} \times E_{i,\mathrm{def}}}, \tag{2}$$

where $P_{\mathrm{PV}}$ is the expected photovoltaic nominal power [$W_p$]; $E_{ch,j}$ is the daily energy needs [Wh/day]; PR is the performance ratio of the photovoltaic field; and $E_{i,\mathrm{def}}$ is the daily solar irradiation received in the plan of the modules in the most unfavorable month of the year [kWh/$m^2$/day].

*2.3.3. Determination of Inverter Power.* The inverter is the device of power electronics which allows converting the direct current (DC) to the alternative current (AC) for AC loads. The nominal power transiting the inverter to serve the demand is given by the following [15]:

$$P_{n,\mathrm{ond}} = \frac{P_{\mathrm{AC}}}{\eta_{\mathrm{ond}} \times \cos\varphi \times k_{\mathrm{loss}}}, \tag{3}$$

where $P_{n,\mathrm{ond}}$ is the nominal output power of the inverter [W]; $P_{\mathrm{AC}}$ is the total power load in alternative current [W]; $\eta_{\mathrm{ond}}$ is the inverter efficiency [%]; $\cos\varphi$ is the power's factor; and $k_{\mathrm{loss}}$ is the reduction coefficient related to the losses in the cables.

Note that the ratio between $P_{\mathrm{PV}}$ and $P_{n,\mathrm{ond}}$ will hold between 0.7 and 1.2 according to PERACOD [16].

*2.3.4. Design of Regulator Output Intensity.* A regulator is the device which monitors the quantity of electricity, injected or tapped, corresponding to the capacity of the batteries installed. It is dimensioned by its input intensity, given by the following [17]:

$$I_{\mathrm{reg}} = \frac{N_{\mathrm{PV}} \times P_{\mathrm{PV},i}}{N_{\mathrm{PV},s} \times \eta_{\mathrm{reg}} \times U_{\mathrm{mod}}}, \tag{4}$$

where $I_{\mathrm{reg}}$ is the regulator input intensity [A], $N_{\mathrm{PV}}$ is the total number of PV modules, $P_{\mathrm{PV},i}$ is the unit nominal power of module [$W_p$], $N_{\mathrm{PV},s}$ is the PV modules number in series, $\eta_{\mathrm{reg}}$ is the regulator efficiency [%], and $U_{\mathrm{mod}}$ is the nominal system operating voltage [V].

*2.3.5. Calculation of Battery Park Size.* Because the periods of consumption always do not correspond to the hours of production, a park of batteries is installed to store produced energy. The batteries are in charge during the periods of day in order to be able to feed the site in the night or the days of very bad weather. The capacity of the park of batteries is calculated by the following equation [15, 18]:

$$C_{\mathrm{bat}} = \frac{E_{ch,j} \times \mathrm{Aut}}{\eta_{\mathrm{bat}} \times \mathrm{DOD} \times U_{\mathrm{bat}}}, \tag{5}$$

where $C_{\mathrm{bat}}$ is the capacity of the batteries park [Ah]; Aut is the charged batteries autonomy [day]; $\eta_{\mathrm{bat}}$ is the battery efficiency at discharge phase [%]; DOD is the battery authorized discharge depth [-]; and $U_{\mathrm{bat}}$ is the battery voltage [V].

*2.4. Financial Analysis.* Financial analysis is ensured by the software RETScreen. The formulas used are based on the current financial terminology which can be found in the majority of the handbooks of financial analysis. The model makes the following assumptions:

(i) the year of initial investment is the year 0;

(ii) the costs and the appropriations are given for year 0 and consequently the inflation rate and the energy indexation rate are applied from year 1;

(iii) the calculation of monetary flows is carried out at the end of each year.

Frequently, it is difficult for the project recipient to cover all the expenses related to the project. In that case, this person can resort to a loan from a bank. Thus, the total cost of the project is composed of the equity at year 0 and annual payments of the debt and the expenses for operations and maintenance and the replacements in the following years.

*2.4.1. Investment Cost.* The calculation of the cost of the components of the solar kit is the most delicate part of the work because that represents the initial capital cost of the solar project. An estimate will be elaborate focusing on the most economic possible aspects beginning with the initial gross investment ($C_i$) calculated by (6) based on Table 2:

$$C_i = P_{\mathrm{PV}} \times A + C_{\mathrm{bat}} \times B + P_{n,\mathrm{ond}} \times C + I_{\mathrm{reg}} \times D, \tag{6}$$

where $C_i$ is the initial gross investment in FCFA and $A$, $B$, $C$, and $D$ are, respectively, the chosen specific price of module, battery, inverter, and regulator in FCFA as shown in Table 1.

The costs of the other elements of the balance-of-system (BOS) such as cables, structure, and all installation costs are applied with a weighting factor ($\delta$) to $C_i$. Thus, the initial total investment ($C_t$) is calculated by the following equation:

$$C_t = (1 + \delta) \times C_{i,\mathrm{syst}}, \tag{7}$$

where $C_t$ is the total initial investment in FCFA and $\delta$ is the weighting factor for the other costs.

The operations and maintenance (O&M) are adjusted on the basis of annual cost during the period of analysis of the

Table 1: Solar energy system's components costs.

| Components | Specific price | Sources | Chosen specific price | |
|---|---|---|---|---|
| | | | FCFA/U | Euro[1]/U |
| Module (FCFA/Wp) | 374 | Sunny Uplands[2] [31], PHOTON[3] | 374 | 0.57 |
| | 577 | Rigter and Vidican[4] [29] | | |
| | 1640 | Szabó et al. [7] | | |
| | 3936 | Bilal et al. [17] | | |
| Battery (FCFA/kWh[5]) | 69536 | Semassou [15] | 69536 | 107.07 |
| | 75440 | Sunny Uplands [31] | | |
| | 82000 | Szabó et al. [7] | | |
| | 113707 | Bilal et al. [17] | | |
| Inverter (FCFA/W) | 190 | PHOTON | 190 | 0.29 |
| | 328 | Semassou [15] | | |
| | 348 | Rigter and Vidican[6] [29] | | |
| | 524 | Bilal et al. [17] | | |
| Regulator (FCFA/A) | 3280 | Intigaia[7] | 3280 | 5.00 |
| | 5051 | Bilal et al. [17] | | |

[1] With 1 Euro = 656.576 FCFA as currencies conversion chosen
[2] Value simulated for the year 2012.
[3] PHOTON-Newsletter for 2013/01/11 concerning inverters and module price index: http://www.photon.info.
[4] Simulation carried out according to the fall of the module cost for the year 2012.
[5] Cost of AGM lead-acid batteries of nominal voltage of 12 V.
[6] This cost refers to a simulation carried out according to the fall of the price of the inverters for the year 2012.
[7] http://intigaia.free.fr/.

Table 2: Estimate of the average cost of the electricity consumed from SONABEL.

| Components | Wemtenga | Dassasgho 01 | Dassasgho 02 | Dassasgho 03 | Zogona |
|---|---|---|---|---|---|
| Characteristic | | | | | |
| Type of bill | Cash-power | Cash-power | Bill per month | Bill per month | Bill per month |
| Amperage | 5A | 5A | 5A | 3A | 3A |
| AC loads (W) | 431 | 2556 | 210 | 1235 | 496 |
| Electricity | | | | | |
| Mean electricity consumption (kWh/month) | 54 | 161 | 15 | 48 | 79 |
| Cost of the first electricity consumption level (FCFA/kWh) | 96 | 96 | 96 | 75 | 75 |
| Rough cost (FCFA/month) | 5198 | 16149[1] | 1440 | 3575 | 6137[2] |
| Total taxes cost[3] (FCFA/month) | 2446 | 3091 | 2326 | 1326 | 1527 |
| Proportion of the taxes [%] | 32 | 16 | 62 | 27 | 20 |
| Monthly total cost (FCFA/month) | 7644 | 19240 | 3766 | 4901 | 7664 |
| Monthly specific cost | | | | | |
| FCFA/kWh | 141 | 119 | 256 | 105 | 97 |
| Euro[4]/kWh | 0.22 | 0.18 | 0.39 | 0.16 | 0.15 |

[1] This cost includes the invoicing of the first section (1 to 50 kWh) and that of the second section (51 to 200 kWh) which costs 102 FCFA/kWh.
[2] This cost includes the invoicing of the first section (1 to 50 kWh) and that of the second section (51 to 200 kWh) which costs 102 FCFA/kWh.
[3] Including all taxes.
[4] With 1 Euro = 656.576 FCFA as currencies conversion chosen.

project. In this work, the O&M relate to the replacement of the batteries, the inverter, and the regulator and we considered that the system is free from other maintenances during the project lifetime.

*2.4.2. Risk Analysis.* An investor or a banker will use the capacities of analysis of sensitivity and risk available in each model in order to evaluate the risk associated with the investment in a given project. For this study, we made only risk assessment on the NPV with RETScreen. That allowed evaluating how uncertainty in the estimate of this parameter (NPV) can affect the financial viability of the project.

*2.4.3. Levelized Cost of Energy.* The Levelized Cost of Energy (LCOE) is calculated by considering the cost of the energy

consumed (8) because in the remote village, most of the energy generated is lost [17, 19] as follows:

$$\mathrm{LCOE} = \frac{(1 - f_d)\, I + \sum_{n=1}^{N} \left[C_{\mathrm{an}} (1 + \lambda)^n + D\right]}{\sum_{n=1}^{N} E_{\mathrm{an}} (1 + r)^n}, \quad (8)$$

where LCOE is the effective cost of the energy consumed from the system (FCFA/kWh), $I$ is the total capital cost of the project [FCFA], $f_d$ is the debt ratio, $N$ is the project lifetime in years, $n$ is the considered year, $C_{\mathrm{an}}$ is the annual expenditure [FCFA], $\lambda$ is the inflation rate, $D$ is the annual debt payment [FCFA], $E_{\mathrm{an}}$ is the annual electricity consumption [kWh/year], and $r$ is the energy indexation rate.

*2.4.4. Retained Assumptions and Financial Viability Parameters Simulation.* The retained PR is 0.75 [6]. The assumed $\eta_{\mathrm{ond}}$ is 92% [20], and $\cos\varphi$ and $k_{\mathrm{loss}}$ are, respectively, set at 0.9 and 0.85 [15]. The assumed $N_{\mathrm{PV},s}$ is 1 and $\eta_{\mathrm{reg}}$ is 95% [21]. The assumed DOD is 80% [22], $\eta_{\mathrm{bat}}$ is 85% [23], and Aut is three (3) days [21, 23]. The weighting factor ($\delta$) is set at 12%. O&M are set at 2.7% per year from the total initial investment.

In order to carry out the financial analyses of the feasibility of the project, we considered a project lifetime of the 25 years. All monetary flows are handled in constant currency with an interest rate of 7.5% for the loan considered. The rate of the loan considered is 75% and the equity is set at 25%. The inflation rate retained is 2.8%, the indexation of the SONABEL energy rate is 4%, and the real discount rate is 5%. All the financial viability parameters such as internal rate of return (IRR), simple payback, equity payback, and net present value (NPV) are simulated by the software RETScreen.

## 3. Results and Discussion

*3.1. Solar Irradiation and Energy Delivered to Load.* Simulation carried out shows that the general trend of yearly global irradiations evolution is similar (Figure 2). Nevertheless, significant differences are observable at monthly scale.

Note that daily solar irradiation on tilted plan is higher than that on horizontal plan from September to March and lower the following months of the year. But on average, solar irradiation on the tilted plan is higher than that on the horizontal plan with 6.03 kWh/m$^2$/day against 5.91 kWh/m$^2$/day, respectively. As result, a transposition factor of 1.022 which represents an increase of 2.2% of productivity is found. August is the month in which the daily solar irradiation is the smallest on the tilted plan with the value of 5.15 kWh/m$^2$/day. This value has been used for the design of the PV modules size.

*3.2. Households Energy Demands and Costs.* Campaigns carried out indicate that the energy consumed in the households is mainly dominated by lighting (lamps), cold (ventilators and refrigerators), and electronic appliances (radios, televisions, iPad, and computers). These uses are the same as that shown by Liebard et al. [24] for 12 studied villages in the province of Kourittenga (Burkina Faso). However, it is remarkable to indicate that refrigerator used at Dassasgho 01 consumes more energy because it belongs to an old energetic class. Domestic iron used as heating is found at Dassasgho 01 and Dassasgho 03.

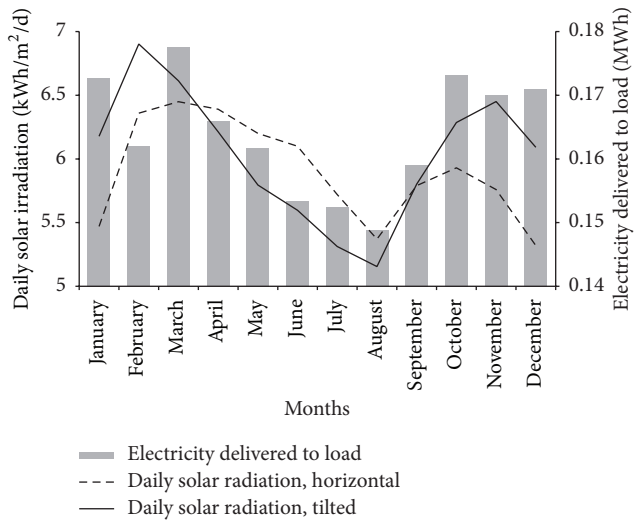


FIGURE 2: Global irradiation on full south fixed plans (principal axis) and energy delivered to load (secondary axis). The inclination angle is 15°. Data simulated by RETScreen.

Once again, Dassasgho 01 uses an electrical appliance (iron) which consumes energy a lot. Note that energy consumptions vary from a household to another. The high energy consumption is observed at Dassasgho 01 and the low one at Dassasgho 02. In fact, the dependent taxes to the bill decrease when the electrical consumptions increase for a given domestic electric calibration meters. When the electrical consumption is less than 161 kWh/month in Burkina Faso, it is desirable to gauge the domestic electric meters at 3A. With these energy consumptions, high specific electricity bills are found at Dassasgho 02 and Wemtenga. The domestic electric meters of inhabitants of these households are gauged at 5A and these inhabitants pay more than 30% of their bill as taxes. However, inhabitants at Dassasgho 01 who use the same electric calibration meters pay only 16% as taxes for their bill. That cost is low at Zogona and Dassasgho 03 where inhabitants' domestic meter calibration is 3A (Table 2).

According to the calibration of the electric meter within each household and the tariff grid used for electricity cost calculation, we classified the households into favorable, unfavorable, and buffer zone (Figure 3). Thus, Wemtenga and Dassasgho 02 are located in the "5A unfavorable area," Dassasgho 03 and Zogona are located in the "3A favorable area," and Dassasgho 01 is located at the boundary of the two evoked areas called "buffer area."

*3.3. Solar Components Characteristics.* According to energy needs collected, the voltage retained for all components (modules, regulator, battery, and inverter) at Wemtenga, Dassasgho 02, Dassasgho 03, and Zogona is 12 V, while it was considered to be 24 V at Dassasgho 01, where the electric consumption is significant. For all households, we

Table 3: Characteristics of the PV system components.

| Components | Modules $P_{PV}$ [$W_p$] | Inverter $P_{n,ond}$ [W] | Battery $C_{bat}$ [Ah] | Regulator $I_{reg}$ [A] |
|---|---|---|---|---|
| Wemtenga | 575 | 500 | 575 | 48 |
| Dassasgho 01 | 1680 | 2000 | 840* | 70 |
| Dassasgho 02 | 155 | 200 | 155 | 15 |
| Dassasgho 03 | 500 | 700 | 500 | 45 |
| Zogona | 840 | 800 | 840 | 70 |

*$U_{bat}$ is 24 V; $C_{bat}$ would be equal to $P_{PV}$ value if $U_{bat}$ was also 12 V.

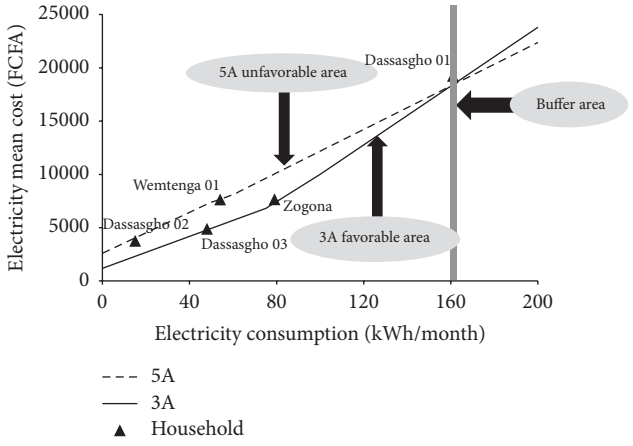


Figure 3: Households consumption according to the calibration of the meters. The cost of the electricity is calculated according to SONABEL tariff grid.

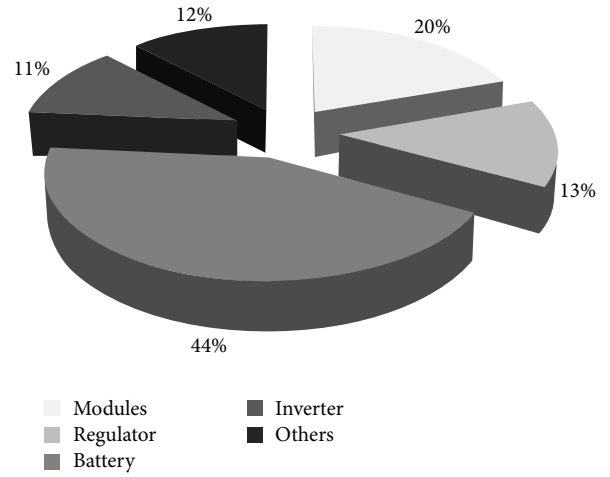


Figure 4: Solar system components costs at the beginning of the project. "Others" represents cables, installation, and transport.

chose the solar polycrystalline silicon modules of PHOTOWATT (PHOTOWATT is only chosen for simulation, not for economic aspects) for the simulation. All characteristics of the PV systems components are illustrated in Table 3. Components parameters values increase with the increase of household inhabitants energy demand. Note that, in value, the module nominal power equals the capacity of the park of batteries, which is interesting to make comparisons between systems' total cost thereafter. However, inverter's power seems strongly overestimated at Dassasgho 03, meaning that system total cost would be increased.

In the same way, it seems to be underestimated at Wemtenga, meaning that the system total cost would be decreased there. All the inverter power misestimation would distort the PV energy cost when analyzing economic aspects.

Figure 4 shows that modules participate at only 20% of the initial cost. Batteries are the most expensive PV component with 44% (Figure 4) and that percentage will reach about 65% of course of their replacements during the project lifetime.

*3.4. Monetary Flows and Financial Viability Parameters Analysis.* By considering the cumulative cash-flows, Wemtenga and Dassasgho 01 and Dassasgho 02 answer favorably to the project reliability because monetary flows are above the "null flow threshold" (Figure 5). That indicates that projects are viable in both households located in 5A unfavorable area and buffer area, justified or not when analyzing economic viability parameters.

Financial viability parameters show different approaches. IRR for equity is positive for Wemtenga and Dassasgho 01 and Dassasgho 02. However, it is lower than 5% at Dassasgho 01, indicating that the project is not viable there. On the one hand, simple payback and equity payback for these three households are less than the expected project lifetime of 25 years, meaning that the projects are viable there. But, by considering the recommendation of PERACOD [16], the project would be more viable at an equity payback of more 15 years.

On the other hand, NPV, main parameter in project analysis, indicate that only Wemtenga and Dassasgho 02 economically satisfy the project. For Zogona and Dassasgho 03, all financial viability parameters are potentially unfavorable for project feasibility (Table 4).

The loan ration taken at 75% seems justified for a kind of project. In fact, according to PERACOD [16], a project with a high loan rate would cost higher than that which is totally financed by the project owner. However, seeing the high investment cost, that project owner would rather become reticent. The interest rate of 7.5% on the loan admitted for the project seems reasonable according to BAfD et al. [25] because this is the rate which is applied by SGB (Société Générale des Banques) for the PV projects in Burkina Faso. However, the management of monetary flows over the

Table 4: Financial viability parameters simulated by RETScreen. Project lifetime was set at 25 years.

| Financial viability | Wemtenga | Dassasgho 01 | Dassasgho 02 | Dassasgho 03 | Zogona |
|---|---|---|---|---|---|
| IRR-equity (%) | 8.6 | 3.5 | 31.5 | −4.7 | −6.1 |
| Simple payback (years) | 16.9 | 21.2 | 8.2 | 30.2 | 31.8 |
| Equity payback (years) | 14.4 | 20.5 | 3.7 | >project | >project |
| NPV | | | | | |
| FCFA | 208340 | −225268 | 491367 | −385479 | −668860 |
| Euro[1] | 317.8 | −343.6 | 749.5 | −588.0 | −1020.3 |

[1] With 1 Euro = 656.576 FCFA as currencies conversion chosen.

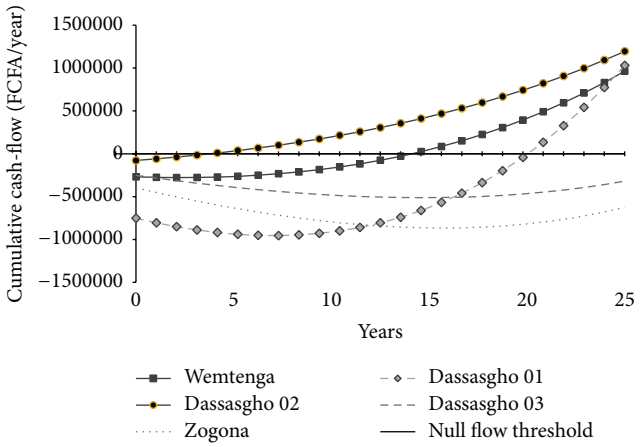


Figure 5: Cumulative cash-flows simulated by RETScreen. Note that cash-flows from Zogona and Dassasgho 03 (in broken line) which use a domestic meter calibration of 3A are below null flow line.

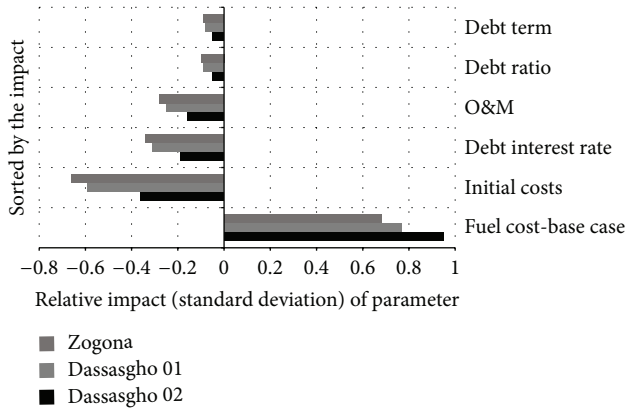


Figure 6: NPV risk analysis at a range of 10% evaluated by RETScreen. All costs in FCFA XOF and the debt term in a year for a real discount rate of 5%. Negative values indicate outcome, while positive values indicate income (savings).

duration of 25 years seems not to correspond to that applied by this company because SGB only allows the refunding of the loan over a loan term of 7 years, which could make the project compared to these 25 years less viable. The inflation rate taken at 2.8% is the same as that simulated by CIA World Factbook (https://www.cia.gov/library/publications/the-world-factbook/geos/uv.html) [26] and BAfD et al. [25] for Burkina Faso for 2013.

Indeed, that rate of 2.7% applied at O&M cost during the project lifetime seems correct. In fact, this value is slightly lower than that fixed by Short et al. [27] who admit it to be at 1-2. The energy indexation rate of 4% is different from AGIR [28] consideration. For that author, this rate was the same as the inflation rate in a study realized in France. We chose this rate because of the fluctuations of electricity cost like oil in Burkina Faso. We also chose a real discount rate of 5% like Liebard et al. [24] and Semassou [15] in their projects analysis in Burkina Faso and Benin, respectively. This rate respects Szabó et al. [7] recommendations for PV projects in Africa.

*3.5. Risk Analysis on NPV.* The analysis of the risk went primarily on the clear brought up to date values related to the project starting from the studied indicators. This is because this economic parameter interests more investors before the realization of their project. This analysis is also carried out in three strategic households such as Dassasgho 02, located in the 5A unfavorable zone, Zogona, located in the 3A favorable area, and Dassasgho 01, located in the buffer zone. For all these indicators, the rate of the risk which is chosen to be at 10% made it possible to show that the risk related to the project is strong for the indicator "fuel cost-base case" followed by the "initial costs" as indicated in Figure 6. The analysis shows that the impact on the NPV is stronger for the "fuel cost-base case" for households located in the 5A unfavorable zone. That means that, in these households, NPV are based on this indicator and are exposed to the risk that their projects could not be viable if the "fuel cost-base case" decreases, conversely to the 3A favorable area. For these households, the "initial costs" rather seem to be the major indicator in the risk on the NPV. A project will be profitable if the cost of the PV system components strongly decreases.

*3.6. PV and SONABEL Energy Costs.* Figure 7 shows that, for households located in the 3A favorable area (Dassasgho 03 and Zogona), LCOE is higher than that of the national network electricity cost, meaning that PV projects are not viable there. When the power consumption is slow and is located in the 5A unfavorable zone, the PV projects become profitable. However, by recommending the energy effectiveness in each household when realizing preliminary projects, Wemtenga and Dassasgho 02 would have their

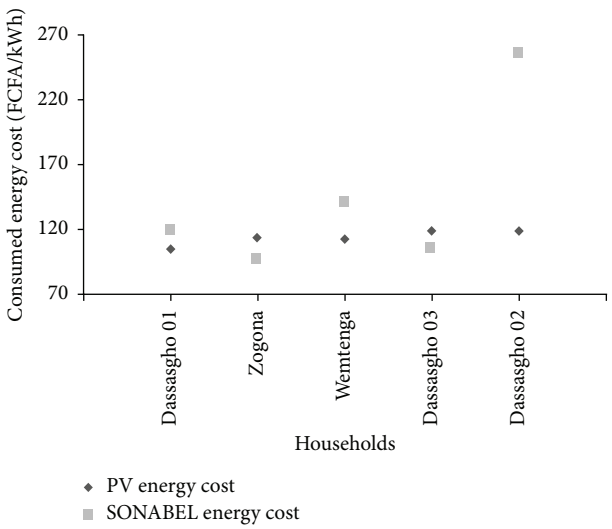


Figure 7: PV and SONABEL consumed energy costs. Households ranged from the highest energy consumption to the lowest one, like PV energy's expected costs.

domestic electric meters being changed into 3A and would not have viable PV projects.

LCOE calculated range is from 105 FCFA/kWh (Dassasgho 01) to 119 FCFA/kWh (Dassasgho 02) that is from the highest energy consumption to the lowest one. In our case, LCOE at Wemtenga is lower than that at Zogona and LCOE at Dassasgho 03 is equal to that at Dassasgho 03. The explanation given to these illogical results could reside on several assumptions carried out and the calculations uncertainties when editing the estimates of the projects especially on the misestimation of inverters nominal powers as revealed before.

The mean LCOE of 112 FCFA/kWh calculated seems realistic. The project carried out by Rigter and Vidican [29] gives an average LCOE of 132 FCFA/kWh with a discount rate of 7% for investments in PV solar project. This cost is slightly higher than those calculated there. According to BNEF, the LCOE in the first quarter of the year 2012 ranged between 81 FCFA/kWh and 126 FCFA/kWh for residential solar projects (NREL 2009 in [4]). This interval of LCOE perfectly includes those calculated in this study. Regarding the LCOE compared to SONABEL energy cost in the favorable cases focusing on the domestic meters calibration, it is clear that LCOE of PV systems remain high. That is proved in almost all countries of Africa as shown by Szabó et al. [7] studies carried out in African rural area. This is why certain authors [4, 5, 7, 18] propose to turn towards hybrid systems in order to make the system more competitive. Indeed, Lemaire [30] simply analyzes that technologies of renewable energy, and mainly the PV systems, are typically expensive, thus out of the rural populations portfolio in a development country. Note that to be economically viable, the PV projects carried out in Burkina Faso at a local scale need aids from the government. Moreover, the recipients of those projects deserve to be encouraged through flexibility on behalf of the banks.

## 4. Conclusion

The objective of this study is to show the hearths in which electric consumption can be ensured by an autonomous system PV instead of national network. In order to reach this objective, investigations near five households with weak average consumption power in Ouagadougou were realized. All these hearths which use the electricity of the national network were initially classified into zones of favorable, unfavorable use, and plug in comparison with the calibration of their electric meters. According to the energy needs for each household, a solar kit was dimensioned. The configuration retained for the success of the project resides in the optimization of the energy received in the field of the fixed sensors by a slope of 15 directed full south from the plan of the module by the use of the RETScreen model. Estimates were published on the most economic possible bases according to the data obtained. Using this model of analysis of clean projects of energies, the evaluation of the financial viability of each autonomous solar project in Ouagadougou was made. The results indicate that only the class of the households which use electric meters of the national network in their discredit has a level of competitiveness raised for solar projects.

The situation becomes even darker if incompressible needs were made and one gave a detailed attention to the calibration of the electric meter before performing the analysis of feasibility of the solar projects in Ouagadougou. However, the recourse for these projects can prove the justification for households with great power consumption or if subsidies could be brought on behalf of the government in order to encourage the recipients. Today, the economic situation of the majority of the countries of West Africa does not favor an ambitious energy policy directed towards the rural world. The funds of research development remain insufficient in spite of the efforts authorized by the countries. Even if it is true that the exploitation of the majority of the solar systems does not require significant expenses apart from some trickle charges, the initial investment makes them less competitive compared to the traditional energy sources.

## Nomenclature

*Abbreviations*

| | |
|---|---|
| CCI-BF: | Chambre de Commerce et d'Industrie du Burkina Faso (Trading and Industry Room of Burkina Faso) |
| ECOWAS: | Economic Community of the of West Africa States |
| FCFA: | Franc de la Communauté Financière Africaine (designating the currency used by many West African and Pacific countries) |
| NPV: | Net present value |
| PNUE: | Programme des Nations Unies pour l'Environnement for United Nation of Environment Program |
| PV: | Photovoltaic |

RETScreen: Renewable Energy Project Analysis Software
SONABEL: Société Nationale d'Electricité du Burkina Faso (National Electricity Society of Burkina)
UNDP: United Nations Development Program.

*Symbols*

$\Delta t_i$: The average daily duration of the operating appliance
$A$, $B$, $C$, and $D$: The chosen specific price of module, battery, inverter, and regulator, respectively
Aut: The charged batteries autonomy
$C_{\text{bat}}$: The capacity of the batteries park
$C_i$: The initial gross investment
$\cos\varphi$: The power's factor
$C_t$: The total initial investment
$D$: The annual debt payment
DOD: The battery authorized discharge depth
$E_{\text{an}}$: The annual electricity consumption
$E_{ch,j}$: The daily energy consumption
$E_{i,\text{def}}$: The daily solar irradiation in the plan of the modules in the most unfavorable month of the year
$f_d$: The debt ratio
$i$: The electric appliance
$I$: The total capital cost of the project
$I_{\text{reg}}$: The regulator input intensity
$k_{\text{loss}}$: The reduction coefficient related to the losses in the cables
LCOE: The effective cost of the energy consumed from the system
$n$: The total number of electric appliances
$N$: The project lifetime in years
$N_{\text{PV},s}$: The PV modules number in series
$N_{\text{PV}}$: The total number of PV modules
$P_{\text{AC}}$: The total power load in alternative current
$P_i$: The nominal power of the electric appliance
$P_{n,\text{ond}}$: The nominal output power of the inverter
$P_{\text{PV},i}$: The unit nominal power of module
$P_{\text{PV}}$: The expected photovoltaic nominal power
PR: The performance ratio of the photovoltaic field
$U_{\text{bat}}$: The battery voltage
$U_{\text{mod}}$: The nominal system operating voltage
$\delta$: The weighting factor for the other costs of the photovoltaic system
$\eta_{\text{bat}}$: The battery efficiency at discharge phase
$\eta_{\text{ond}}$: The inverter efficiency
$\eta_{\text{reg}}$: The regulator efficiency
$\lambda$: The inflation rate.

## Conflict of Interests

The authors declare that there is no conflict of interests regarding the publication of this paper.

## References


[1] UNDP, "Sustainability and equity: a better future for all," Human Development Report 2011, UNDP, New York, NY, USA, 2011, http://hdr.undp.org/sites/default/files/reports/271/hdr_2011_en_complete.pdf.

[2] PNUE, "Vers une économie verte: Pour un développement durable et une éradication de la pauvreté," Synthèse à l'intention des décideurs, 2011, http://www.unep.org/greeneconomy/.

[3] CCI-BF, *Note Sectorielle sur l'Énergie au Burkina Faso*, Direction de la Prospective et de l'Intelligence Economique (DPIE), 2010.

[4] M. Bazilian, I. Onyeji, M. Liebreich et al., *Re-Considering the Economics of Photovoltaic Power*, Bloomberg New Energy Finance (BNEF), 2012.

[5] M. Bhatia, J. Levin, and V. Atur, "Financing renewable energy: options for developing financing instruments using public funds," World Bank & CIF, 2012.

[6] M. Suri, T. A. Huld, E. D. Dunlop, M. Albuisson, and L. Wald, "Online data and tools for estimation of solar electricity in Africa: the PVGIS approach," in *Proceedings of the 21st European Photovoltaic Solar Energy Conference and Exhibition*, p. 4, Dresden, Germany, October 2006.

[7] S. Szabó, K. Bódis, T. Huld, and M. Moner-Girona, "Energy solutions in rural Africa: mapping electrification costs of distributed solar and diesel generation versus grid extension," *Environmental Research Letters*, vol. 6, no. 3, Article ID 034002, 2011.

[8] G. L. Leng, A. Monarque, S. Graham, S. Higgins, and H. Cleghorn, *RETScreen International: Results and Impacts 1996–2012*, Natural Resources Canada, CTEC-Varennes, 2004.

[9] RNCan, *Logiciel RETScreen: Manuel de l'Utilisateur en Ligne*, NASA, PNUE et GEF, 2005.

[10] RNCan, *Analyse de projets d'énergies propres: manuel d'ingénierie et d'études de cas RETScreen, chapitre introduction à l'analyse de projets d'énergies propres*, Centre de la technologie de l'énergie de CANMET—(CTEC), Varennes, Canada, 2006.

[11] J. S. Gifford, R. C. Grace, and W. H. Rickerson, *Renewable Energy Cost Modeling: A Toolkit for Establishing Cost-Based Incentives in the United States*, National Renewable Energy Laboratory, 2011.

[12] A. Mermoud, *Note about PHOTON PV Software Survey*, Institut des Sciences de l'Environnement, Université de Genève, 2011, http://www.pvsyst.com.

[13] A. Mermoud and T. Lejeune, "User's Guide PVsyst: Contextual Help," PVsyst SA, 2012, http://www.pvsyst.com.

[14] M. Chikh, A. Mahrane, and F. Bouachri, "PVSST 1.0 sizing and simulation tool for PV systems," *Energy Procedia*, vol. 6, pp. 75–84, 2011.

[15] C. Semassou, *Aide à la décision pour le choix de sites et systèmes énergétiques adaptés aux besoins du Benin [Ph.D. thesis]*, University of Bordeaux, Talence, France, 2011.

[16] PERACOD, "Etude de faisabilité technico-économique de la filière photovoltaïque raccordée réseau au Sénégal," Direction de l'énergie, Sénégal et GTZ, Allemagne, 2006.

[17] B. O. Bilal, V. Sambou, C. M. F. Kébé, P. A. Ndiaye, and M. Ndongo, "Methodology to size an optimal stand-alone PV/wind/diesel/battery system minimizing the levelized cost of energy and the $CO_2$ emissions," in *Proceedings of the 2nd International Conference on Advances in Energy Engineering (ICAEE '11)*, vol. 14 of *Energy Procedia*, pp. 1636–1647, Bangkok, Thailand, December 2011.

[18] SMA, "Approvisionnement en énergie solaire des sites isolés et systèmes de secours: principes, applications et solutions SMA," Recueil Technologique 2, INSELVERSOR-AFR104310, 2010.

[19] P. G. Nikhil and D. Subhakar, "An improved algorithm for photovoltaic system sizing," *Energy Procedia*, vol. 14, pp. 1134–1142, 2012, Proceedings of the 2nd International Conference on Advances in Energy Engineering.

[20] S. S. Tassembedo, S. Z. Kam, Z. Koalaga, and F. Zougmore, "Modélisation, dimensionnement et simulation d'un système photovoltaïque autonome: cas d'un centre multimédia rural burkinabè," in *2eme Colloque International Francophone d'Energétique et de Mécanique (CIFEM '12)*, ART-5-35, p. 6, 2012.

[21] PACER, *Installations Photovoltaïques Autonomes: Guide Pour le Dimensionnement et la Réalisation*, PACER & Direction du Développement et de la Coopération, 2007.

[22] A. Ricaud, *Modules et Systèmes Photovoltaïques*, 2008.

[23] V. Acquaviva, *Analyse de l'intégration des systèmes énergétiques à sources renouvelables dans les réseaux électriques insulaires [Ph.D. thesis]*, University of Corse, Corte, France, 2011.

[24] A. Liebard, Y. B. Civel, Y. Maigne, N. Guichard, C. Rigaud, and S. Salès, "De l'électricité verte pour cent mille ruraux au Burkina Faso," Fondation Energies Pour le Monde, Ministère des Mines, des Carrières et de l'Energie, 2010.

[25] BAfD, OCDE, PNUD et CEA 2012, "Burkina Faso—Perspectives économiques en Afrique", http://www.africaneconomicoutlook.org.

[26] CIA World Factbook 2012, Taux d'inflation (indice des prix à la consommation)—Monde, March 2013, https://www.cia.gov/library/publications/the-world-factbook/geos/uv.html.

[27] W. Short, D. J. Packey, and T. Holt, "Manual for the economic evaluation of energy efficiency and renewable energy technologies," Tech. Rep. NREL/TP-462-5173, National Renewable Energy Laboratory, 1995.

[28] AGIR, "Générez des revenus grâce au photovoltaïque," Guide du Photovoltaïque, 2010.

[29] J. Rigter and G. Vidican, "Cost and optimal feed-in tariff for small scale photovoltaic systems in China," *Energy Policy*, vol. 45, no. 11, pp. 6989–7000, 2010.

[30] X. Lemaire, "Fee-for-service companies for rural electrification with photovoltaic systems: the case of Zambia," *Energy for Sustainable Development*, vol. 13, no. 1, pp. 18–23, 2009.

[31] Sunny Uplands, "Alternative energy will no longer be alternative," The Economist, 2012, http://www.economist.com/news/21566414-alternative-energy-will-no-longer-be-alternative-sunny-uplands.

Hindawi Publishing Corporation
International Journal of Photoenergy
Volume 2016, Article ID 5410759, 10 pages
http://dx.doi.org/10.1155/2016/5410759

*Research Article*

# Design and Implementation of Automatic Wheat Mower Based on Smart Sensor Fed by a Photovoltaic

**Hikmet Esen,[1] Abdullah Kapicioglu,[2] and Onur Ozsolak[3]**

[1]*Department of Energy Systems Engineering, Faculty of Technology, Firat University, 23119 Elazig, Turkey*
[2]*Department of Automotive Engineering, Faculty of Technology, Cumhuriyet University, 58100 Sivas, Turkey*
[3]*Department of Manufacturing Engineering, Faculty of Technology, Cumhuriyet University, 58100 Sivas, Turkey*

Correspondence should be addressed to Hikmet Esen; esenhikmet@gmail.com

Received 4 August 2015; Revised 19 November 2015; Accepted 30 November 2015

Academic Editor: Clito Afonso



The biggest problems of our time are environmental pollution and the reduction of fossil fuel resources. In recent years, photovoltaic (PV) has started to be used efficiently in order to produce electrical energy from solar energy throughout the world. In this study, a wheat mover machine taking its energy with PV technology transformation from the sun was designed supported by smart sensors. The designed vehicle was tested in two wheat fields in Sivas in Turkey. It was seen that daily average sunshine rates were not lower than 700 Watt/$m^2$ during the testing dates and time. The amounts of electrical charge used to mow 5 $m^2$ and 50 $m^2$ areas are obtained as 500 mAh and 3395 mAh, respectively. Also maximum power is calculated from used PV panel as 26.15 Watt during the day of the experiments. The range of solar radiation intensity is found 4.5 kWh/$m^2$/day at the studied kWh which was \$0.140 USD on the date of November 2015. This system is 94.5% more economic than conventional mowers over an area of 1000 $m^2$.

## 1. Introduction

The energy resources used in the world are formed as a result of burning of fossil fuels. But burning of fossil fuels generates carbon dioxide ($CO_2$) and other greenhouse gases and increases density of them in the atmosphere. The accumulation of $CO_2$, methane ($CH_4$), and di-nitrogen monoxide ($N_2O$) gases in the atmosphere has increased because of human effects since 1750 and this value has reached the highest level for the last 800.000 years. Accumulation of these gases for the year 2011 has raised by 40%, 150%, and 20%, respectively, when compared to preindustrial levels and increased to 391 parts per million (ppm), 1803 parts per billion (ppb), and 324 ppb, respectively. The oceans have been acidified by absorbing about 30% of human related carbon. Average global surface temperature is predicted to increase 1.4–5.8°C at the end of 21th century depending on humans' fossil fuel usage [1]. Average sea level is predicted to increase 0.59 m depending on thermal expansion. This evaluation is presented based on the sea level between the years 1980 and 1999. Europe countries are mostly affected by these climatic changes. According to 2013 energy report, amount of carbon dioxide emission of EU countries caused by using fossil fuel was 4.174 millions of tons and 22% of this emission is generated by transportation [2]. A way of decreasing emission of greenhouse gases is to use electric vehicles instead of vehicles with internal combustion engine [3]. Using electric vehicles instead of diesel fuel powered vehicles that are commonly used in agriculture is inevitable in this change [4]. However, hybrid systems can be used with PV for these areas [5, 6]. When hybrid PV-diesel-battery systems that provide power for electricity supply in hot areas were analyzed, results demonstrated that 3 hours of battery storage of a 4 kWp PV panel with 10 kW diesel generator system can provide 22% of electricity supply [7]. It was reported that in agriculture 75% of chemical energy in batteries of an electrical vehicle whose energy requirement is provided by PV panel and lead acid batteries can be converted to mechanical energy [8]. In addition, usage of electric vehicle systems prevents 23% of carbon dioxide emission. However, lead acid batteries of this vehicles generate lead emission by 20.5% [9]. However, eliminating lead emission and achieving higher conversion

rates are possible with new technology batteries [10]. Battery sourced electric vehicles were analyzed in rural agricultural areas in South Mediterranean Region. It was found that usage of these vehicles instead of entirely internal combustion vehicles will provide 63% of required energy [11]. Stand-alone hybrid PV-diesel-battery power systems were assessed in a research for the purpose of using renewable energy in rural electrification in Saudi Arabia. Results of this study show that a hybrid system that consists of 2.5 MWp PV panel, 4.5 MW diesel generator, and 1-hour battery storage can provide 27% of electricity required and decreases the carbon emission by 24% compared to only diesel system [12].

The biggest problems of our time are environmental pollution and the reduction of fossil fuel resources. Vehicle manufacturers are making big research and development investments in order to produce vehicles having low emission values and fuel consumption. The rapid reduction of fossil fuel resources causes fluctuation of the fuel prices. The fluctuations affect mostly the agricultural sector heavily based on use of fossil fuels. In parallel to this development, since they do not produce emission and they are limitless, renewable energy resources attract more attention and they are more widely used day by day.

In this study, discrepantly from previous study, a vehicle with renewable energy that will be used for wheat mowing was designed and tested under real environment conditions. A prototype vehicle was tested for two mowing areas. Reactive working and being programmed for different conditions were enabled for the vehicle by supporting it with smart sensor system (SSS).

## 2. System Design

When smart sensor based wheat mower with photovoltaic power source (SPWM) is set as a prototype, a carrier vehicle is required. Sizes of this carrier vehicle are 85 cm × 64 cm. Prototype scheme and photograph of SPWM are shown in Figures 1(a) and 1(b), respectively.

Suspension system existing in daily vehicles also exists in the vehicle power transfer system where its design provides good movement ability for the prototype vehicle. There is a flexible solar panel placed on the carrier vehicle. Since this panel is both light and bendable it is useful for mobile applications. Charge control unit was placed underside of the panel. Function of this unit is making irregular voltage and current stable. Irregular voltage and current come from the panel. The charge control unit distributes the power that will feed all the system. Lithium polymer batteries are used in order to store required power for the system. Lithium polymer batteries are developed version of lithium-ion batteries that are already being used in electric vehicles. The batteries are formed by joining of 3.7 V cells. The batteries used in the system are two 5100 mAh batteries that have 11.1 V voltage and composed of joining of 3 cells. The reason for using a pair of batteries is allowing one of the batteries to be charged by the solar panel when the other one is functioning. The cost of batteries, inadequate space, and increment in weight of vehicle are other important factors for using only two batteries. Batteries are placed on the side of the carrier vehicle. Since these batteries need specifically developed chargers, they must be placed on the vehicle. The electrical energy that comes from charge control unit was primarily used for charging batteries with the help of lithium polymer charger. The batteries are charged with certain current and voltage. A higher current and voltage level shortens the lifetime of the batteries. Brushless DC motor that works within the ranges of 7.4 V and 22.2 V power was used in order to provide movement power that the vehicle requires. There is a sintered neodymium magnet with 19 mm diameter in rotor part of this brushless motor. A 2200 Kv brushless motor was used in our system. "Kv" mentioned here is a motor voltage constant that is used only for brushless motors and it means rotation rate of the motor per minute and per volt. This value is calculated as follows [13]:

$$\text{RPM} = \text{Kv}.\ \text{V}. \tag{1}$$

Brushless motors get required energy directly from the battery and they need special equipment named electronic speed control card. Electronic speed control unit arranges the rotation speed of the motor by regulating the voltage that flows to motor. The batteries also provide energy that SSS and cutting equipment requires. SSS used in SPWM system consists of two elements that evaluate the objects around itself in terms of distance and location. This evaluation is made by two-dimensional surface scanning. The former of these parts is the laser scanner that performs surface scanning with the help of laser beams and the latter is the connection module. The connection module is electronic devices that process data coming from laser scanner and submit to the last user as output. SSS used in this study can determine the location of all objects up to 270° and has the 3 W power consumption. While laser detector of SSS is placed in front of the vehicle, the connection module is placed to the back. The connection module which has 16 outputs is run by the help of a computer program. The program provides arrangement of many regulations from setting of the area that will be scanned to determination of sensors that will activate the output power. Power connections of cutting equipment are connected to first and second outputs of connection module. The area is determined by the help of program. Then, when the laser detectors detect an object, the connection module completes the circuit and so power is supplied for the cutting equipment.

Operating mechanism of the vehicle can be briefly explained as follows: PV that converts sun beam to electrical energy gives current and voltage which vary depending on the position of the sun and the value of solar radiation. This voltage and current are regulated by the help of charge control unit and transferred to LiPo charger. The LiPo charger uses this voltage and current in order to charge the batteries. The batteries are used to supply power for SPWM system. The power coming from batteries feeds both electronic control unit and connection module. Electronic control unit transmits the power from batteries to the motor, after regulating the motor transmits this power to the wheels with the help of differential (mechanical device). The connection module ensures operation of cutting equipment by turning on and

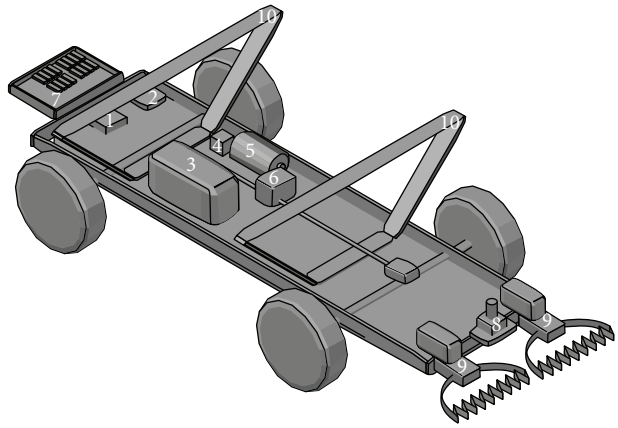


(1) Charge control unit
(2) LiPo charger
(3) Battery
(4) Electronic speed control unit
(5) DC motor
(6) Differential
(7) Connection module
(8) Smart sensor
(9) Cutting equipment
(10) Carrier feet

(a) (b)

Figure 1: SPWM system, (a) prototype scheme and (b) photograph.

turning off the outputs on itself with the data from SSS. It is clear that a proper budget is necessary in order to create a valid system. Prototype for SPWM is prepared with a budget of approximately $4.560 USD. Parts of SPWM and costs of these parts are given in Table 1.

## 3. Analysis of Solar Panel

*3.1. General Characteristics of Solar Panel.* It will be useful to analyze PV panel performance before analyzing general performance of the system. Therefore, characteristics of solar panel are considered under a separated heading in this study. A PV panel consists of generator solar cells, junctions, protector parts, and secondary elements. Solar cells consist of *p-n* junctions that are aggregated on a thin silicon circuit sheet or on a semiconductor layer.

*I-V* outcome characteristics of a solar panel in the dark are similar to exponential characteristics of a diode. When solar energy (photons) arrives in solar cell with an amount of energy greater than band gap energy of the semiconductor, collision occurs and then electron pair arises. These carriers are swept to a separated area under the influence of interior electric field of *p-n* junctions and create a current proportional to incident radiation. This current flows to external circuit when short circuit occurs in the panel cell and it is directed to interior parallel circuit by *p-n* junction diode when the circuit is open. Thus, characteristics of this diode shape the open circuit characteristics of the panel cell. Therefore, the simplest solar cell equivalent circuit is a parallel current source with the diode. Output acquired from current source is directly proportional to radiation on the panel cell. Solar cell is not an active element in dark. It performs as a diode. It does not generate current or voltage. However, if it is connected to an external source, it generates a current named as "diode current" or "dark current" [14, 15].

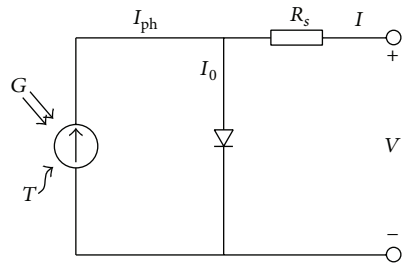


Figure 2: Solar cell circuit diagram of a single parallel diode. $I_{ph}$: photocurrent, $I_0$: diode saturation current, $R_s$: serial resistance, $T$: ambient temperature, $G$: ambient irradiance, and $V$: output voltage.

Diode determines the *I-V* characteristics of the cell. In order to achieve the best chart curve match-up, the diode ideality factor and a single parallel diode were used. This model is the simplified version of two-diode model by Gow and Manning [16]. Solar cell circuit diagram of a single parallel diode is shown in Figure 2.

$I_0$ and $I_{ph}$ depend on temperature. $R_s$ is included in the circuit in order to explain the description of maximum power point and open circuit voltage better. $R_s$ refers to interior losses caused by flow of the current. $R_{sh}$ is parallel with the diode and it corresponds to the leakage current to the ground. $R_{sh}$ is usually negligible and is not shown in the equivalent circuit. $R_s = R_{sh} = 0$ in the ideal panel cell [16].

*I-V* characteristics of a solar panel can be calculated by the equations given below. Middle level complexity model was used in the following equations:

$$I_{ph} = I_d + I, \tag{2}$$

Table 1: The main components specification and characteristics of the system studied.

| System | Element | Technical specifications | Price (US$) |
|---|---|---|---|
| Photovoltaic system | Flexible solar panels | 35 crystal cell, max. power 68 W, average daily output 272 Wh/d, open circuit voltage 22 V, current at maximum power 3.67 A, short circuit current 3.80 A, and system voltage 12 V, 800 × 646 × 2 mm, 5.4 kg | 1025 |
| | Charge control unit | Current at maximum power 8 A, system voltage 12 V, consumption value 4 mA, and dimensions 80 × 100 × 32 mm | 58 |
| Carrier system | Carrier vehicle | 2200 Kv brushless motor, max 25.2 V, ESC 25.2 V 120 A, Servo Motor (6 Volt 12 kg torque) (770 × 470 × 290 mm) | 1490 |
| | Remote control | 2.4 GHz, 4-channel S-FHSS Computer radio system | 382 |
| Storage system | Lithium polymer battery | 12.6 V, 5100 mAh, 40°C, 56.61 Wh. | 372 (2 pcs) |
| | Charger | Input voltage: 11–18 V DC charge power: max. 50 W, discharge power: max. 5 W, charge current range: 0.1–5.0 A, discharge current range: 0.1–1.0 A, current drain for balancing LiPo: 300 mAh/cell, LiPo/LiIo/LiFe battery cell count: 1–6 series, dimension: 135 × 125 × 34 mm and weight: 800 g | 93 |
| Smart sensor system | Sensor | Light source: infrared (850 nm), laser class: 1 (EN 60825-1 (2007–10)), eye-safe, field of view: 270°, scanning frequency: 15 Hz, angular resolution: 1°, and operating range: 0.05 m. . .4 m Max. range with 10% reflectivity: 2 m Operating voltage: 10 V DC. . .28 V DC, power consumption: type 3 W, without output load | 884 |
| | Connection module | USB interface, input voltage: 10 to 30 V DC, power consumption 1 W, and "touch and teach" | 93 |
| Mowing system | Cutting equipment | Cutting edge width 160 mm Operating voltage: 10.8 V, rotation speed 1100 rpm, Dimension 330 × 172 × 135 mm, 1.1 kg | 161 (2 pcs) |
| Total | | | **4558** |

Table 2: Ideality factor of several PV types.

| PV type | $n$ |
|---|---|
| Monocrystalline silicon | 1.2 |
| Polycrystalline silicon | 1.3 |
| Cadmium telluride | 1.5 |
| Gallium arsenide | 1.3 |
| Amorphous silicon | 1.8 |

$$I_d = I_0\left(e^{q(V+\mathrm{IR}_s)/nkT} - 1\right), \tag{3}$$

$$I = I_{\mathrm{ph}} - I_0\left(e^{q(V+\mathrm{IR}_s)/nkT} - 1\right), \tag{4}$$

where $I_d$ is short explaining of the $I_0(e^{q(V+\mathrm{IR}_s)/nkT} - 1)$, $q$ is elementary charge ($1.602 \times 10^{-19}$ C), $k$ is Boltzman constant ($1.381 \times 10^{-23}$ J/K), and $n$ is diode ideality factor; it depends on the PV technology as it is shown in Table 2.

Equations (2), (3), and (4) are not enough to draw the $I$-$V$ curve: $I_{\mathrm{ph}}$, $V_{\mathrm{oc}}$, and $I_0$ are required to complete the model:

$$I_{\mathrm{ph}} = I_{\mathrm{ph}}\left\langle T_{\mathrm{ref}}\right\rangle + K_0\left(T - T_{\mathrm{ref}}\right), \tag{5}$$

$$I_{\mathrm{ph}}\left\langle T_{\mathrm{ref}}\right\rangle = I_{\mathrm{sc}}\left\langle T_{\mathrm{ref}}\right\rangle \frac{G}{G_{\mathrm{ref}}}, \tag{6}$$

$$I_0\left\langle T_{\mathrm{ref}}\right\rangle = \frac{I_{\mathrm{sc}}\left\langle T_{\mathrm{ref}}\right\rangle}{\left(e^{qV_{\mathrm{oc}}\left\langle T_{\mathrm{ref}}\right\rangle/nkT_{\mathrm{ref}}} - 1\right)}, \tag{7}$$

$$I_0 = I_0\left\langle T_{\mathrm{ref}}\right\rangle\left(\frac{T}{T_{\mathrm{ref}}}\right)^{3/n} e^{qV_g(T_{\mathrm{ref}})/nk(1/T - 1/T_{\mathrm{ref}})}, \tag{8}$$

where Ref. identifies the standard test conditions ($T_{\mathrm{ref}}$ = 25°C, $G_{\mathrm{ref}}$ = 1000 W/m$^2$), $K_0$ is temperature coefficient of the current, $I_{\mathrm{sc}}$ is short circuit current, and $V_{\mathrm{oc}}$ is open circuit voltage.

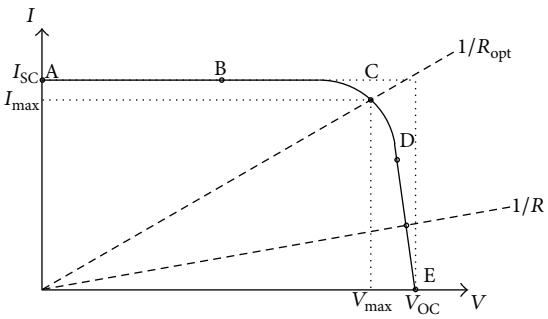


Figure 3: Specific $I$-$V$ characteristics of solar cell.

We should know the values of $R_s$ because it has a considerable effect on $I$-$V$ characteristic curves:

$$R_s = -\frac{dV}{dI_{V_{oc}}} - \frac{1}{X_v},$$
$$X_V = I_O(T_{ref}) \frac{q}{nkT_{ref}} e^{qV_{oc}(T_{ref})/nkT_{ref}}. \quad (9)$$

Constants in these equations can be determined by analyzing $I$-$V$ curve charts which are measured or published in product catalogues of PV system manufacturers.

Specific $I$-$V$ characteristics of solar cell for a determined $G$ and $T$ are shown in Figure 3. Characteristic of a resistive charge is a linear line within the scope of $I/V = 1/R$. Also it should be mentioned that power delivered to this charge is based only on the resistance value [15].

However, panel has an effect on A-B part of the curve chart if $R$ value is low. Cell acts as a constant current source here and it is almost equal to short circuit current. On the other hand, panel has an effect on D-E part of the curve chart if $R$ value is high. Cell acts as a constant voltage source here and it is almost equal to open circuit voltage [17].

A real solar cell can be characterized by following basic parameters shown in Figure 3.

For *short circuit current*, $I_{sc} = I_{ph}$. This is the maximum current value produced by the cell. It can be produced by short circuit conditions $V = 0$.

*Open circuit voltage* corresponds to diminished voltage in the diode ($p$-$n$ junction) when it is crossed by $I_{ph}$. In other words, it represents the cell voltage in dark, when the produced voltage is $I = 0$,

*Maximum power point* is the operating point C in Figure 3. This is the consumed power when the resistive charge level is maximum: $P_{max} = V_{max} \cdot I_{max}$.

*Maximum efficiency* is the ratio between maximum power and incident light:

$$\eta = \frac{P_{max}}{P_{in}} = \frac{I_{max}V_{max}}{AG}. \quad (10)$$

$A$ is the panel cell area. The efficiency of our system was calculated and result was found as 19.92%.

Fill factor is the ratio between maximum power delivered to charge and output of $I_{sc}$ and $V_{oc}$:

$$FF = \frac{P_{max}}{V_{oc}I_{sc}} = \frac{I_{max}V_{max}}{V_{oc}I_{sc}}. \quad (11)$$

Fill factor is a measure of actual $I$-$V$ characteristics. This value is higher than 0.7 for the cells that can be accepted as good. The fill factor of the panel used in our system is 0.81. Fill factor decreases as cell temperature increases.

While $I_{sc}$ is a linear function of ambient radiation, $V_{oc}$ shows a logarithmic increase with ambient radiation. Dominant effect caused by the increase in cell temperature is the linear decrease of $V_{oc}$. Thus, the cell functions less efficiently. $I_{sc}$ shows only a slight increase with cell temperature.

The effects of the $G$ and cell temperature on characteristics of the cell can be found by equations. $I_{ph}(A)$ is directly proportional to solar radiation. When solar cell is short circuited, a negligible current arises in the diode. Thus, a proportional constant short circuit current $I_{sc}$ related to calculated radiation value (6) is set. Generally panel data are calculated under $G_{ref}$ on the conditions where sea level, humidity, and aerosol particle density are at average levels. PV cell performance does not change significantly in terms of full sunniness and cloudiness. With the received solar energy, power output shows approximately a linear decrease; however, efficiency rate approximately coincides with the preferred values.

The relationship between photocurrent and temperature is linear (5) and this result is obtained by recording the temperature changes caused by photocurrent differences. The relationship between terminal voltage and current of the cell is given by Shockley equation when there is no radiation on panel cell. When the cell is open circuited and there is radiation on it, current occurs entirely in the diode. $I$-$V$ curve is shifted from the origin by the current produced by radiation (4). Saturation current value $I_0$ in the temperature of 25°C is calculated by open circuit voltage and short circuit current in that temperature (7). Ideality factor is offered as 1.2–1.3 under normal operation conditions and then it is stated that it can be used as initial until a more accurate value is calculated by curve chart simulation. $I_0$ has a complicated relationship with temperature; however, it does not include any variables that require evaluation (8). $R_s$ on the panel does not have a strong influence on tendency at the $V = V_{oc}$ point of the $I$-$V$ curve chart. Equations (9) are found by derivation of (4) and evaluation at the $V = V_{oc}$ point and by making reformation in terms of $R_s$ [15].

*3.2. MATLAB Model of the Solar Panel.* The solar panel used in our system is S225M36 which provides a maximum power of 68 W and has 35 polycrystalline silicon cells. Catalogue data of solar panel are given in Table 3.

Model of solar panel is calculated by using a MATLAB software program. Parameters of the model are assessed during the implementation by using equations listed in the previous section. The program calculates the current by using electrical parameters ($I_{sc}$, $V_{oc}$) specific to this program, voltage, radiation, and temperature variables. In addition

Table 3: Catalogue data of solar panel.

| Parameter | Symbol | Value |
|---|---|---|
| Maximum power | $P_M$ | 68 W |
| Voltage at maximum power | $V_M$ | 19 V |
| Open circuit voltage | $V_{oc}$ | 22.6 V |
| Current at maximum power | $I_M$ | 3.67 A |
| Short circuit current | $I_{sc}$ | 3.8 A |
| Number of cells | $N_p$ | 35 |

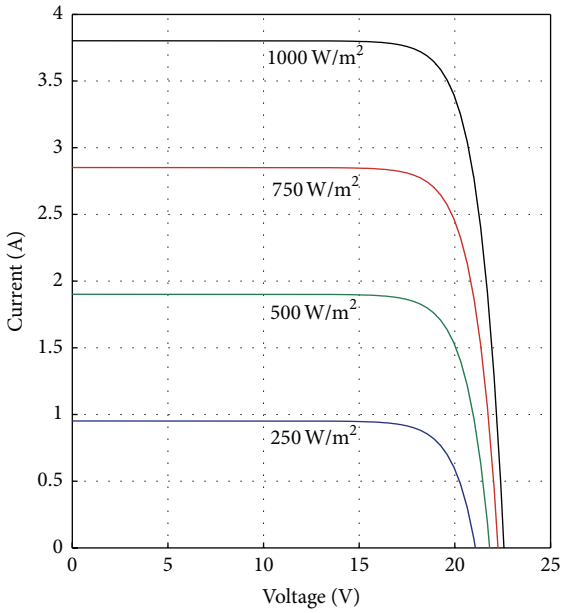


Figure 4: MATLAB model $I$-$V$ curves for various irradiation levels.

to this, this program takes series resistors of the model into account as well. This resistance creates a solution for current (4). Newton-Raphson method is used in this program because this method provides a much more quick calculation of both positive and negative currents. Output of MATLAB function is shown in Figures 4 and 5. Figure 4 shows the output for varying levels of radiation and Figure 5 shows the output for varying temperature.

The values for variable temperatures are shown on the curve chart in Figure 5. These lines are taken directly from the manufacturer's published curves and show excellent correspondence to the model. It is shown in the curve charts of S225M36 that $I_{ph}$ varies from 3.80 A to 4.00 A (5%) by the increase in $T$ from 25°C to 75°C. Figure 6 shows the power voltage tendencies for some temperature levels.

Values observed in the model results show the power, current, and voltage values that can be produced by the panel at different levels of temperature. These results coincide with that obtained from the literature and PV producer.

## 4. Experimental Study and Findings

Experiments are performed during sunny day time between the dates 27.07.2013 and 03.08.2013. Experiments are analyzed

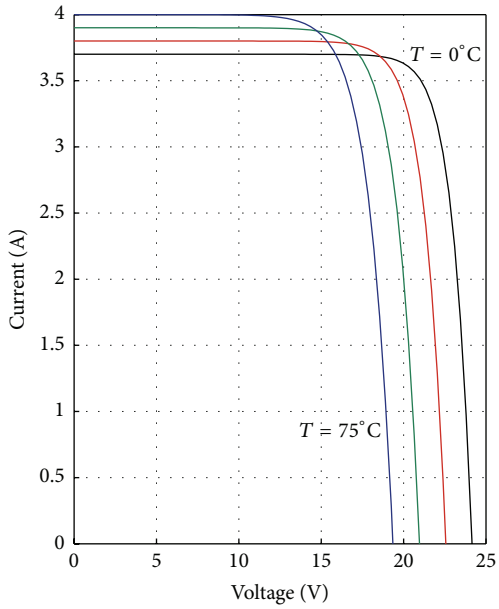


Figure 5: MATLAB model $I$-$V$ curves for various temperatures.

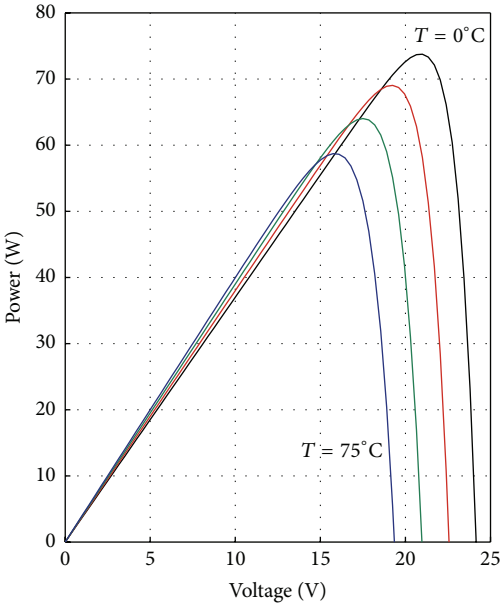


Figure 6: MATLAB model $P$-$V$ curves for various temperatures.

under three headings which are PV data experiments, field experiments, and vehicle (mower) experiments. In this study, PV system consists of two parts that are solar cell and charge control unit. Solar cell converts the radiation from the sun to electrical energy and charge control unit regulates and transmits this electrical energy to the system. Current and voltage values provided by the panel were measured at intervals of 15 minutes on sunny days. Fill factors of PV charged batteries were measured in terms of mAh with regular intervals. The device applied in the study is able to show the given current value and battery current value separately for each cell. Daily radiation values were measured by solarimeter during

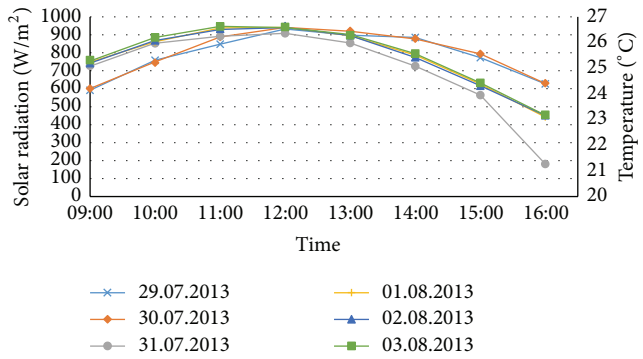


Figure 7: Hourly solar radiation and temperature changes in the experimental period.

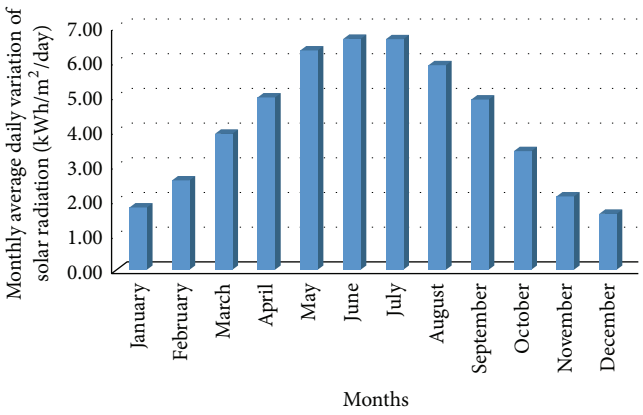


Figure 8: Monthly average daily variation of solar radiation over the year.

the experiments. A program that renders the data delivered from the SSS is used for field measurements. Field measurement values, locations of objects, and different scanning fields can be achieved by means of this program.

The most important factor during the PV based experiments is undoubtedly the sunshine rate. The changes which occurred during the experiment period of 6 days are included in Figure 7. It was seen that daily average sunshine rates were not lower than 700 Watt/m$^2$ during the experimentation dates and time. This value provides a radiation value enough to charge the batteries.

The province of Sivas located in Central Anatolia Region in Turkey has 6.5 kWh/m$^2$/day monthly average daily variation of solar radiation over the year as pointed out in Figure 8.

Uncharged voltage value of the system differs between 20 and 22 V depending on the solar radiation value. This value falls to 15 V when the charge is connected to the system. Output voltage shows variations depending on the temperature and on the radiation rates of the panel. Nonetheless, there is not any fluctuation on the voltage which is used to charge polymer batteries by charge control unit due to the panel provided output power is greater than required power (see Table 4).

Time related panel data values are given in Table 4 and descriptions of parameters are as follow: $T_{avr}$ (°C) refers to hourly average temperature; $G_{avr}$ refers to hourly average radiation values provided by the panel; $V_{po}$ refers to panel output voltage; $V_{co}$ refers to charge control unit output voltage; $I_{cd}$ refers to current drawn from the panel during charging.

Table 4: Time related environment and panel data value.

| Time | $T_{avr}$(°C) | $G_{avr}$ (W/m$^2$) | $V_{po}$ | $V_{co}$ | $I_{cd}$ |
|---|---|---|---|---|---|
| 09:00 | 23.9 | 592 | 14.6 | 11.5 | 1.3 |
| 10:00 | 24.1 | 759 | 14.7 | 11.5 | 1.8 |
| 11:00 | 24.2 | 848 | 15 | 11.5 | 1.9 |
| 12:00 | 25.1 | 932 | 15.4 | 11.5 | 2.1 |
| 13:00 | 24.1 | 899 | 15.2 | 11.5 | 1.8 |
| 14:00 | 23.5 | 886 | 15.2 | 11.5 | 1.7 |
| 15:00 | 22.9 | 773 | 15 | 11.5 | 1.7 |
| 16:00 | 20.3 | 627 | 14.6 | 11.5 | 1.3 |

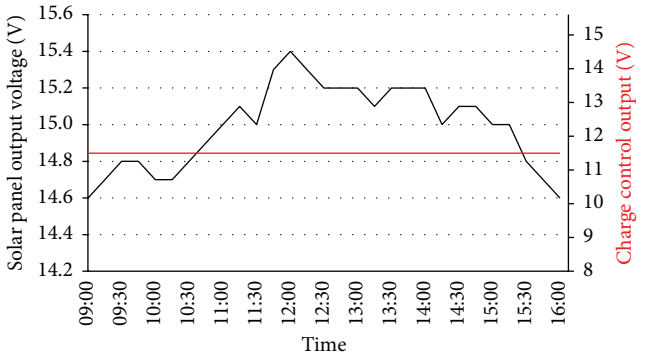


Figure 9: Change in solar panel and charge control output voltages during charge of battery.

Voltage values that vary depending on 15-minute periods when LiPo batteries are connected to the circuit are shown in Figure 9.

In the experiments conducted between the hours 09:00 and 16:00 on the date shown in Figure 9, it was seen that the PV provided energy is enough to charge the battery. Observations from the experiments show that output voltage values of the PV system vary between 14.6 V and 15.4 V. Afterwards, voltage values were read on charge control unit and it was seen that the voltage of charge control unit is reduced to 11.5 V and this value is enough to meet the required voltage for the system. It was also seen that PV system cannot satisfy the special charge conditions of LiPo batteries except for the measurement time periods (solar radiation is insufficient before 09:00 and after 16:00).

Besides voltage rating during charging of the batteries, the current transmitted to the batteries is also of high importance. Charging the batteries depends on the current value. Current values obtained from PV by batteries with charge control unit are shown in Figure 10.

If the value of current coming from the solar panel is higher than 2.1 A when the batteries are charged, the charger warns about the insufficient power; thus, maximum charge current is determined as 2.1 A. Lower current value affects

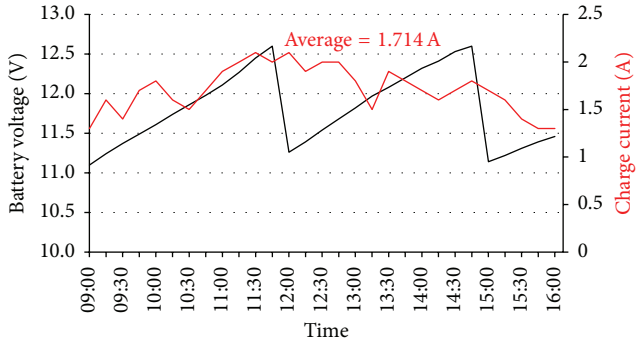


Figure 10: Change in voltage and charge flow values during charge of batteries.

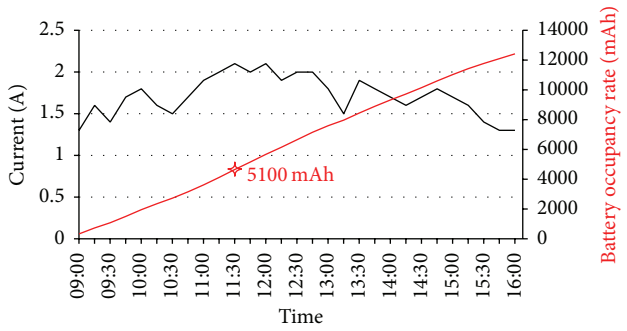


Figure 11: Change in input and current values during charge of batteries.

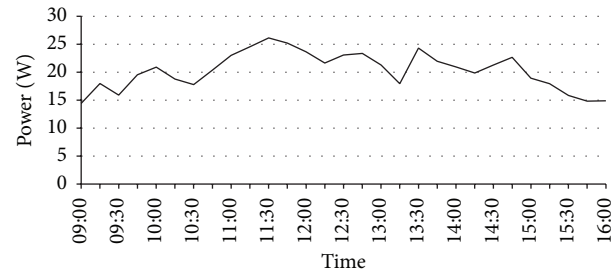


Figure 12: Instantaneous power change during charge of battery.

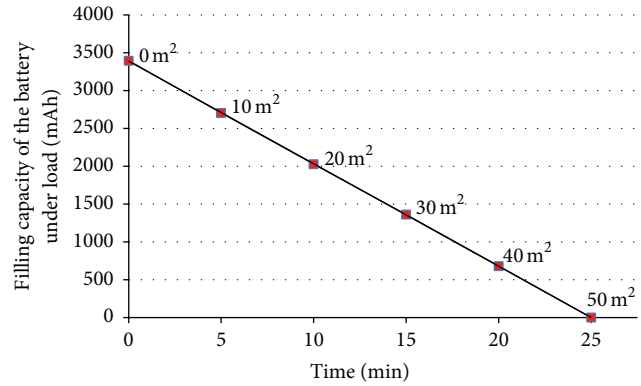


Figure 13: Time related change graph of field to be mowed and consumed electrical charge.

the time required to charge the batteries and battery cycle rate. Battery cycle rate, mentioned here, means recharging the battery after being used during the day. The longer the battery cycle is the longer the operating time of the vehicle is. For LiPo batteries, one of the parameters indicating that the battery is fully charged is the voltage rate of each cell. As mentioned before, nominal voltage rate of LiPo batteries used in the experiment is 3.7 V for each cell and in total 11.1 V for 3 cells. Maximum fill factor of one cell is determined as 4.2 V by the manufacturer. It was observed that in the experiments performed on 27.07.2013, the battery that began to be charged at 09:00 was fully charged at 11.38 then the second battery began to be charged. During the experiments, charge duration of a battery is determined as 2 hours and 40 minutes. Input current values that are transmitted to batteries from PV via charge control unit between the hours 09:00 and 16:00 and changes in current values that charge the battery are given in Figure 11.

Instant power rates during the charge of the battery are calculated by using current and voltage values measured in the experiments. Equation used for this calculation is shown below [13]:

$$P(t) = V(t) \cdot I(t), \tag{12}$$

where $P(t)$ is instant power (W), $V(t)$ is voltage (V), and $I(t)$ is current (A).

Instantaneous power changes during charge of batteries are given in Figure 12. On the days of experiment maximum power coming from the flexible PV is 26.15 W and daily average power rate is calculated as 20.31 W.

The energy stored by help of panel and batteries enables the vehicle to mow on the experiment field. One of the fields where mowing was performed was a field with an area of 5 $m^2$ where there were wheatears and the other was a field with an area of 50 $m^2$ where there were earless wheat stems.

Prototype has performed mowing activity successfully during the experiments. It was observed that overall performance during the mowing is related to the surface of the area to be mowed. Vehicle that had some difficulties mowing inclined areas had no difficulty in mowing ears of grains on plain areas.

Digital remote control is used in order to direct the movements of the vehicle. Many parameters, such as vehicle acceleration, turning circle, and maximum speed, can be controlled with the help of this digital control. Approximately 500 mAh of electrical charge has been spent over the course of mowing experiments for an area of 5 $m^2$ and this value is 3395 mAh for an area of 50 $m^2$. The graph which shows time based change in the usage of electrical charge and mowed area is shown in Figure 13.

While all these activities are being implemented the vehicle scans the surface. The vehicle can be programmed in many different ways and it is programmed to start operation as soon as wheat is detected. The scanning area where the vehicle operates is divided into three separate parts. The vehicle starts operating when wheat stems are detected where they are closest to the sensor. This closest area is illustrated

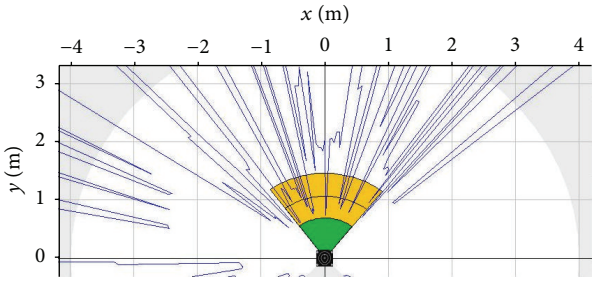


Figure 14: The most proper area for SPWM system detected by sensor.

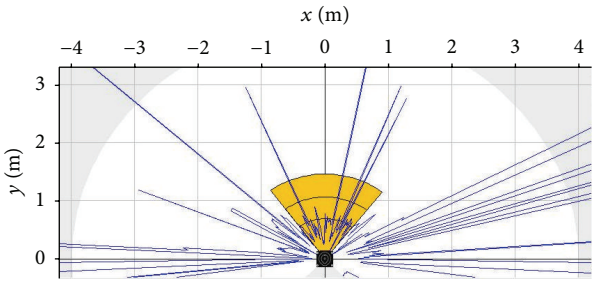


Figure 15: View of beginning to wheat mowing process.

in green in Figure 14. Area scanning image before the system operation is given in Figure 14. At this stage, SSS scans the area but does not operate. System begins to operate when the scanning imagery in Figure 15 is obtained. Here, the programmed scanning area is seen in the shape of 1/6-circle. This shape of circle allows us to approach to the vehicle on both right and left sides and provides safe implementation of control and maintenance activities for the vehicle.

Experimental areas where the mowing process are performed present successful results when the sizes of these areas are taken into consideration.

When the vehicle designed in this research is compared with a mower that has 127 cm cutting width and 7.5 kW single cylinder diesel engine and has a sale price of \$10.250 USD, the results are as follows. Catalogue values of the vehicle show that the required amount of fuel to mow an area of 1000 $m^2$ is 1.4 L. Price of fuel per unit was \$1.56 USD on the date of November 2015 (Turkey). When this unit price is taken into account, mowing an area of 1000 $m^2$ costs \$2.18 USD in total. The same calculation is done for our designed vehicle: 3395 mAh for 50 $m^2$; 3395 mAh × 20 = 67900 mAh, and this value is approximately equal to 68 Ah (for 1000 $m^2$). By the help of the equation $P = IV$; 68 × 14.9 = 1013 Watts = 1 kW electrical energy is spent for mowing the area of 1000 $m^2$. Unit price of kWh was \$0.140 USD on the date November 2015. On the other hand, the cost of mowing 1000 $m^2$ area by using our wheat mower is \$0.140 USD. Our system saves money by 90% when compared to conventional mowers over an area of 1000 $m^2$ for Turkey economic condition of November 2015. However sizes, battery capacities, and PV power of designed vehicle are relatively smaller due to the fact that it is a prototype. Therefore, its daily storage capacity is approximately 12 Ah as shown in Figure 10. According to these values, mowing activity lasts approximately 6 days.

## 5. Conclusions

In this study, applicability of solar energy which is available in Turkey abundantly to agriculture has been investigated. In recent years, PV has started to be used efficiently in order to produce electrical energy from solar energy throughout the world. PV and battery prices corresponding to the cost of the manufacturing, module efficiency, and market features vary worldwide. Besides, an estimate for the global price of basic PV modules in 2008 was \$4/W USD and this price reduces to 1.05/W in 2015 by declining 75% over the five years. Wheat mower which runs on PV has been designed. PV used in this study is modeled in MATLAB. Returns necessary for the system are provided by equipping the wheat mower prototype with sensor system. Results and suggestions of this study are listed below:

(i) Effective mowing is performed by this system and there is no other system similar to this one.

(ii) Operating time of prototype vehicle is increased by 30% with the help of PV.

(iii) The amounts of electrical charge used to mow 5 $m^2$ and 50 $m^2$ areas are obtained as 500 mAh and 3395 mAh, respectively.

(iv) Operating time for an area of 75 $m^2$ is calculated as 37 minutes with a battery used in the system at a constant level of power.

(v) Maximum power is calculated from used PV panel as 26.15 Watt during the day of the experiments.

(vi) It is proved that laser scanner systems can be used in any field.

(vii) This system is 94.5% more economic than conventional mowers over an area of 1000 $m^2$. However, sizes, battery capacities, and PV power of designed vehicle are relatively smaller due to being a prototype.

(viii) It is observed that flexible PVs are proper to be used on agricultural fields but better studies can be achieved by increasing output power levels.

## Conflict of Interests

The authors declare that there is no conflict of interests regarding the publication of this paper.

## Acknowledgment

The authors gratefully acknowledge the financial support from the Scientific Research Projects Administration Unit of Firat University for this study performed under projects with Grant no. TEKF 2013/13.07.

## References


[1] Climate Change Synthesis Report, *Contribution of Working Groups I, II and III to the Fourth Assessment Report of the Intergovernmental Panel on Climate Change*, IPCC, Geneva, Switzerland, 2007.

[2] European Commission, *EU Energy and Transport Figures—Statistical Pocketbook*, European Commission, Brussels, Belgium, 2013.

[3] SET-Plan, Strategic Energy Technology Plan, 2014, http://ec.europa.eu/energy/technology/set_plan/set_plan_en.htm.

[4] M. Farhoodnea, A. Mohamed, H. Shareef, and H. Zayandehroodi, "Power quality impacts of high-penetration electric vehicle stations and renewable energy-based generators on power distribution systems," *Measurement*, vol. 46, no. 8, pp. 2423–2434, 2013.

[5] B. A. Stout and M. McKiernan, "New technology-energy implications," in *Energy in World Agriculture. Energy in Farm Production*, R. C. Fluck, Ed., vol. 16, chapter 11, pp. 131–171, Elsevier, Amsterdam, The Netherlands, 1992.

[6] K. D. Edwards, R. M. Wagner, T. E. Briggs, and T. J. Theiss, "Defining engine efficiency limits," in *Proceedings of the 17th Directions in Engine-Efficiency and Emissions Research (DEER '11)*, Detroit, Mich, USA, 2011.

[7] S. M. Shaahid and M. A. Elhadidy, "Economic analysis of hybrid photovoltaic-diesel-battery power systems for residential loads in hot regions—a step to clean future," *Renewable & Sustainable Energy Reviews*, vol. 12, no. 2, pp. 488–503, 2008.

[8] H. Mousazadeh, A. Keyhani, H. Mobli, U. Bardi, G. Lombardi, and T. el Asmar, "Environmental assessment of RAMseS multipurpose electric vehicle compared to a conventional combustion engine vehicle," *Journal of Cleaner Production*, vol. 17, no. 9, pp. 781–790, 2009.

[9] H. Mousazadeh, A. Keyhani, H. Mobli, U. Bardi, G. Lombardi, and T. el Asmar, "Technical and economical assessment of a multipurpose electric vehicle for farmers," *Journal of Cleaner Production*, vol. 17, no. 17, pp. 1556–1562, 2009.

[10] G. Albright, J. Edie, and S. Al-Hallaj, *A Comparison Lead Acid to Lithium-Ion in Stationary Storage Applications*, The Alternative Energy eMagazine, AllCell Technologies, 2012.

[11] D. A. G. Redpath, D. McIlveen-Wright, T. Kattakayam, N. J. Hewitt, J. Karlowski, and U. Bardi, "Battery powered electric vehicles charged via solar photovoltaic arrays developed for light agricultural duties in remote hilly areas in the Southern Mediterranean region," *Journal of Cleaner Production*, vol. 19, no. 17-18, pp. 2034–2048, 2011.

[12] S. M. Shaahid and I. El-Amin, "Techno-economic evaluation of off-grid hybrid photovoltaic-diesel-battery power systems for rural electrification in Saudi Arabia-a way forward for sustainable development," *Renewable & Sustainable Energy Reviews*, vol. 13, no. 3, pp. 625–633, 2009.

[13] W. Brown and D. C. Brusless, "Motor control made easy," Microchip Technology DS00857, 2002.

[14] G. Walker, "Evaluating MPPT converter topologies using a matlab PV model," *Journal of Electrical & Electronics Engineering*, vol. 21, no. 1, pp. 49–55, 2001.

[15] E. Lorenzo, *Electricity Engineering of Photovoltaic Systems*, Artes Graficas Gala, Madrid, Spain, 1994.

[16] J. A. Gow and C. D. Manning, "Development of a photovoltaic array model for use in power-electronics simulation studies," *IEE Proceedings: Electric Power Applications*, vol. 146, no. 2, pp. 193–200, 1999.

[17] F. M. González-Longatt, Model of Photovoltaic Module in Matlab, 2do Congreso Iberoamericano de Estudiantes de Ingeniería Eléctrica, Electrónica Computación, II Cibelec, 2005.

Hindawi Publishing Corporation
International Journal of Photoenergy
Volume 2015, Article ID 907282, 8 pages
http://dx.doi.org/10.1155/2015/907282

*Research Article*

# Safety Analysis of Solar Module under Partial Shading

**Wei He,[1] Fengshou Liu,[1] Jie Ji,[1] Shengyao Zhang,[2] and Hongbing Chen[3]**

[1]*Department of Thermal Science and Energy Engineering, University of Science and Technology of China, 96 Jinzhai Road, Hefei, Anhui 230026, China*
[2]*Guangdong Fivestar Solar Energy Co., Ltd., Liuchongwei Industrial Area, Wanjiang District, Dongguan, Guangdong Province 523051, China*
[3]*School of Environment and Energy Engineering, Beijing University of Civil Engineering and Architecture, Beijing 100044, China*

Correspondence should be addressed to Wei He; hwei@ustc.edu.cn

Received 24 July 2015; Revised 14 November 2015; Accepted 16 November 2015

Academic Editor: Elias Stathatos



Hot spot often occurs in a module when the qualities of solar cells mismatch and bypass diodes are proved to be an efficient alternative to reduce the effect of hot spot. However, these principles choosing a diode are based on the parameters of bypass diodes and PV cells without consideration of the maximum heating power of the shaded cell, which may cause serious consequences. On this basis, this paper presents a new approach to investigate partially shaded cells in different numbers of PV cells and different shading scenarios, including inhomogeneous illumination among solar cells and incomplete shading in one cell, which innovatively combines the same cells or divides one affected cell into many small single cells and then combines the same ones, and analyzes the shaded cell. The results indicate that the maximum power dissipation of the shaded cell occurs at short-circuit conditions. With the number of solar cells increasing, the shaded cell transfers from generating power to dissipating power and there is a maximum point of power dissipation in different shading situations that may lead to severe hot spot. Adding up the heat converted from solar energy, the heating power can be higher. In this case, some improvements about bypass diodes are proposed to reduce hot spot.

## 1. Introduction

With the increasingly environmental problems and shortages of traditional fossil fuels, solar energy as clean and renewable energy has attracted more and more attention. Photovoltaic power generation which has advantages of simplicity and convenience can directly convert solar energy to electrical energy. Coupled with the advancement of technology, such as improving conversion efficiency of solar cells and reducing the cost of devices, photovoltaic power generation is used more widely and has developed many different forms, including grid-connected or utility-interactive PV systems and stand-alone photovoltaic systems. But some undesirable problems such as hot spot and islanding effect occur correspondingly.

Hot spot occurs if the characteristics of solar cells mismatch are shaded or faulty, which reduces the short current of the shaded cell. Once the operating current of module or system exceeds the short current of the affected cell, the cell is forced into reverse bias and starts to consume the power generated by unshaded cells, resulting in overheating [1]. When the temperature of the shaded cell rises highly enough, the encapsulant, like EVA, will melt and the back sheet, like TPT, will be broken down, even leading to fire [2]. In general, bypass diodes are adopted to inhibit the shaded cell to crack and reduce the formation of hot spot. And the necessary parameters of bypass diodes and the number of cells in a string protected by a diode are determined by the parameters of normal cells [3]. The typical group size is approximately 12–24 cells per bypass diode. However, these principles neglect whether or not the maximum heating power of the shaded cell can meet the requirement. It is also shown that bypass diodes are effective at preventing hot spot in short PV string lengths but cannot satisfy the demands in typical panel string lengths [4].

Herrmann et al. presented an improved methodology for hot spot testing due to the shortages of two current hot spot tests and introduced the worst case power dissipation

Table 1: Parameters of solar cell and bypass diode.

| Standard solar cell (1000 W/m$^2$, 25°C, 12.5 cm ∗ 12.5 cm, monocrystalline silicon) | | | | | Bypass diode (25°C) | |
|---|---|---|---|---|---|---|
| $I_{ph}$ (A) | $R_s$ (Ω) | $R_{sh}$ (Ω) | $I_o$ (A) | $n$ | $I_o$ (A) | $n$ |
| 5.61 | 0.005 | 8.72 | $2.34e-08$ | 1.27 | $7.02e-05$ | 1.57 |

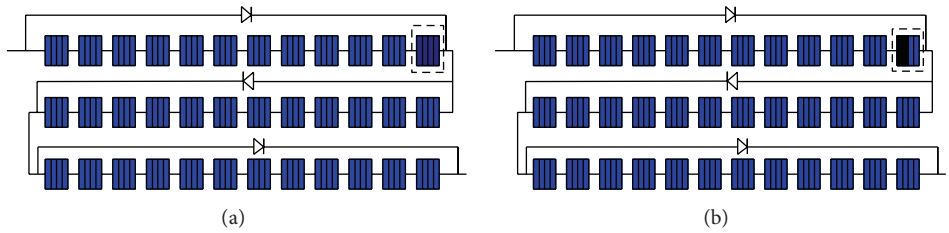


Figure 1: (a) The radiation of the shaded cell is different from the normal ones in inhomogeneous illumination. (b) The radiation of unshaded part is equal to the normal ones and the radiation of the shaded part is zero in incomplete shading.

of the shaded cell but did not consider the great influence of radiation [5]. Silvestre et al. simulated solar cells and PV modules with bypass diodes working in partial shading conditions and verified with real measure data. A method on estimating the number of cells protected by bypass diode was proposed according to the correlation of the voltage not considering dissipated power of the shaded cell [6]. Quaschning and Hanitsch and Kawamura et al., respectively, conducted a simulation research about the current and voltage of photovoltaic systems in partial shading [7, 8]. Bende et al. performed a simulation study of the partially shaded cell by varying the breakdown voltage and the shunt resistance of cells and analyzed the effect of these parameters on the maximum power dissipation [9]. Fertig et al. investigated the impact of reverse breakdown of solar cells on the hot spot, simulated the distribution of the temperature of the shaded cell, and validated it with experimental data [10–12]. Alsayid et al. analyzed the effect of partial shading on the PV system but the results only contained inhomogeneous illumination and neglected incomplete shading [13–15].

Considering the previous researches and the defects of principles of choosing bypass diodes, a new approach to study solar module is proposed and the influence of inhomogeneous illumination and incomplete shading of solar cells is investigated, respectively. For a certain circuit, the maximum power dissipation of the shaded cell happens at short-circuit conditions. Power dissipation of the shaded cell in different shading degrees is analyzed in order to find the worst working condition. As a result, the number of solar cells in a string should consider the worst case.

## 2. The Mathematical Model

The situations of shaded cells can be simply classified into inhomogeneous illumination and incomplete shading.

Inhomogeneous illumination means that incident radiation amongst solar cells in the same string are uneven. Meanwhile, the radiation of the shaded cell is less than that of the unshaded cells, but not falling to zero, as illustrated in Figure 1(a). If a part of one cell is completely shaded (in other words the radiation of the shaded part is zero) and the remaining part can still absorb radiation as the unshaded cells, it will be incomplete shading, as illustrated in Figure 1(b).

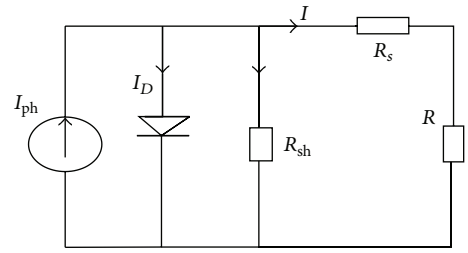


Figure 2: Equivalent circuit.

Once a cell is shaded, its parameters also alter, including the light current $I_{ph}$, the series resistance $R_s$, and the parallel resistance $R_{sh}$ in addition to output current and voltage which leads to the mismatch between normal cells and abnormal cells [16–20].

*2.1. Parameters of a Solar Cell and the Equivalent Circuit.* A commercial solar cell and a bypass diode are randomly chosen, and the corresponding parameters of solar cells at reference conditions, including $I_{ph}$, $R_s$, $R_{sh}$, $n$, and $I_o$, are calculated based on [21], where the current and voltage characteristics of a cell are supplied by manufacturers. The results are shown in Table 1. Under certain conditions, solar cells with the same characteristics can be combined as one cell with other parameters and the circuit can be simplified [22, 23].

The general equation of PV cell can be expressed as follows:

$$I = I_{ph} - I_o * \left(e^{q*((V+I*R_s)/(n*k*T))} - 1\right) - \frac{V + I * R_s}{R_{sh}}. \quad (1)$$

And the equivalent circuit is illustrated as in Figure 2.

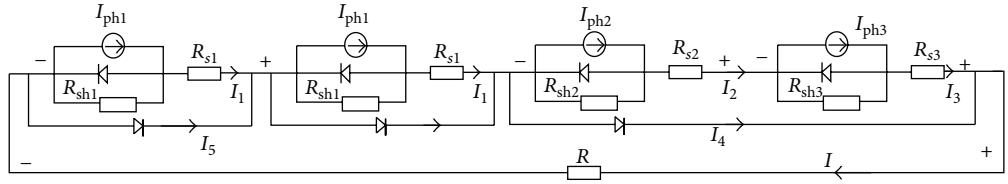


Figure 3: Equivalent circuit of inhomogeneous illumination.

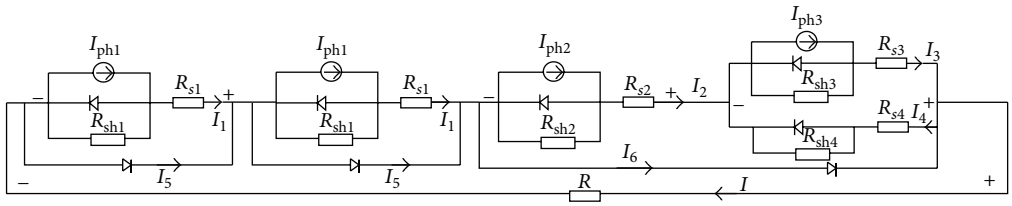


Figure 4: Equivalent circuit of incomplete shading.

For $M$ cells with the same parameters in series [22, 23],

$$I = I_{\text{ph}} - I_o * \left(e^{q*((V+I*M*R_s)/(M*n*k*T))} - 1\right) - \frac{V + I * M * R_s}{M * R_{\text{sh}}}. \quad (2)$$

The equation of PV cell in dark can be expressed as (positive and negative are related to the direction of current) [24]

$$I = I_o * \left(e^{q*((V-I*R_s)/(n*k*T))} - 1\right) + \frac{V - I * R_s}{R_{\text{sh}}}. \quad (3)$$

The general current and voltage equation of bypass diode is expressed as follows:

$$I = I_o * \left(e^{(q*V)/(n*k*T)} - 1\right). \quad (4)$$

*2.2. Equivalent Circuit of the PV Module in Inhomogeneous Illumination.* Although incident radiation among solar cells is uneven, the basic construction of the equivalent circuit of each cell keeps the same, except for the parameters of the circuit. By solving the parameters of solar cells in different radiation and/or temperature based on [16–18] and combining the same ones, the parameters of the shaded cell and unshaded equivalent cells can be calculated. The final equivalent circuit can be illustrated as in Figure 3.

*2.3. Equivalent Circuit of the PV Module in Incomplete Shading.* Incompletely shaded cells can be separated into two parts: shaded part and unshaded part. Since every PV cell can be regarded as many small single cells in parallel, each incompletely shaded cell can be divided into 100 small cells or more. It is assumed that there are $(X)$ small cells completely shaded and the remaining $(100-X)$ small cells receive normal radiation. Just as suggested in [22, 23], the parameters of every single cell whether shaded or not can be solved. By combining the same cells and calculating the parameters of unshaded and shaded equivalent cell like in Section 2.2, the equivalent circuit can be illustrated as in Figure 4.

*2.4. Simulation Solution.* Basing on Kirchhoff's Voltage and Current Law, and integrating the equation of current and voltage of every branch circuit, the simultaneous solution of these equations yields the $I$-$V$ curve and the $P$-$V$ curve of circuit in different radiation and shading degrees. Furthermore, the power output or dissipation of shaded cells, shaded part, and unshaded part can also be calculated, which is equal to the product of the current and the voltage. The equations are expressed in Table 2.

## 3. Numerical Simulation and Result Analysis

Situations in both inhomogeneous illumination and incomplete shading are investigated, respectively. In order to simplify the simulation, the temperature of cells is set as 25°C and the normal radiation is 1000 W/m$^2$. Each cell string contains 12 solar cells protected by a bypass diode in parallel.

*3.1. Power Output or Dissipation of the Shaded Cell.* To obtain the relation between the power of the shaded cell and working current of circuit, a PV module with 36 cells in series arranged with three strings with parallel bypass diode is selected, as shown in Figures 1(a) and 1(b). The incident radiation of the shaded cell is 500 W/m$^2$ for inhomogeneous illumination and the percentage of the shaded part for the incomplete shading is 50%.

The result demonstrates that the maximum power dissipation of the shaded cell occurs at short-circuit conditions, when working current reaches the maximum in a certain shading degree and fixed radiation, as illustrated in Figures 5(a) and 5(b). The results coincide with [1], which has demonstrated that the maximum power is dissipated in the short-circuit current condition for any radiance level. Bypass diode can conduct a part of current and reduce the effect of hot spot on the shaded cell as we expect. However, the current flowing through bypass diode is proportional to the reverse bias voltage of the cell string in parallel, which conversely requires the shaded cell to conduct more current to increase reverse bias voltage of the shaded cell. When

Table 2: Calculation equation.

| Inhomogeneous illumination | Incomplete shading |
|---|---|
| $I_1 = I_{ph1} - I_{o1} * \left(e^{q*((V_1+I_1*R_{s1})/(n_1*k*T))} - 1\right) - \dfrac{V_1 + I_1 * R_{s1}}{R_{sh1}}$<br>$I_5 = I_{o5} * \left(e^{(-q*V_1)/(n_5*k*T)} - 1\right)$<br>$I = I_1 + I_5$<br>$I_2 = I_{ph2} - I_{o2} * \left(e^{q*((V_2+I_2*R_{s2})/(n_2*k*T))} - 1\right) - \dfrac{V_2 + I_2 * R_{s2}}{R_{sh2}}$<br>$I_3 = I_{ph3} - I_{o3} * \left(e^{q*((V_3+I_3*R_{s3})/(n_3*k*T))} - 1\right) - \dfrac{V_3 + I_3 * R_{s3}}{R_{sh3}}$<br>$I_2 = I_3$<br>$I_4 = I_{o4} * \left(e^{(-q*(V_2+V_3))/(n_4*k*T)} - 1\right)$<br>$V = N * V_1 + V_2 + V_3$<br>$I = I_2 + I_4$ | $I_1 = I_{ph1} - I_{o1} * \left(e^{q*((V_1+I_1*R_{s1})/(n_1*k*T))} - 1\right) - \dfrac{V_1 + I_1 * R_{s1}}{R_{sh1}}$<br>$I_5 = I_{o5} * \left(e^{(-q*V_1)/(n_5*k*T)} - 1\right)$<br>$I_2 = I_{ph2} - I_{o2} * \left(e^{q*((V_2+I_2*R_{s2})/(n_2*k*T))} - 1\right) - \dfrac{V_2 + I_2 * R_{s2}}{R_{sh2}}$<br>$I_3 = I_{ph3} - I_{o3} * \left(e^{q*((V_3+I_3*R_{s3})/(n_3*k*T))} - 1\right) - \dfrac{V_3 + I_3 * R_{s3}}{R_{sh3}}$<br>$I_4 = I_{o4} * \left(e^{q*((V_3-I_4*R_{s4})/(n_4*k*T))} - 1\right) + \dfrac{V_3 - I_4 * R_{s4}}{R_{sh4}}$<br>$I_2 = I_3 - I_4$<br>$I_6 = I_{o6} * \left(e^{(-q*(V_2+V_3))/(n_6*k*T)} - 1\right)$<br>$I = I_2 + I_6$<br>$I = I_1 + I_5$<br>$V = N * V_1 + V_2 + V_3$ |
| 1: equivalent cell of an unshaded cell string<br>2: equivalent cell of remaining unshaded cells in a string<br>3: shaded cell in a string<br>4: diode paralleling with a string having shaded cells<br>5: diode paralleling with a normal cell string | 1: equivalent cell of an unshaded cell string<br>2: equivalent cell of remaining unshaded cells in a string<br>3: unshaded part of a cell in a string<br>4: shaded part of a cell in a string<br>5: diode paralleling with a normal cell string<br>6: diode paralleling with a string having shaded cells |

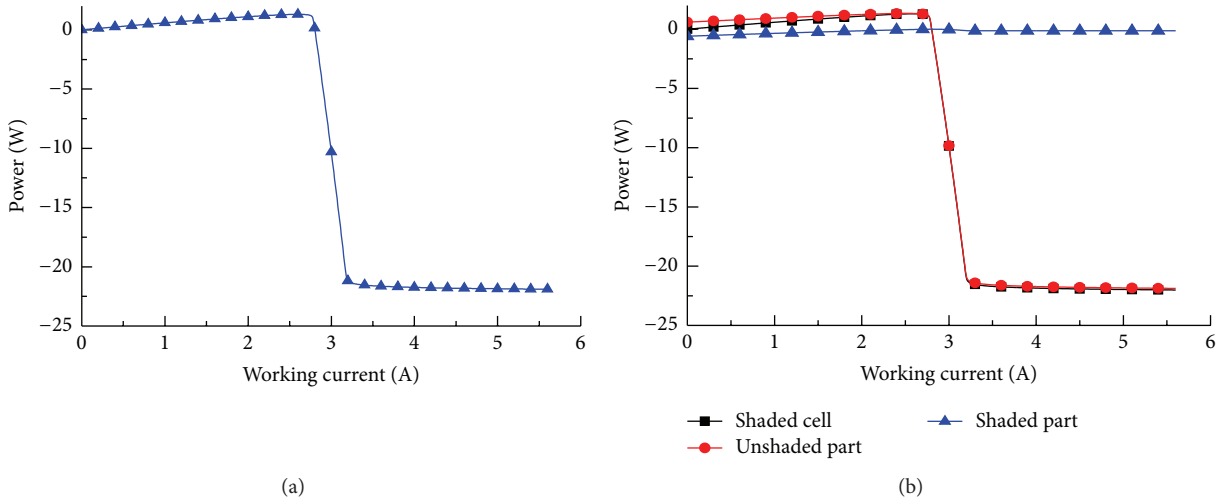


Figure 5: (a) Power of the shaded cell with the variation of working current in inhomogeneous illumination. (b) Power of the shaded cell, shaded part, and the unshaded part with the variation of working current in incomplete shading.

working current reaches the maximum, the current flowing through the shaded cell and diode rises to the maximum too, which leads to the maximum power dissipation of the shaded cell. It is also shown that the power dissipation of the shaded part is far less than that of the unshaded part for the latter can conduct more current.

*3.2. Effect of the Number of Cells on the Shaded Cell in MPPT.* In general, PV modules or systems operate at the maximum power point to achieve the maximal power output. The influence of the number of cells on the shaded cell, therefore, is investigated at the maximum power point, as illustrated in Figures 6(a) and 6(b). The radiation of the shaded cell is 800 W/m$^2$ for inhomogeneous illumination and the shading ratio for incomplete shading is 20%. The remaining conditions keep the same as those in Section 3.1.

With the variation of the number of PV cells in a certain situation, the currents of reverse bias point of the shaded cell and forward bias point of bypass diode remain constant as the short current of the module for these are just related to PV cells. But the *P-V* curve and the *I-V* curve of PV module have altered. If the number of solar cells is few and output power is little, the proportion of the shaded cell to the module is comparatively large. The maximum power point is mainly determined by the shaded cell, which will generate power at that point. With the number of PV cells increasing,

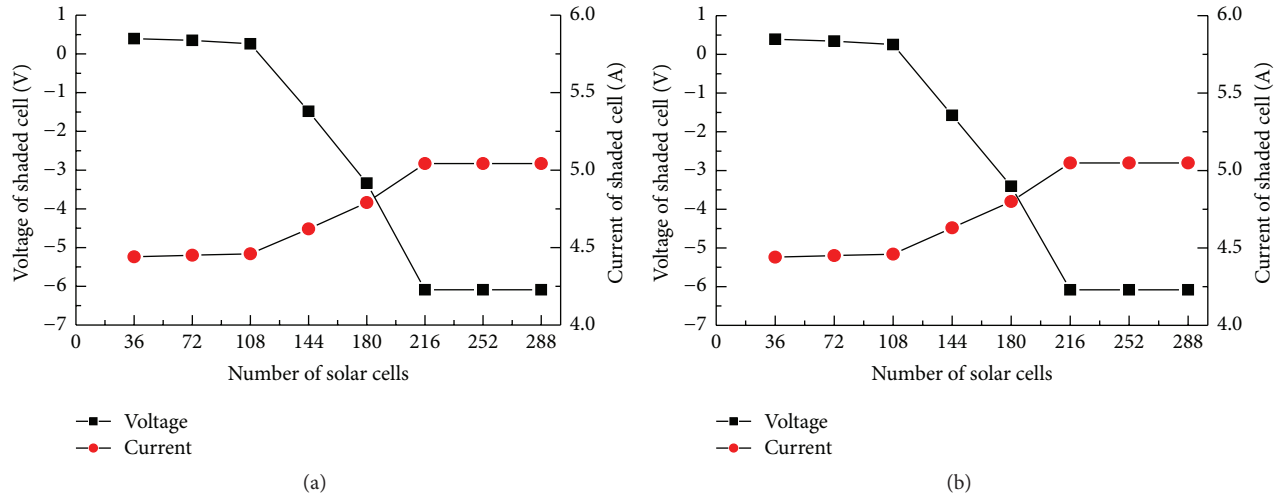


Figure 6: (a) The current and voltage of the shaded cell at MPPT in inhomogeneous illumination. (b) The current and voltage of the shaded cell at MPPT in incomplete shading.

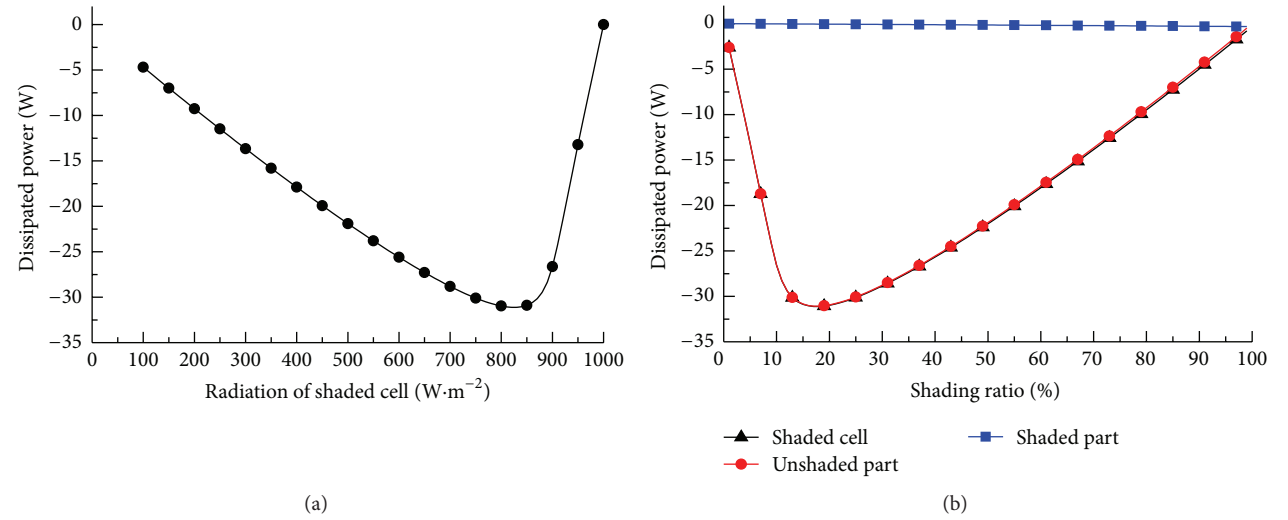


Figure 7: (a) The maximum dissipated power of the shaded cell with the variation of radiation in inhomogeneous illumination. (b) The maximum dissipated power of the shaded cell with the variation of shading ratio in incomplete shading (the incident radiation of normal cells or unshaded part is 1000 W/m$^2$).

normal cells can generate more power and the proportion of the shaded cell to the module decreases comparatively. Finally the maximum power point is mainly determined by unshaded cells and the shaded cell begins to reverse bias to consume power generated by normal cells. It verifies that the shaded cell transfers from generating power to consuming power with the increase of the number of solar cells. In addition, the power dissipation can be very large, which will damage the shaded cell operating at the maximum power point for a long time.

*3.3. The Worst Case Power Dissipation of the Shaded Cell.* Power dissipation of shaded cells in different shading degrees has been extensively studied in detail to find the worst case at the short-circuit condition when the maximum power dissipation of the shaded cell occurs. Simulation conditions remain the same as those in Section 3.1 and the results are illustrated in Figures 7(a) and 7(b). The results indicate that power dissipation reaches the maximum with a radiation of 825 W/m$^2$ and the current across the shaded cell is 5.19 A, which almost approaches the maximum power point current of unshaded cells in 1000 W/m$^2$. That means the shaded cell can dissipate the maximum power generated by the remaining cells in the same string and simultaneously confirms that the maximum power dissipation is approximately equal to the generating capability of all cells in the group [23]. It also indicates that the power dissipation of the shaded cell has exceeded 30 W in a large range of radiation which may lead to hot spot.

When the complete shading ratio is high and/or the radiation is low, reverse bias current of the shaded cell is low for the high shunt resistance which makes the power

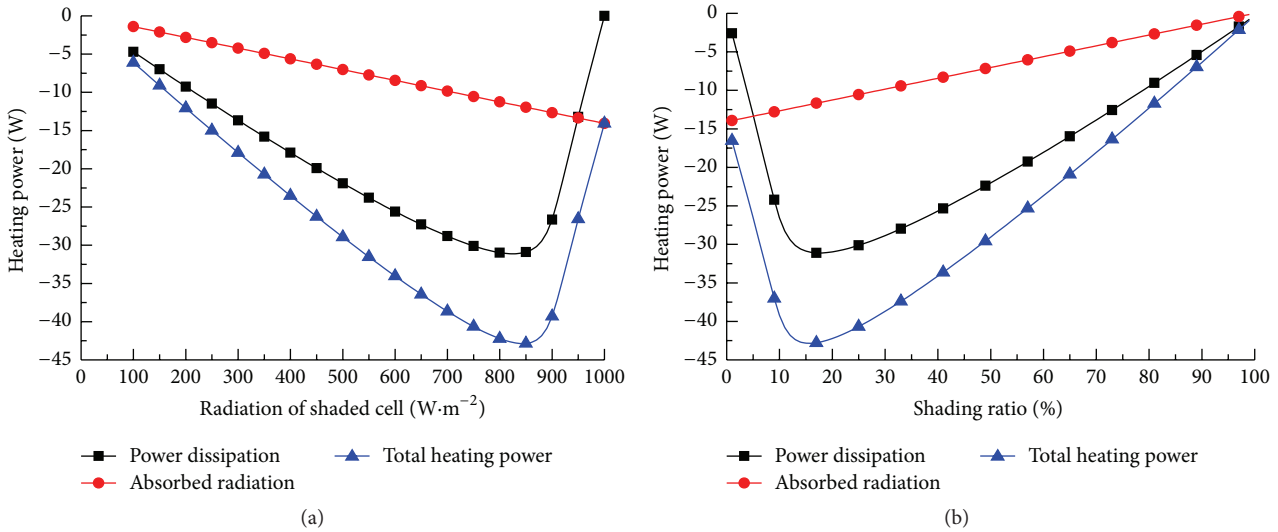


FIGURE 8: (a) Heating power of the shaded cell with the variation of radiation in inhomogeneous illumination. (b) Heating power of the shaded cell with the variation of shading ratio in incomplete shading (the incident radiation of normal cell or unshaded part is 1000 W/m$^2$).

dissipation low too. However, short current of the shaded cell increases nearly proportionally with the reduction of the shading ratio and/or the increase of incident radiation. In addition, reverse bias current increases significantly so the power dissipation of the shaded cell increases. In contrast, when the complete shading ratio is low and/or the radiation is high, short current is large and the shaded cell can reach the necessary reverse current easily; meanwhile, the voltage is small, resulting in low power dissipation. With the increase of shading ratio of cells or the decrease of incident radiation, short current of the shaded cell reduces but voltage increases significantly so power dissipation increases as well. At last, there is a maximum power dissipation point, which can attribute to the nonlinear relationship between current and voltage of solar cells.

*3.4. The Maximum Heating Power.* The worst case power dissipation is not the situation of the maximum heating power. In fact, PV cells can also convert some absorbed radiation into heat. The sharp increase of temperature of shaded cells should attribute to the combined effect of the two parts, dissipated power and heat converted from radiation. Hence, we should add the two parts up to find the worst situation, and the results are shown in Figures 8(a) and 8(b). In the study, the absorbance of a PV cell is 0.9; hence, 90% of solar energy is assumed to convert into heat. The results indicate that the maximum heating power has already reached up to 40 W and the dissipated power generated by unshaded cells occupies the more part than that generated by absorbed solar energy.

Irreversible damage can happen, especially in incomplete shading scenarios, where the heating power of the shaded part is higher than that of unshaded part significantly. Therefore, we have to take both the maximum heating power and the parallel number of cells per bypass diode into consideration to ensure whether it is acceptable or not. If it is not, it is needed to reduce the number of parallel cells per bypass diode or choose another diode and calculate again until it is reasonable in the worst case.

## 4. Conclusion

According to Kirchhoff's Voltage and Current Law, and integrating the equation of current and voltage of each branch circuit, this paper presents a new approach to study PV module by combining the same cells in inhomogeneous illumination or dividing one affected cell into many small single cells, then combining the same ones, and analyzing the shaded cell in incomplete shading. The results are shown as follows.

(1) Under certain radiation and shading condition, the maximum power dissipation of the shaded cell always happens at short-circuit conditions in both inhomogeneous illumination and incomplete shading.

(2) The variation of the number of cells has no influence on the reverse bias point of the shaded cell but can change the current of the shaded cell at the maximum power point. With the number of PV cells increasing, the shaded cell gradually transfers from generating power to dissipating power and power dissipation can be very large. Neglecting this there will be a disadvantageous effect on the shaded cell operating at the maximum power point for a long time.

(3) Different shading degrees affect the power dissipation of the shaded cell at short-circuit conditions, and there is a maximum power dissipation point, for the equation of solar cells is nonlinear.

(4) The maximum heating power of the shaded cell should be the maximum of the sum of power dissipation and the heat converted from solar energy. It appears that the maximum heating power should

play an important role in choosing bypass diode not just the parameters of bypass diodes and PV cells. If bypass diode cannot meet the requirement, altering another bypass diode characterized by lower forward turn-on voltage and/or reducing the number of PV cells in parallel per bypass diode are reasonable proposals. Of course, a diode integrated into each cell is a better proposal that has been proposed in [25].

Hot spot endurance test requires a strict test condition. Adopting the maximum heating power can provide a good reference for the safety of PV module with bypass diodes, decreasing the effect of hot spot and increasing the lifetime of PV module as soon as possible.

## Nomenclature

$I$: Current, A
$R_s$: Series resistance, Ω
$I_o$: Diode reverse saturation current, A
$R_{sh}$: Shunt resistance, Ω
$I_{ph}$: Light current, A
$T$: Temperature, K
$M$: Number of solar cells in series
$V$: Voltage, V
$N$: Number of cell string protected by bypass diode
$k$: Boltzmann's constant (1.38066$e$ − 23 J/K)
$R$: Resistance, Ω
$q$: Electron charge (1.60218$e$ − 19 Coulomb)
$I_D$: Dark current, A.

## Conflict of Interests

The authors declare that there is no conflict of interests regarding the publication of this paper.

## Acknowledgments

This work is funded by Program for New Century Excellent Talents in University (no. NCET-11-0876), the Twelfth Five-Year Science and Technology Support Key Project of China (no. 2012BAJ08B04), and Dongguan Innovative Research Team Program (no. 2014607101008).

## References

[1] Standard I. 61215, *Crystalline Silicon Terrestrial Photovoltaic (PV) Modules—Design Qualification and Type Approval*, 2005.

[2] H. Yoshioka, S. Nishikawa, S. Nakajima et al., "Non hot-spot PV module using solar cells with bypass diode function," in *Proceedings of the 25th IEEE Photovoltaic Specialists Conference*, pp. 1271–1274, IEEE, May 1996.

[3] Standards Australia, "Installation of photovoltaic PV arrays," AS/NZS 5033, 2005.

[4] K. Kim and P. T. Krein, "Reexamination of photovoltaic hot spotting to show inadequacy of the bypass diode," *IEEE Journal of Photovoltaics*, vol. 5, no. 5, pp. 1435–1441, 2015.

[5] W. Herrmann, W. Wiesner, and W. Vaassen, "Hot spot investigations on PV modules-new concepts for a test standard and consequences for module design with respect to bypass diodes," in *Proceedings of the 26th IEEE Photovoltaic Specialists Conference*, pp. 1129–1132, IEEE, Anaheim, Calif, USA, September-October 1997.

[6] S. Silvestre, A. Boronat, and A. Chouder, "Study of bypass diodes configuration on PV modules," *Applied Energy*, vol. 86, no. 9, pp. 1632–1640, 2009.

[7] V. Quaschning and R. Hanitsch, "Numerical simulation of current-voltage characteristics of photovoltaic systems with shaded solar cells," *Solar Energy*, vol. 56, no. 6, pp. 513–520, 1996.

[8] H. Kawamura, K. Naka, N. Yonekura et al., "Simulation of I–V characteristics of a PV module with shaded PV cells," *Solar Energy Materials and Solar Cells*, vol. 75, no. 3-4, pp. 613–621, 2003.

[9] E. Bende, N. Dekker, and M. Jansen, "Performance and safety aspects of PV modules under partial shading: a simulation study," in *Proceedings of the 29th European Photovoltaic Solar Energy Conference and Exhibition (EU PVSEC '14)*, September 2014.

[10] F. Fertig, S. Rein, M. Schubert, and W. Warta, "Impact of junction breakdown in multi-crystalline silicon solar cells on hot spot formation and module performance," *Cell*, vol. 40, article 80, 2011.

[11] I. Geisemeyer, F. Fertig, W. Warta, S. Rein, and M. C. Schubert, "Impact of reverse breakdown in shaded silicon solar cells on module level: simulation and experiment," in *Proceedings of the 27th European Photovoltaic Solar Energy Conference*, Frankfurt, Germany, 2012.

[12] I. Geisemeyer, F. Fertig, W. Warta, S. Rein, and M. C. Schubert, "Prediction of silicon PV module temperature for hot spots and worst case partial shading situations using spatially resolved lock-in thermography," *Solar Energy Materials and Solar Cells*, vol. 120, pp. 259–269, 2014.

[13] B. A. Alsayid, S. Y. Alsadi, J. S. Jallad, and M. H. Dradi, "Partial shading of pv system simulation with experimental results," *Smart Grid and Renewable Energy*, vol. 4, no. 6, pp. 429–435, 2013.

[14] S. Hamdi, D. Saigaa, and M. Drif, "Modeling and simulation of photovoltaic array with different interconnection configurations under partial shading conditions for fill factor evaluation," in *Proceedings of the International Renewable and Sustainable Energy Conference (IRSEC '14)*, pp. 25–31, IEEE, Ouarzazate, Morocco, October 2014.

[15] M. Abdulazeez and I. Iskender, "Simulation and experimental study of shading effect on series and parallel connected photovoltaic PV modules," in *Proceedings of the 7th International Conference on Electrical and Electronics Engineering (ELECO '11)*, pp. I28–I32, Bursa, Turkey, December 2011.

[16] L. S. Kothari, P. C. Mathur, A. Kapoor, P. Saxena, and R. P. Sharma, "Determination of optimum load for a solar cell," *Journal of Applied Physics*, vol. 53, pp. 5982–5984, 1982.

[17] T. U. Townsend, *A Method for Estimating the Long-Term Performance of Direct-Coupled Photovoltaic Systems*, University of Wisconsin, Madison, Wis, USA, 1989.

[18] A. Virtuani, E. Lotter, and M. Powalla, "Performance of Cu(In,Ga)$Se_2$ solar cells under low irradiance," *Thin Solid Films*, vol. 431-432, pp. 443–447, 2003.

[19] W. Herrmann and W. Wiesner, "Current voltage translation procedure for PV generators in the German 1.000 roofs-programme," in *Proceedings of the International Conference on Solar Energy and Buildings (EuroSun '96)*, pp. 701–705, Freiburg, Germany, September 1996.

[20] G. M. Masters, *Renewable and Efficient Electric Power Systems*, John Wiley & Sons, 2013.

[21] J. A. Duffie and A. William, *Beckman Solar Engineering of Thermal Processes*, John Wiley & Sons, New York, NY, USA, 2006.

[22] Z. Zhai, *The output characteristic predicting of PV array in arbitrary condition [Ph.D. thesis]*, University of Science and Technology of China, Hefei, China, 2008.

[23] S. R. Wenham, *Applied Photovoltaics*, Routledge, London, UK, 2012.

[24] A. K. Sharma, R. Dwivedi, and S. K. Srivastava, "Performance analysis of a solar array under shadow condition," *IEE Proceedings G—Circuits, Devices and Systems*, vol. 138, no. 3, pp. 301–306, 1991.

[25] M. A. Green, "Integrated solar cells and shunting diodes," Google Patents, 1982.

Hindawi Publishing Corporation
International Journal of Photoenergy
Volume 2015, Article ID 545831, 12 pages
http://dx.doi.org/10.1155/2015/545831

*Research Article*

# Method to Calculate the Electricity Generated by a Photovoltaic Cell, Based on Its Mathematical Model Simulations in MATLAB

**Carlos Morcillo-Herrera,[1] Fernando Hernández-Sánchez,[1] and Manuel Flota-Bañuelos[2]**

[1]*Scientific Research Center of Yucatan, A.C., 43 Street, No. 130, Chuburná Hidalgo, 97200 Mérida, YUC, Mexico*
[2]*Department of Engineering, Autonomous University of Yucatán, Nonpolluting Industries Avenue, No. 150, Cordemex, 97310 Mérida, YUC, Mexico*

Correspondence should be addressed to Fernando Hernández-Sánchez; fhs@cicy.mx

Received 18 May 2015; Revised 7 September 2015; Accepted 8 September 2015

Academic Editor: Xudong Zhao



This paper presents a practical method for calculating the electrical energy generated by a PV panel (kWhr) through MATLAB simulations based on the mathematical model of the cell, which obtains the "Mean Maximum Power Point" (MMPP) in the characteristic $V$-$P$ curve, in response to evaluating historical climate data at specific location. This five-step method calculates through MMPP per day, per month, or per year, the power yield by unit area, then electrical energy generated by PV panel, and its real conversion efficiency. To validate the method, it was applied to Sewage Treatment Plant for a Group of Drinking Water and Sewerage of Yucatan (JAPAY), México, testing 250 Wp photovoltaic panels of five different manufacturers. As a result, the performance, the real conversion efficiency, and the electricity generated by five different PV panels in evaluation were obtained and show the best technical-economic option to develop the PV generation project.

## 1. Introduction

According to the World Energy Outlook 2014, the global demand for electricity continues to rise at a high rate [1]. This incremental demand is supplied by fossil fuels by 70%, while the remaining 24% is supplied by nuclear energy and hydropower, and only 6% is supplied by renewable energy. Renewable energy sources have the characteristics of generating clean energy available in nature, contributing to supplying energy demanded of users, reducing the fossil fuels exhaustion, and mitigating the emission of greenhouse gases [2].

Renewable energy with the largest power generation capacity installed is wind power; however, solar energy is growing at a faster rate than any other form of renewable energy. Solar energy is available everywhere in the world; it is considered inexhaustible and has a higher annual generation potential than the annual electricity generation worldwide. The solar energy potential is harnessed by thermal and photovoltaic systems to generate electricity either on a large scale as a solar farm or on small scale as an autonomous or grid connected photovoltaic system (SFV) [3]. Today, the SFV begins to penetrate the world market as an opportunity for electrical energy microgeneration, thanks to the opening in regulations, rules, and policies worldwide, increasing the conversion efficiency of the new cells and the cost reduction per kilowatt installed [4]. However photovoltaic technology still has significant challenges; one of them is its perception as a source of energy with a prolonged and unreliable return of investment. This is caused by uncertainty in the amount of electricity generation, due to the daily variations of climatic factors, at the locality where the SFV is installed. A determining factor for investment in photovoltaic generation projects is to have the most realistic estimate of electricity generated by SFV from solar energy available in the locality; therefore, a practical method to calculate this energy is required.

The first proposed works in the literature focus the efforts to calculate theoretically the energy potential radiated per square meter ($kW/m^2$) for a locality, due to the high cost

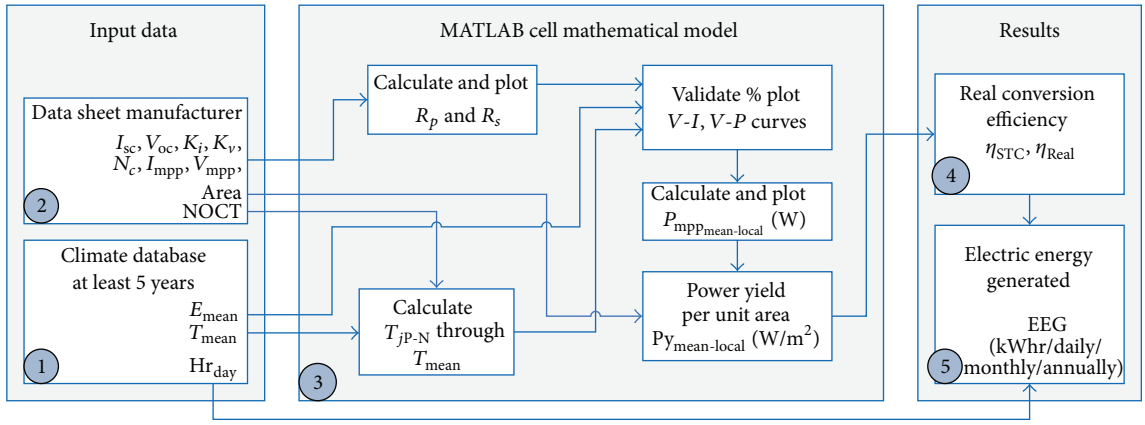


Figure 1: Proposed method flowchart.

associated with instruments measuring solar radiation. The proposed methods are based on solar radiation data, as C. Hotel's model that is based on direct radiation [5], Liu-Jordan's model that is based on diffuse radiation [6], and other theoretical models that are based on both radiations [7]. From the earlier works, a second-step model is presented in the literature to estimate energy potential in available areas such as roofs and facades in urban buildings or houses, with the target of estimating incident energy radiated (kWhr/m$^2$), for planning SFV applications. These proposals are based on digital or mathematical surface models (DSM) [8, 9], climatic data simulations [10], geographic information systems (GIS) [11–13], and photovoltaic geographical information system (PVGIS) [14]. All previous methods estimate the energy potential but not the electricity generation by the panel PV. Recently a model was presented for estimating the cell power considering ambient conditions [15] and their dependence on irradiance and temperature [16]; however, this methodology does not consider the number of sunlight hours and the intrinsic cells characteristic. These previous models are based on the GIS, using the available annual average radiation data and efficiency of PV panel to estimate the generation.

Therefore, the methods stated above estimate the potential for solar radiant energy for a specific location, but they do not estimate the real electric energy generation of PV panel. In practice, the difference between the potential energy radiated regarding the electric power generated by a PV panel is significant; this is due to the panels only generating their maximum power peak, under conditions of 1000 W/m$^2$ at a cell temperature of 25°C, known as standard test conditions (STC). It is known that there are locations around the world where STC is not reached and therefore the cell never reaches the maximum power point specified by the manufacturer.

Then, the electricity generated by PV cell is a function of the solar incident radiation ($E$); the cell junction temperature ($T_{JP\text{-}N}$); the sunlight exposure hours ($Hr_{day}$); the cell conversion efficiency ($\eta$); and its maximum power point (MPP) [17].

The last two factors depend on the intrinsic characteristics of the cells and will be reflected in the $V$-$I$ and $V$-$P$ characteristic curves, so there are differences between different manufacturers.

The aim of this paper is to provide a method using MATLAB to calculate the electrical energy generation of a cell based on its mathematical model and a reliable historical climate database.

## 2. Method Development

The proposed method is based on a photovoltaic cell mathematical model and requires, as input, manufacturer cell data sheet and a climate database. As output, the efficiency and electrical energy generated by a PV panel are obtained.

The flowchart (Figure 1) shows the sequence of the five-step method, which was implemented in the MATLAB simulation software.

*Step 1* (historical climate database). PV panels are sensitive to radiation and temperature variations. When the P-N junction temperature of the cell is increased, the output voltage is reduced. Likewise when the incident radiation in the cell reduces, its current output reduces too. The reductions of voltage, current, or both are reflected directly in an output power reduction and therefore reduce the energy conversion efficiency [18]. Given the influence of these parameters on the electricity generation of PV panels, it is necessary to have a reliable climate database of the location, at least five years of records to have a tendency. The parameters required by database are as follows: temperature daily mean ($T_{mean}$), radiation daily mean ($E_{mean}$), and daylight hours daily mean ($Hr_{day}$).

Globally, there are several databases available that can be used such as the Center for Atmospheric Sciences NASA Langley Research Data (LaRC), which provide 22 years of historical data from any quadrant of the globe defined by longitude and latitude [19], and the database of the European Solar Radiation Atlas (ESRA) [20]. Most countries have an official climate database; in Mexico the Water National Commission (CONAGUA) provides a database with records for each state over the last 50 years [21]. Several governmental or educational institutions maintain climate records such as the Advanced Research Center (CINVESTAV) in Merida, Yucatan, Mexico [22].

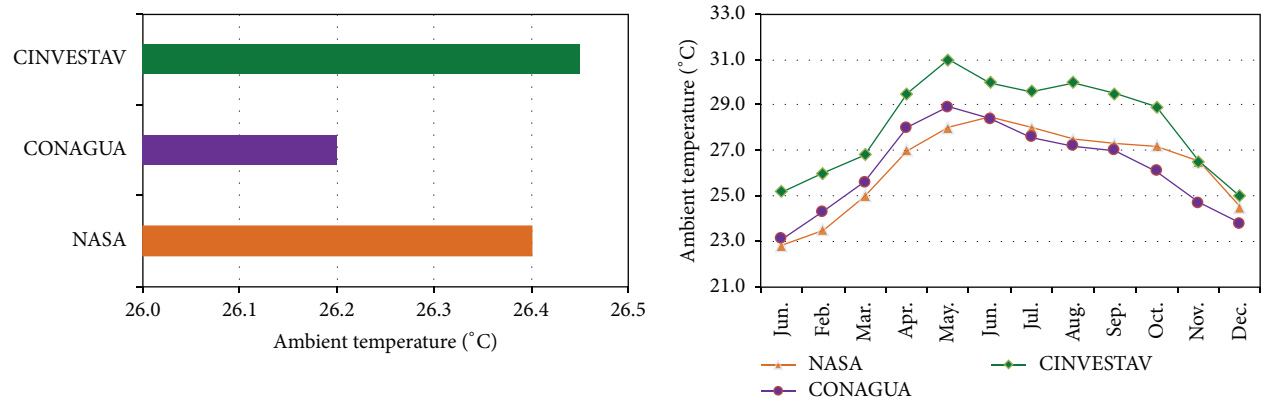


Figure 2: Temperature annual and monthly daily mean.

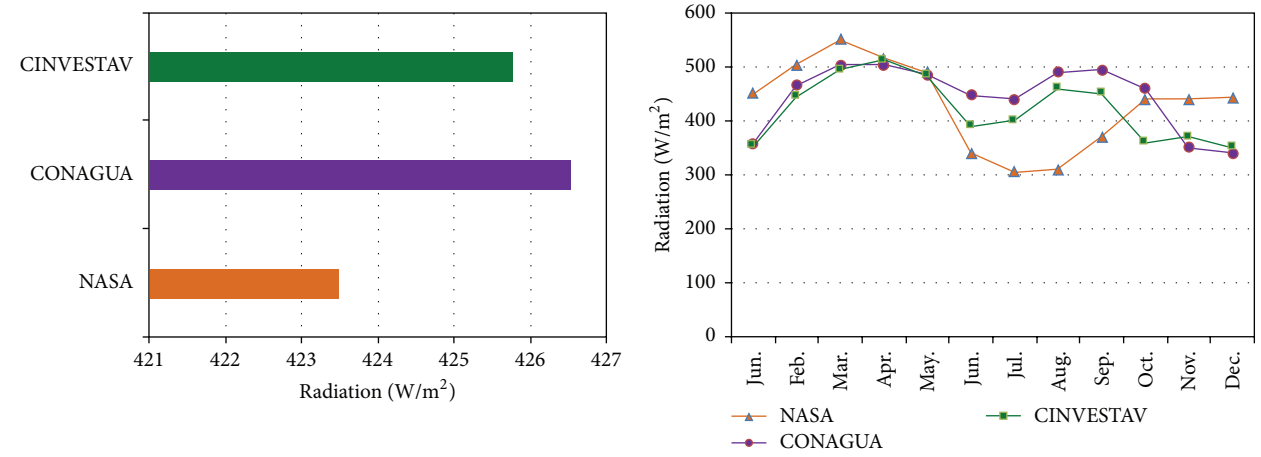


Figure 3: Radiation annual and monthly daily mean.

While a database for a location is more specific, the calculation of the method has major approximation to reality; therefore a local database is recommended.

In this case the proposed method was applied to a PV project in a Sewage Treatment Plant for a Group of Drinking Water and Sewerage of Yucatan (JAPAY) located at Merida, same place as CINVESTAV.

*Temperature Annual Daily Mean*. Using CINVESTAV climate database to validate the proposed method and using the NASA and CONAGUA database as reference, Figure 2 shows the temperature annual and monthly mean ($T_{mean}$), averaging at least five years for Merida city.

CINVESTAV database indicates that $T_{mean}$ per year is 26.45°C, NASA database indicates 26.4°C, and CONAGUA database indicates 26.2°C. These records validate the CINVESTAV database which will be used in this method. $T_{mean}$ value for Merida is 26.45°C.

*Radiation Annual Daily Mean*. Using the same procedure, the radiation daily mean ($E_{mean}$) of at least 5 years was obtained. In Figure 3 the database records of annual and monthly radiation are presented. According to the CINVESTAV database, in Merida city, $E_{mean}$ is 425.78 W/m$^2$.

*Daylight Hours Annual Daily Mean*. Applying the same procedure, the number of hours of daylight ($Hr_{day}$) is shown in Figure 4, for an annual and monthly daily mean of at least five years. The CINVESTAV database indicates that the number of hours with daylight for Merida is 12.17 hr.

*Step 2* (data cell manufacturer). The intrinsic characteristic of photovoltaic cells is that other factors determine the performance and efficiency conversion of radiant energy into electrical energy.

Therefore, it is important to identify in the manufacturer data sheet the following parameters: short-circuit current ($I_{sc}$), open circuit voltage ($V_{oc}$), the temperature coefficient of $I_{sc}$ ($K_i$), the temperature coefficient of $V_{oc}$ ($K_v$), the total number of cells connected in the panel ($N_c$), the current at the maximum power point ($I_{mpp}$), the voltage at the maximum power point ($V_{mpp}$), the nominal operating cell temperature (NOCT), and the panel area (m$^2$). In order to implement

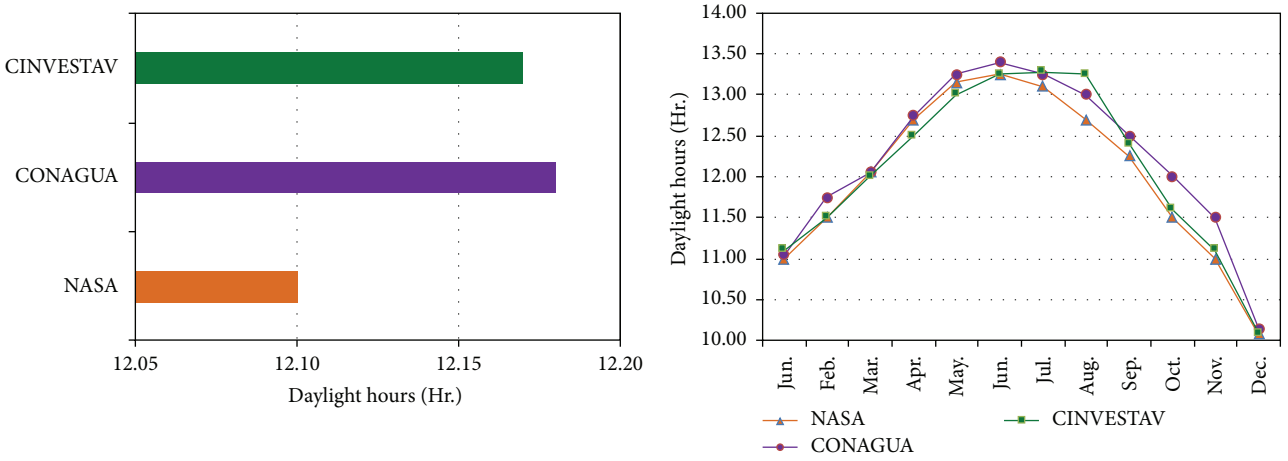


Figure 4: Daylight hours annual and monthly daily mean.

Table 1: Data sheet parameters of 250 Wp PV panel.

| NOCT | $V_{mpp}$ | $I_{mpp}$ | $V_{oc}$ | $I_{sc}$ | $K_i$ | $K_v$ | $N_c$ | Area |
|---|---|---|---|---|---|---|---|---|
| 45 | 30.12 | 8.3 | 37.85 | 8.65 | 0.005 | −0.17 | 60 | 1.62 |

the proposed method, a 250 Wp polycrystalline photovoltaic panel S60PC, Solartec brand, is used as an example for calculation [23]. Table 1 shows the values of the parameters of S60PC PV panel at STC.

*Step 3* (cell mathematical model in MATLAB). In order to determine the maximum electrical power point ($P_{mpp}$) that a PV panel generates with a specific junction temperature value ($T_{JP\text{-}N}$) and radiation ($E_{mean}$) a mathematical model of the photovoltaic cell is necessary to approximate the nonlinear behavior, through its $V$-$I$ and $V$-$P$ curves.

The simplest mathematical model reported includes one diode parallel to a current source [24, 25], where the current source represents $E_{mean}$ and the diode represents the P-N cell junction. An improved version adds the series resistance ($R_s$) effects at the output circuit, to enhance model accuracy, but it exhibited deficiencies with high values of junction temperature [26, 27].

Later it was suggested to add the effect of a parallel resistance ($R_p$) with diode and current source to improve the behavior of the model [28, 29]. Recently Ishaque et al. proposed a mathematical model that adds a second diode in parallel, increasing accuracy without losing the simplicity, modeling with better yield to partial shading, and will be applied to monocrystalline and polycrystalline PV panels with low errors [30].

The last two diodes' mathematical model, represented by the equivalent circuit of the PV cell shown in Figure 5, will be used to derive equations that will lead to the mathematical model which is the base of this step.

The values of the series and parallel resistance ($R_s$ and $R_p$), appearing in the equivalent circuit of the cell, are not

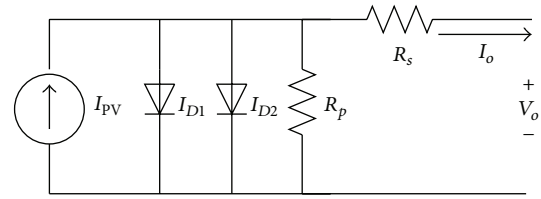


Figure 5: Two diodes' PV cell equivalent circuit.

available in the manufacturer data sheet. To obtain these values, clearing $R_p$ and $R_s$ from the mathematical equations was required. Applying Norton's theorem for nodes analysis, the following equation is derived:

$$I_o = I_{PV} - I_{D1} - I_{D2} - I_{R_p}, \tag{1}$$

where $I_o$ is the output current of PV cell; $I_{PV}$ is the current generated by the incidence of light; $I_{D1}$ and $I_{D2}$ are currents of diode 1 and diode 2, respectively; and $I_{R_p}$ is the current of parallel resistance.

Replacing $I_{D1}$ and $I_{D2}$ by the diode characteristic equation and replacing $I_{R_p}$ in terms of output voltage ($V_o$) and output current ($I_o$), (1) can be rewritten as

$$\begin{aligned} I_o &= I_{PV} - I_{SAT1}\left[\exp\frac{q\left(V_o + I_oR_s\right)}{N_cKT_{jP\text{-}N}}\right] \\ &\quad - I_{SAT2}\left[\exp\frac{q\left(V_o + I_oR_s\right)}{N_cKT_{jP\text{-}N}}\right] - I_{R_p}, \\ I_o &= I_{PV} - \left[I_{SAT1} + I_{SAT2}\right]\left[\exp\frac{q\left(V_o + I_oR_s\right)}{N_cKT_{jP\text{-}N}}\right] \\ &\quad - \frac{V_o + I_oR_s}{R_p}, \end{aligned} \tag{2}$$

where $I_{SAT1}$ and $I_{SAT2}$ are the reverse saturation currents of diode 1 and diode 2, respectively; $K$ is the Boltzmann

constant; $q$ is the electron charge; $N_c$ is the number of cells; and $T_{j\text{P-N}}$ is the junction temperature of cell.

To obtain $R_p$ value in terms of $R_s$ in the $P_{\text{mpp}}$, it is necessary to replace $V_o$ with $V_{\text{mpp}}$ and $I_o$ with $I_{\text{mpp}}$, and this was obtained after cleaning and replacing:

$$R_p = \frac{V_{\text{mpp}} + I_{\text{mpp}} R_s}{I_{\text{PV}} - \left[I_{\text{SAT1}} + I_{\text{SAT2}}\right]\left[\exp\left(\left(q\left(V_{\text{mpp}} + I_{\text{mpp}} R_s\right)\right)/N_c K T_{j\text{P-N}}\right) - 1\right] - I_{\text{mpp}}}. \tag{3}$$

*Calculation of $R_p$ and $R_s$*. From (3), $R_p$ is function of $R_s$, and then, for a finite and positive $R_s$ value, $R_p$ is obtained through iterations of $R_s$ so that it approximates $P_{\text{mpp}}$. Applying the equations in MATLAB simulation for photovoltaic panel subject to test, a series or family of curves $V$-$I$ and $V$-$P$ is obtained, which permitted finding $R_s$ and $R_p$ value, closest to $P_{\text{mpp}}$. Several techniques have been demonstrated with simulations by Shongwe and Hanif [31], Xiao et al. [32], Ishaque and Salam [33], and Márquez et al. [34] to model one or two diodes.

Figure 6 shows the result in MATLAB of the characteristic curves $V$-$I$ and $V$-$P$, which through iterations obtained the value of $R_s = 0.37\ \Omega$ and $R_p = 400\ \Omega$ for the 250 Wp panel S60PC.

*Calculation of Junction P-N Temperature*. From the annual daily average of temperature ($T_{\text{mean}}$) that was obtained from climate database, it was necessary to calculate the value of $T_{J\text{P-N}}$ that causes the effect on output voltage. Definitely there is a relationship between the ambient temperature and the junction temperature cell. However this relationship is not direct or linear.

In practice, it is a complex task to measure the cell junction temperature and other variables involved such as solar radiation, wind speed, the spectral distribution of the irradiation, the absorption capacity and heat dissipation, and the intrinsic construction material, as was reported by Lasnier and Gang-Ang [35]. In the literature, there are several studies of methods and procedures for determining the coefficient of temperature junction cell, as were presented by King et al. [36], which uses the short current and open circuit voltage of the PV cell. A practice equation for estimating the junction temperature cell is presented by García and Balenzategui [37], through calculations based on the nominal operating cell temperature (NOCT) in compliance with international standards EN-61646, EN-61215, and E1036M applicable to polycrystalline, monocrystalline, and thin film cells.

The value for NOCT of a cell is available on the manufacturer data sheet. The procedure for determining the junction temperature from NOCT is based on the fact that the difference between ambient temperature and the junction temperature is associated but is independent, and it also has a directly proportional relationship to the radiation for values between 400 and 1000 W/m$^2$. This allows for determining the junction temperature based on the following equation:

$$T_{J\text{P-N}} = T_{\text{mean}} + (\text{NOCT} - 20)\,\frac{E_{\text{mean}}}{800}. \tag{4}$$

Replacing the value of $T_{\text{mean}} = 26.45^{\circ}$C, $E_{\text{mean}} = 425.78$ W/m$^2$, and NOCT = 45, the value of $T_{J\text{P-N}} = 39.75^{\circ}$C is obtained for 250 Wp PV panel.

*Validating V-I and V-P Characteristic Curves*. Starting from (2) that describes the mathematical model of the photovoltaic cell in terms of the output voltage and output current, it is required to rewrite $I_{\text{PV}}$, $I_{\text{SAT1}}$, and $I_{\text{SAT2}}$ in terms of $E_{\text{mean}}$ and $T_{J\text{P-N}}$:

$$\begin{aligned} I_{\text{PV}} &= I_{\text{sc}} + K_i * (T_{J\text{P-N}} - 25)\,\frac{E_{\text{mean}}}{1000}, \\ I_{\text{SAT1}} &= I_{\text{SAT2}} \\ &= \frac{I_{\text{sc}} + K_i * (T_{J\text{P-N}} - 25)}{\exp\left[\left(q\left(V_{\text{oc}} + \left[K_v * (T_{J\text{P-N}} - 25)\right]\right)\right)/\left(N_c * K * T_{J\text{P-N}}\right)\right] - 1}, \end{aligned} \tag{5}$$

where the values of $K_i$, $K_v$, and $N_c$ are available in the manufacturer data sheet as described in Step 2.

Using MATLAB Simulink language, the proposed method was implemented and integrated in a scheme that is shown in Figure 7. The values of data sheet parameter PV panel and $T_{\text{mean}}$ and $E_{\text{mean}}$ from climate database were described. After the value declarations, there are two "interpreted MATLAB function blocks" that represent MATLAB programs to calculate $T_{J\text{P-N}}$ from $T_{\text{ambient}}$ value and calculate $R_s$ and $R_p$ values. The center of the figure is a mask which was the main equation (2) developed (Figure 8). In the mask, the value of mean maximum power point (MMPP) and the power yield per unit area was obtained by evaluating and simulating all historic parameters. In the end, there is a third "interpreted MATLAB function block" to calculate the aim of this method and the efficiency and the electricity energy generated by the PV panel.

To prove the mathematical model, the characteristic curve $V$-$P$ with different values of $T_{J\text{P-N}}$ and $E$ was plotted, from the values defined for the STC. To validate the performance cell simulated in MATLAB, the $V$-$P$ characteristic curve provided by the manufacturer was compared with the curve plotted in MATLAB. The maximum power point ($P_{\text{mpp}}$) had to match with the PV panel power peak defined by the manufacturer. The characteristic curves families obtained for the 250 Wp PV panel are shown in Figure 9, denoting that $P_{\text{mpp}}$ is 250 W.

*Mean Maximum Power Point for Locality*. Evaluating and simulating the historic climate data of $T_{J\text{P-N}}$ and $E_{\text{mean}}$, in the same $V$-$P$ curve, plotted the result of evaluating the cell mathematical model for a specific PV panel and location. As a result, the Mean Maximum Power Point, now called MMPP,

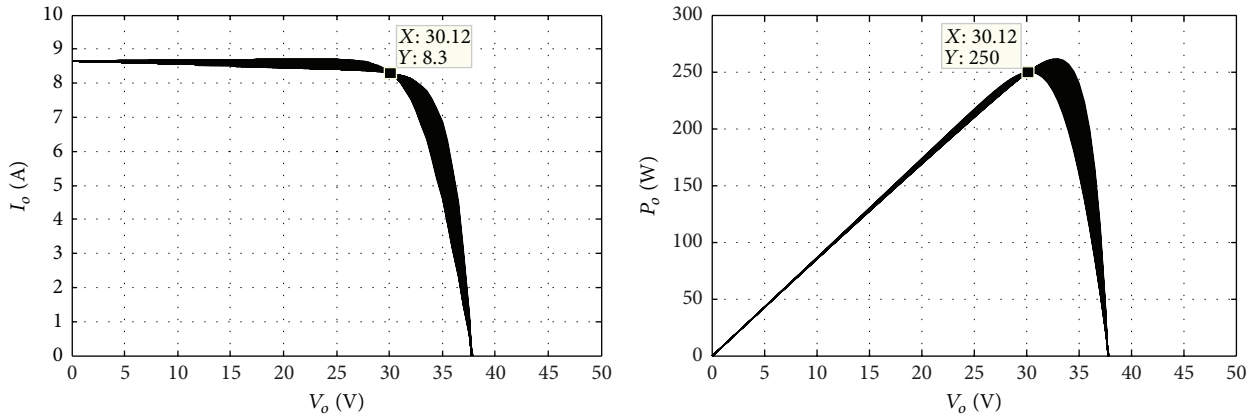


Figure 6: MATLAB iteration result to calculate $R_s$ and $R_p$.

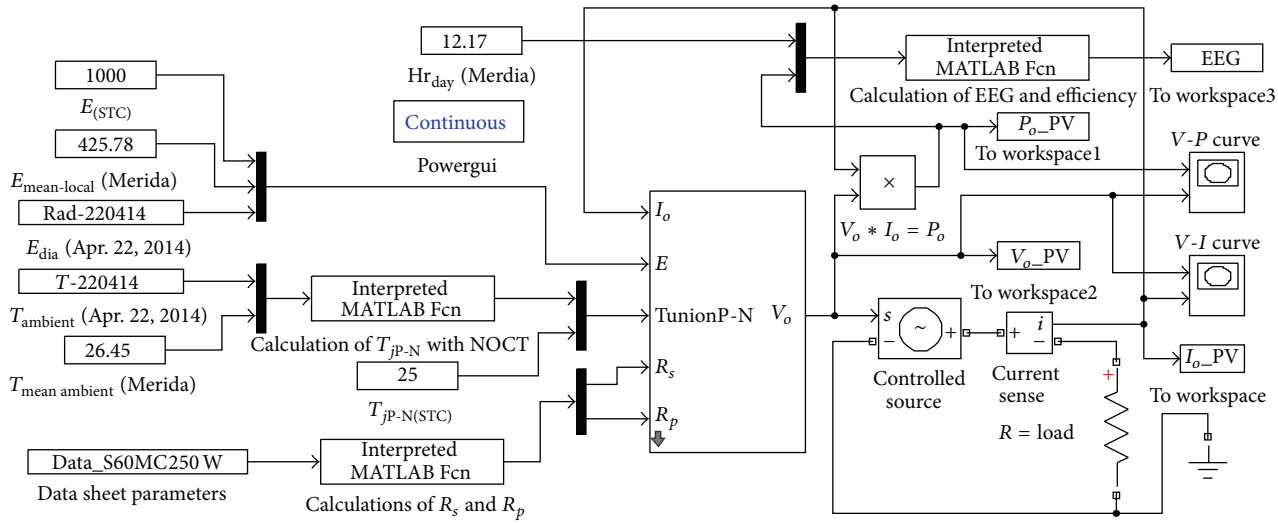


Figure 7: Implementation of proposed mathematical method in MATLAB Simulink.

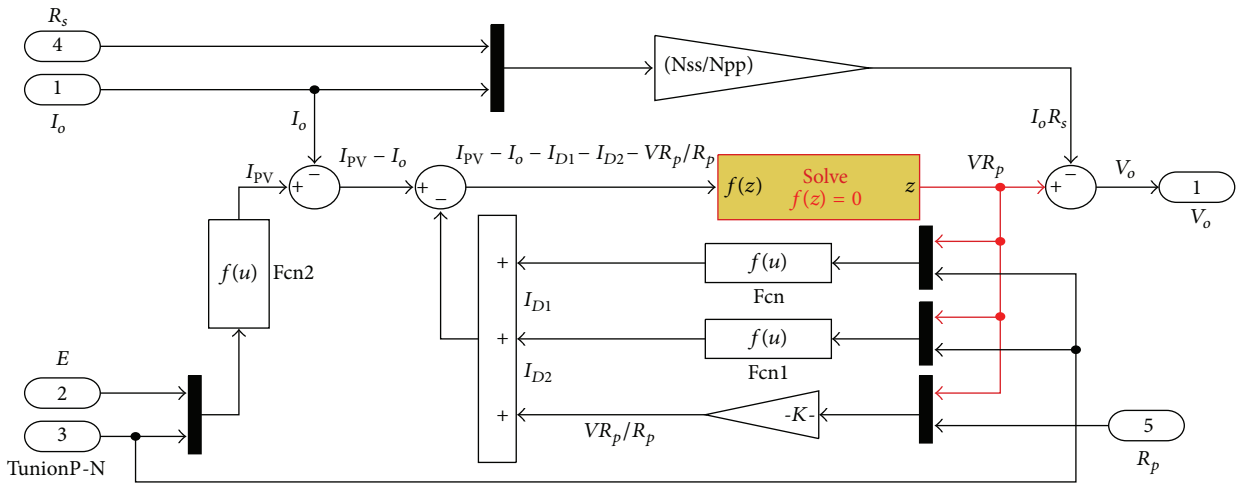


Figure 8: Cell mathematical model inside of MATLAB Simulink mask.

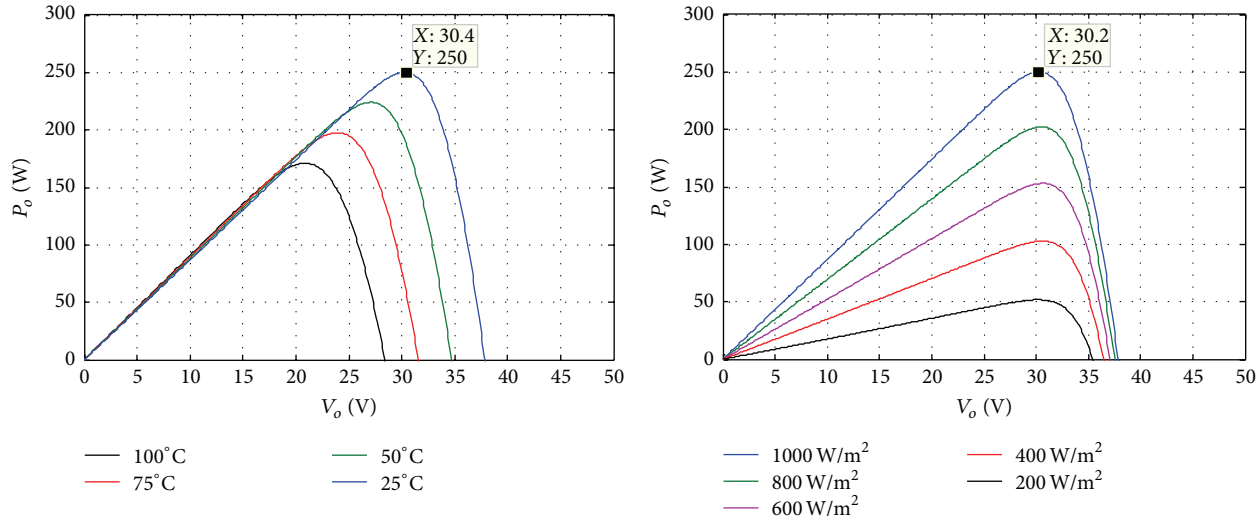


Figure 9: $V$-$P$ curves evaluating values of $E_{\text{mean}}$ and $T_{\text{JP-N}}$ respect STC values.

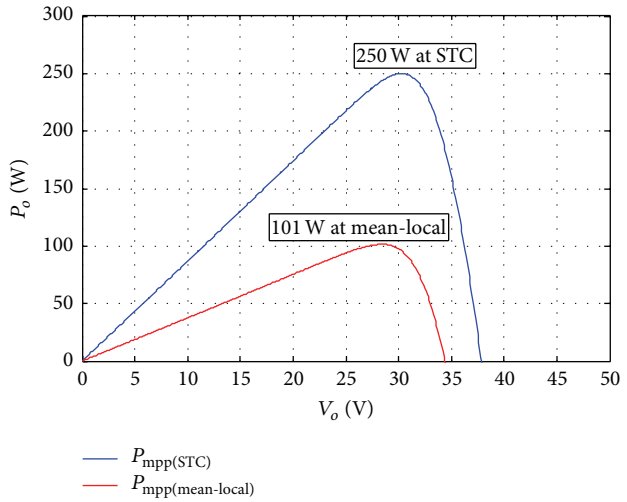


Figure 10: $V$-$P$ curves result for $P_{\text{mpp(STC)}}$ versus MMPP.

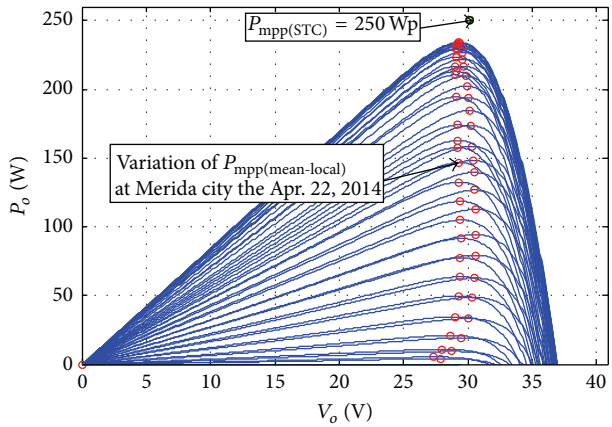


Figure 11: Simulation of $P_{\text{mpp}}$ at Merida for all of one day.

corresponds to the annual daily average of power for the last five years in Mérida city. Figure 10 shows the significant difference between $P_{\text{mpp}}$ displayed under STC, compared to MMPP at Mérida according to its historical weather.

The simulation result shows that, depending on the historical values of the temperature and radiation of a locality, the difference between $P_{\text{mpp(STC)}}$ and MMPP should be more or less significant. For Merida city the result between both is $P_{\text{mpp(STC)}}$ = 250 W respect MMPP = 101 W.

Using the same method implemented in MATLAB Simulink, Figure 10 shows the results for a full day (Apr. 22, 2014) in Merida using the different values along the day of temperature and radiation.

Figure 11 demonstrates the behavior and variation of $P_{\text{mpp}}$ throughout the day. In the morning $P_{\text{mpp}}$ increased, in the middle of the day it reached its maximum, and in the afternoon it decreased its value. In fact, for this particular day and location, $P_{\text{mpp}}$ did not reach the value of $P_{\text{mpp(STC)}}$. This is the relevance to work with MMPP.

*Power Yield per Unit Area.* An important parameter in the planning electrical generation projects with photovoltaic energy is to know the PV panel power yield (Py) per unit area (W/m$^2$). This data allows quantifying the area required for the SFV installation.

The Py can be calculated under two conditions: for real values corresponding to a locality, as described by (6), and for the values in STC conditions, as described by (7). $P_{\text{mpp(STC)}}$ is the power peak provided for manufacturer data sheet:

$$\text{Py}_{\text{local}} = \frac{\text{MMPP}}{\text{Area}_{\text{PV}}}, \tag{6}$$

$$\text{Py}_{\text{STC}} = \frac{P_{\text{mpp(STC)}}}{\text{Area}_{\text{PV}}}. \tag{7}$$

Applying (6) and (7), the result for Merida and the 250 Wp PV panel selected is $Py_{STC} = 154.32\,W/m^2$ whereas $Py_{local} = 62.65\,W/m^2$.

There is a loss of yield greater than 60%. So this fall should be attenuated or enhanced depending on the panel under test and the locality. A PV panel with high Py requires lower area than any other one with low Py. Therefore dimensioning the area with values at STC is not the most appropriate, because the MMPP varies from one locality to another, but this value is almost lower than $P_{mpp(STC)}$.

*Step 4* (real conversion efficiency). The real conversion efficiency ($\eta_{real}$) indicates the rate between the power yield at locality and the annual daily mean radiation ($E_{mean}$) per unit area in the same location. Substituting the values previously obtained of local power yield for the panel 250 Wp at Merida city $\eta_{real} = 14.71\%$,

$$\eta_{real} = \frac{Py_{local}}{E_{mean}}. \tag{8}$$

The manufacturer conversion efficiency ($\eta_{STC}$) described in the data sheet was obtained through (9), comparing the power yield in contrast to the incident radiation at standard condition test. $Py_{STC}$ was obtained in (7), and $E_{STC}$ was defined as $1000\,W/m^2$. The efficiency at STC is $\eta_{STC} = 15.43\%$:

$$\eta_{STC} = \frac{Py_{STC}}{E_{STC}}. \tag{9}$$

The difference between the real efficiency and standard efficiency indicates that even though it is the same panel, out of standard values, the efficiency always drops.

*Step 5* (electric energy generated by a PV panel). The last step is to know the electric energy generated (EEG) by the PV panel. It can be obtained in two ways: by multiplying the instantaneous value of $P_{mpp}$ for the duration of each sample and after adding all energy obtained or using MMPP and multiplying by daylight hours annual daily mean. The result was the same, so this paper uses the latter way to obtain EEG. EEG by PV panel in Merida can be calculated by the next equation:

$$EEG = MMPP * Hr_{day}. \tag{10}$$

Applying the equation above the electricity generated was obtained for annual daily mean for each 250 Wp PV panel S60MC at Mérida as a result of evaluating in MATLAB, historical climate data in the mathematical model of the photovoltaic cell. EEG = 1.22 kWhr/day.

## 3. Results

The proposed method was applied to a project for the Sewage Treatment Plant for Group of Drinking Water and Sewerage of Yucatan (JAPAY), México, testing 250 Wp PV panels of five different manufacturers, to generate 95% of electric power consumption daily average. Table 2 show the PV panel subject test.

Table 2: 250 Wp PV panel of different manufacturers.

| Jinshi | Solartec | LDK | Canadian | Kewell |
|---|---|---|---|---|
| NBJ-250W | S60MC250 | LDK250D2 | VirtusII250 | KWP-250W |
| 250 Wp | 250 Wp | 250 Wp | 250 Wp | 250 Wp |

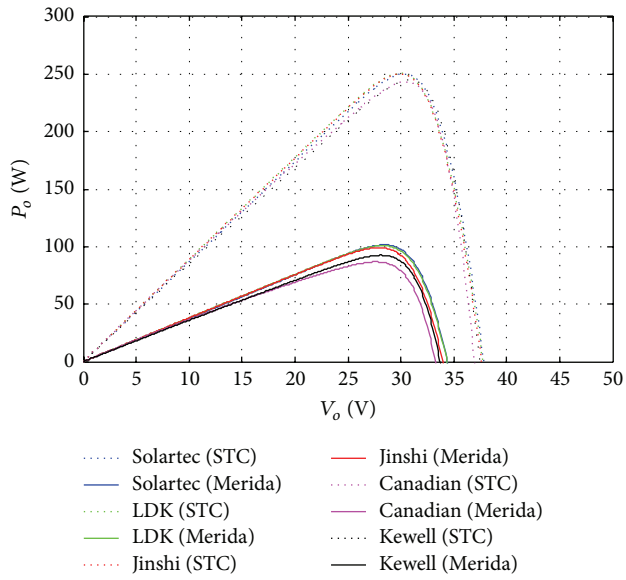


Figure 12: Simulation result of $P_{mpp(STC)}$ versus MMPP in Merida for the 5 PV panels.

The aim of using the proposed method in this project is to determine the electricity generated for each PV panel tested, likewise, to evaluate and select the best efficiency option, to reduce the cost of investment, and to lower the installation area, providing greater certainty and reliability for investment return.

Applying the three first steps of proposed method the results are presented in Table 3 for five PV panels tested.

To continue with the step there, the simulation results are evaluating simultaneously the 5 different PV panels to visualize and validate in the same graph the results of $P_{mpp(STC)}$ regarding MMPP. The resulting $V$-$P$ curves are shown in Figure 12.

Table 4 shows the result of applying Step 4 to obtain the power yield and the real conversion efficiency, evaluating at STC and for Merida city for the same 5 PV panels.

Table 4 indicates that there are differences between the MMPP generated under Merida climatic conditions regarding $P_{mpp(STC)}$, and therefore the power yield and the efficiency present differences. Some PV panels have greater efficiency than others.

Finally, applying Step 5, Table 5 presents the results of the electrical energy generated (EEG) at Merida, for each 250 Wp PV panel evaluated in MATLAB simulations under the proposed method. Table 5 presents the EEG for a day, month, and year.

Table 3: Results of three first steps in Merida city.

| Manufac. | NOCT | $R_p$ | $R_s$ | $V_{mpp}$ | $I_{mpp}$ | $V_{oc}$ | $I_{sc}$ | $K_i$ | $K_v$ | $N_c$ |
|---|---|---|---|---|---|---|---|---|---|---|
| Jinshi | 47 | 381.5 | 0.38 | 29.95 | 8.35 | 37.66 | 8.92 | 0.0051 | −0.124 | 60 |
| Solartec | 45 | 400.7 | 0.37 | 30.12 | 8.31 | 37.85 | 8.65 | 0.0053 | −0.123 | 60 |
| LDK | 45 | 550.1 | 0.4 | 29.9 | 8.38 | 37.8 | 8.92 | 0.0053 | −0.118 | 60 |
| Candian | 45 | 341.2 | 0.31 | 30.11 | 8.31 | 37.42 | 8.83 | 0.0035 | −0.112 | 60 |
| Kewell | 47 | 156.5 | 0.25 | 30.72 | 7.99 | 37.55 | 8.68 | 0.0017 | −0.127 | 60 |

Table 4: Py and $\eta$ for 5 PV panels at Merida city.

| Manufac. | MMPP (W) | $P_{mpp(STC)}$ (W) | Area ($m^2$) | $Py_{(local)}$ ($W/m^2$) | $Py_{STC}$ ($W/m^2$) | $\eta_{(STC)}$* (%) | $\eta_{Real}$** (%) |
|---|---|---|---|---|---|---|---|
| Jinshi | 99.5 | 250 | 1.63 | 61.04 | 153.37 | 15.34 | 14.34 |
| Solartec | 101.5 | 250 | 1.62 | 62.65 | 154.32 | 15.43 | 14.72 |
| LDK | 100.8 | 250 | 1.63 | 61.84 | 153.37 | 15.34 | 14.52 |
| Canadian | 86.72 | 250 | 1.63 | 53.20 | 153.37 | 15.34 | 12.50 |
| Kewell | 92.55 | 250 | 1.62 | 57.13 | 154.32 | 15.43 | 13.42 |

* $E_{STC} = 1000\ W/m^2$; ** $E_{mean} = 425.78\ W/m^2$.

Table 5: EEG at Merida per day, month, and year.

| Manufact. | $Py_{(local)}$ ($W/m^2$) | $Hr_{day}$ (hr) | $EEG_{(day)}$($kWhr/m^2$) | $EEG_{(month)}$ ($kWhr/m^2$) | $EEG_{(annual)}$ ($kWhr/m^2$) |
|---|---|---|---|---|---|
| Jinshi | 99.5 | 12.17 | 1.21 | 36.93 | 443.19 |
| Solartec | 101.5 | 12.17 | 1.24 | 37.68 | 452.10 |
| LDK | 100.8 | 12.17 | 1.23 | 37.42 | 448.99 |
| Canadian | 86.72 | 12.17 | 1.06 | 32.19 | 386.27 |
| Kewell | 92.55 | 12.17 | 1.13 | 34.35 | 412.24 |

Table 6: Investment and total area required for JAPAY project at Merida.

| Manufact. | $EEG_{(day)}$ ($kWhr/m^2$) | Cost ($USD) | *Panels (#) | Investment ($USD) | Tot. area ($m^2$) |
|---|---|---|---|---|---|
| Jinshi | 1.21 | 337.5 | 490 | $165,375 | 798.70 |
| Solartec | 1.24 | 329.8 | 480 | $158,304 | 777.60 |
| LDK | 1.23 | 347.2 | 483 | $167,698 | 787.29 |
| Candian | 1.06 | 335.4 | 562 | $188,495 | 916.06 |
| Kewell | 1.13 | 347.1 | 526 | $182,575 | 852.12 |

* To generate 95% of 623.6 kWhr/day.

According to the simulation results of the method, the Solartec S60MC250 PV panel had the best yield and electrical energy production. However, for the JAPAY project, now it is important to know the PV panel investment and the area required for the project.

Therefore it is necessary to determine the number of PV panels needed for installation in order to cover the 95% of Sewage Treatment Plant consumption. Starting with the consumption annual daily mean ($C_{mean}$) from Federal Commission of Electricity (CFE) billings, $C_{mean} = 623.6$ kWhr:

$$N_{panel} = \frac{C_{mean} * 0.95}{EEG_{(day)}},$$
$$\text{Tot. Area} = N_{panel} * \text{Area}_{PV}. \quad (11)$$

Table 6 shows the application of (11) for the same five PV panels to obtain the investment and total area required.

The proposed method was the base of the study developed for the JAPAY project, which was implemented successfully, which ensured the projected electric power generation and ensured the planned investment. Figure 13 shows the photovoltaics facilities.

Nowadays the Sewage Treatment Plant produces its own electric energy, and it is an example of photovoltaics project for Merida city. Figure 14 demonstrates the power generated by PV panels that reaches 48 kWp and it is close to the power calculated by the proposed method. Figure 15 shows how the power delivered by electric energy supply company (CFE) was the supplement of total electric power demanded by Sewage Treatment Plant (Figure 16).

Figure 13: PV facilities of JAPAY in Merida city.

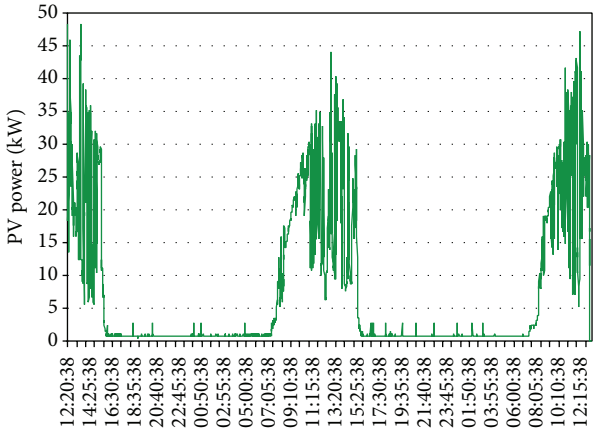


Figure 14: Photovoltaic power generated.

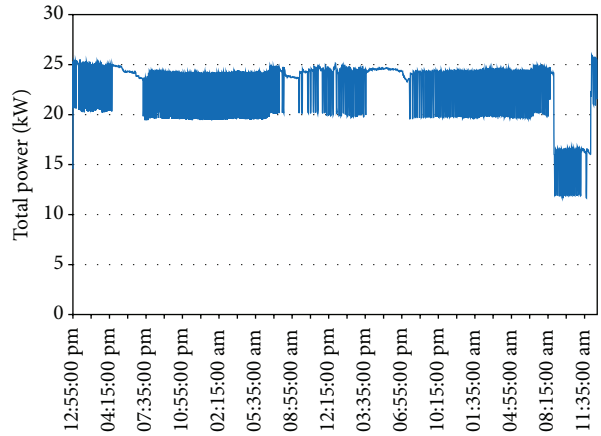


Figure 16: Power demand by Sewage Treatment Plant.

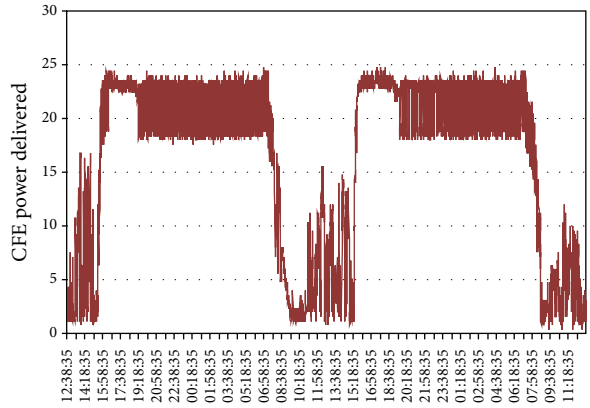


Figure 15: CFE power delivered.

## 4. Conclusions

In this paper a practical five-step method is presented to estimate the electrical energy generated by PV panel per day, month, and year, based on the MATLAB Simulink mathematical model of the PV cell and the evaluation of historic climatic variables for a specific locality.

Most of the literature works only estimate the energy potential by geographic information systems (GIS) and PVGIS, maps of solar radiation ($W/m^2$), digital surface models (DSM), and simulations of climate variables, but any reported method calculates the energy generated and considers any simultaneity to the response due to intrinsic characteristic between different PV panels and the historical climatic database, so the proposed method incorporates these conditions allowing for a more realistic calculation.

It has been demonstrated that there are significant differences in electric energy generation and power yield and its efficiency between the five different PV panels under test. These differences are always lower than STC and therefore are important and critical to estimate the number of panels, the facilities total area, and the PV panels investment required on a project.

The proposed method developed represents a powerful software tool for calculating the electric energy generated by a PV panel. The proposed method provides a good reliability and certainty for PV project investment and allows application in different geographical locations, different PV power peaks, and different panels manufacturers.

## Conflict of Interests

The authors declare that there is no conflict of interests regarding the publication of this paper.

## Acknowledgments

The authors thank CONAGUA Mérida for the assistance provided with the database. Likewise, the authors would like to express their gratitude to Dr. David Valdes Lozano, CINVESTAV, Mérida, for providing weather database. Finally, the authors acknowledge researchers and reviewers of Scientific Research Center of Yucatan A.C. (CICY).

## References

[1] International Energy Agency (IEA), *World Energy Outlook 2013*, International Energy Agency (IEA), Paris, France, 2013.

[2] Renewable Energy Policy Network for the 21st Century (REN21), "Renewable 2012," Global Status Report, Renewable Energy Policy Network for the 21st Century (REN21), Paris, France, 2012.

[3] B. Parida, S. Iniyan, and R. Goic, "A review of solar photovoltaic technologies," *Renewable and Sustainable Energy Reviews*, vol. 15, no. 3, pp. 1625–1636, 2011.

[4] B. van der Zwaan and A. Rabl, "The learning potential of photovoltaics: implications for energy policy," *Energy Policy*, vol. 32, no. 13, pp. 1545–1554, 2004.

[5] H. C. Hottel, "A simple model for estimating the transmittance of direct solar radiation through clear atmospheres," *Solar Energy*, vol. 18, no. 2, pp. 129–134, 1976.

[6] B. Y. H. Liu and R. C. Jordan, "The interrelationship and characteristic distribution of direct, diffuse and total solar radiation," *Solar Energy*, vol. 4, no. 3, pp. 1–19, 1960.

[7] I. R. Pillai and R. Banerjee, "Renewable energy in India: status and potential," *Energy*, vol. 34, no. 8, pp. 970–980, 2009.

[8] S. N. Benger, S. Zhou, and H. Guan, "A dynamic solar irradiance model for assessing solar PV power generation potential in urban areas," in *Proceedings of the International Conference and Utility Exhibition on Green Energy for Sustainable Development (ICUE '14)*, pp. 1–4, March 2014.

[9] K. Shukla, S. Rangnekar, and K. Sudhakar, "Mathematical modelling of solar radiation incident on tilted surface for photovoltaic application at Bhopal, M.P., India," *International Journal of Ambient Energy*, 2015.

[10] M. D. Siegel, S. A. Klein, and W. A. Beckman, "A simplified method for estimating the monthly-average performance of photovoltaic systems," *Solar Energy*, vol. 26, no. 5, pp. 413–418, 1981.

[11] J. Hofierka and J. Kaňuk, "Assessment of photovoltaic potential in urban areas using open-source solar radiation tools," *Renewable Energy*, vol. 34, no. 10, pp. 2206–2214, 2009.

[12] M. R. Hossain, A. M. T. Oo, and A. B. M. S. Ali, "The effectiveness of feature selection method in solar power prediction," *Journal of Renewable Energy*, vol. 2013, Article ID 952613, 9 pages, 2013.

[13] A. F. A. Kadir, T. Khatib, and W. Elmenreich, "Integrating photovoltaic systems in power system: power quality impacts and optimal planning challenges," *International Journal of Photoenergy*, vol. 2014, Article ID 321826, 7 pages, 2014.

[14] M. Šúri, T. A. Huld, E. D. Dunlop, and H. A. Ossenbrink, "Potential of solar electricity generation in the European Union member states and candidate countries," *Solar Energy*, vol. 81, no. 10, pp. 1295–1305, 2007.

[15] R. Ayaz, I. Nakir, and M. Tanrioven, "An improved Matlab-Simulink model of PV module considering ambient conditions," *International Journal of Photoenergy*, vol. 2014, Article ID 315893, 6 pages, 2014.

[16] K. J. Sauer, T. Roessler, and C. W. Hansen, "Modeling the irradiance and temperature dependence of photovoltaic modules in PVsyst," *IEEE Journal of Photovoltaics*, vol. 5, no. 1, pp. 152–158, 2015.

[17] M. E. Meral and F. Diner, "A review of the factors affecting operation and efficiency of photovoltaic based electricity generation systems," *Renewable and Sustainable Energy Reviews*, vol. 15, no. 5, pp. 2176–2184, 2011.

[18] K. Nishioka, T. Hatayama, Y. Uraoka, T. Fuyuki, R. Hagihara, and M. Watanabe, "Field-test analysis of PV system output characteristics focusing on module temperature," *Solar Energy Materials and Solar Cells*, vol. 75, no. 3-4, pp. 665–671, 2003.

[19] Atmospheric Sciencie Data Center (ASDC), National Aeronautics and Space Administration (NASA), Langley Reserch Center, https://eosweb.larc.nasa.gov/.

[20] ESRA (European Solar Radiation Atlas)—HelioClim Solar Radiation, http://www.helioclim.org/esra/.

[21] Comisión Nacional del Agua, CONAGUA, http://www.cna.gob.mx/.

[22] Weather Link Station and Centro de Investigacion Cientifica y Avanzada, CINVESTAV, http://www.mda.cinvestav.mx/weather.

[23] Solartec, Photovoltaic Multicrystaline Module 250 Watt, Model S60MC, http://www.solartec.mx/productos.html.

[24] Y. T. Tan, D. S. Kirschen, and N. Jenkins, "A model of PV generation suitable for stability analysis," *IEEE Transactions on Energy Conversion*, vol. 19, no. 4, pp. 748–755, 2004.

[25] A. Kajihara and A. T. Harakawa, "Model of photovoltaic cell circuits under partial shading," in *Proceedings of the IEEE International Conference on Industrial Technology (ICIT '05)*, pp. 866–870, IEEE, Hong Kong, December 2005.

[26] E. Matagne, R. Chenni, and R. El Bachtm, "A photovoltaic cell model based on nominal data only," in *Proceedings of the International Conference on Power Engineering, Energy and Electrical Drives (POWERENG '07)*, pp. 562–565, Setubal, Portugal, April 2007.

[27] R. Chenni, M. Makhlouf, T. Kerbache, and A. Bouzid, "A detailed modeling method for photovoltaic cells," *Energy*, vol. 32, no. 9, pp. 1724–1730, 2007.

[28] M. G. Villalva, J. R. Gazoli, and E. R. Filho, "Comprehensive approach to modeling and simulation of photovoltaic arrays," *IEEE Transactions on Power Electronics*, vol. 24, no. 5, pp. 1198–1208, 2009.

[29] D. Sera, R. Teodorescu, and P. Rodriguez, "PV panel model based on datasheet values," in *Proceedings of the IEEE International Symposium on Industrial Electronics (ISIE '07)*, pp. 2392–2396, Vigo, Spain, June 2007.

[30] K. Ishaque, Z. Salam, H. Taheri, and Syafaruddin, "Modeling and simulation of photovoltaic (PV) system during partial shading based on a two-diode model," *Simulation Modelling Practice and Theory*, vol. 19, no. 7, pp. 1613–1626, 2011.

[31] S. Shongwe and M. Hanif, "Comparative analysis of different single-diode PV modeling methods," *IEEE Journal of Photovoltaics*, vol. 5, no. 3, pp. 938–946, 2015.

[32] W. Xiao, F. F. Edwin, G. Spagnuolo, and J. Jatskevich, "Efficient approaches for modeling and simulating photovoltaic power systems," *IEEE Journal of Photovoltaics*, vol. 3, no. 1, pp. 500–508, 2013.

[33] K. Ishaque and Z. Salam, "An improved modeling method to determine the model parameters of photovoltaic (PV) modules using differential evolution (DE)," *Solar Energy*, vol. 85, no. 9, pp. 2349–2359, 2011.

[34] A. Márquez, E. Gómez, D. Aranda, and M. Bohorquez, "Sistema para la generación automática de curvas V-I, V-P y monitorización de módulos fotovoltaicos," in *XXV Jornadas Automática*, Ciudad Real, Spain, September 2004.

[35] F. Lasnier and T. Gang-Ang, *Photovoltaic Engineering Handbook*, Adam Hilger, Bristol, UK, 1990.

[36] D. L. King, J. A. Kratochvil, and W. E. Boyson, "Temperature coefficients for PV modules and arrays: measurement methods, difficulties, and results," in *Proceedings of the IEEE 26th Photovoltaic Specialists Conference*, pp. 1183–1186, October 1997.

[37] M. C. A. García and J. L. Balenzategui, "Estimation of photovoltaic module yearly temperature and performance based on Nominal Operation Cell Temperature calculations," *Renewable Energy*, vol. 29, no. 12, pp. 1997–2010, 2004.

Hindawi Publishing Corporation
International Journal of Photoenergy
Volume 2015, Article ID 256101, 12 pages
http://dx.doi.org/10.1155/2015/256101

*Review Article*

# Price-Efficiency Relationship for Photovoltaic Systems on a Global Basis

**Mehmet Sait Cengiz[1] and Mehmet Salih Mamiş[2]**

[1]*Department of Technical Vocational School, Bitlis Eren University, 13000 Bitlis, Turkey*
[2]*Department of Electrical and Electronics Engineering, Inonu University, 44280 Malatya, Turkey*

Correspondence should be addressed to Mehmet Sait Cengiz; msaitcengiz@gmail.com

Received 30 August 2015; Revised 29 September 2015; Accepted 1 October 2015

Academic Editor: Xudong Zhao



Solar energy is the most abundant, useful, efficient, and environmentally friendly source of renewable energy. In addition, in recent years, the capacity of photovoltaic electricity generation systems has increased exponentially throughout the world given an increase in the economic viability and reliability of photovoltaic systems. Moreover, many studies state that photovoltaic power systems will play a key role in electricity generation in the future. When first produced, photovoltaic systems had short lifetimes. Currently, through development, the technology lifecycle of photovoltaic systems has increased to 20–25 years. Studies showed that photovoltaic systems would be broadly used in the future, a conclusion reached by considering the rapidly decreasing cost of photovoltaic systems. Because price analysis is very important for energy marketing, in this study, a review of the cost potential factors on photovoltaic panels is realized and the expected cost potential of photovoltaic systems is examined considering numerous studies.

## 1. Introduction

Similar to other essential needs, such as food and shelter, energy is a basic need of individuals throughout the world. The global increase in energy demand and environmental pollution is motivating related research and technological investments to improve energy efficiency and generation. The main objective of replacing a major portion of the fossil fuel use can be achieved using renewable energy. This possibility has led investigators to research on renewable energy resources and energy efficiency for the present consumption of energy, because renewable energy technology transforms natural phenomena into beneficial types of energy. Among renewable energy resources, solar power is the most beneficial, limitless, effective, and dependable. Above all, solar power is ecologically friendly.

Energy is regarded as indispensable to the socioeconomic progress of developing and developed nations. However, maladministration of power generation has a detrimental effect on the ecosystem. Recently, concerns related to the environment, such as global warming, have been increasing throughout the world. The consumption of world energy resources and the excessive emission of dangerous greenhouse gases have become a serious problem that has a material effect on climate change—an important subject discussed around the world. One of the main causes of climate change is the extreme amount of global greenhouse gas emissions (e.g., carbon dioxide and methane) into the atmosphere as a consequence of activities performed by humans. Human activities primarily cause significant $CO_2$ discharge. In 2002, universal $CO_2$ discharge related to human activities reached 2.6 billion tonnes. This discharge is estimated to reach 4.2 billion tonnes annually in 2030. In addition, unless prevented, the surface temperature of the earth might reach 1.4°C–5.8°C in the future. Given these developments, we may face droughts, floods, a rising sea level, glacial melting, and critical spoilage of agriculture. Therefore, it is essential to reduce these emissions as soon as possible. To realize such a reduction, conventional energy applications must be turned into renewable energy technologies [1, 2].

Solar power is certainly favourable in terms of the environment. When compared with other energy types such as coal and oil, the sun is considered a satisfactory energy resource because it is reliable and clean. Because the sunshine needed to meet our energy requirement in the future is sufficient, many scientists are highlighting the significance of solar power. Sunlight is considered an alternative energy source, as are hydrogen and wind. Solar power has the capacity to transform ecologically friendly energy into a more elastic, common, and cheaper energy resource. Therefore, currently, solar power is frequently used in many applications such as water heating systems, satellite power systems, and electrical power generation.

As is known, the best-known renewable energy technology is the photovoltaic (PV) system. To produce electrical energy, these PV systems use sunlight. PV electricity generation systems appear quite attractive for electricity generation given low carbon dioxide emission during simple and noiseless operations, flexibility in scale, and easy maintenance compared to other sustainable energy sources. To accelerate the extension of renewable energies and PV in particular, environmental profits and the prevention of fossil fuel spoilage underlying the relevant price imbalance are essential. Therefore, renewable energies significantly contribute to supply security. In addition, photovoltaic systems can be applied to small or large applications without restriction. These systems have been installed on individual homes, housing developments, and public and industrial buildings and generate energy around the world. Existing solar cell technologies are solidly installed and provide safe products with the efficiency and energy that can last for 25 years. Increasing power failure potential and an increase in electricity prices advertise PV systems [3].

The available solar irradiation required to meet the world's energy requirements is more than adequate. Current technology enables the sunlight irradiating on a square metre to have the capacity to produce an average of 1,700 kWh of energy annually. When the overall energy consumption is considered, the solar power reaching the earth's surface has the capacity to satisfy the present energy requirement more than 10,000 times. More sunlight can produce more energy. Solar energy is best produced in subtropical areas. Europe produces an average of 1,200 kWh/m$^2$ of energy annually, whereas the Middle East produces 1,800 to 2,300 kWh/m$^2$ annually [4].

Depending on connection methods and working principles, PV-based electricity generation systems may be classified as stand-alone or grid-connected PV systems. PV panels are integrated with equipment such as batteries, charge controllers, and inverters to generate electricity. The majority of the PV modules were used in independent applications in areas with no network connections [5].

In 2014, more than 100 nations enhanced their solar PV capacity, which also made PV the world's fastest-growing power generation technology. In 2014, the enhanced capacity of PV was approximately 139 GW. Figure 1 indicates the solar PV and existing world PV capacity from 2004 to 2014 [6, 7].

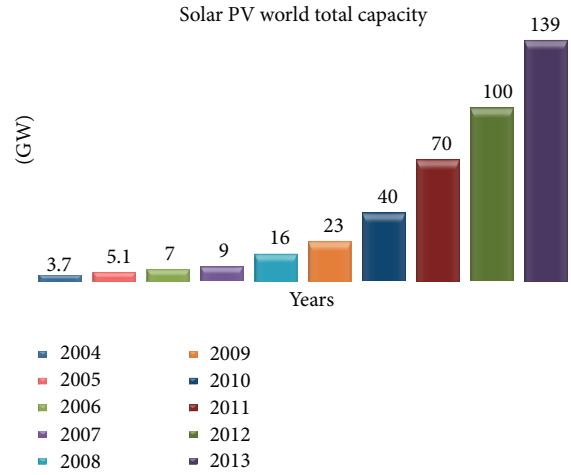


Figure 1: Solar PV, existing world PV capacity, 2004–2014 [7].

## 2. Basic of Electricity Generation Process for Photovoltaic Systems

PV systems have higher capital costs per unit and much lower operating costs than traditional fossil-based electrical resources [8]. However, progress in the PV industry continues with reasonable scope for further cost reductions in the near future. In addition, the economics of PV panels are closely related to the capacity of solar radiation and the sunshine duration of the system. PV systems are highly influenced by the local availability of solar radiation.

PV panels generate electricity when integrated with other system equipment, which can be described as a balance of the system. These systems operate on or off the grid and can be used where electricity is required. Numerous PV system applications exist throughout the world such as communications, remote monitoring, hotels, hospitals, houses, lighting, water pumping, and rural areas. In general, the key parts of a PV energy generation system are as follows [4]:

(i) PV panels to absorb sunlight.

(ii) An inverter to turn direct current (DC) into alternative current (AC).

(iii) A set of batteries for off-grid-connected PV systems.

(iv) A charge controller between the PV panel and batteries.

(v) Support structures to direct PV modules towards the sun (to enhance the efficiency of PV electricity production systems).

## 3. Technical Analysis of Cost Reduction Potential of Photovoltaic Panel Integrated Equipment

*3.1. Photovoltaic Panel Technology.* In recent years, PV systems have developed rapidly and researchers have focused on reducing the cost of these systems to enhance their efficiency.

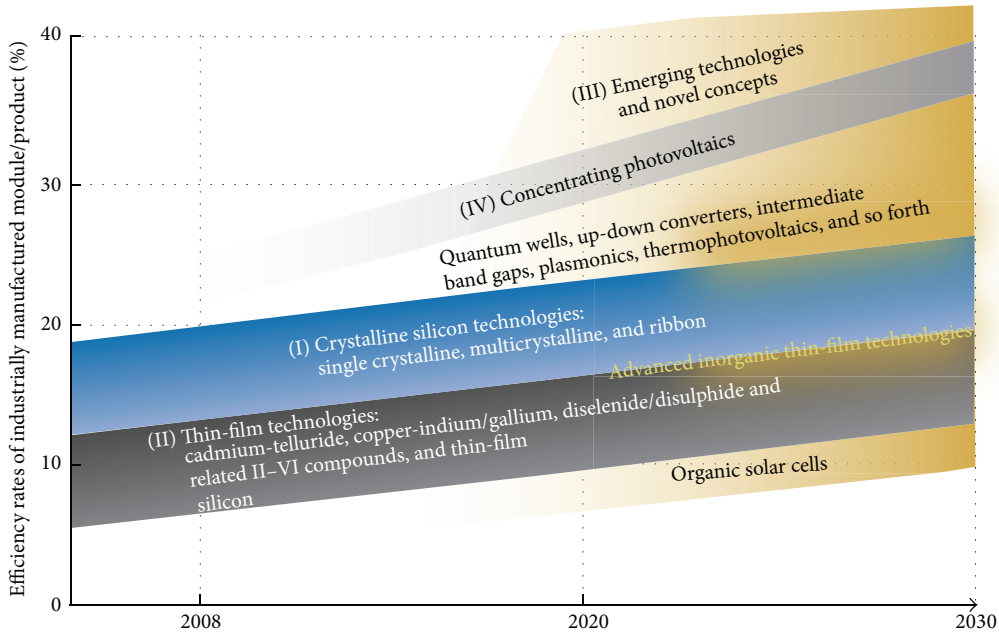


Figure 2: Developing PV technology status and prospects [10].

Table 1: Production chain with cost shares and technology improvement opportunity units for [9].

| Supply chain | Cost share | Factors |
|---|---|---|
| Ingot (silicon) | 17% | Ingot casting |
| Wafer | 20% | Kerf loss<br>Wafer thickness<br>Wafer size<br>Yield |
| Cell | 22% | Cell efficiency<br>Stability<br>Lifetime<br>Yield |
| Module | 41% | Module |

R&D studies currently conducted have enabled the development of production methods for PV module technologies. Therefore, PV panels can be manufactured at lower costs and can generate energy at a higher efficiency. Production costs per watt are reduced every day [11]. However, silicon technologies have higher costs according to thin-film technologies, and the conversion efficiency of these systems is high. Therefore, these panels are widely used throughout the world. In addition, the developing technology and future perspectives of PV panels (Figure 2) indicate that thin-film (TF) and other advanced technologies dominate and will be preferred in the future. The crystalline PV production chain comprises four product stages. Their respective cost shares (of total processing costs) are provided in Table 1 [9].

Through the adoption of a low-cost labour force and mass production methods in PV panel systems, costs have significantly reduced in the last 50 years. However, simply reducing production costs is not enough. Achieving an increase in efficiency is also an important parameter [9].

Approximately, 85%–90% of the PV market is represented by single and multicrystalline silicon cells. Ten to fifteen percent of the PV market is represented by various thin-film PV panels that also have different categories. Crystalline silicon cells are expensive and thin-film cells are less expensive and less efficient [12]. However, powerful progress has been made in the world in this aspect, and research showed that PV panels with different materials have been developed in recent years.

Moreover, preferred PV panels depend on a cost analysis of the installation of PV systems because the lifecycle of these systems is a very important issue. PV systems with long lifecycles are preferred. Examining module prices according to PV panel technology enables an understanding of why silicon technology is preferred. Figure 3 shows the efficiency and price development for different PV module technologies [10].

Module efficiency varies between 10% for thin-film cells and 20% for single crystalline cells. Moreover, because efficiency significantly affects cost, it is essential in determining module prices. Greater efficiencies provide higher energy output for each square metre. In Figure 4, the reductions in module prices are indicated. Moreover, the relevant extra charge covered by multicrystalline silicon technology (mc-Si) is partially offset by the lower area-related system costs [12], given the higher electricity should be considered.

In Figure 5, the learning curve of the PV industry from the past to today is indicated. Over the next 2 to 8 years, the industry learning curve will achieve grid parity around the world. The overall costs per watt are related to PV panel production: raw material costs, yield, equipment costs, factory utilization, shipment, and others. Depending on these

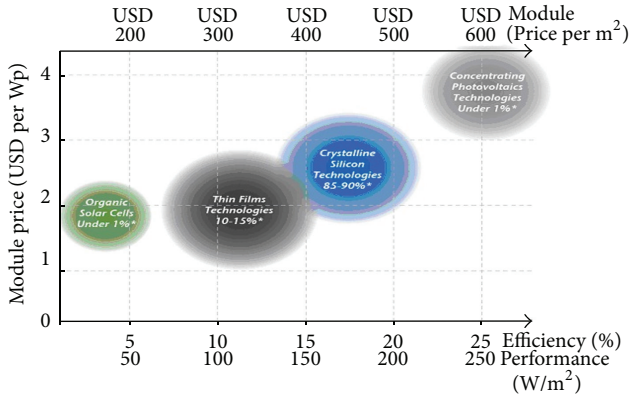


Figure 3: Efficiency and price development for different PV module technologies in 2010 [10].

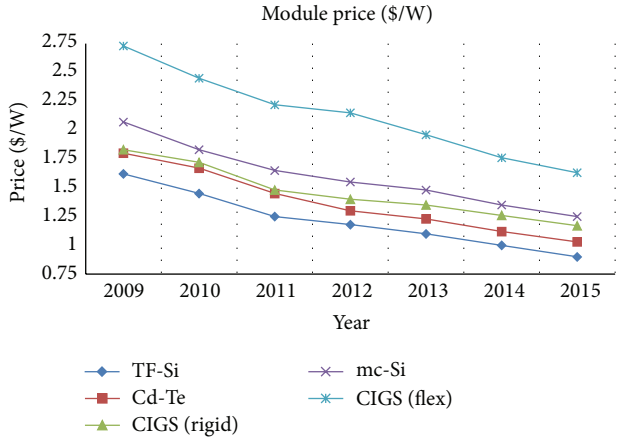


Figure 4: Estimated price development for different PV technologies [13].

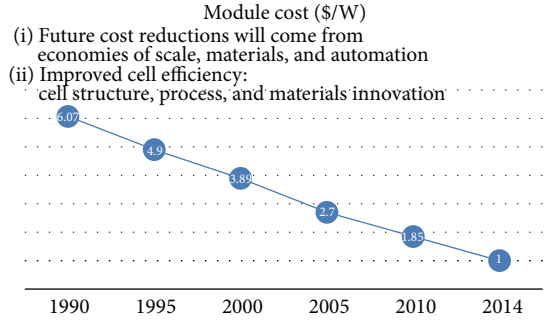


Figure 5: Photovoltaic industry learning curve cost per watt [14].

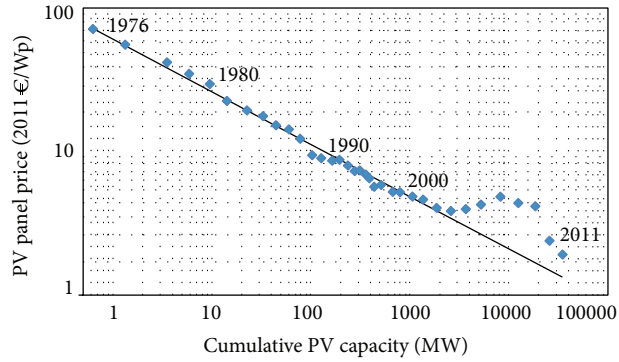


Figure 6: Learning curve for photovoltaic panel price development with 22% learning rate [16].

data, since 2000, the experience or learning curve has affected the PV industry at 80%–85%, which is nearly the same as in many other industries, such as aerospace, shipbuilding, and machinery [14]. For a floor-mounted system, panel prices correspond to 60% of the capital cost. Between 1976 and 2003, the PV panel costs have been reduced at a 15% to 22% learning rate [12].

In a 20-year period, many industries proved that making significant cost reductions is possible by increasing volumes [15]. The PV industry is among these industries. The capacity of established PV systems has increased 40% during the past 10 years, and this rate is growing rapidly. Many studies showed that electricity generation in the future, throughout the world, will be primarily from PV systems because these systems have many advantages. However, the PV panel price is the most important factor in anticipating this development. As the industry developed, PV module costs decreased along a well-established learning curve in which a 22% cost reduction for each cumulative capacity was observed in the last few decades, as is shown in Figure 6 [16].

Material charges covered by PV systems correspond to 50% to 70% of the overall cost of the technology. In addition, cost reductions are significantly affected by location, and the reduction in material consumption and the increase in conversion efficiency might affect material prices per watt. Figure 7 shows a summation of the costs for PV systems using different technologies [20].

Today, PV technology meets the demand for any power amount—from a few watts to the MW level. The superiority of PV-based production enables the manufacture of PV modules from various mines, thus the maintenance of energy generation [21]. Wafer-based crystalline silicon technology is used by approximately 80% of the existing energy production systems [18]. Figure 8 shows the annual PV production capacities of thin-film and crystalline silicon-based solar modules.

Although PV installation capacity is increasing, the cost of PV panels has decreased. PV installation capacity is also associated with cost reductions, because when installation capacity is increased, technological improvements and scale economies increase for generation of PV panels. In addition, the PV panel manufacturing process is examined to determine the cost reduction potential of PV panels. Figures 9 and 10 show the crystalline Si all standard value chain, in addition to the shared cost of processing PV modules.

The c-Si PV module was adopted because the c-Si share of the PV market is approximately 70% to 80%, and the module has broad application globally. A current cost analysis of PV systems shows that the cost of the PV module is approximately $1.75–$1.41. In addition, developing technology and

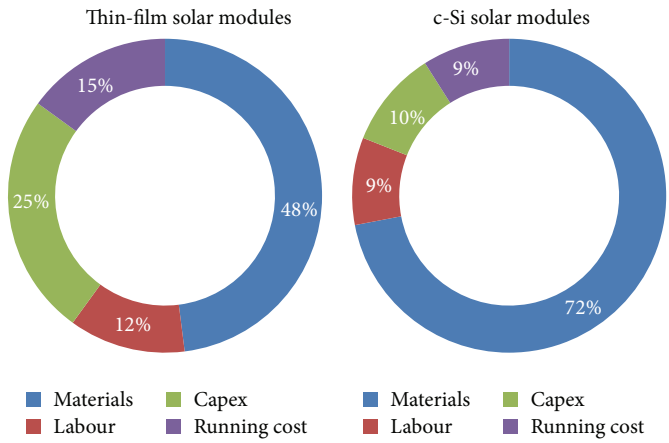


Figure 7: Cost reduction—material consumption for different photovoltaic panel technologies [17].

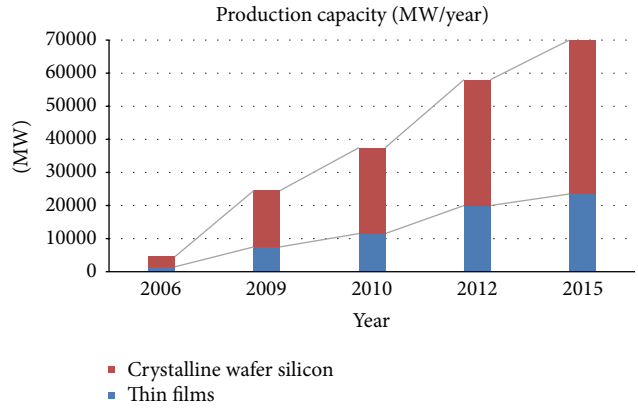


Figure 8: Annual PV production capacities of thin-film and crystalline silicon-based solar modules [18].

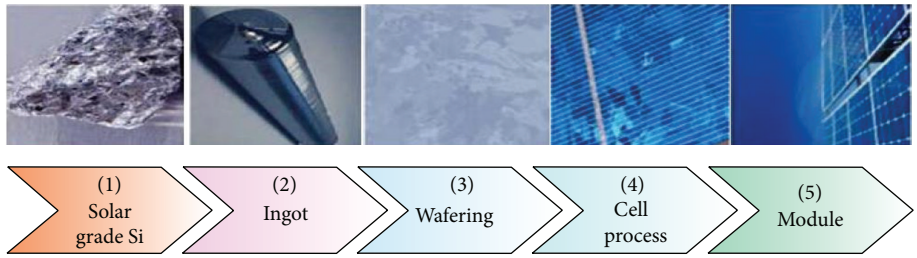


Figure 9: Crystalline Si cell standard chain: bulk of photovoltaics today [19].

the increased capacity of PV electricity generation show that PV system prices will decrease until 2020. The expected cost of the PV module is approximately \$0.85–\$0.73. This target PV module cost is very important given the need for electricity generation throughout the world and the broad use of low-cost PV modules.

In addition, researchers studied numerous cost reduction techniques to improve cost potential. The cost reduction potential techniques for c-Si module technology are noted as follows.

Si shortage influences technology choices:

(i) Accelerated trend towards thinner wafers (more wafers per kg Si): >150–200.

(ii) Trend towards larger wafers slowing down, with 156 mm seeming as the standard for several years ahead.

(iii) Interest in alternative ways to use PV grade silicon more effectively.

More interest in high-efficiency solar cell technology:

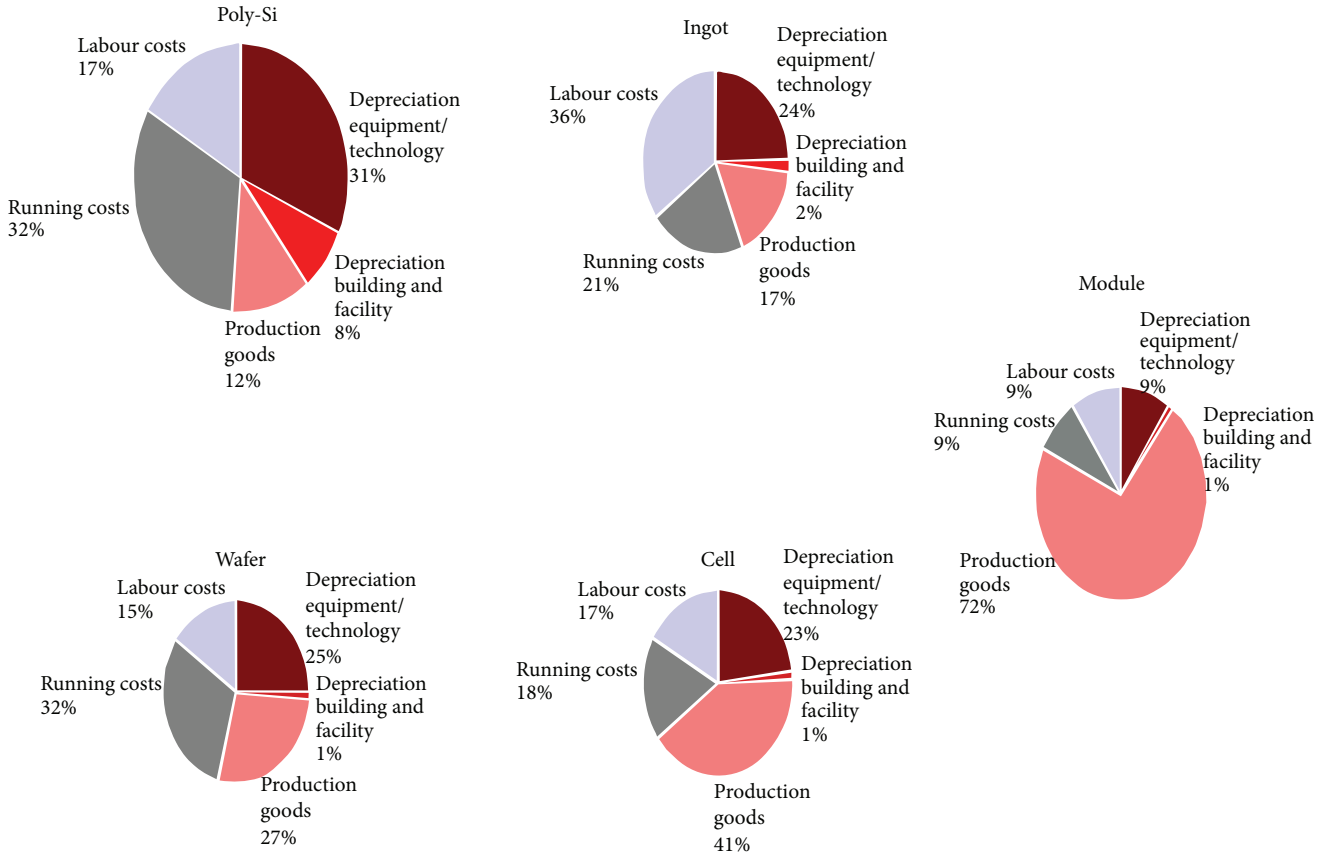


Figure 10: Sharing the cost of processing photovoltaic modules [22].

(i) More Wp per kg Si.

(ii) Reduction in system costs for applications requiring high installation costs per $m^2$ [23].

Needed for €/Wp reduction:

(i) Reduction in materials usage.

(ii) Simplification of module manufacturing process.

(iii) Improving cell and module efficiency.

To increase the use of PV modules in the future, minimizing production costs is essential [24].

The c-Si PV module is obtained from the share of c-Si in the PV market, which is 70% to 80%, and the module is commonly used globally. A current cost analysis of PV systems shows that the cost of a PV module is approximately \$1.41–\$1.75. In addition, developing technology and increased capacity of PV electricity generation show that PV system prices have decreased until 2015, when the cost of a PV module is expected to be approximately \$0.85 to \$0.73. This target PV module cost is very important because of the need for electricity generation throughout the world, and low-cost PV modules will become commonly used. Table 2 shows a detailed analysis of the cost reduction potential from 2010 to 2015 for PV and shows that this cost reduction was positively affected by the price of PV systems. Figure 11 indicates a reduction in PV system prices.

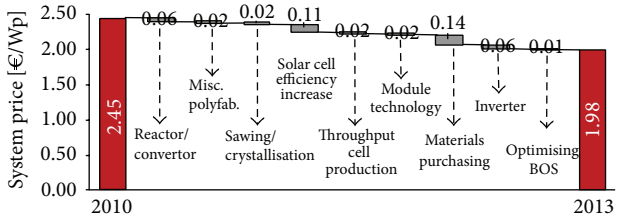


Figure 11: Reduction in photovoltaic system prices [26].

*3.2. Balance of the System (BOS) for Photovoltaic Systems.* The PV industry is constantly developing to improve product efficiency and to make use of more environmentally friendly materials because the equipment is an important parameter for the cost efficiency of PV systems. PV systems have two parameters: the cost of a PV panel and the balance of the system.

Certain factors affect the reduction in the cost of PV systems. Technological innovation, production optimization, economies of scale, increased performance ratio of PVs, and the extended lifetime of PV systems can be known as the lifecycle development of standards and specifications [4]. Capital costs, solar resources, and discounts are significant parameters for managing PV power system prices. Operations, labour costs, and maintenance costs are the remaining variable costs. The capital cost is the most significant of

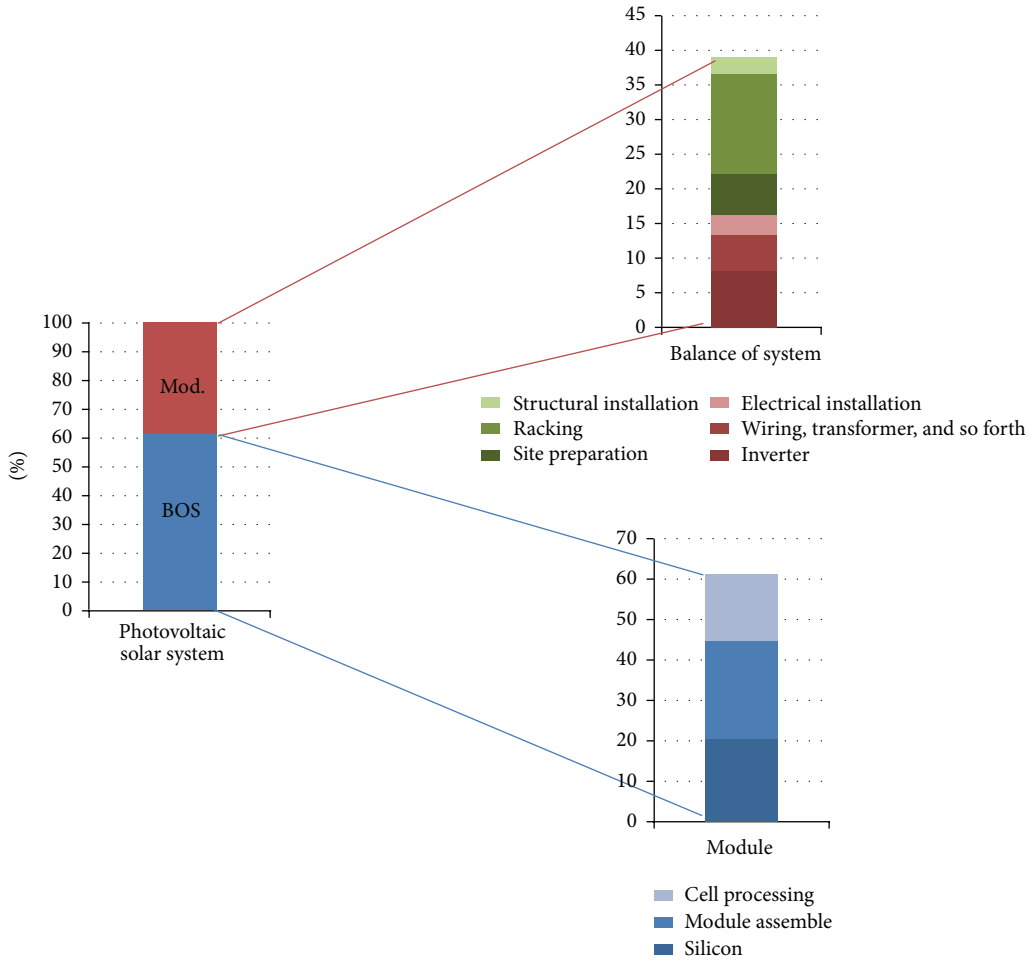


Figure 12: Price structure of photovoltaic systems for installations [4, 12].

Table 2: Crystalline Si: estimated total module cost [25].

(a)

| EUR/US/JP | 2010 | 2011 | 2012 | 2013 | 2014 | 2015 |
|---|---|---|---|---|---|---|
| Scale increase over time | 150 | 400 | 650 | 900 | 1150 | 1400 |
| Polysilicon | $0.43 | $0.33 | $0.23 | $0.18 | $0.15 | $0.13 |
| Wafer | $0.46 | $0.37 | $0.33 | $0.29 | $0.27 | $0.25 |
| Cell | $0.36 | $0.29 | $0.25 | $0.23 | $0.20 | $0.19 |
| Module | $0.50 | $0.42 | $0.37 | $0.33 | $0.31 | $0.29 |
| Total | **$1.75** | **$1.41** | **$1.18** | **$1.03** | **$0.93** | **$0.85** |

(b)

| Low cost | 2010 | 2011 | 2012 | 2013 | 2014 | 2015 |
|---|---|---|---|---|---|---|
| Scale increase over time | 350 | 600 | 850 | 1100 | 1350 | 1600 |
| Polysilicon | $0.47 | $0.39 | $0.25 | $0.20 | $0.16 | $0.14 |
| Wafer | $0.34 | $0.28 | $0.26 | $0.24 | $0.22 | $0.20 |
| Cell | $0.24 | $0.21 | $0.19 | $0.18 | $0.16 | $0.15 |
| Module | $0.36 | $0.31 | $0.29 | $0.27 | $0.25 | $0.23 |
| Total | **$1.41** | **$1.20** | **$0.99** | **$0.87** | **$0.79** | **$0.73** |

these parameters and has the greatest capacity to reduce costs [12]. In addition, the capacity of solar radiation and solar time for the location are very important factors for the cost of the system. When the factors are limited, the system's payback period will be low. Capital costs are included in two categories: the module and the balance of the system (BOS). The module is the sequence of PV cells that are connected to each other, and it contains feedstock silicon prices, cell processing, and module assembly costs. Structural and electrical system expenses are included in the BOS [12]. Within 5 years, PV modules' share in the overall system's price was reduced from approximately 60%–75% to the minimum level of 40%–60%, regarding the technology. The inverter corresponds to 10% of the overall system price. Engineering cost and procurement amount to approximately 7% of the overall system price. The remaining costs are related to other system components and installation costs. Figure 12 is an example of the price structure of PV systems for installations [4].

When PV systems are evaluated against each other, Table 3 provides a framework for measuring the rationality of the cost distributions. Under current market conditions, the production method and labour costs of the PV module

Table 3: Pathways of cost reduction potential for photovoltaic systems [27].

| Characteristic | Value or qualifier |
|---|---|
| Module | |
| Efficiency | >25% |
| Substrate | Lower cost and weight than glass |
| Reliability | 30 years or can be replaced with minimum labour |
| Materials | Earth-abundant, nontoxic, or established or recycling plan |
| BOS/installation | |
| Labour | Can be done with nonspecialized labour |
| Process | Lightweight (ease of handling, no special equipment) |
| Assembly | Snap together mechanical and electrical |
| Power electronics | |
| Efficiency | >95%, improved module-peak power management |
| Reliability | 30 years |
| Assembly | Integration of wiring, components to minimize electrical connections |

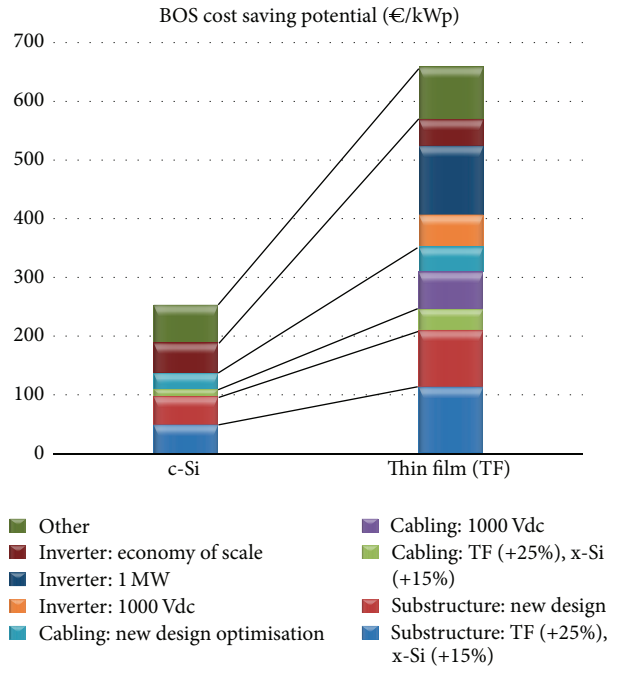


Figure 13: BOS cost saving potential in €/kWp for c-Si and TF modules [28].

correspond to two-thirds of the total cost. Setup expenses for modules are approximated and thus do not affect the cost. However, because the project designing phase affects efficiency, it is a parameter that should be considered. Figure 13 shows a detailed cost analysis of PV systems for separate c-Si, which has a large portion of the current PV market, and TF, which has a small portion of the PV market but is a new technology and is still being developed [29, 30].

c-Si (€/kWp 250) is less cost efficient than TF (€/kWp 650) regarding BOS. The reasons for this phenomenon are that cost saving measures support TF systems because they generally have a higher BOS cost percentage and because an expectation exists that a significant increase in TF efficiency will occur despite the fact that c-Si systems include 1,000 V DC and have the capacity to use MWp inverters. Another point to be considered is that, in the past 15 years, numerous efforts were made to enhance BOS components in accordance with c-Si module requirements [28].

Managing the reduction in these costs by decreasing panel costs as much as BOS costs is possible. Because they are less efficient and have lower system working voltage, BOS costs are higher for TF plants. In particular, when compared with TF plants, crystalline plants are less expensive regarding the auxiliary structure, DC cabling, and inverters. The reference to DC cabling means that the increase in panel efficiency that is expected to occur requires fewer cables for gross power. Using higher system working voltages means using more panels in each row and a decrease in the amount of field boxes required to observe these rows. Prefabricated DC cables are also cost efficient. Panel packing, installation process, project management, and standardized blocks of panels are also cost efficient [31].

DC power can be converted to AC power by inverters. This conversion makes the electricity distribution network and the best-known electrical devices compatible with the system. Inverters include power classes that vary from a few hundred watts to several kW and sometimes up to 2000 kW central inverters for larger systems [4].

The inverters are a significant development point. The DC–AC inverters, which contribute to 10% of the system costs, provide the opportunity for significant discoveries in engineering design. For the utility scale PV systems, inverters are produced at larger capacities. Whereas these latest units facilitate system design and installation and support increases in energy efficiency, they are still not used frequently [32]. Prices for all but the largest inverters are continuing to decline, although offers for small-scale units vary by almost 60 euro cents per W. An examination of the leader markets showed that, for a long time, the price trend in Germany for inverters in the 10 and 100 kW range remained stable at 24 euro cents per W but declined briefly in January 2020 to 23 euro cents. In early April 2020, the price increased by 4.2% to 25 euro cents per W, which was down 7.4% from October level of 27 euro cents. As usual, prices for inverters in this category show the least variation. In particular, prices for smaller devices continue to vary significantly.

To preserve the electric power produced from sunlight, batteries are primarily used in independent PV systems [33]. Acid batteries are also used in PV systems. Newly produced high quality batteries have a maximum lifetime of 15 years. The lifetime of a battery is also related to its management. Using a charge controller, these batteries can be connected to the PV array and the controller prevents the battery from overcharging or discharging. The controller also provides

information about the state of the system and metering and payment related to electricity consumed [4].

The most frequently used batteries are deep-cycle lead-acid ones. These flooded or valve-regulated batteries can be found in different sizes. When compared with valve-regulated batteries, flooded batteries require more maintenance and last longer when used properly [33].

PV electricity prices are compared with other electricity production sources using cost per kilowatt hour (kWh). In 2010, electricity production costs for large systems varied: €0.29/kWh in northern Europe, €0.15/kWh in the south, and €0.12/kWh in the Middle East [4]. The cost of raw materials (typically copper, steel, and stainless steel) has been unsteady. In relation to the market maturity and application type, the costs of installation have reduced at different rates.

In Europe and the United States, the summer season is always a key period in the year, and this peak can often be exacerbated when it coincides with country or local subsidy programmes change as consumers seek to beat those reductions. In particular, in this period, the demand from Germany and Italy affects prices throughout the world. Module costs correspond to 50% to 60% of the cost of a completely installed solar energy system [27].

Cost reduction brings about improvements in module and system efficiency. Efficiency improvements decreased the cost of PV modules, BOS, and fixed systems. For instance, when the efficiency of the modules doubled, the energy generated increases twofold; thus, BOS cost also decreased [34].

The key cost reduction points related to electricity generation from PV systems are as follows [35]:

(i) Higher efficiency of energy conversion.

(ii) Less consumption of materials.

(iii) Cost efficient materials.

(iv) Optimized manufacturing and mass production.

(v) Optimized PV module technologies.

(vi) Optimized grid integration (smart grids).

(vii) New concepts of PV electricity energy conversion.

Research and developments indicated that PV system prices will decline in the near future, even as the ratio of PV system use will increase exponentially. In addition, PV industry researchers determined a variety of pathways given the aim of the cost reduction potential for PV systems.

PV system components are indicated and are separately examined. Table 3 indicates the pathways of the cost reduction potential for PV systems.

The minimum efficiency of the PV module should be 25% and its lifetime should be 30 years. To reduce costs, material production costs per watt in today's conditions should be reduced from 50 cents to 23 cents using the latest technology instead of conventional methods, and labour costs should be reduced from 10 cents to 6 cents [34].

## 4. Past and Present Learning Curve Approach for Photovoltaic Systems

Today, the main agenda of the world's countries is energy. The price analysis factor is very important for electricity energy generation because energy generation costs are increasing throughout the world [36]. Therefore, the cost of PV energy systems is crucial. In this section, a technical analysis of the cost reduction potential of PV systems is realized.

High costs and low efficiency limit electricity production from solar energy. However, developments in the PV sector indicate that costs will decline in the near future. Therefore, low-cost and more efficient PV modules are envisaged as being manufactured for the PV sector each passing day.

Although the installation costs of PV systems are fairly high, these systems have many advantages. The major problem is that PV panels have low electricity generation conversion efficiency. To be broadly used, the electricity generation system should be economical and feasible. Systems with the highest capacity for electricity generation require maximum sunlight. Moreover, factors such as panel technology, the environment, and selection of material, among others, influence the operation and efficiency of PV-based electricity production systems.

Fifty years ago, in the beginning days of PV panels, the energy needed to produce a PV panel was more than the energy that the panel could produce in its lifetime. In the last 10 years, payback periods were reduced to 3–5 years through improvements in the efficiency of the panels and production methods based on the sunshine available at the installation area. Today, the peak cost of PV panel systems is approximately €1.34 per watt.

In many countries, PV systems markets have yet to reach maturity. However, in Germany, today's system prices represent the lowest rational prices that can be reached in other parts of the world. In 2010, the average price for PV systems was €2.80/Wp. Until the middle of 2010, prices were a minimum €2.20/Wp for large floor-mounted systems in some nations. Prices are reduced in accordance with production volume [4]; however, when compared with fossil fuel generated electricity prices, PV panel systems are still regarded as expensive.

When we assess the existing situation, PV systems installed on a turnkey basis in major markets include the same manufacturing costs but prices differ from nation to nation [37–39]. For instance, studies showed that Germany continues to set the standard for managing PV incentives because the world's largest solar market is also home to the most inexpensive PV systems. In markets with more generous funding, operators pay more for systems, essentially passing the larger incentives back up the value chain. Today, in Germany, PV systems with a capacity of between 2 kW and 5 kW cost an average of €2.772 ($3.930) per kW, including installation. Prices are as low as €2.300 ($3.620) per kW for some PV systems in this category because the incentive policies highly influence the capacity of PV electricity generation.

PV panel efficiency, correct product selection, ensuring the balance of the system equipment, and accurate predictions of electricity generation are essential for gaining reliable

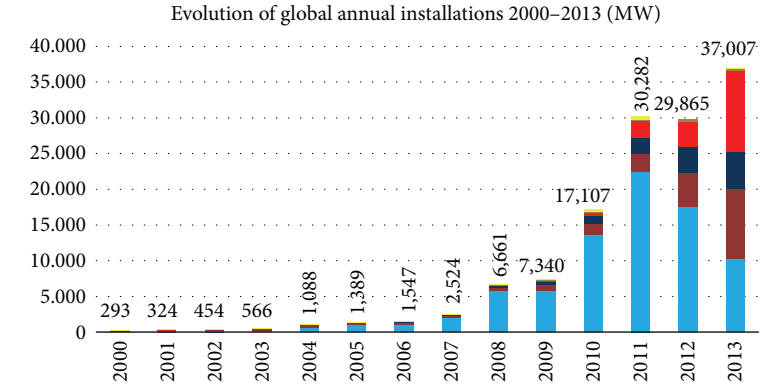


| | 2000 | 2001 | 2002 | 2003 | 2004 | 2005 | 2006 |
|---|---|---|---|---|---|---|---|
| Row | 88 | 56 | 80 | 77 | 29 | 10 | 105 |
| Mea | — | — | — | — | 1 | 0 | 0 |
| China | 19 | 5 | 19 | 10 | 10 | 8 | 10 |
| America | 2 | 3 | 30 | 48 | 61 | 82 | 110 |
| Apac | 126 | 128 | 190 | 230 | 282 | 304 | 325 |
| Europe | 58 | 133 | 134 | 202 | 705 | 985 | 997 |
| Total | 293 | 324 | 454 | 566 | 1.088 | 1.389 | 1.547 |

| | 2007 | 2008 | 2009 | 2010 | 2011 | 2012 | 2013 |
|---|---|---|---|---|---|---|---|
| Row | 42 | 76 | 80 | 284 | 508 | — | 85 |
| Mea | 1 | 1 | 22 | 46 | 125 | 365 | 383 |
| China | 20 | 40 | 160 | 500 | 2.500 | 3.500 | 11.300 |
| America | 166 | 306 | 500 | 1.082 | 2.181 | 3.774 | 5.153 |
| Apac | 271 | 530 | 745 | 1.578 | 2.562 | 4.646 | 9.833 |
| Europe | 2.023 | 5.708 | 5.833 | 13.616 | 22.407 | 17.580 | 10.253 |
| Total | 2.524 | 6.661 | 7.340 | 17.107 | 30.282 | 29.865 | 37.007 |

Figure 14: Annual installed capacity of photovoltaic electricity generation throughout the world [30].

knowledge of PV systems. Therefore, the feasible work is very important to installing PV systems. In addition, the location of the installation of a PV system is important because of the solar irradiance that directly affects the capacity of electricity generation from PV panels.

Ten years ago, when a few MW of energy was needed to be produced annually, 16 cell and module production facilities survived because they produced sufficient solar modules. Today, market leaders own facilities that have capacities higher than 1 GW, several hundred times that of 10 years ago. Along with technological changes and production optimization, increases in capacity have decreased the cost per unit. Doubling of production output decreases the cost per unit by approximately 22% [4].

In the last 10 years, growth in the PV market has been unprecedented. In 2010, capacity increased to 16.6 GW from 7.2 GW in 2009. Despite difficult financial conditions, the EU enhanced its 1 GW capacity in 2003 to 13 GW in 2010 and, today, continues to rapidly increase its PV capacity. Germany is the lead in the PV sector, with the United States and China also continuing their investments to ensure a stronger influence in this sector. In Figure 14, the evolution of global cumulative installed capacity between 2000 and 2010 is indicated [30].

In the last 30 years, significant price reductions occurred in the PV industry. The cost of PV modules declined by 22% each time the cumulative installed capacity (in MW) increased twofold. Reductions in PV modules and systems prices also decreased power generation costs, caused by broad innovation, research and development, and continuing political support for the development of the PV market [4]. In particular, the PV industry has developed in recent years in a manner that indicates continual and rapid growth in the future. The most important factor in this situation is the falling cost of the PV industry's equipment. Most global studies support this notion.

Yet, costs—for panels, inverters, mounting systems, and other components—are the same in each market. However, system prices seem to depend largely on anticipated rates of return; thus, the stronger the incentives, the higher the prices.

## 5. Conclusions

Energy generation costs are known to be very important for all countries and their efforts to ensure low-cost energy generation. Solar energy is an indispensable source of energy generation, and the most important parameter is the cost of the generated energy.

Solar energy is the most abundant, useful, efficient, environmentally friendly, and unlimited type of energy among all renewable energy sources. In addition, in recent years, the capacity of electricity generation systems from solar energy

increased rapidly throughout the world given an increase in the economic viability and reliability of PV systems.

In this study, the cost of PV systems is examined and investigated in detail. Current costs are obtained and a discussion on the advantages or disadvantages of PV systems is included. The capacity of PV electricity generation systems throughout the world is considered separately and this study is extended to address expected future developments.

Enhanced efficiency of installations results from experience, scale, and learning. The general opinion is that automatic tools and higher preassembly levels caused by economies of scale and standardization also reduce installation costs. Predictions suggest that these strategies might save approximately 30% in work time and costs. "Plug and play" installations, which reduce the need for specialized labour, might become possible for inverters.

Moreover, this paper presents certain crucial techniques that contain the cost reduction potential of PV systems. First, current manufacturing costs of PV modules are examined in detail. Second, future PV module costs are predicted regarding developed techniques and technology.

The c-Si PV module is obtained from c-Si and it has obtained an approximate 70% to 80% share of the PV market and broad applications throughout the world. An analysis of the current cost of PV systems indicates that PV modules cost approximately \$1.75–\$1.41. In addition, developing technology and the increasing capacity of PV electricity generation indicate that PV systems prices are expected to decrease until 2020, for which the expected cost of a PV module is approximately \$0.85–\$0.73. This target PV module cost is very important given the need for electricity generation throughout the world and the broad use of low-cost PV modules.

Ultimately, the primary factor in determining system prices seems to be the amount of profit available for PV system operators in each market. The larger the returns from feed-in tariffs and other incentives such as tax breaks and subsidies, the higher the system prices.

## Conflict of Interests

The authors declare that there is no conflict of interests regarding the publication of this paper.

## References


[1] H. Müller-Steinhagen, M. R. Malayeri, and A. P. Watkinson, "Heat exchanger fouling: environmental impacts," *Heat Transfer Engineering*, vol. 30, no. 10-11, pp. 773–776, 2009.

[2] L. El Chaar, L. A. Lamont, and N. El Zein, "Review of photovoltaic technologies," *Renewable and Sustainable Energy Reviews*, vol. 15, no. 5, pp. 2165–2175, 2011.

[3] PV Status Report, March 2014, http://www.cetcsolarenergy.com/downloads/PV_Status_Report_2009.pdf.

[4] Solar Generation 6, 2015, http://buildgreenworld.co/PDF/2/EPIA%20Solar%20PV%20Electricity%20Empowering%20World%202011.pdf.

[5] Solar energy engineering: processes and systems, 2015, http://library.uniteddiversity.coop/Energy/Solar/Solar_Energy_Engineering-Processes_and_Systems.pdf.

[6] Renewables Global Report Status, 2015, http://germanwatch.org/klima/gsr2011.pdf.

[7] European Photovoltaic Industry Association, "Global Market Outlook for Photovoltaic Until 2015," 2015, http://www.epia.org/.

[8] Solar Photovoltaics, 2015, https://www.irena.org/DocumentDownloads/Publications/RE_Technologies_Cost_Analysis-SOLAR_PV.pdf.

[9] Survey of Photovoltaic Industry and Policy in Germany and China, July 2015, http://climatepolicyinitiative.org/wp-content/uploads/2011/12/PV-Industry-Germany-and-China.pdf.

[10] Technology Roadmap Solar photovoltaic energy, http://www.poweracrosstexas.org/wp-content/uploads/2011/01/solar-technology-roadmap.pdf.

[11] Technology Roadmap Solar Photovoltaic Energy, May 2015, http://www.iea.org/publications/freepublications/publication/pv_roadmap.pdf.

[12] Renewable Energy Technology Cost Review, May 2015, http://www.garnautreview.org.au/update-2011/commissioned-work/renewable-energy-technology-cost-review.pdf.

[13] Renewable Energy Technology Cost Review, May 2015, http://www.energy.unimelb.edu.au/files/site1/docs/39/Renewable%20Energy%20Tech%20Cost%20Review.pdf.

[14] Global Photovoltaic Business, May 2015, http://www.interpv.net/market/market_view.asp?idx=94&part_code=03.

[15] Achieving Low-Cost Solar PV, June 2015, http://www.rmi.org/Content/Files/BOSReport.pdf.

[16] *The Garnaut Review 2011*, 2011, http://www.garnautreview.org.au/update-2011/commissioned-work/renewable-energy-technology-cost-review.pdf.

[17] M. Kezunovic and S. T. Waller, "PHEVs and BEVs in coupled power and transportation systems," in *Encyclopedia of Sustainability Science and Technology*, pp. 7847–7865, Springer, New York, NY, USA, 2012.

[18] JRC Scientific and Technical Report: PV Status Report, June 2015, http://www.rpia.ro/wp-content/uploads/2012/03/LBXB11001ENC_0021.pdf.

[19] C. Ballif, *Innovative Forschungsprojekte im Bereich Solar und Photovoltaik EPFL*, vol. 5 of *Energie-Cluster*, Institute of Microengeering, IMT, Photovoltaics and Thin Film Electronics Laboratory, Neuchâtel, Switzerland, 2011.

[20] The State of the PV Industry—An Association Perspective, July 2015, http://avsusergroups.org/joint_pdfs/2011-2savala.pdf.

[21] The Photovoltaic Industry, June 2015, http://www.evwind.es/2010/09/14/the-photovoltaic-industry.

[22] Webcast: centrotherm's "grid parity factory", June 2015, http://www.centrotherm.de/fileadmin/ct_group/Downloads/IR_Sonstige/Konferenzen/090204_WebCast_IntegrierteFabrik_EN.pdf.

[23] N. Mori, "Current status and future prospect of photovoltaic technologies in Japan," in *Proceedings of the Conference Record of the 28th IEEE Photovoltaic Specialists Conference*, PVTEC (Photovoltaic Power Generation Technology Research Association), Septemper 2000, http://ieeexplore.ieee.org/stamp/stamp.jsp?tp=&arnumber=916238.

[24] F. Diner, "The analysis on photovoltaic electricity generation status, potential and policies of the leading countries in solar energy," *Renewable and Sustainable Energy Reviews*, vol. 15, no. 1, pp. 713–720, 2011.

[25] S. Mehta, *PV Technology, Production and Cost Outlook: 2010–2015*, GTM Research, 2011.

[26] Photovoltaics—potential, markets and technological progress: Solar Energy Research Institute of Singapore, July 2015, http://www.seris.sg/main/Download/4322/pdf_13052011_semcon_%202011html.

[27] Module Prices, July 2015, http://solarbuzz.com/facts-and-figures/retail-price-environment/module-prices.

[28] NREL—Photovoltaics Research, July 2015, http://www.nrel.gov/pv/.

[29] Solar Photovoltaics: Technology Brief, 2015, https://www.irena.org/DocumentDownloads/Publications/IRENA-ETSAP%20Tech%20Brief%20E11%20Solar%20PV.pdf.

[30] PES Essential: EPİA Report, January 2015, http://www.pes.eu.com/assets/misc_new/epa-market-outlook-2015pdf-680788895531.pdf.

[31] Renewable Energy Technology Cost Review, June 2015, http://mei.insights4.net.au/files/site1/docs/39/Renewable%20Energy%20Tech%20Cost%20Review.pdf.

[32] Photovoltaic System Pricing Trends, 2014, http://www.nrel.gov/docs/fy14osti/62558.pdf.

[33] Solar Energy Engineering-Processes and Systems, June 2015, http://library.uniteddiversity.coop/Energy/Solar/Solar_Energy_Engineering-Processes_and_Systems.pdf.

[34] $1/W Photovoltaic Systems White Paper to Explore A Grand Challenge for Electricity from Solar, June 2015, http://www1.eere.energy.gov/solar/pdfs/dpw_white_paper.pdf.

[35] The International Energy Agency, *Technology Roadmap: Solar Photovoltaic Energy*, The International Energy Agency, 2015, https://www.iea.org/publications/freepublications/publication/pv_roadmap.pdf.

[36] Ç. Cengiz and A. M. Karakaş, "Estimation of weibull renewal function for censored data," *International Journal of Scientific and Technological Research*, vol. 1, no. 1, pp. 123–132, 2015.

[37] M. S. Cengiz, M. S. Mamiş, M. Akdağ, and C. Cengiz, "A review of prices for photovoltaic systems," *International Journal of Technolgy Physical Problems of Engineering*, vol. 7, no. 3, pp. 8–13, 2015.

[38] Current and Future Cost of Photovoltaics, Long-term Scenarios for Market Development: System Prices and LCOE of Utility-Scale PV Systems Study, 2015, http://www.euractiv.com/files/euractiv_agora_solar_pv_study.pdf.

[39] M. S. Cengiz, M. S. Mamiş, M. Akdağ, and Ç. Cengiz, "A review of prices for photovoltaic systems," in *Proceedings of the 11th International Conference on Technical and Physical Problems of Electrical Engineering (ICTPE '15)*, pp. 300–305, Bucharest, Romania, September 2015.

Hindawi Publishing Corporation
International Journal of Photoenergy
Volume 2015, Article ID 537538, 10 pages
http://dx.doi.org/10.1155/2015/537538

*Research Article*

# Electrical and Thermal Performance Analysis for a Highly Concentrating Photovoltaic/Thermal System

**Ning Xu, Jie Ji, Wei Sun, Wenzhu Huang, and Zhuling Jin**

*Department of Thermal Science and Energy Engineering, University of Science and Technology of China, No. 96 Jinzhai Road, Hefei, Anhui 230027, China*

Correspondence should be addressed to Jie Ji; jijie@ustc.edu.cn

Received 9 July 2015; Revised 11 October 2015; Accepted 12 October 2015

Academic Editor: Elias Stathatos



A 30 kW highly concentrating photovoltaic/thermal (HCPV/T) system has been constructed and tested outdoors. The HCPV/T system consists of 32 modules, each of which consists of point-focus Fresnel lens and triple-junction solar cells with a geometric concentrating ratio of 1090x. The modules are connected to produce both electrical and thermal energy. Performance analysis has been conducted from the viewpoint of thermodynamics. The experimental results show that highest photovoltaic efficiency of 30% and instantaneous thermal efficiency of 30% can be achieved at the same time, which means the total solar energy conversion efficiency of the HCPV/T system is higher than 60%. The photovoltaic efficiency increases with direct irradiance when the direct irradiance is below 580 W/m$^2$, but it remains nearly unchanged when the direct irradiation is higher than 580 W/m$^2$. The instantaneous thermal efficiency decreases during water heating process. However, the electrical performance of the system is not affected obviously by water temperature. Highest exergetic efficiency of 35.4% can be produced by the HCPV/T system. The exergetic efficiency is mainly affected by irradiation level, which is similar to the characteristics of photovoltaic performance.

## 1. Introduction

Concentrator photovoltaic technology has been developed for over 30 years since the first modern PV concentrator was made at Sandia National Laboratories. Highly concentrating photovoltaic (HCPV) could be an important avenue for solar electricity to become economical in mass production [1]. The general idea of concentrator photovoltaic is to use optics to focus sunlight on a small receiving solar cell. Therefore, the cell area in the focus of the concentrator can be reduced by the concentration ratio ($C > 300$ for HCPV systems). Consequently, this reduction allows the utilization of expensive but highly efficient multijunction solar cells in an economical manner. The efficiency of multijunction solar cells is reported to be higher than 40% [2–4]. On the CPV module level, photovoltaic above 30% has been reported [5–7].

CPV is developing very fast, and more and more researchers and entrepreneurs are joining in this field. Substantial CPV plants and demonstration systems have been established in China, Australia, Spain, and Japan and elsewhere. Compared with other high concentrators, Fresnel lens recently has been one of the best choices because of its advantages such as small volume, light-weight, and mass production with low cost as well as effectively increasing the energy density. Araki et al. [8] present a 30 kW concentrator photovoltaic system using dome-shaped Fresnel lenses. Its photovoltaic efficiency can reach 25.8%. Xie et al. [9] give a review on concentrated solar energy applications using Fresnel lenses in the last two decades, the highest photovoltaic conversion efficiency based on imaging Fresnel lens and nonimaging Fresnel lens is reported as over 30% and 31.5 ± 1.7%, respectively. Among the existing point-focus Fresnel CPV systems, almost all the modules are passively cooled. One point of view [10] believes that passive cooling could work well for single-cell geometries for flux levels as high as 1000x suns, because there is large area available for heat sinking. However, the fact is that a large part of the already collected solar energy is dissipated as heat to the environment for modules with passive cooling design.

An active thermal circulation with coolant fluid can enable heat transfer from the central receiver to a thermal load so that the dissipated heat is collected as usable energy. Hence, the total solar energy conversion efficiency


Figure 1: Photograph of the 30 kW HCPV/T system.

is significantly increased. This thermal energy can be used directly for domestic or industrial heating. Besides, some poly generation approaches can also generate either cooling power or drinking water from the heat using solar cooling and air conditioning [11–13] or solar desalination [14, 15] technologies. Therefore, the integration of PV/T system and CPV system with point-focus Fresnel lens deserves to be respected. Unfortunately, although researches on PV/T technology, highly concentrators, multijunction solar cells, and point-focus Fresnel photovoltaic system with passive cooling methods have been carried out for years; the attempt to combine them in a hybrid system is rarely reported, especially on array level.

In this paper, a novel highly concentrating photovoltaic/thermal (HCPV/T) system based on point-focus Fresnel lens is originally proposed. Both electrical and thermal power can be cogenerated by this system. The system whose overall peak power is 30 kW is established and tested outdoors. Both electrical and thermal performance analyses are conducted from the point of view of thermodynamics. Besides, a detailed description for the main components of the system and their principles is also introduced in this paper. This work is developed aiming to supply a reference or guidance on system design and performance analysis for similar attempts and projects.

## 2. Description of the HCPV/T System

*2.1. Overview of the 30 kW HCPV/T System.* The arrangement of the 30 kW HCPV/T system is shown in Figure 1. The system is located in Huainan (32.37°N 116.59°E), Anhui Province, China. It mainly consists of 32 point-focus Fresnel modules which are mounted on a dual-axis tracking structure, as shown in Figure 1. The HCPV/T array has two strings, each of which consists of 16 modules connected in series. The array is connected to an inverter. The dual-axis tracking system ensures that the HCPV/T array tracks the sun accurately and the inverter helps to output electrical power at the maximum power point. Thanks to specific design of the receiver, dissipated heat on the receiver is collected by circulating water which flows through the modules, the pipelines, the pump, and the water tank. Under operating condition, photovoltaic power is parallel in the grid and water in the storage tank is heated. In this way, solar energy is converted to both electrical energy and thermal energy.

Table 1: Typical electrical characteristic of the HCPV/T module.

| Parameter | Variable | Value |
|---|---|---|
| Maximum power | $P_m$ | 402 W ± 5% |
| Voltage at $P_m$ | $V_m$ | 38.3 V |
| Current at $P_m$ | $I_m$ | 10.5 A |
| Open circuit voltage | $V_{OC}$ | 45.2 V |
| Short circuit current | $I_{SC}$ | 11.1 A |

*2.2. Design of the HCPV/T Module.* A typical structure of the HCPV/T module used in this system is depicted in Figure 2. There are 15 point-focus Fresnel lenses and 15 CPV/T components in a single module. The Fresnel lens and CPV/T components are mounted one by one on the aluminum frame. High efficiency InGaP/GaAs/Ge solar cells whose photovoltaic efficiency is 31.4% (AM1.5D, 25°C) under 1x sun are adopted in this system. Each cell is laminated on an aluminum heat-sink with tube formulated directly on the rear side. On the top of the solar cell, a secondary optical prism is pasted by optical silicone. The schematic and photograph of a CPV/T component are shown in Figure 3. The heat-sink is designed with a structure of axis grooved tube. The solar cells are allowed to operate at highest temperature of 90°C for a short period. It has been proved that this kind of structure can guarantee that the solar cells operate safely based on our previous work [16]. Incident sunlight is refracted by Fresnel lens and then by optical prism to distribute uniform irradiance on solar cell. All the 15 solar cells are connected in series and adjacent tubes are connected by pipes. The electrical characteristic for the module offered by the manufacturer is listed in Table 1. They are achieved by indoor testing under steady condition (DNI 900 W/m$^2$, 20°C, 4 m/s). As the areas of each Fresnel lens and solar cell are 330.2 × 330.2 mm$^2$ and 10 × 10 mm$^2$, respectively, the geometric concentration ratio of the module is 1090x. With respect to the optical loss in the concentration process, the module can achieve an optical concentration ratio of 952x.

*2.3. Dual-Axis Tracking System.* Point-focus lens concentrator requires that the module is always pointed at the sun so that the concentrated light falls precisely on the cell. A dual-axis tracking system with roll-tilt configuration is adopted, as shown in Figure 4. Although this kind of structure contains more rotating bearings and linkages, the wind loads on drive components are considerably reduced. The roll axis is placed in a northsouth direction, as this minimizes shadowing by adjacent modules along the roll axis and further minimizes space between them. A couple of light sensors are installed in the middle of the tracking structure. The sensor is essentially composed of a pair of photodiodes and a shading device which casts a different shade on these photodiodes, thereby generating different photocurrents whenever it is not aligned with the local sun vector. The sensors are mounted with the same angle that the module tilts and one per tracking axis. The tracking controller works on a two-stage basis, first coarsely aiming based on sun-ephemeris computed coordinates, followed by fine pointing using the light sensors.

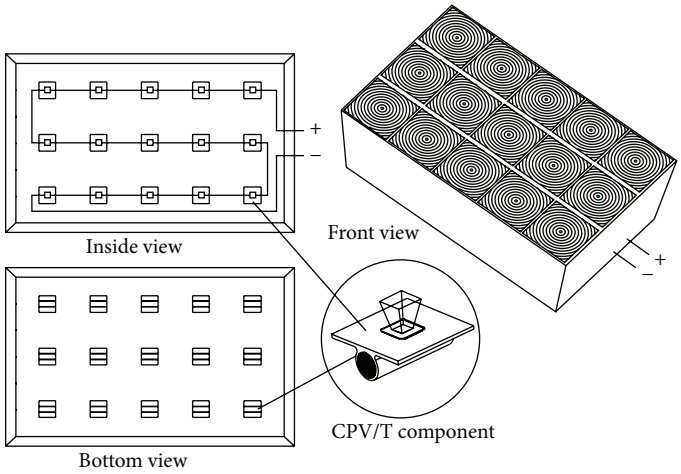


Figure 2: Schematic of the HCPV/T module based on point-focus Fresnel lens.

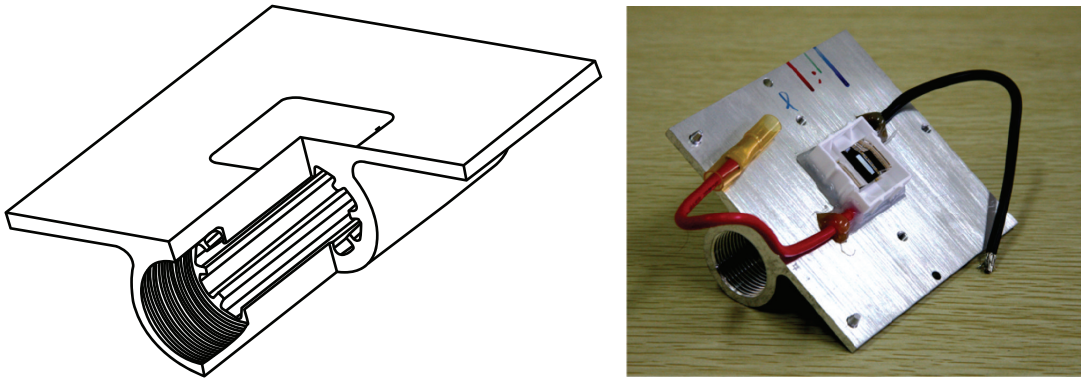

Figure 3: Schematic and photograph of a CPV/T component with grooved tube.


Figure 4: Photograph of the dual-axis tracking system.

In this system, the angle of incidence remains within a range of 0.3° with the help of the tracking system.

*2.4. Water Circulation System.* Figure 5 shows the schematic of the water circulation system. Water is pumped from the bottom of the storage tank and flows through the tubes below the heat-sinks. Heated water flows back to the tank. Every 60 heat-sink tubes of modules which are mounted on the same tilt axis are connected in series by pipes. This arrangement divides the water circulation system into eight branches and it also reduces mass flow discrepancy due to reversed return water circulation. At the inlet of main pipeline, a valve and a flowmeter are installed to control and measure the water flow rate, respectively. Two pressure gauges are installed at the inlet and outlet of the main pipeline, respectively. All pipes and heat-sink tubes are insulated by insulation cotton with a thickness of 15 mm. The volume of the tank in this system is 1000 L. Temperature measurement locations are also shown in Figure 5. Eight temperature measuring points are arranged uniformly in the water storage tank to eliminate the measurement error caused by water stratification.

*2.5. Data Acquisition System.* In the data acquisition system, temperature is measured by T-type thermocouples; direct normal irradiance (DNI) is measured by a pyrheliometer. Both temperature and DNI are recorded by a data logger (HIOKI LR8402-21) at an interval of 10 s. Pressure and water flow rate are also recorded. An inverter is used to measure and record the electrical power output of the HCPV/T modules. The electrical data is recorded every 5 minutes by the inverter. The details of all the measurement instruments are listed in Table 2.

## 3. Mathematical Model

*3.1. Energy Balance Model.* As stated before, both electrical and thermal energy are converted from solar energy by the

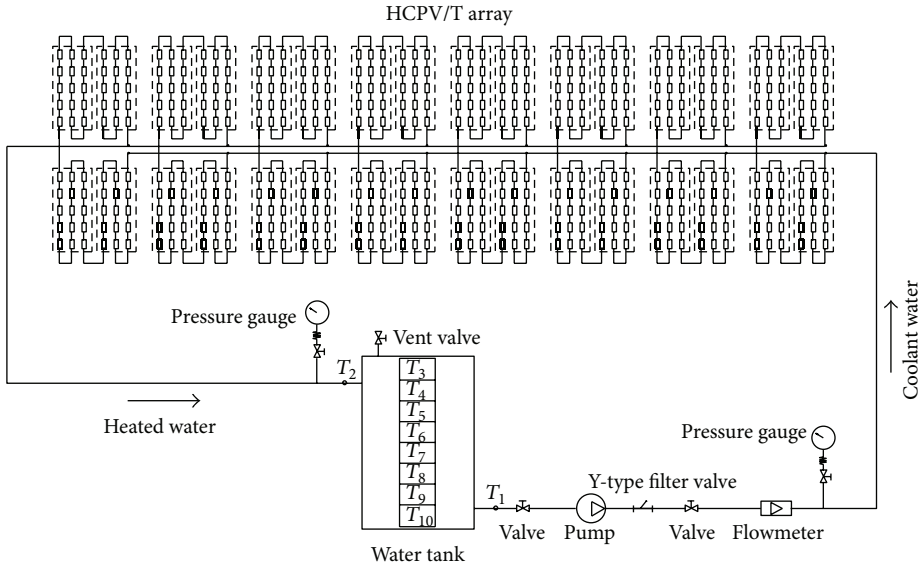


Figure 5: Schematic of water circulation and measuring point positions.

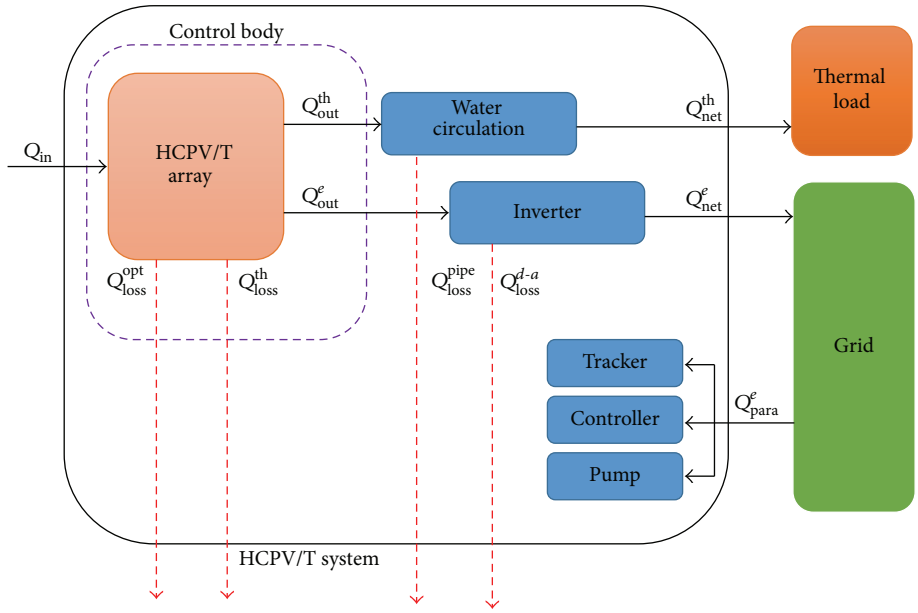


Figure 6: Schematic of the energy balance of a HCPV/T system.

Table 2: Characteristics of sensors and measurement instruments.

| Device | Accuracy | Specification |
|---|---|---|
| Thermocouple | ±0.2°C | T-type |
| Pyrheliometer | 2% | TBS 2-2 |
| Data logger | | HIOKI LR8402-21 |
| Flow rate | 2% | LXS-40E |
| Inverter | 3% | Guanya GSG-100KTT-TV |

HCPV/T array. In this system, power output is tapped into the grid by an inverter directly and thermal output is collected without secondary heat exchange. Considering the energy losses caused by optical, electrical, and thermal reasons, the schematic drawing of the energy balance for the HCPV/T system is illustrated in Figure 6.

Based on the first law of thermodynamics, the general energy balance for the HCPV/T array can be expressed as

$$Q_{in} = Q^{e}_{out} + Q^{th}_{out} + Q^{opt}_{loss} + Q^{th}_{loss}, \quad (1)$$

where $Q_{in}$ is the total incoming radiation power on all modules, $Q^{e}_{out}$ is the photovoltaic output by the array, and $Q^{th}_{out}$

is thermal output at the same time. Calculations for them are illustrated by

$$Q_{\text{in}} = G_d A_m N_s N_p, \tag{2}$$

$$Q_{\text{out}}^{\text{th}} = c_p \dot{m} \left(T_{w,o} - T_{w,i}\right). \tag{3}$$

In (2), $G_d$ is the incident beam radiation on the array, namely, the direct normal irradiance. $A_m$ is the total Fresnel lens area of a single module. $N_s$ is the number of modules in a series and $N_p$ is the number of branches of the array. In (3), $c_p$ is the specific heat of water, $\dot{m}$ is the total mass flow rate, and $T_{w,i}$ and $T_{w,o}$ are the inlet temperature and outlet temperature in the circulation, respectively.

In (1), $Q_{\text{loss}}^{\text{opt}}$ is the optical loss and it can be derived from (4). The optical efficiency $\eta_{\text{opt}}$ considers optical losses caused by both Fresnel lens and prims; thereby it is the dot product of their transmittance, as shown in (5):

$$Q_{\text{loss}}^{\text{opt}} = Q_{\text{in}} \left(1 - \eta_{\text{opt}}\right), \tag{4}$$

$$\eta_{\text{opt}} = \tau_{\text{Fresnel}} \tau_{\text{prism}}. \tag{5}$$

The last part in (1), namely, $Q_{\text{loss}}^{\text{th}}$, is the thermal loss of the array caused by heat convection and radiation to the ambient. It is difficult to be calculated accurately. However, this part contributes insignificantly when evaluating the performance of the system.

It is should be emphasized that in an integrated system some parasitic power consumption from components inevitably exists. On the other hand, some energy losses such as thermal loss from pipes to the ambient are unavoidable even if the design is optimized. On account of these power consumption and losses, the net power generated by the HCPV/T system can be defined as

$$Q_{\text{net}}^{e} = Q_{\text{out}}^{e} - Q_{\text{loss}}^{d\text{-}a} - Q_{\text{para}}^{e}, \tag{6}$$

$$Q_{\text{net}}^{\text{th}} = Q_{\text{out}}^{\text{th}} - Q_{\text{loss}}^{\text{pipe}}. \tag{7}$$

In (6), $Q_{\text{net}}^{e}$ is the net electrical power supplied by the system; $Q_{\text{loss}}^{d\text{-}a}$ is the energy loss due to inversion and grid connection. $Q_{\text{para}}^{e}$ is parasitic power consumption which includes power dissipation from tracker, controller and pump. In (7), $Q_{\text{loss}}^{\text{pipe}}$ defines the heat loss from the pipes and storage tank. Because all the pipes and tank are thermally insulated perfectly, this part can usually be neglected.

*3.2. First-Law Efficiency of Thermodynamics.* Instantaneous efficiency is widely used to evaluate PV/T systems. The photovoltaic efficiency represents the ability of the HCPV/T array to convert solar energy to electrical energy. It is obtained by

$$\eta_{\text{PV}} = \frac{Q_{\text{out}}^{e}}{Q_{\text{in}}} = \frac{Q_{\text{out}}^{e}}{G_d A_m N_s N_p}. \tag{8}$$

The instantaneous thermal efficiency of the HCPV/T array is defined by (9), which reflects the heat conversion capability of the array:

$$\eta_{\text{th}} = \frac{Q_{\text{out}}^{\text{th}}}{Q_{\text{in}}} = \frac{c_p \dot{m} \left(T_{w,o} - T_{w,i}\right)}{G_d A_m N_s N_p}. \tag{9}$$

From the first-law of thermodynamics, the overall performance of a PV/T system can be evaluated by the energetic (first-law) efficiency $\eta_{\text{PVT}}$. It is widely used in previous studies [17, 18]. The first-law efficiency is defined as

$$\eta_{\text{PVT}} = \eta_{\text{PV}} + \eta_{\text{th}}. \tag{10}$$

*3.3. Second-Law Efficiency of Thermodynamics.* Although the first-law efficiency reveals the overall performance of a PV/T system directly, it ignores the difference between thermal energy and electrical output produced by a module in "quality," even if they are the same in "quantity" and measurable by the same physical unit. In fact, thermal energy cannot produce work until a temperature difference exists between a high temperature heat source and a low-temperature heat-sink, while electrical energy can completely transform into work irrespective of the environment. In other words, the second-law efficiency, namely, the exergetic efficiency, offers a qualitative and standardized evaluation of the overall performance of a PV/T system. Exergy is simply the available energy obtained by subtracting the unavailable energy from the total energy and is equivalent to the work transformable.

According to the work conducted by Fujisawa and Tani [19], the second-law efficiency of a PV/T system is expressed as (11). This definition is based on the assumption that the initial temperature of the fluid medium is equal to the ambient temperature:

$$\varepsilon_{\text{PVT}} = \varepsilon_{\text{PV}} + \varepsilon_{\text{th}} = \eta_{\text{PV}} + \left(1 - \frac{T_a}{T_w}\right) \eta_{\text{th}}, \tag{11}$$

where $\varepsilon_{\text{PV}}$ and $\varepsilon_{\text{th}}$ are the exergetic efficiency of PV array and thermal collectors, respectively. $T_a$ is the ambient temperature and $T_w$ is the water temperature which can be calculated by

$$T_w = \frac{\left(T_{w,i} + T_{w,o}\right)}{2}. \tag{12}$$

In (11), the calculation of the exergy of solar radiation is not considered. Instead, the energy of radiation is taken as the exergy of radiation directly. Exergetic efficiency is the ratio of total exergy output to total exergy input [20]. Therefore, the exergetic efficiency can be defined as

$$\varepsilon_{\text{PVT}} = \frac{\text{Ex}_{\text{PV}} + \text{Ex}_{\text{th}}}{\text{Ex}_{\text{in}}} = \varepsilon_{\text{PV}} + \varepsilon_{\text{th}}, \tag{13}$$

where $\text{Ex}_{\text{PV}}$ and $\text{Ex}_{\text{th}}$ are the electrical exergy output and thermal exergy output of the array, respectively. $\text{Ex}_{\text{in}}$ is the

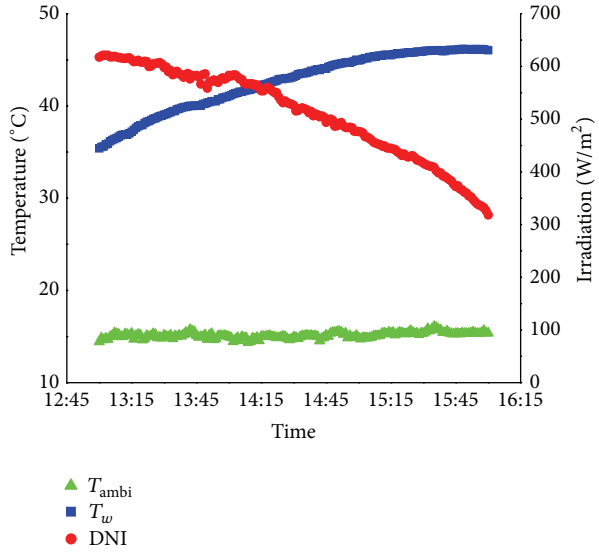


Figure 7: Environmental parameters in the testing period.

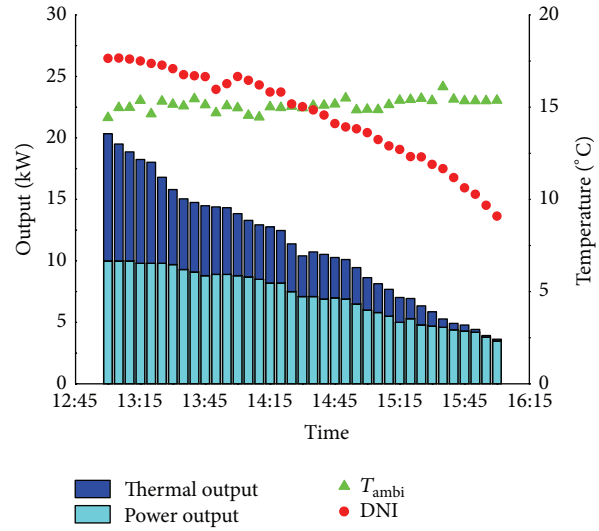


Figure 8: Photovoltaic and thermal output of the HCPV/T system in the testing period.

exergy input of solar radiation. The exergy outputs are related to the energy outputs as follows:

$$\begin{aligned} \mathrm{Ex}_{\mathrm{PV}} &= Q^{e}_{\mathrm{out}}, \\ \mathrm{Ex}_{\mathrm{th}} &= \left(1 - \frac{T_a}{T_w}\right) Q^{\mathrm{th}}_{\mathrm{out}}. \end{aligned} \tag{14}$$

There are different methods to determine the exergy of radiation in evaluating the performance of PV/T system when using the exergy method. Among them, three most commonly used calculation methods are summarized by Chow et al. [17]; namely,

$$\mathrm{Ex}_{\mathrm{in}} = \left[1 + \frac{1}{3}\left(\frac{T_a}{T_{\mathrm{sun}}}\right)^4 - \frac{4T_a}{3T_{\mathrm{sun}}}\right] Q_{\mathrm{in}}, \tag{15}$$

$$\mathrm{Ex}_{\mathrm{in}} = \left[1 - \frac{4T_a}{3T_{\mathrm{sun}}}\right] Q_{\mathrm{in}}, \tag{16}$$

$$\mathrm{Ex}_{\mathrm{in}} = \left[1 - \frac{T_a}{T_{\mathrm{sun}}}\right] Q_{\mathrm{in}}, \tag{17}$$

where $T_{\mathrm{sun}}$ is the solar radiation temperature at 6000 K. Actually, the difference between results calculated by these three methods is less than 2%. In this study, (17) is adopted.

## 4. Results and Discussion

The experiment was firstly conducted on December, 2014. Figure 7 shows changes of meteorological parameters and temperature of water in storage tank from 13:00 to 16:00 in a testing day. As seen in Figure 7, the ambient temperature changes in a small range of 15~17°C, and the DNI changes within 300~650 W/m$^2$. 1000 L water is heated from 35°C to 47°C in three hours. Water flow rate is controlled at 2.8 m$^3$/h which means the flow rate in each branch is nearly at 0.34 m$^3$/h. This flow rate makes the flow in tubes behavior

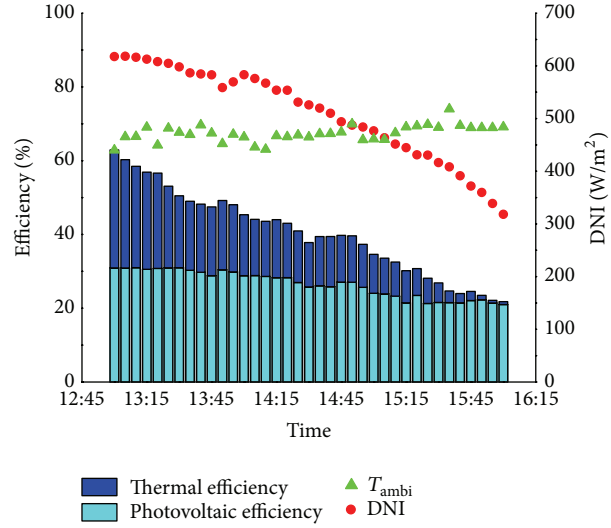


Figure 9: Efficiency characteristics of the HCPV/T system in the testing day.

a turbulent flow, thereby enhancing the heat convection effectiveness.

Figures 8 and 9 illustrate the output and efficiency of the HCPV/T system during the testing period, respectively. It can be seen in Figure 8 that the total output of the system exceeds 20 kW. Both power output and thermal output decrease as DNI decreases and water heated. Considering that the maximum DNI in the selected data is not higher than 650 W/m$^2$, more power can be obtained when the DNI level is higher. On the other hand, the heat collection capability can be definitely improved with a lower initial water temperature. Figure 9 depicts both photovoltaic efficiency and thermal efficiency changes in the testing period which can reflect the energy conversion effect directly. It is obvious that photovoltaic efficiency changes little with irradiation or water

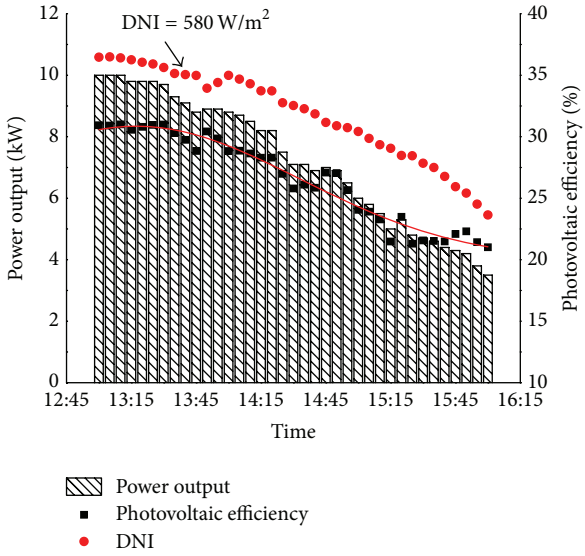


Figure 10: Photovoltaic performance of the HCPV/T array.

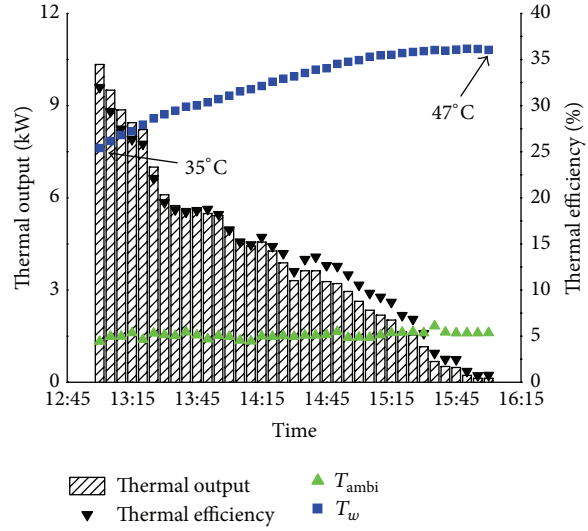


Figure 11: Thermal performance of the HCPV/T array.

temperature. However, thermal efficiency reduces quickly because of increasing water temperature and decreasing irradiation. Combining results revealed by Figures 8 and 9, it is conspicuous that higher power and thermal output can be obtained if the irradiation level is higher or water temperature is lower. Based on the electrical parameters of module and thermal characteristic of the system, it can be estimated that the total peak output generated by the system can be over 30 kW.

To investigate the photovoltaic characteristics of the system in particular, the relationship between power output, photovoltaic efficiency, and DNI is constructed in Figure 10. It can be found that the photovoltaic efficiency changes within 20~30%. Besides, the photovoltaic efficiency of the system increases with DNI when DNI is below 580 W/m$^2$ but remains nearly unchanged when DNI is higher than 580 W/m$^2$. This sign explains why the power output decreases more quickly when the irradiation is at a low level. It also indicates that the HCPV/T system will maintain a relatively high photovoltaic efficiency if it is arranged at a location with high direct irradiation level.

Figure 11 shows the thermal characteristics of the HCPV/T system. The thermal efficiency reduces because of the weaker heat capture ability resulting from higher water temperature and less energy input. In consequence, the thermal output decreases accordingly. It can be seen that thermal efficiency drops nearly to zero after 16:00, which means water circulation cannot collect heat positively. This gives signs that water cannot be heated sequentially under the current condition and the measure we should take is to stop pumping. It can be concluded that the thermal efficiency of the system will be higher than it is like currently if a larger tank is adopted because there is more low-temperature water to be heated up. However, the larger volume water may not be heated up to a relatively high temperature if the irradiation level is lower or the energy loss is higher, let alone the increasing cost of tank. It can be seen that water is heated up to 47°C. In fact, water with this grade of temperature can be used for domestic heating directly.

Performance of the HCPV/T array is compared with performance on the module level, which is investigated in our previous work [16]. The comparison is depicted in Figure 12. As to the selected data, water was heated from 35°C to 47°C, and the ambient temperature remained near 16°C without large fluctuation. The distinct difference exists in direct irradiation levels. It can be seen that at high irradiation level the HCPV/T array can obtain a higher photovoltaic efficiency than the module, but this difference is very small. This is mainly caused by measurement error due to different measuring instruments. Power output of the array is controlled by an inverter, while the module is measured by a photovoltaic analyzer. Even so, a photovoltaic efficiency of more than 28% can be obtained no matter on module level or array level. As to the thermal performance, thermal efficiency of the HCPV/T array is lower than that of module, and it decreases much faster than thermal efficiency of module. This is because there are longer and more complicated pipe routes in array compared to the module, and they will lead to larger heat loss.

The variation of overall efficiency of the HCPV/T system is shown in Figure 13. From the viewpoint of the first law of thermodynamics, highest overall efficiency of 62% can be obtained. It drops because of increasing water temperature and decreasing DNI. However, water temperature is found to play an insignificant role when the overall performance is viewed from the second law viewpoint. Highest exergetic efficiency of 35.4% can be produced by the HCPV/T system. The exergetic efficiency is mainly affected by irradiation level, which is similar to the characteristics of photovoltaic performance.

## 5. Conclusion

A 30 kW HCPV/T system based on the point-focus Fresnel lens is built and an outdoor experiment was performed

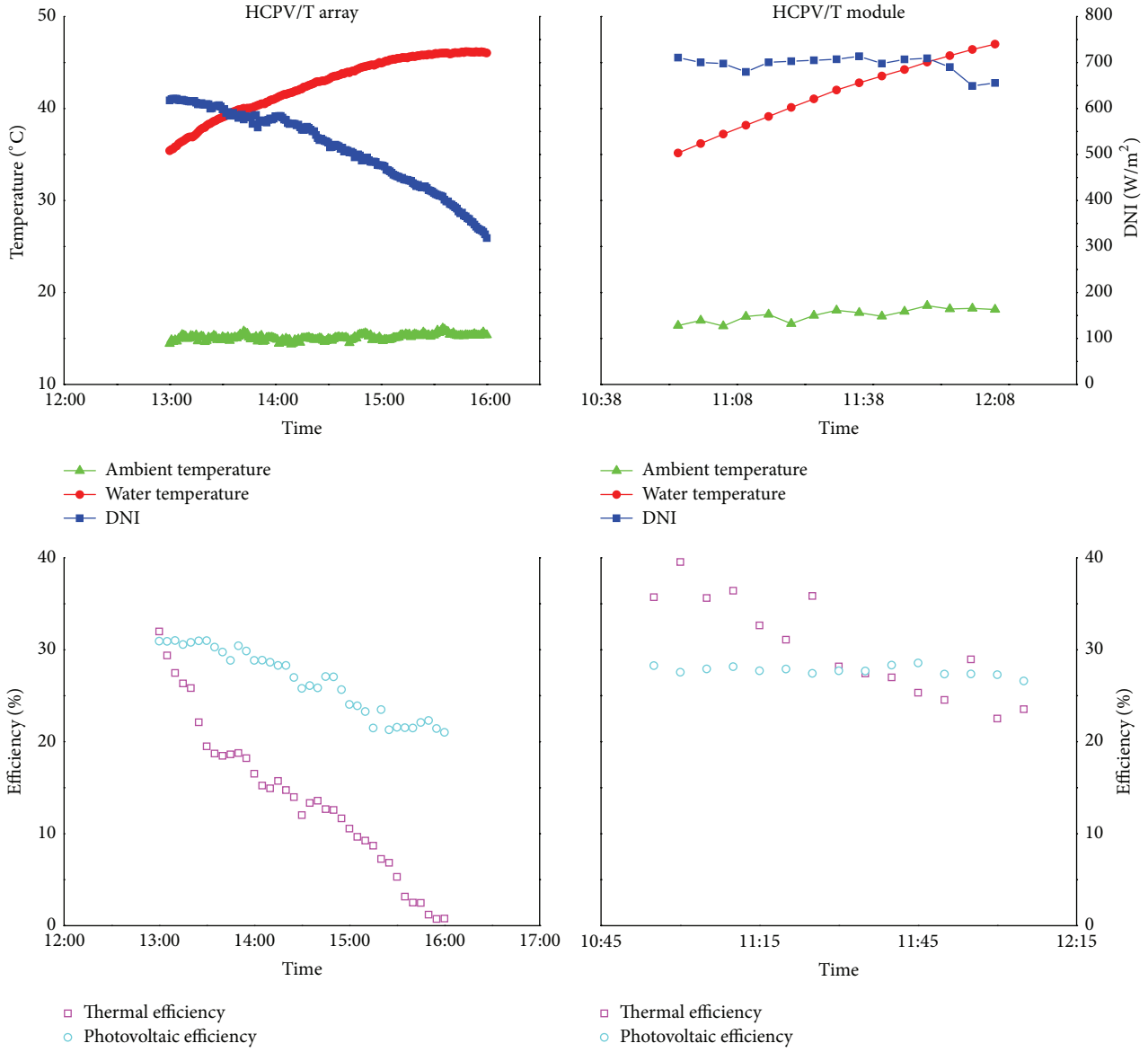


Figure 12: Comparison of performance between the HCPV/T array and a HCPV/T module.

in consecutive days. Outdoor performance of the system was also investigated based on periodical representative measurement data. Design principles and descriptions of each of several parts of the system are given in detail, aiming to present reference or guidance for similar attempts and projects. Performance analysis has been conducted from the viewpoint of thermodynamics with energetic analysis and exergetic analysis. The experimental results show that highest photovoltaic efficiency of 30% and instantaneous thermal efficiency of 30% could be achieved at the same time, which means the total solar energy conversion efficiency of the HCPV/T system is higher than 60%. The photovoltaic efficiency of the system increases with DNI when DNI level is below 580 W/m$^2$ but remains nearly unchanged when DNI is higher than 580 W/m$^2$. The instantaneous thermal efficiency decreases during water heating process because it strongly depends on water temperature as well as irradiation level. However, the electrical performance of the system is not affected obviously by the increase of water temperature. Highest exergetic efficiency of 35.4% can be produced by the HCPV/T system. The exergetic efficiency is mainly affected by irradiation level, which is similar to the characteristics of photovoltaic performance.

## Nomenclature

*Symbols*

$A$: Area, m$^2$
$c_p$: Specific heat, J/(kg·K)
$G_d$: Direct normal irradiation, W/m$^2$
$I$: Current, A
$\dot{m}$: Mass flow rate, kg/s
$N$: Number of modules

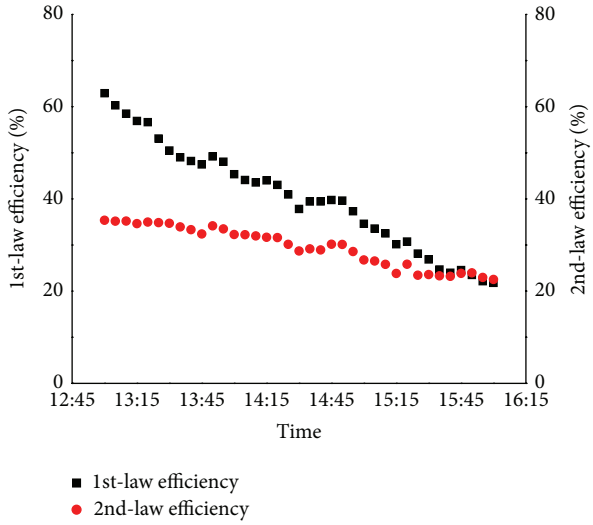


FIGURE 13: Variation of overall efficiency of the HCPV/T system.

$Q$: Energy, W
Ex: Exergy, W
$T$: Temperature, ˚C
$V$: Voltage, V.

*Subscript/Superscript*

*d-a*: DC to AC
*e*: Electrical
Fresnel: Fresnel lens
*i*: Inlet
in: Input
loss: Energy loss
*m*: Module
net: Net output
*o*: Outlet
opt: Optical
out: Output
*p*: In parallel
para: Parasitic
pipe: Pipe in circulation
prism: Optical prism
*s*: In series
th: Thermal
*w*: Water.

*Greek Symbols*

$\varepsilon$: Exergetic efficiency
$\eta$: Energetic efficiency
$\tau$: Transmittance.

## Conflict of Interests

The authors declare that there is no conflict of interests regarding the publication of this paper.

## Acknowledgments

This work is supported by a grant from the National High Technology Research and Development Program of China (863 Program) (no. 2013AA050403) and Dongguan Innovative Research Team Program (no. 2014607101008).

## References

[1] A. L. López and V. M. Andreev, *Concentrator Photovoltaics*, Springer, Berlin, Germany, 2010.

[2] S. Kurtz and J. Geisz, "Multijunction solar cells for conversion of concentrated sunlight to electricity," *Optics Express*, vol. 18, no. 9, pp. A73–A78, 2010.

[3] M. Yamaguchi, T. Takamoto, K. Araki, and N. Ekins-Daukes, "Multi-junction III-V solar cells: current status and future potential," *Solar Energy*, vol. 79, no. 1, pp. 78–85, 2005.

[4] F. Dimroth, M. Grave, P. Beutel et al., "Wafer bonded four-junction GaInP/GaAs//GaInAsP/GaInAs concentrator solar cells with 44.7% efficiency," *Progress in Photovoltaics: Research and Applications*, vol. 22, no. 3, pp. 277–282, 2014.

[5] K. Araki, H. Uozumi, T. Egami et al., "Development of concentrator modules with dome-shaped fresnel lenses and triple-junction concentrator cells," *Progress in Photovoltaics: Research and Applications*, vol. 13, no. 6, pp. 513–527, 2005.

[6] G. S. Kinsey, A. Nayak, M. Liu, and V. Garboushian, "Increasing power and energy in amonix CPV solar power plants," *IEEE Journal of Photovoltaics*, vol. 1, no. 2, pp. 213–218, 2011.

[7] S. van Riesen, A. Gombert, E. Gerster et al., "Concentrix Solar's progress in developing highly efficient modules," *AIP Conference Proceedings*, vol. 1407, p. 235, 2011.

[8] K. Araki, T. Yano, and Y. Kuroda, "30 kW concentrator photovoltaic system using dome-shaped Fresnel lenses," *Optics Express*, vol. 18, no. 1, pp. A53–A63, 2010.

[9] W. T. Xie, Y. J. Dai, R. Z. Wang, and K. Sumathy, "Concentrated solar energy applications using Fresnel lenses: a review," *Renewable and Sustainable Energy Reviews*, vol. 15, no. 6, pp. 2588–2606, 2011.

[10] A. Royne, C. J. Dey, and D. R. Mills, "Cooling of photovoltaic cells under concentrated illumination: a critical review," *Solar Energy Materials and Solar Cells*, vol. 86, no. 4, pp. 451–483, 2005.

[11] H.-M. Henning, "Solar assisted air conditioning of buildings—an overview," *Applied Thermal Engineering*, vol. 27, no. 10, pp. 1734–1749, 2007.

[12] C. A. Balaras, G. Grossman, H.-M. Henning et al., "Solar air conditioning in Europe—an overview," *Renewable and Sustainable Energy Reviews*, vol. 11, no. 2, pp. 299–314, 2007.

[13] G. Mittelman, A. Kribus, and A. Dayan, "Solar cooling with concentrating photovoltaic/thermal (CPVT) systems," *Energy Conversion and Management*, vol. 48, no. 9, pp. 2481–2490, 2007.

[14] J. Koschikowski, M. Wieghaus, and M. Rommel, "Membrane distillation for solar desalination," in *Seawater Desalination*, Green Energy and Technology, pp. 165–187, Springer, Berlin, Germany, 2009.

[15] G. Mittelman, A. Kribus, O. Mouchtar, and A. Dayan, "Water desalination with concentrating photovoltaic/thermal (CPVT) systems," *Solar Energy*, vol. 83, no. 8, pp. 1322–1334, 2009.

[16] N. Xu, J. Ji, W. Sun, L. Han, H. Chen, and Z. Jin, "Outdoor performance analysis of a 1090× point-focus Fresnel high concentrator photovoltaic/thermal system with triple-junction solar cells," *Energy Conversion and Management*, vol. 100, pp. 191–200, 2015.

[17] T. T. Chow, G. Pei, K. F. Fong, Z. Lin, A. L. S. Chan, and J. Ji, "Energy and exergy analysis of photovoltaic-thermal collector

with and without glass cover," *Applied Energy*, vol. 86, no. 3, pp. 310–316, 2009.

[18] J. Ji, J.-P. Lu, T.-T. Chow, W. He, and G. Pei, "A sensitivity study of a hybrid photovoltaic/thermal water-heating system with natural circulation," *Applied Energy*, vol. 84, no. 2, pp. 222–237, 2007.

[19] T. Fujisawa and T. Tani, "Annual exergy evaluation on photovoltaic-thermal hybrid collector," *Solar Energy Materials and Solar Cells*, vol. 47, no. 1–4, pp. 135–148, 1997.

[20] A. Hepbasli, "A key review on exergetic analysis and assessment of renewable energy resources for a sustainable future," *Renewable and Sustainable Energy Reviews*, vol. 12, no. 3, pp. 593–661, 2008.

Hindawi Publishing Corporation
International Journal of Photoenergy
Volume 2015, Article ID 863248, 5 pages
http://dx.doi.org/10.1155/2015/863248

*Research Article*

# PID Testing Method Suitable for Process Control of Solar Cells Mass Production

**Xianfang Gou,[1,2] Xiaoyan Li,[1] Su Zhou,[2] Shaoliang Wang,[3] Weitao Fan,[2] and Qingsong Huang[2]**

[1]*Beijing University of Technology, Beijing 100124, China*
[2]*CECEP Solar Energy Technology (Zhenjiang) Co., Ltd., Zhenjiang 212132, China*
[3]*Beijing Jiaotong University, Beijing 100044, China*

Correspondence should be addressed to Su Zhou; zhousu2003@hotmail.com

Received 4 September 2015; Accepted 5 October 2015

Academic Editor: Xudong Zhao



Voltage bias of several hundred volts which are applied between solar cells and module frames may lead to significant power losses, so-called potential-induced degradation (PID), in normal photovoltaic (PV) installations system. Modules and minimodules are used to conduct PID test of solar cells. The test procedure is time consuming and of high cost, which cannot be used as process monitoring method during solar cells fabrication. In this paper, three kinds of test including minimodule, $R_{sh}$, and V-Q test are conducted on solar cells or wafers with $SiN_x$ of different refractive index. All comparisons between test results of $R_{sh}$, V-Q, and minimodule tests have shown equal results. It is shown that $R_{sh}$ test can be used as quality inspection of solar cells and V-Q test of coated wafer can be used as process control of solar cells.

## 1. Introduction

In standard photovoltaic (PV) installations system, PV modules are exposed to voltage bias of several hundred volts with respect to the module frames/mounting [1–3]. Due to those high voltages, solar modules may suffer so-called potential-induced degradation (PID) which may lead to significant performance loss [4–6]. It is reported that high voltages may lead to leakage currents through the encapsulating material, being responsible for degradation effects [7]. Some investigation revealed that soda lime glass, ethylene vinyl acetate (EVA), and the solar cell's antireflective coating (ARC) play important roles in the formation of PID [8–10].

Among those factors, antireflective coating (ARC) was the important part and was widely studied to avoid PID [11, 12]. Solar cells with $SiO_2/SiN_x$ double coating layer or $SiN_x$ with high reflective index all have great improvement. At present, most PID test methods about solar cells are conducted on modules [13] or minimodules [9, 14]. Solar cells firstly should be made into module and then placed in an environmental chamber under defined conditions, finally connected to a power supply in order to generate a typical bias voltage for defined times. The test procedure is time consuming and of high cost, which cannot be used as process monitoring method during solar cells fabrication.

The purpose of this work was to provide simple and fast PID test methods about solar cells which are suitable for quality inspection of solar cells and process control of ARC deposition during mass production.

## 2. Experimental

Solar cells based on p-type multicrystalline wafers with resistivity of 1–3 Ω·cm and thicknesses of about 190 $\mu$m were used as test samples. Solar cells with different $SiN_x$ refractive index were divided into different groups according to various anti-PID properties. The PID performances of solar cells were evaluated by three methods, including minimodule test, shunt resistance $R_{sh}$ test, and voltage-corona charge (V-Q) test for solar cells. Same EVA and glasses were used for minimodule test and $R_{sh}$ test. The test results of three different methods were compared to each other to investigate the substitutability of those methods.

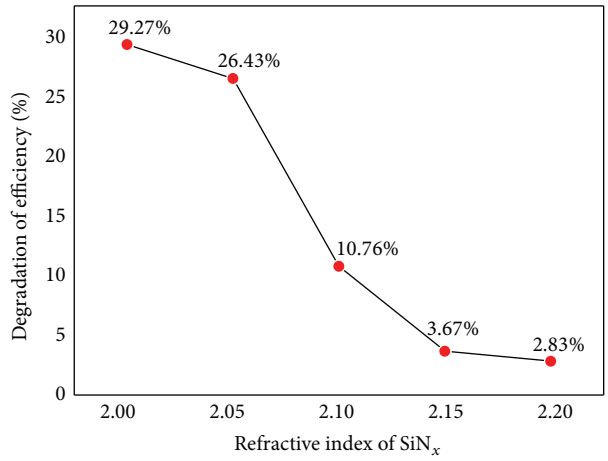


Figure 1: Different PID power loss of cells with ARC of different refractive index.

Frameless minimodules (one mc-Si cell, dimensions 30 ∗ 30 cm$^2$) were used for the lab testing with a self-adhesive aluminum tape as a substitute for the frame. Some water was dropped on the surface of glass and then another aluminum foil was applied on the top of glass to ensure full contact between glass and aluminum tape. The PID test was conducted in environment chamber with temperature of 85°C, humidity of 85%, applied voltage of 1000 V, and time of 96 h. The electrical parameters and EL image were measured to evaluate the PID performance of solar cells.

$R_{sh}$ test was performed using PIDcon which was developed by Fraunhofer CSP and now is commercially available by Freiberg Instruments [15] as follows: the solar cell was placed on a temperature-controlled aluminum chuck to achieve a constant temperature throughout the testing process. On the front side, a sheet of EVA and glass were placed on top of the solar cell. The front surface of the solar cell was connected to a needle to measure the solar cell parameters. A solid metal block was then placed on top of the front glass to achieve a uniform high voltage across the glass surface within the test area. A voltage of 1000 V was then applied between the front metal block and aluminum chuck. During the degradation, the shunt resistance of the solar cells was measured to indicate the performance change of solar cells. Cells of different group with similar initial $R_{sh}$ were chosen as test samples.

V-Q characteristics of ARC films were also measured to evaluate the conductivity of these films using WT-2000 PVN from Semilab [8]. After ARC coating, silicon wafers are charged by corona continuously. Kelvin Probe was used to measure the surface voltage of silicon wafer under different charged electric quantity. Generally, the surface voltage initially increases with the charged electric quantity and then is gradually saturated with a certain voltage which was named $V_{limit}$. The value of $V_{limit}$ can be used to evaluate the conductivity of ARC film.

## 3. Results and Discussion

*3.1. Minimodule Test.* Figure 1 shows the different PID power loss of cells with ARC of different refractive index. The thickness of film was controlled to the same (85 nm), and different refractive index is produced by adjusting the flow rate of silane and ammonia in the process of deposition. It can be seen from the figure that the PID power loss decreases from 29.27% to 2.83% while the refractive index changes from 2.0 to 2.2. The results show that the PID decreases by the increasing of refractive index of SiN$_x$, especially when the refractive increases from 2.0 to 2.15, and the PID shows sharply downward trend and then comes to a slightly decreased trend. By the increasing of refractive index of SiN$_x$, the brightness in EL is enhanced gradually before PID test. After PID test, the point of darkness in EL picture increases for the low refractive index. When the refractive index increased to 2.2, the testing results show it is stable after the PID, indicating a good anti-PID performance. The EL images also verified that higher refractive index of SiN$_x$ can weaken PID of solar cells and even eliminate this phenomenon (Figure 2).

*3.2. PIDcon Test.* Figure 3 shows the degradation of $R_{sh}$ of different SiN$_x$ refractive index. In order to make accurate comparison, solar cells with $R_{sh}$ of 100–300 Ω were chosen to apply PIDcon test. It can be seen that, in the process of refractive index changing from 2.0 to 2.2, the $R_{sh}$ degradation rate varies from being rapid to almost stable. It indicates that the $R_{sh}$ degradation rate decreases by the increasing of refractive index of SiN$_x$. Plenty of reports claim that the decrease of $R_{sh}$ is a very important parameter in evaluation of the PID problem. When $R_{sh}$ of solar cells decreases to an extremely low level, for example, lower than 5%, it will have an obvious negative effect on solar cell output parameters.

*3.3. V-Q Test.* Figure 4(a) shows the relation between the surface voltage of silicon with SiN$_x$ films and the deposited corona charge density under different refractive index of SiN$_x$. The surface voltage increases with more positive corona charge on the surface. For samples with high refractive index, such as 2.1, 2.15, and 2.2, the voltage is easy to become saturate. And for samples with low refractive index, such as 2.0 and 2.05, it seems that it needs higher corona charge density to lead the voltage to saturation. It can be seen that, by

| Refractive index of $SiN_x$ | 2.0 | 2.05 | 2.1 | 2.15 | 2.2 |
|---|---|---|---|---|---|
| Before test |  | 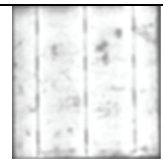 | 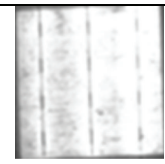 | 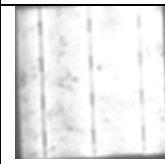 |  |
| After test | 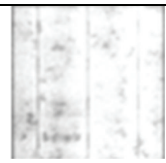 | 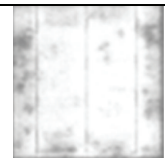 |  | 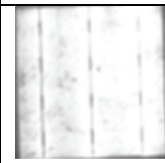 |  |

Figure 2: Different EL images of cells with ARC of different refractive index before and after PID test.

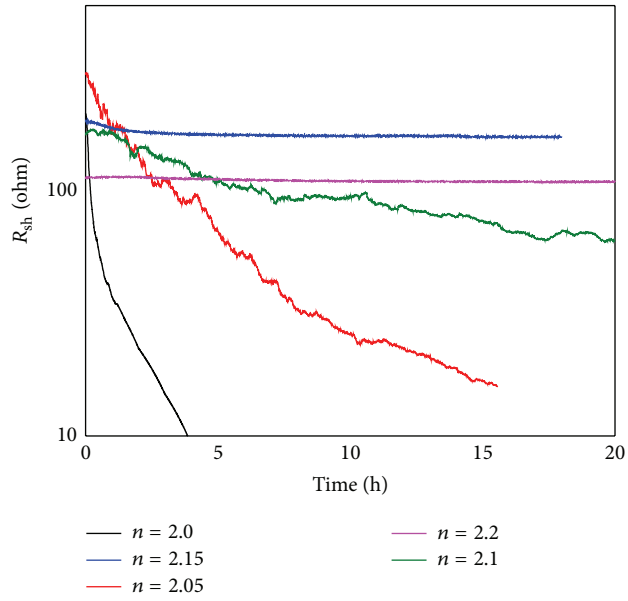


Figure 3: Degradation of $R_{sh}$ of different $SiN_x$ refractive index.

the increasing of the refractive index of $SiN_x$, while positive corona charge was applied on the ARC surface, the voltage may reach the saturation state more easily. Once the voltage reached the saturation state, the voltage does not change by more corona charging. It can be explained by the leakage current through ARC. Continuous positive charging will leak out because of the electrical conductivity of ARC film. The saturation voltage was extracted from Figure 4(a) and plotted with refractive index of $SiN_x$ in Figure 4(b). It has to be mentioned that, for samples with refractive index of 2.0 and 2.05, the saturation voltage is extracted by the voltage of the maximum corona charge density (3000 nC/cm$^2$).

The saturation voltage decreases with the increasing of refractive index. When the refractive index increased from 2.0 to 2.1, the saturation voltage decreased from 29.1 V to 6.6 V rapidly. Then the value of $V_{limit}$ changes slightly by increasing refractive index. Low $V_{limit}$ indicates an increased electronic conductivity, arising from more mobile electrons, in the silicon rich $SiN_x$ layer with higher refractive index. In comparison of the minimodule, $R_{sh}$, and V-Q result, the function of represented parameter with refractive index takes the same trend. Then they are the equal test tool to evaluate the performance of PID in silicon solar cells.

## 4. Conclusion

Modules or minimodules PID tests are quite time consuming and of high cost. In this paper two sample methods for checking the PID performance of solar cells and ARC coating were provided to solve the monitoring problem during mass production of anti-PID solar cells. All comparisons between $R_{sh}$, V-Q test of silicon solar cell, and minimodule tests in climate chambers have shown equal results. And $R_{sh}$ and V-Q test are much simpler than minimodule test. It is shown that

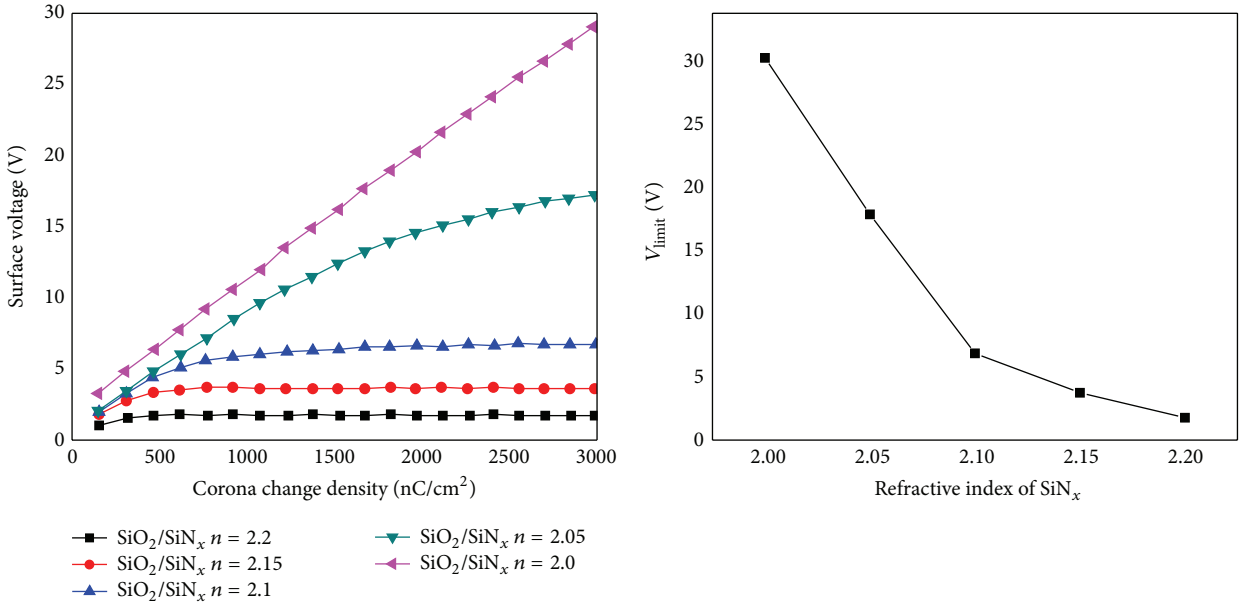


(a) V-Q measurement

(b) Relation between $V_{limit}$ and refractive index of $SiN_x$

FIGURE 4: Testing results of V-Q and $V_{limit}$ with different refractive index of $SiN_x$.

$R_{sh}$ test can be used as quality inspection of solar cells and V-Q test of coated wafer can be used as process control of solar cells. Those two methods can be helpful to eliminate PID in mass production level.

## Conflict of Interests

The authors declare that there is no conflict of interests regarding the publication of this paper.

## Acknowledgments

The authors would like to thank Dr. Chunlan Zhou for helpful discussions and review of this paper. The authors would also like to thank Dr. Jacky Ren from Semilab Co., Ltd., for the measurement of V-Q test and helpful discussions.

## References

[1] R. Swanson, M. Cudzinovic, D. DeCeuster et al., "The surface polarization effect in high-efficiency silicon solar cells," in *Proceedings of 15th International Photovoltaic Science and Engineering Conference (PVSEC '05)*, Shanghai, China, 2005.

[2] P. Hacke, R. Smith, K. Terwilliger et al., "Acceleration factor determination for potential-induced degradation in crystalline silicon PV modules," in *Proceedings of the IEEE International Reliability Physics Symposium (IRPS '13)*, pp. 4B.1.1–4B.1.5, Anaheim, Calif, USA, April 2013.

[3] P. Hacke, R. Smith, K. Terwilliger et al., "Testing and analysis for lifetime prediction of crystalline silicon PV modules undergoing degradation by system voltage stress," in *Proceedings of the 38th IEEE Photovoltaic Specialists Conference (PVSC '12)*, pp. 1750–1755, IEEE, Austin, Tex, USA, June 2012.

[4] S. Pingel, O. Frank, M. Winkler et al., "Potential induced degradation of solar cells and panels," in *Proceedings of the 35th IEEE Photovoltaic Specialists Conference (PVSC '10)*, pp. 2817–2822, Honolulu, Hawaii, USA, June 2010.

[5] P. Hacke, R. Smith, K. Terwilliger et al., "Testing and analysis for lifetime prediction of crystalline silicon PV modules undergoing degradation by system voltage stress," *IEEE Journal of Photovoltaics*, vol. 3, no. 1, pp. 246–253, 2013.

[6] C. Taubitz, M. Schütze, and M. Köntopp, "Towards a kinetic model of potential-induced shunting," in *Proceedings of the 27th European Photovoltaic Solar Energy Conference*, pp. 3172–3176, Frankfurt, Germany, September 2012.

[7] M. Schütze, M. Junghänel, M. B. Koentopp et al., "Laboratory study of potential induced degradation of silicon photovoltaic modules," in *Proceedings of the 37th IEEE Photovoltaic Specialists Conference (PVSC '11)*, pp. 821–826, IEEE, Seattle, Wash, USA, June 2011.

[8] K. Mishina, A. Ogishi, K. Ueno et al., "Investigation on antireflection coating for high resistance to potential-induced degradation," *Japanese Journal of Applied Physics*, vol. 53, no. 3, 2014.

[9] P. Hacke, K. Terwilliger, R. Smith et al., "System voltage potential-induced degradation mechanisms in PV modules and methods for test," in *Proceedings of the 37th IEEE Photovoltaic Specialists Conference (PVSC '11)*, pp. 000814–000820, Seattle, Wash, USA, June 2011.

[10] H. Nagel, P. Saint-Cast, M. Glatthaar, and S. Glunz, "Inline processes for the stabilization of *p*-type crystalline Si solar cells against potential-induced degradation," in *Proceedings of the 29th European PV Solar Energy Conference and Exhibition*, Amsterdam, The Netherlands, September 2014.

[11] M. Wilson, A. Savthouck, J. D'Amico et al., "Importance of defect photoionization in silicon-rich SiNx dielectrics for high PID resistance," in *Proceedings of the 39th IEEE Photovoltaic Specialists Conference (PVSC '13)*, pp. 218–222, IEEE, Tampa, Fla, USA, June 2013.

[12] M. Wilson, A. Savtchouk, P. Edelman, D. Marinskiy, and J. Lagowski, "Drift characteristics of mobile ions in SiNx films and solar cells," *Solar Energy Materials and Solar Cells*, vol. 142, pp. 102–106, 2015.

[13] S. Goranti and G. TamizhMani, "Potential induced degradation (PID) study on accelerated stress tested PV modules," in *Proceedings of the 38th IEEE Photovoltaic Specialists Conference (PVSC '12)*, pp. 2438–2441, IEEE, Austin, Tex, USA, June 2012.

[14] V. Naumann, D. Lausch, S. Großer et al., "Microstructural analysis of crystal defects leading to potential-induced degradation (PID) of Si solar cells," *Energy Procedia*, vol. 33, pp. 76–83, 2013.

[15] D. Lausch, V. Naumann, O. Breitenstein et al., "Potential-induced degradation (PID): introduction of a novel test approach and explanation of increased depletion region recombination," *IEEE Journal of Photovoltaics*, vol. 4, no. 3, pp. 834–840, 2014.

Hindawi Publishing Corporation
International Journal of Photoenergy
Volume 2015, Article ID 191603, 7 pages
http://dx.doi.org/10.1155/2015/191603

*Research Article*

# Experimental Investigation of the Effects of Partial Shading on Photovoltaic Cells' Electrical Parameters

**W. B. Xiao,[1,2] F. Y. Hu,[1,2] H. M. Zhang,[1,2] and H. M. Wu[1,2]**

[1] *Jiangxi Engineering Laboratory for Optoelectronics Testing Technology, Nanchang Hangkong University, Nanchang 330063, China*
[2] *Key Lab of Non Destructive Test (Ministry of Education), Nanchang Hangkong University, Nanchang 330063, China*

Correspondence should be addressed to W. B. Xiao; xiaowenbo1570@163.com

Received 5 September 2015; Revised 16 October 2015; Accepted 18 October 2015

Academic Editor: Clito Afonso



The short-circuit current ($I_{sc}$), the open-circuit voltage ($V_{oc}$), and the maximum power point ($V_{MPP}$, $I_{MPP}$) of monocrystalline and multicrystalline silicon solar cells under three kinds of partial shading patterns have been investigated experimentally. The partial shades are, respectively, the nine shelter locations by 1 cm × 1 cm black card, the six shelter locations by 2 cm × 1 cm black card, and the center shelters with isosceles triangle, circle, square, and two rectangles black cards whose areas are 2 $cm^2$. Firstly, the results show that the partial shading causes disproportional high losses on those parameters of both cells but will have a minimal effect on $V_{oc}$. Secondly, it is found that those parameters of the monocrystalline cell are less dependent on the shading than that of the multicrystalline cell. Thirdly, it is noted that $I_{sc}$ and $I_{MPP}$ of both cells will be decreasing dramatically as a rectangular black shading card with a long side parallel to cell's finger, compared with that normal to cell's finger. Finally, it can be seen that the effects of shading on the electrical parameters of both cells will be suppressed when the border lines of shading match the size of the shaded cell.

## 1. Introduction

Photovoltaic (PV) power is now becoming an important energy source. Not only is PV power environmentally friendly but also it has been becoming economically competitive with conventional fuels [1, 2]. However, PV energy production is easily influenced by the shadow of natural and human made objects [3–5]. The shaded cells absorb electric power generated by the unshaded cells, causing hot spots that can irreversibly damage PV cells. Therefore, the output performances of PV cells under partial shading conditions have been drawing increasing attention [6–11]. Over the years, the theoretical researches are mainly based on the single-diode model [12–15] and the double-diode model [16–18]. However, it is obvious that those theoretical models do not always fit to complex and changeable shading environments. In addition, several researchers have adopted an experimental approach to study the characteristics of PV cells under partial shading conditions. The behaviors of the solar cell electrical parameters have been compared with the central and edge shading [19, 20]. It was found that edge shading is a problem occurring in PV concentrator systems. The effects of shading percentage on electrical parameters of solar cells have been analyzed [21, 22]. The results showed that the generated current is decreasing as the shading profile is increasing. However, none of the above researches clarifies the effects of shading shape on cell's performances. Furthermore, there are also lacks of detailed comparative studies of different kinds of solar cells under same shading condition. As a result, the nonlinear characteristics of electrical parameters of PV cells under partial shading still remain elusive.

In this paper, the electrical parameters (the short-circuit current ($I_{sc}$), the open-circuit voltage ($V_{oc}$), and the maximum power point ($V_{MPP}$, $I_{MPP}$)) of monocrystalline and multicrystalline silicon solar cells under three kinds of partial shading patterns have been investigated experimentally. The results firstly show that the partial shading causes disproportional high losses on electrical parameters of monocrystalline and multicrystalline cells. But the shading will have a minimal effect on the open-circuit voltage of both cells. Secondly, it is found that the electrical parameters of the monocrystalline cell are less dependent on the shading than those parameters

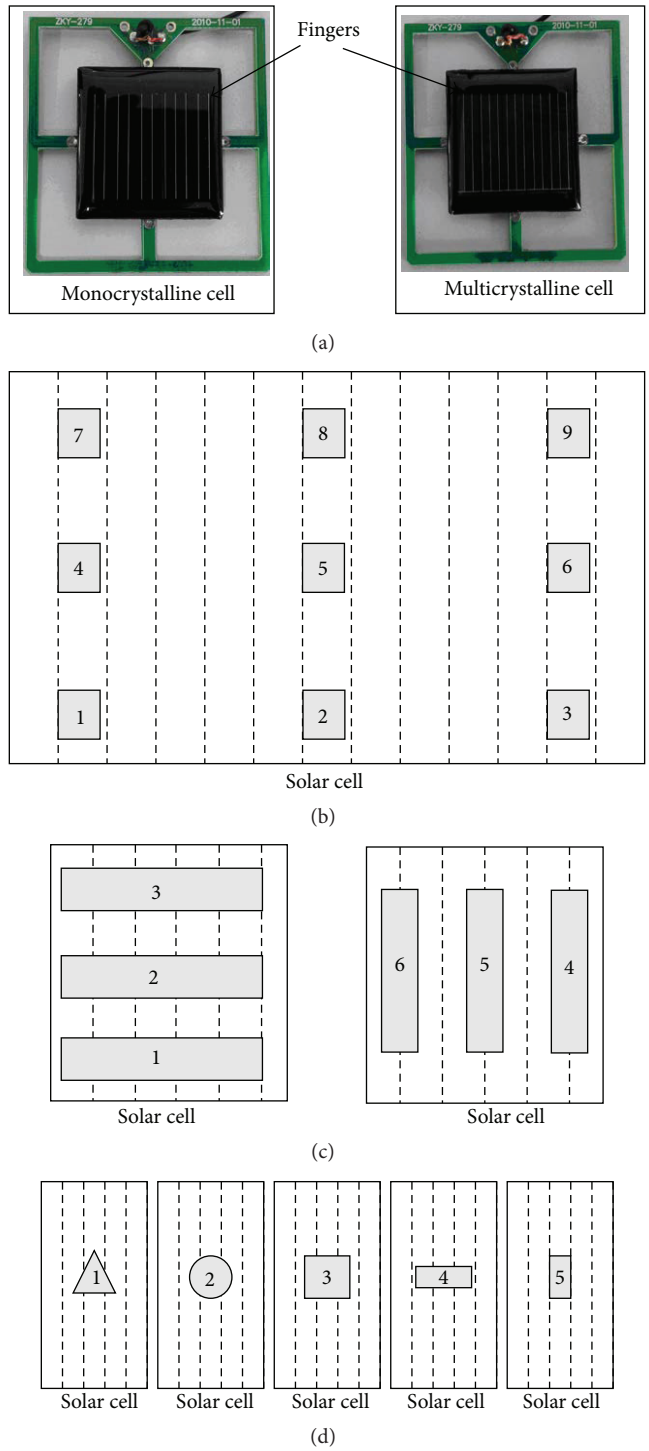


Figure 1: Experimental samples (a), the nine shelter locations by using 1 cm × 1 cm black square card (b), the six shelter locations by using 2 cm × 1 cm black rectangle card (c), and the center shelters with isosceles triangle, circle, square, and two rectangles black cards whose areas are 2 $cm^2$ (d). The dashed lines are the cell's fingers (not to scale).

of multicrystalline cell. Thirdly, it is noted that the short-circuit current and current at maximum power point of both cells will be decreasing dramatically as a rectangular black shading card with a long side parallel to cell's finger, compared with that normal to cell's finger. Finally, it can be seen that the effect of shading on the electrical parameters of both cells will be significantly suppressed when the border lines of shading match the shaded cell.

## 2. Experimental Samples, Setup, and Shading Patterns

The experimental samples are 2.8 cm × 2.5 cm monocrystalline and multicrystalline silicon solar cells manufactured by QS Solar Company (Figure 1(a)). The distance between fingers of monocrystalline and multicrystalline cells is about 0.25 cm. The PV testing system (number SAC- III + G

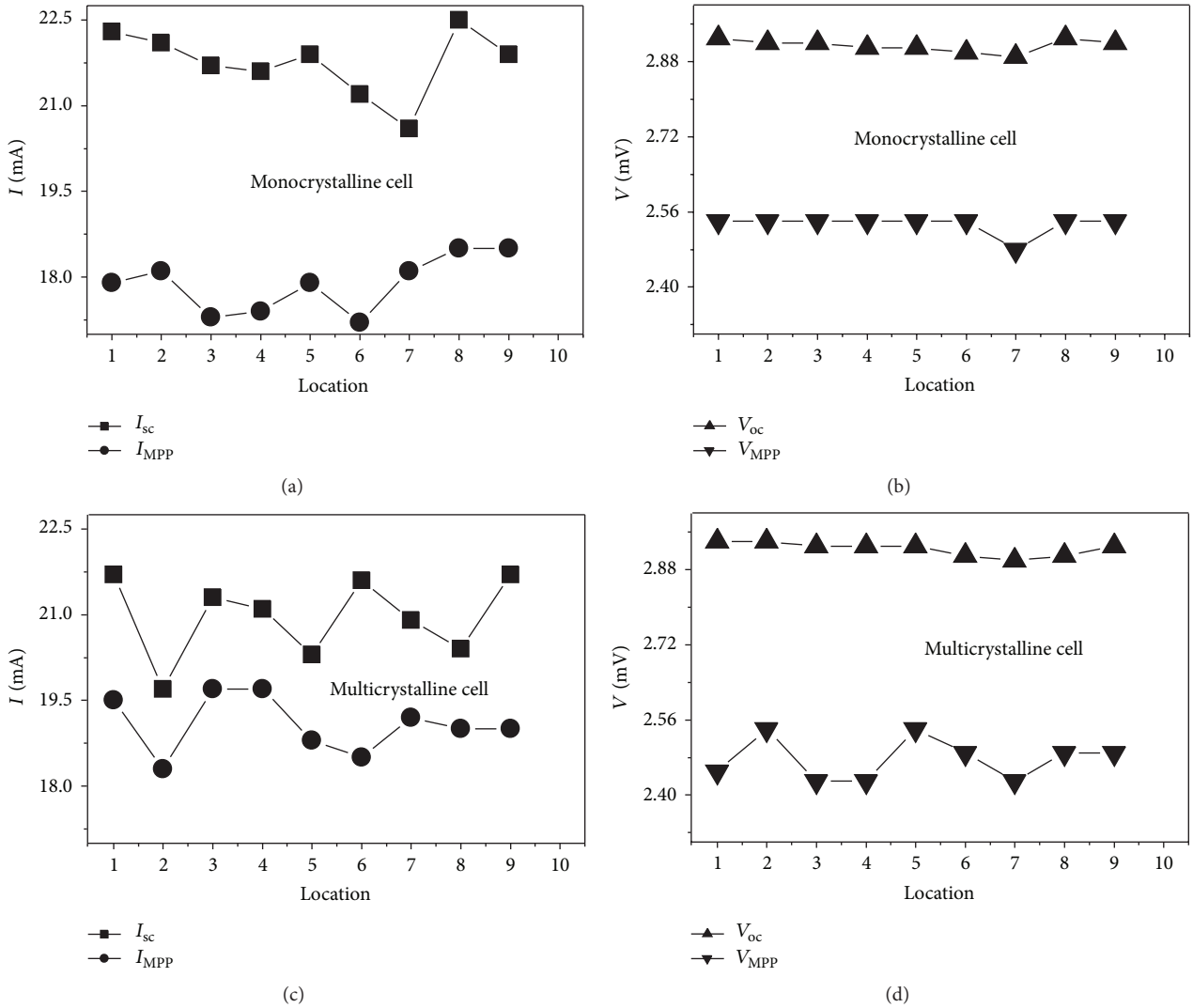


FIGURE 2: $I_{sc}$, $I_{MPP}$, $V_{oc}$, and $V_{MPP}$ of monocrystalline ((a) and (b)) and multicrystalline ((c) and (d)) silicon solar cells against nine square shelter locations.

made by Chengdu ZKY Instrument Co. Ltd.) is used for data acquisition. The testing system mainly includes a solar simulator, an electric signal reading device, and temperature control equipment, which are enclosed in a dark box. The simulated sunlight is achieved by Xenon light source. The beam impinges perpendicularly on the cell. The cell is placed in a temperature control room wherein temperature can be controlled by temperature control equipment, a semiconductor refrigeration device. The photoelectric signal of cell is recorded by the electric signal reading device. All the experiments were done at a temperature of 25°C and a light intensity of 1000 W/m$^2$. In the above condition, $I_{sc}$, $V_{oc}$, $I_{MPP}$, and $V_{MPP}$ of unshaded monocrystalline (multicrystalline) cell are 30.5 (30.1) mA, 3.02 (2.99) mV, 27.6 (29.3) mA, and 2.49 (2.48) mV.

In order to study the effects of shading on solar cell's performances, three kinds of partial shading patterns are designed as shown in Figures 1(b), 1(c), and 1(d). Those configurations are not scaled in relation to cell dimensions, which purpose is to mark all the shading parts in a schematic diagram of a solar cell. The partial shades are, respectively, the nine shelter locations by 1 cm × 1 cm black card, the six shelter locations by 2 cm × 1 cm black card, and the center shelters with isosceles triangle, circle, square, and two rectangles black cards whose areas are 2 cm$^2$. In the real experiment, the numbers of measurements are, respectively, nine for the square shelter configuration, six for the rectangle shelter configuration, and five for the center shelter configuration.

## 3. Results and Discussion

*3.1. Nine Square Shelter Locations.* In Figure 2, $I_{sc}$, $I_{MPP}$, $V_{oc}$, and $V_{MPP}$ of monocrystalline and multicrystalline cells are measured against nine square shelter locations. Firstly, it can be seen that $I_{sc}$, $I_{MPP}$, $V_{oc}$, and $V_{MPP}$ of both cells are obviously less than those of the unshaded cells. The reason is that the

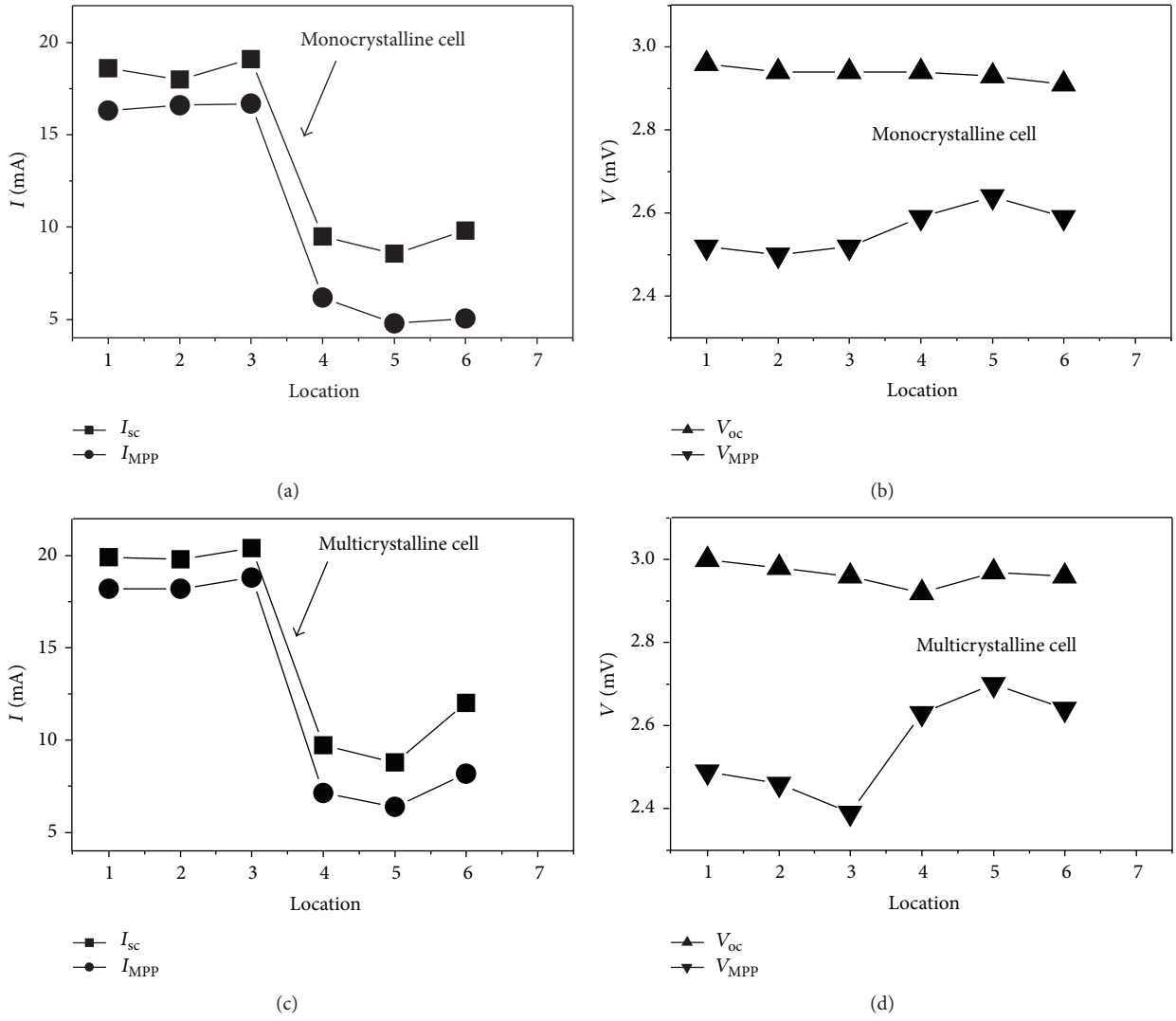


FIGURE 3: $I_{sc}$, $I_{MPP}$, $V_{oc}$, and $V_{MPP}$ of monocrystalline ((a) and (b)) and multicrystalline ((c) and (d)) silicon solar cells against six rectangle shelter locations.

light-receiving area of the cell is reduced. The average $I_{sc}$ of monocrystalline and multicrystalline cells under nine square shelter locations are about 21.75556 mA and 20.96667 mA. In fact, PV cell can be divided into a number of subcells by the cell's fingers. In other words, cell can be regarded as subcells in series. The $I_{sc}$ of unshaded monocrystalline and multicrystalline cells are 30.5 mA and 30.1 mA. Namely, the $I_{sc}$ of each subcell of monocrystalline and multicrystalline cells are about 30.5 mA and 30.1 mA. When the cell is sheltered by using 1 cm × 1 cm black square card, the light-receiving area of each sub-cell is 0.45 $cm^2$ but not 0.7 $cm^2$. According to previous research work [21, 22], it is known that the $I_{sc}$ are approximately proportional to the light-receiving area. As a result, the short-circuit current under shaded condition should be equal to 19.6 mA and 19.3 mA for the monocrystalline and multicrystalline cells, which are very close to the above experimental results. Therefore, the above conclusion is correct. Secondly, it is observed that those parameters vary with the shading positions. It is due to the fact that the devices themselves owned uniform defects [23]. Thirdly, it is noted that the standard deviations of $I_{sc}$, $I_{MPP}$, $V_{oc}$, and $V_{MPP}$ of monocrystalline (multicrystalline) cell are, respectively, 0.579032 (0.705337) mA, 0.486769 (0.499444) mA, 0.013333 (0.01424) mV, and 0.02 (0.044441) mV. Those show that shading locations have a minimal effect on $V_{oc}$, which also can be seen in Figure 2. The reason is that $V_{oc}$ is mainly determined by the band gap of the solar cell material, the device temperature, and the incident light intensity [24, 25]. In addition, it is found that the shading has more influence on the electrical parameters of the monocrystalline cell than that of the multicrystalline cell from the standard deviation. The differences can be regarded as the multicrystalline cell has much more nonuniformity defects.

*3.2. Six Rectangle Shelter Locations.* In Figure 3, $I_{sc}$, $I_{MPP}$, $V_{oc}$, and $V_{MPP}$ of monocrystalline and multicrystalline cells

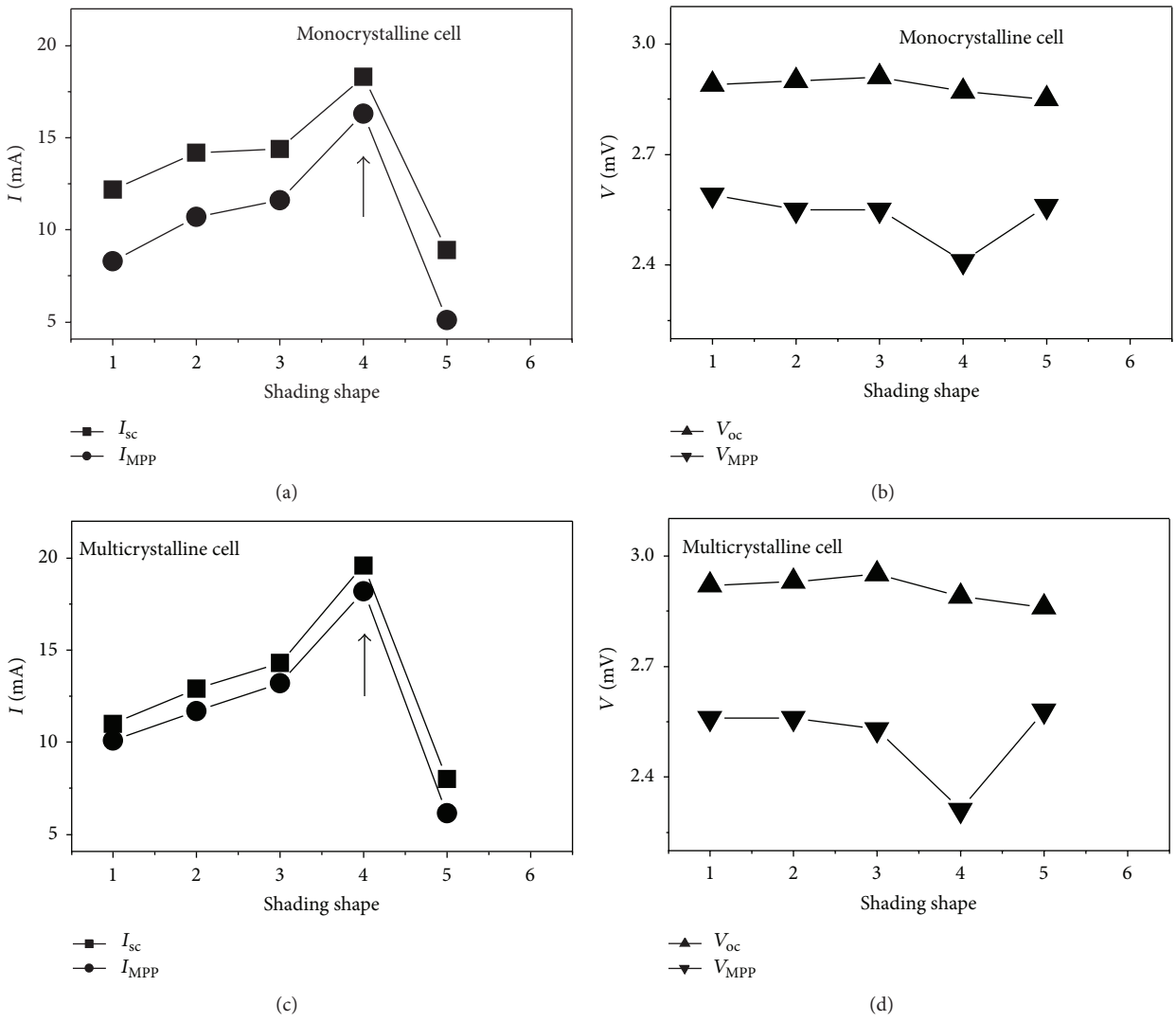


FIGURE 4: $I_{sc}$, $I_{MPP}$, $V_{oc}$, and $V_{MPP}$ of monocrystalline ((a) and (b)) and multicrystalline ((c) and (d)) silicon solar cells against center shelters with isosceles triangle, circle, square, and two rectangles black cards.

are measured against six rectangle shelter locations. It can also be seen that $I_{sc}$, $I_{MPP}$, $V_{oc}$, and $V_{MPP}$ of both cells are changing with the shading positions. The standard deviations of $I_{sc}$, $I_{MPP}$, $V_{oc}$, and $V_{MPP}$ of monocrystalline (multicrystalline) cell are, respectively, 5.105865 (5.505853) mA, 6.1555 (6.146448) mA, 0.01633 (0.026646) mV, and 0.054772 (0.121888) mV, which also show that the shading has a minimal effect on $V_{oc}$ for both cells and on electrical parameters of monocrystalline cell. Those experimental results give a direct proof verifying the above conclusions. What should be noticed is that there are mutation process of $I_{sc}$ and $I_{MPP}$ for both cells between the third and fourth locations as arrows shown in the Figures 3(a) and 3(c). This may be the differences between the long side of rectangular shading card normal to cell's finger and the long side of rectangular shading card parallel to cell's finger. When PV cell is covered by a black rectangular shading card with a long side normal to cell's finger, only 1 cm length is sheltered along the longitudinal direction for each subcell. The results of this shading mode are similar to the above case. So the short-circuit current under shaded condition should be equal to 19.6 mA and 19.3 mA for the monocrystalline and multicrystalline cells, which are also very close to the above experimental data. When PV cell is covered by a black rectangular shading card with a long side parallel to cell's finger, the 2 cm length is sheltered along the longitudinal direction for each subcell. Therefore, the short-circuit current under shaded condition should be equal to 8.7 mA and 8.6 mA for the monocrystalline and multicrystalline cells, which are also roughly consistent with experimental observation. As a result, the short-circuit current of cell is determined by the weakest subcell when the cell is partially shaded.

*3.3. Center Shelters with Different Shapes.* In Figure 4, $I_{sc}$, $I_{MPP}$, $V_{oc}$, and $V_{MPP}$ of monocrystalline ((a) and (b)) and multicrystalline ((c) and (d)) silicon solar cells are measured

against isosceles triangle, circle, square, and two rectangles black cards whose areas are 2 $cm^2$. As it can be seen, the impacts of shading shapes on the electrical parameters of both cells are different. The standard deviations of $I_{sc}$, $I_{MPP}$, $V_{oc}$, and $V_{MPP}$ of monocrystalline (multicrystalline) cell are, respectively, 3.432929 (4.304997) mA, 4.145301 (4.411136) mA, 0.024083 (0.035355) mV, and 0.070143 (0.112116) mV. The above conclusion can also be drawn from those results. It is particularly noticed that $I_{sc}$ and $I_{MPP}$ of both cells under square shading are maximum values for isosceles triangle, circle, and square shading, as shown in Figures 4(a) and 4(c). This can be explained by the fact that the border lines of square shading match the shaded cell's size. In addition, it is found that $I_{sc}$ and $I_{MPP}$ of both cells under a rectangular shading card with a long side parallel to cell's finger are minimum values. It is because of the combined effect of the above two factors. One factor is that a greater portion of each subcell is shaded in the above condition. Another is that the border lines of rectangle shading do not match the shaded cell's size. Therefore, $I_{sc}$ and $I_{MPP}$ of both cells under rectangles black card with a long side normal to cell's finger present a peak, as arrows shown in Figures 4(a) and 4(c).

## 4. Conclusion

In order to explain clearly the shading effects on the solar cell's performances, experiments under three kinds of partial shading patterns were carried out. Firstly, the results show that the partial shading causes disproportional high losses on electrical parameters of monocrystalline and multicrystalline cells but will have a minimal effect on $V_{oc}$ for both cells. The reason is that $V_{oc}$ is mainly determined by the band gap of the solar cell material, the device temperature, and the incident light intensity. Secondly, it is found that electrical parameters of the monocrystalline cell are less dependent on the shading than that of multicrystalline cell. The differences can be regarded as the multicrystalline cell has much more nonuniformity defects. Thirdly, it is noted that the $I_{sc}$ and $I_{MPP}$ of both cells will be decreasing dramatically as a rectangular black shading card with a long side parallel to cell's finger, compared with that normal to cell's finger. The reason of this behavior is due to the subcell in series being much more sheltered while card's long side parallel to cell's finger. Finally, it can be seen that the effects of shading on the electrical parameters of both cells will be suppressed when the border lines of shading match the size of the shaded cell.

## Conflict of Interests

The authors declare that there is no conflict of interests regarding the publication of this paper.

## Acknowledgments

This work was in part supported by National Natural Science Foundation of China under Grants nos. 11264031 and 11304145, Jiangxi Province Science Major Program for Youths under Grant no. 20143ACB21011, and the Invention Patent Foundation of Jiangxi province under Grant no. 20143BBM26116.

## References

[1] B. Sinha, "Trends in global solar photovoltaic research: silicon versus non-silicon materials," *Current Science*, vol. 100, no. 5, pp. 654–660, 2011.

[2] J.-T. Liu, X.-H. Deng, W. Yang, and J. Li, "Perfect light trapping in nanoscale thickness semiconductor films with a resonant back reflector and spectrum-splitting structures," *Physical Chemistry Chemical Physics*, vol. 17, no. 5, pp. 3303–3308, 2015.

[3] B. Parida, S. Iniyan, and R. Goic, "A review of solar photovoltaic technologies," *Renewable and Sustainable Energy Reviews*, vol. 15, no. 3, pp. 1625–1636, 2011.

[4] G. Makrides, B. Zinsser, M. Schubert, and G. E. Georghiou, "Energy yield prediction errors and uncertainties of different photovoltaic models," *Progress in Photovoltaics: Research and Applications*, vol. 21, no. 4, pp. 500–516, 2013.

[5] F. Lu, S. Y. Guo, T. M. Walsh, and A. G. Aberle, "Improved PV module performance under partial shading conditions," *Energy Procedia*, vol. 33, pp. 248–255, 2013.

[6] D. La Manna, V. Li Vigni, E. R. Sanseverino, V. Di Dio, and P. Romano, "Reconfigurable electrical interconnection strategies for photovoltaic arrays: a review," *Renewable and Sustainable Energy Reviews*, vol. 33, pp. 412–426, 2014.

[7] C. R. Sánchez Reinoso, D. H. Milone, and R. H. Buitrago, "Simulation of photovoltaic centrals with dynamic shading," *Applied Energy*, vol. 103, pp. 278–289, 2013.

[8] C. R. S. Reinoso, D. H. Milone, and R. H. Buitrago, "Efficiency study of different photovoltaic plant connection schemes under dynamic shading," *International Journal of Hydrogen Energy*, vol. 35, no. 11, pp. 5838–5843, 2010.

[9] H. Patel and V. Agarwal, "MATLAB-based modeling to study the effects of partial shading on PV array characteristics," *IEEE Transactions on Energy Conversion*, vol. 23, no. 1, pp. 302–310, 2008.

[10] M. C. Alonso-García, J. M. Ruiz, and F. Chenlo, "Experimental study of mismatch and shading effects in the I-V characteristic of a photovoltaic module," *Solar Energy Materials and Solar Cells*, vol. 90, no. 3, pp. 329–340, 2006.

[11] Y. Sun, S. Chen, L. Xie, R. Hong, and H. Shen, "Investigating the impact of shading effect on the characteristics of a large-scale grid-connected PV power plant in northwest china," *International Journal of Photoenergy*, vol. 2014, Article ID 763106, 9 pages, 2014.

[12] T. Ma, H. X. Yang, and L. Lu, "Development of a model to simulate the performance characteristics of crystalline silicon photovoltaic modules/strings/arrays," *Solar Energy*, vol. 100, pp. 31–41, 2014.

[13] Y.-J. Wang and P.-C. Hsu, "An investigation on partial shading of PV modules with different connection configurations of PV cells," *Energy*, vol. 36, no. 5, pp. 3069–3078, 2011.

[14] M. Seyedmahmoudian, S. Mekhilef, R. Rahmani, R. Yusof, and E. T. Renani, "Analytical modeling of partially shaded photovoltaic systems," *Energies*, vol. 6, no. 1, pp. 128–144, 2013.

[15] J. B. Bai, Y. Cao, Y. Z. Hao, Z. Zhang, S. Liu, and F. Cao, "Characteristic output of PV systems under partial shading or mismatch conditions," *Solar Energy*, vol. 112, pp. 41–54, 2015.

[16] S. Silvestre, A. Boronat, and A. Chouder, "Study of bypass diodes configuration on PV modules," *Applied Energy*, vol. 86, no. 9, pp. 1632–1640, 2009.

[17] K. Ishaque, Z. Salam, and Syafaruddin, "A comprehensive MATLAB Simulink PV system simulator with partial shading capability based on two-diode model," *Solar Energy*, vol. 85, no. 9, pp. 2217–2227, 2011.

[18] K. Ishaque, Z. Salam, H. Taheri, and Syafaruddin, "Modeling and simulation of photovoltaic (PV) system during partial shading based on a two-diode model," *Simulation Modelling Practice and Theory*, vol. 19, no. 7, pp. 1613–1626, 2011.

[19] A. E. Ghitas and M. Sabry, "A study of the effect of shadowing location and area on the Si solar cell electrical parameters," *Vacuum*, vol. 81, no. 4, pp. 475–478, 2006.

[20] M. Sabry and A. E. Ghitas, "Effect of edge shading on the performance of silicon solar cell," *Vacuum*, vol. 80, no. 5, pp. 444–450, 2006.

[21] V. Quaschning and R. Hanitsch, "Influence of shading on electrical parameters of solar cells," in *Proceedings of the 25th IEEE Photovoltaic Specialists Conference*, pp. 1287–1290, Washington, DC, USA, May 1996.

[22] A. Dolara, G. C. Lazaroiu, S. Leva, and G. Manzolini, "Experimental investigation of partial shading scenarios on PV (photovoltaic) modules," *Energy*, vol. 55, pp. 466–475, 2013.

[23] Z. T. Zhai, *The output characteristic predicting of PV array in arbitrary condition [Ph.D. thesis]*, University of Science and Technology of China, Hefei, China, 2008.

[24] K. Ding, J. W. Zhang, X. G. Bian, and J. W. Xu, "Simplified model for photovoltaic modules based on improved translation equations," *Solar Energy*, vol. 101, pp. 40–52, 2014.

[25] A. N. Celik and N. Acikgoz, "Modelling and experimental verification of the operating current of mono-crystalline photovoltaic modules using four- and five-parameter models," *Applied Energy*, vol. 84, no. 1, pp. 1–15, 2007.

Hindawi Publishing Corporation
International Journal of Photoenergy
Volume 2015, Article ID 308541, 9 pages
http://dx.doi.org/10.1155/2015/308541

*Research Article*

# Technique for Outdoor Test on Concentrating Photovoltaic Cells

**Paola Sansoni,[1] Daniela Fontani,[1] Franco Francini,[1] David Jafrancesco,[1] Giacomo Pierucci,[2] and Maurizio De Lucia[2]**

[1]*CNR-INO Istituto Nazionale di Ottica, Largo E. Fermi 6, 50125 Firenze, Italy*
[2]*Dipartimento di Ingegneria Industriale, Università di Firenze, Via di S. Marta 3, 50139 Firenze, Italy*

Correspondence should be addressed to Paola Sansoni; paola.sansoni@ino.it

Received 2 September 2015; Accepted 4 October 2015

Academic Editor: Xudong Zhao



Outdoor experimentation of solar cells is essential to maximize their performance and to assess utilization requirements and limits. More generally tests with direct exposure to the sun are useful to understand the behavior of components and new materials for solar applications in real working conditions. Insolation and ambient factors are uncontrollable but can be monitored to know the environmental situation of the solar exposure experiment. A parallel characterization of the photocells can be performed in laboratory under controllable and reproducible conditions. A methodology to execute solar exposure tests is proposed and practically applied on photovoltaic cells for a solar cogeneration system. The cells are measured with concentrated solar light obtained utilizing a large Fresnel lens mounted on a sun tracker. Outdoor measurements monitor the effects of the exposure of two multijunction photovoltaic cells to focused sunlight. The main result is the continuous acquisition of the $V$-$I$ (voltage-current) curve for the cells in different conditions of solar concentration and temperature of exercise to assess their behavior. The research investigates electrical power extracted, efficiency, temperatures reached, and possible damages of the photovoltaic cell.

## 1. Introduction

To exploit the recent improvements in the development of photovoltaic (PV) cells and new materials for solar applications, it is important to test them both in laboratory and with direct exposure to the sun. The optical characterization of PV cells, optical components, and material samples can be performed using solar simulators [1–6]. For measurements on photovoltaic cells [7] the solar simulator usually needs to be suitably modified from a commercial product in order to reduce the output beam size [8, 9]. The solar divergence is hardly reproduced by solar simulators, while measurements with solar trackers [10] consent to replicate the real operative conditions. Alternatively, laboratory tests can be performed using a solar divergence collimator [11] that exactly reproduces the sun's divergence, thus permitting a precise evaluation of optical parameters and optical behavior of solar components. Analogously solar rays, concentrated over a sample, allow to study the optical properties and performance of PV cells or other components applicable to solar installations.

The laboratory test of PV cells makes extensive use of simulators having the characteristic of reproducing the intensity and spectrum of natural sunlight [12–14]. When the cells to be tested are of concentration type, these devices must provide an adequate amount of light, even hundreds of times greater than the natural one. The technology used in these devices employs very powerful lamps appropriately filtered to reproduce the solar spectrum and optical systems capable of concentrating this light on a target of few squared centimeters [3, 15, 16]. The cost of these solar simulators, however, is very high and the large dimensions of the device hardly permit its allocation on a normal laboratory table. In addition, if the light source used has a power of several hundred kW also a system for disposal of the ozone gas produced by the lamp must be arranged. Alternatively, for concentrated photovoltaics, pulsed systems can be employed: they reach considerable powers but only for short time intervals [17–19].

The test methodology proposed in this paper uses solar light instead of a lamp and a Fresnel lens to concentrate light on the PV cell. The device is equipped with a solar tracking

system, which ensures the continuity of the measurement, and with accessories that allow to stabilize the temperature of the cell under test. It is extremely useful for their practical application to experiment with solar photocells exposed to concentrated sunlight, analyzing their behavior.

An experimentation on two multijunction photovoltaic cells is performed for their application in a cogeneration system for solar energy exploitation. This system includes a linear parabolic concentrator, which focuses the light over row of PV cells, located on a side of a tube with rectangular section. The photocells are squared with dimensions $10 \times 10$ mm. The working principle of this cogeneration system consists in furnishing both electric energy and hot water: the energy is obtained through the PV cells, which are cooled by the water flowing on the tube; the water is heated using the same fluid.

The system is optically designed using ray-tracing simulations carried out with the calculation program *Zemax-EE* by Radiant Zemax. The working conditions of the photocell (solar concentration, incident power density, focused light distribution, image dimension, etc.) are estimated by simulating the concentered light distribution in the image plane. The measurements parameters for the outdoor tests are then chosen on the basis of these simulations of the cogeneration system in order to reproduce the actual operative conditions. A preliminary characterization of the cells is carried out in laboratory, in a controllable and reproducible situation, to serve as reference for the field measurements. During the outdoor experimentation, in direct exposure to the sun, measurement conditions are monitored with controls similar to those made in laboratory. This control of the parameters during the actual operation of the solar device permits to assess the working temperature of the cells and possible damages of the system components.

Hence the main advantage of solar outdoor experimentation is to work in the real operating conditions of a solar installation. Insolation (solar irradiance) and ambient factors are not controllable but the outdoor test conditions can be surveyed and recorded by measuring proper physical quantities with appropriate instruments. Another benefit of using direct sunlight is to avoid the employment of artificial sources, lamps, or solar simulators, which can only try to reproduce spectral distribution, divergence and intensity of sunlight. Moreover the proposed device (essentially composed of a sun tracker) permits to test the photocell with its proper collection system (with primary collector and possible secondary optics).

## 2. Device for Tests with Concentrated Sunlight

The optical experimentation consisted in exposing the samples to solar light concentrated by a large Fresnel lens. The lens has a diameter of 470 mm and a focal ratio of about $F/1$ and is installed on the solar tracking system shown in Figure 1.

The device in Figure 1 is a two-axis solar tracker, an equatorial mounting equipped with stepper motors; it was developed entirely within the Solar Collectors Laboratory of the National Institute of Optics [10]. The blue supporting frame is equipped with a series of pins to allow the rotation of the central perforated grid, which is constantly oriented

Figure 1: The sun tracker employed in the optical tests.

perpendicularly to the direction of solar rays. The lens is constrained to the grid by means of small columns, which hold it fixed at a certain distance and parallel to the grid plane. The sample is mounted on the same grid using a small support, with which it is possible to adjust the power density incident on the sample simply by varying the distance from the focus of the lens: by approaching the sample to the focus $F$ the power density increases, while increasing the distance from $F$ the power density is reduced. It has been verified that with this Fresnel lens it is possible to achieve power density levels of about 90 kW/m$^2$ in the proximity of the focal point.

The tracking technique utilizes a sun pointer [10], whose scheme is based on the principle of the pinhole camera: in fact it is a pinhole camera without lenses equipped with a four-quadrant photodiode. Sunlight enters the pinhole and illuminates the sensor; a software processes the signal arriving from each quadrant. The pointer is perfectly aligned with the solar rays' direction when the four signals are equal. The imbalance between the signals determines the misalignment of the center of gravity of the solar image with respect to the sensor. The same software provides to actuate the motors of the tracker until the solar image is equally distributed between the four quadrants, meaning that the tracker is aligned with the sun.

## 3. Laboratory Determination of the Lens-Cell Distance

To ensure proper operation, as well as to prevent damage of thermal type, a photovoltaic cell must be uniformly illuminated. The Fresnel lens used, visible in Figure 1, produces a spot with diameter of a few millimeters on the focal plane. Thus placing the cell in the vicinity of the lens focus would generate on the sensitive surface a density gradient of sufficient power to damage the photocell itself. Some preliminary measurements are performed in laboratory with the purpose of determining the suitable positions for the cell in order to have an acceptable uniformity of illumination.

A schematic view of the laboratory setup used is shown in Figure 2: it is a solar divergence collimator [11]. The optical

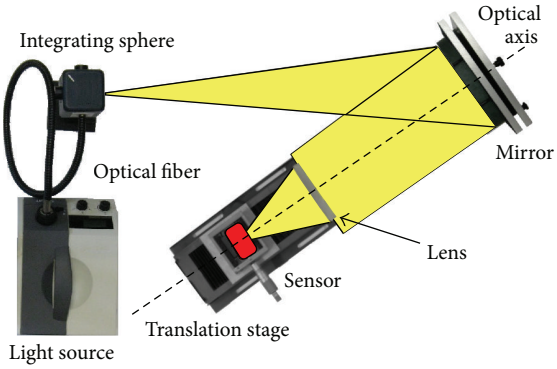


Figure 2: Scheme of the setup for the tests in laboratory.

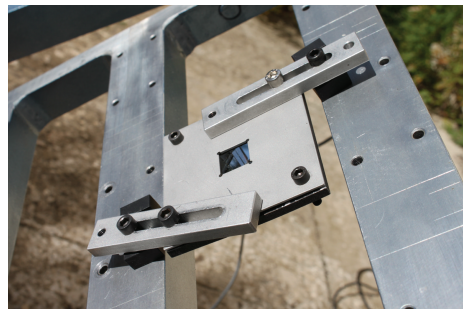

Figure 3: Optical system to protect the PV cell.

system, constituted by source system, integrating sphere and mirror, produces a luminous beam with solar divergence of about 240 mm in diameter. The beam illuminates the lens and is concentrated on the focal plane. The sensor used for the measurements is positioned on the optical axis after the lens. The sensor is mounted on a linear micrometric shifter with excursion along the optical axis, in order to be able to vary the distance between sensor and lens. Since the diameter of the beam incident on the lens is about 250 mm (widened due to the divergence) and the lens diameter is 470 mm, the laboratory setup of Figure 2 can illuminate only a portion of the lens. The measurements are then carried out by separately examining different areas of the large Fresnel lens.

The first optical analysis is devoted to determine the focal length of the Fresnel lens [20–22]. The focal distance can be defined and consequently measured in various ways; in this case it is assessed with the purpose of using this value in the outdoor tests to place the PV cell. The focal distance is measured from the lens in the point where the lens concentrated the maximum of power density. A first estimate is visually obtained using an opaque target. A more precise measurement is realized by placing a photodiode on the micrometric shifter; the focal plane is identified as the plane where the photodiode detects the maximum signal. The focal length so determined is equal to $460 \pm 3$ mm: it is almost equal to the Fresnel lens diameter, thus confirming the focal ratio near $F/1$ [22].

In order to evaluate the uniformity of illumination a CMOS camera is mounted on a shifter. The camera sensor has dimensions $7.74 \times 10.51$ mm, so the size is similar to that of the PV cell under examination, which is $10 \times 10$ mm. The CMOS camera acquired images of the central portion of the beam at different distances from the focal point. These images are used to qualitatively evaluate the suitable distance at which the area of the cell results illuminated with sufficient uniformity. In general, when the image plane is displaced from the focal plane the luminous spot results enlarged; it becomes more uniformly illuminated and the solar concentration decreases. Referring to the distance $d_S$ between cell plane and focal plane, the cell position for the outdoor tests is chosen depending on the solar concentration obtained: for $d_S = 30$ mm there is an optimal concentration, while for $d_S = 40$ mm the concentration is acceptable. When $d_S = 30$ mm an area of $10 \times 10$ mm results fully illuminated, but for $d_S = 40$ mm the image shows a good uniformity over the entire cell area.

It should be noted that in the experiments in laboratory only a side portion of the lens is illuminated, while in the field tests the lens is completely illuminated. Therefore in the outdoor tests both a greater width of the spot and a higher quality of the image are expected; so the overall conditions appear to be a better situation than that obtained in laboratory at equal distance between lens and cell. From the laboratory measurements, the suitable distances $d_S$ for placing the sample are 30 and 40 mm. In the field tests it is more practical to consider the distance $D$ between Fresnel lens and PV cell. Since the focal length of the Fresnel lens is 460 mm, the related values are $D = 430$ mm for $d_S = 30$ mm and $D = 420$ mm for $d_S = 40$ mm.

## 4. Setup for the Outdoor Tests and Exposure Procedure

The exposure of the cells is carried out utilizing the sun tracker described in Section 2: the tracking system used in the tests is obtained introducing two modifications on the device of Figure 1. These changes consist in installing two accessories: a Peltier module and a pyrheliometer. The Peltier module is a thermoelectric cooler that uses the Peltier effect. This module, which is necessary for the cooling of the cell, is installed on the perforated grid, and the cell is applied on the module itself. The second modification concerns the installation of a pyrheliometer for measuring the direct component of the solar radiation during the exposure. The pyrheliometer is an instrument that measures the direct beam solar irradiance.

At the considered lens-cell distances (420 and 430 mm) the size of the illuminated area is much larger than that of the cell; hence there is the risk that sensitive parts of the board are hit by concentrated light with high power density. To avoid problems the protection system illustrated in Figure 3 is realized and mounted: it includes a reflective truncated pyramid surrounded by a squared screen. The truncated pyramid is composed only of reflection elements, which are four mirrors with trapezoidal shape. The smaller squared base of the truncated pyramid has the dimensions of the cell. Therefore the reflective truncated pyramid is mounted on the grid of the tracker with the bottom aperture placed exactly

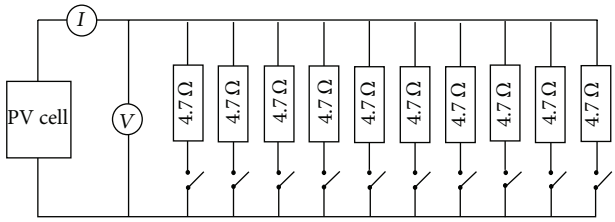


Figure 4: Electrical scheme of the variable load applied to the cell to determine the $V$-$I$ curve.

over the cell, so as to limit the illumination area to the cell itself.

The cell temperature during solar exposure is controlled by the Peltier module. The actual temperature is recorded, for the whole test duration, acquiring the values given by a thermocouple. To perform the measurement, the probe is applied on the lateral edge of the sample, and the cell is positioned so that the edge of the illuminated area is as close as possible to the probe. This solution is chosen because it is impracticable to apply the probe directly on the illuminated area, as this would involve the direct exposure of the probe to the focused light, greatly influencing the measurement and probably damaging the probe itself. During most of the tests the temperature of the cell is kept at relatively low values compared to those of the expected working conditions (about 70–80°C). Only in one case it is increased for testing the operating of the cell and of the whole system at different temperatures.

The signal of the pyrheliometer is always acquired by a NI-DAQ card throughout the solar exposure. The measurement gives the value of solar irradiance $E_{\text{sun}}$ on the basis of the conversion factor provided by the manufacturer.

A variable resistive load is applied to the terminals of the PV cell; its circuit diagram is shown in Figure 4. The switches shown in the diagram are manually operated in sequence, inserting the resistors in parallel. In total there are ten resistors of identical value of $R = 4.7\,\Omega$. At each insertion the load value decreases according to $R/N$, where $N$ is the number of switches that are closed. The values of current ($I$) and voltage ($V$) across the cell are read with a pair of digital volt-amperometers.

The density of solar power incident on the sample is regulated by varying the distance between lens and grid, where reflective truncated pyramid, PV cell, and board are mounted. For the placement of the sample, the reference parameter is not the power density on the cell, but the lens-cell distance, since the main concern is to illuminate the active surface of the cell as uniformly as possible. The power density on the cell is then obtained through subsequent concentration measurements.

The optical tests are executed following a repeatable procedure in exposing the samples to solar concentrated light: the main steps of this exposure procedure are summarized below. Once the tracker is aligned with the sun, the lens-cell distance is defined based on the value of power density that one wishes to impinge on the cell. The power density can be checked with a calibrated radiometer Ophir Nova, moving the head along the optical axis. The value of power density is assumed constant for the whole duration of solar exposure. The sample is mounted at the selected distance and kept exposed to solar concentrated light for a few hours. During sample exposure, at regular intervals, $V$-$I$ curves characterizing the cell are acquired (by the volt-amperometers), while cell temperature (using the thermocouple) and solar irradiance (with the pyrheliometer) are continuously recorded.

## 5. Measurements of Solar Concentration

Concentration measurements are executed using a calibrated radiometer Ophir Nova. This measurement is performed for both lens-cell distances $D$ considered, 420 and 430 mm. It allows to determine the geometric factor $C$ of concentration of the Fresnel lens. The concentration factor [23] is defined as the ratio between the power density $E_{\text{cell}}$ incident on the cell, which is the light focused by the lens, and the power density $E_{1\text{sun}}$, where "1sun" refers to a measurement performed without concentration:

$$C = \frac{E_{\text{cell}}}{E_{1\text{sun}}}. \tag{1}$$

The measurement procedure employed is as follows. The radiometer measures the optical power $P_{1\text{sun}}$ incident on the sensor associated to 1 sun. The corresponding power density is obtained by dividing this value by the area $A_{\text{det}}$ of the detector:

$$E_{1\text{sun}} = \frac{P_{1\text{sun}}}{A_{\text{det}}}. \tag{2}$$

With the same instrument the optical power $P_{\text{cell}}$ is measured in correspondence with the cell, removing the support of the cell and replacing it with the sensor of the radiometer, keeping the rest of the setup unchanged. The power density on the cell $E_{\text{cell}}$ is obtained by dividing the optical power by the area $A_{\text{cell}}$ of the PV cell, equal to 100 mm$^2$:

$$E_{\text{cell}} = \frac{P_{\text{cell}}}{A_{\text{cell}}}. \tag{3}$$

For the latter measurement it is not binding to know the illuminated area of the detector; it is sufficient that it captures all of the light exiting from the bottom aperture of the reflective truncated pyramid. This aperture has in fact the same shape and size of the cell; therefore it can be assumed that all the light coming out from it illuminates the cell, if this is placed in contact with the bottom aperture of the truncated pyramid.

The factor $C$ is determined for both lens-cell distances considered. Knowing the concentration $C$, it is easy to calculate the power density $E_{\text{cell}}$ incident on the cell at the time of exposure based on the value of solar irradiance $E_{\text{sun}}$ obtained using the pyrheliometer:

$$E_{\text{cell}} = C \cdot E_{\text{sun}}. \tag{4}$$

## 6. Outdoor Tests and Results

The results of cell characterization are discussed and compared only for two exemplificative solar cells, to evidence

their different behavior and values. These two samples are tested exposing them to concentrated sunlight for a determined time interval. In order to obtain a characterization of each sample the $V$-$I$ (voltage-current) curves are acquired. For having a more complete information about the photocell behavior, the $V$-$I$ curves are measured in different conditions, varying exposure time, concentration, and cell temperature. The outdoor experimentation is carried out in condition of clear sky. The purpose of this analysis is to show the differences in behavior between two samples of the same type of multijunction PV cell, indicated as Cell_A and Cell_B.

This section presents the $V$-$I$ curves acquired in the various tests performed outdoor. To complete this optical characterization of the cells, some other significant data are acquired together with the values of voltage $V$ and current $I$. These parameters, characterizing the tests, are

(i) measurement time, with respect to the starting time ($t = 0$), in min: $t$;

(ii) power density incident on the cell in kW/m$^2$: $E_{\text{cell}}$;

(iii) optical power incident on the cell in W: $P_{\text{cell}} = E_{\text{cell}} \cdot A_{\text{cell}}$;

(iv) cell temperature in °C: $T_{\text{cell}}$;

(v) open-circuit voltage in Volt: $V_{\text{OC}}$;

(vi) maximum electrical power extracted in W: $P_{\text{out}}$.

All the detections are made using calibrated instruments in order to limit the uncertainty of the final result below 10%.

The cell is squared with side 10 mm; the area of the photocell $A_{\text{cell}}$ is 100 mm$^2$. The cell temperature is approximated to the temperature measured on the board by the thermocouple. The approximation is justified by the fact that the probe is positioned very close to the cell and the heat exchange in the space between the two is significant. The open-circuit voltage $V_{\text{OC}}$ is the voltage measured in the absence of external load. It corresponds to the maximum value of the voltage and is given by the intersection of the $V$-$I$ curve with the abscissa axis ($I = 0$).

Sections 6.1 and 6.2 separately present the results of the outdoor characterization for Cell_A and Cell_B, while Section 6.3 describes the results obtained varying the temperature of the cell. The $V$-$I$ plots represent the characterization of each cell at different values of incident power density ($E_{\text{cell}}$). The tables report, for each $V$-$I$ curve, some parameters measured during the characterization of the cell.

### 6.1. Results for Cell_A

*Test_1*. Specifications are as follows: lens-cell distance: 420 mm; exposure duration: 3 hours; sample: Cell_A.

*Test_2*. Specifications are as follows: lens-cell distance: 430 mm; exposure duration: 2 hours; sample: Cell_A.

### 6.2. Results for Cell_B

*Test_3*. Specifications are as follows: lens-cell distance: 420 mm; exposure duration: 3 hours and 30 min; sample: Cell_B.

*Test_4*. Specifications are as follows: lens-cell distance: 430 mm; exposure duration: 3 hours; sample: Cell_B.

As can happen in outdoor tests, the conditions of solar illumination have changed in the third hour of Test_4: this modification of input power is visible in column 4 of Table 4 and in Figure 8, corresponding to a lower $V$-$I$ curve.

The results reported in Sections 6.1 and 6.2 represent the characterization of two multijunction photovoltaic cells performed exposing them to concentrated sunlight. The tests considered exposure times $t$ up to 3.5 hours and lens-cell distances $D$ selected in order to have the required concentration of solar light. At $D = 430$ mm the $10 \times 10$ mm cell is entirely illuminated and the concentration $C$ is optimal (circa 150). For $D = 420$ mm the cell is fully and uniformly illuminated and $C$ is acceptable (about 100).

The principal characterization of the behavior of the optoelectronic component is illustrated by the $V$-$I$ curves: Figures 5 and 6 refer to Cell_A, while Figures 7 and 8 concern Cell_B. In all $V$-$I$ curves the current $I$ decreases when the voltage $V$ increases; but for Cell_B the current maintains elevated values for $V < 2.3$ V. This trend of the curves in Figures 7 and 8 represents a correct behavior for a photovoltaic cell.

Tables 1–4 summarize the working conditions measured in correspondence with the $V$-$I$ curves plotted in Figures 5–8: incident power density $E_{\text{cell}}$ (kW/m$^2$), incident optical power $P_{\text{cell}}$ (W), cell temperature $T_{\text{cell}}$ (°C), open-circuit voltage $V_{\text{OC}}$ (V), and maximum extracted power $P_{\text{out}}$ (W). The parameters characterizing the tests are completed by the efficiency $\eta$.

How the cell performance changes with the exposure time is indicated in Tables 1–4 that present exactly the same parameters, while Table 5 examines the variation of cell temperature.

A significant parameter is the power density incident on the cell $E_{\text{cell}}$: for both examined cells it results around 90 kW/m$^2$ for $D = 420$ mm, while it is circa 150 kW/m$^2$ for $D = 430$ mm (there is an exception: $E_{\text{cell}} = 82$ kW/m$^2$ for $D = 430$ mm and $t = 3$ h). The corresponding values for the optical power incident on the cell $P_{\text{cell}}$ are about 9 W for $D = 420$ mm and around 15 W for $D = 430$ mm (but $P_{\text{cell}} = 8$ W after 3 h of exposure).

The open-circuit voltage $V_{\text{OC}}$ is lower using Cell_A; it is around 2.1–2.3 V for both $D$ values, while the $V_{\text{OC}}$ measured with Cell_B is higher, circa 2.7-2.8 V for both lens-cell distances.

Probably the most significant parameter is the maximum electrical power extracted $P_{\text{out}}$. For Cell_A the values attained for $P_{\text{out}}$ are circa 0.9 W at $D = 420$ mm and 1.7–1.9 W at $D = 430$ mm. Higher $P_{\text{out}}$ values are obtained with Cell_B: 2.7–3.3 W at $D = 420$ mm and 2.5–4.0 W at $D = 430$ mm. These more satisfying data are in agreement with the correct characteristic curves in Figures 7 and 8: Cell_B works as a photocell and furnishes more electrical power. The bad

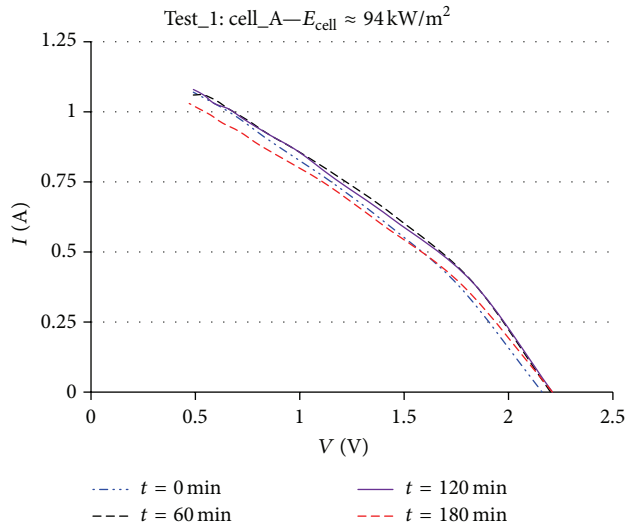


Figure 5: $V$-$I$ curves acquired during Test_1, at the beginning and after 1, 2, and 3 hours of exposure.

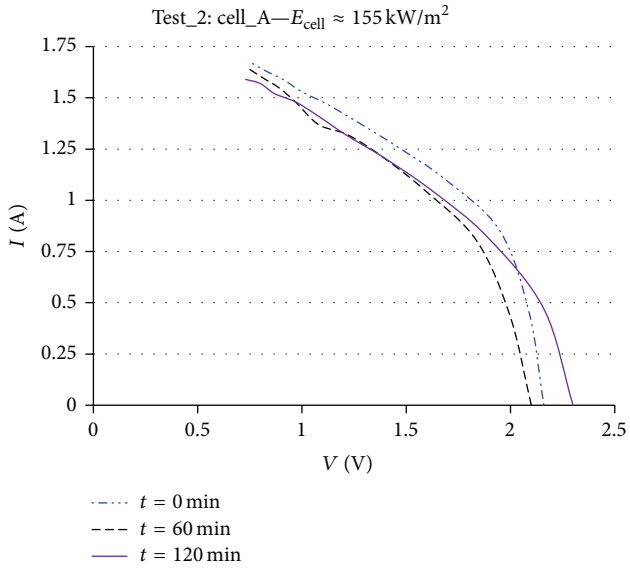


Figure 6: $V$-$I$ curves acquired during Test_2, at the beginning and after 1 and 2 hours of exposure.

Table 1: Parameters characterizing Test_1.

| $t$ (min) | 0 | 60 | 120 | 180 |
|---|---|---|---|---|
| $E_{cell}$ (kW/m$^2$) | 94.6 | 93.6 | 94.0 | 93.1 |
| $P_{cell}$ (W) | 9.46 | 9.36 | 9.40 | 9.31 |
| $T_{cell}$ (°C) | 38 | 43 | 41 | 40 |
| $V_{OC}$ (Volt) | 2.16 | 2.20 | 2.21 | 2.21 |
| $P_{out}$ (W) | 0.86 | 0.91 | 0.89 | 0.84 |
| $\eta$ ($P_{out}/P_{cell}$) | 9.1% | 9.7% | 9.5% | 9.0% |

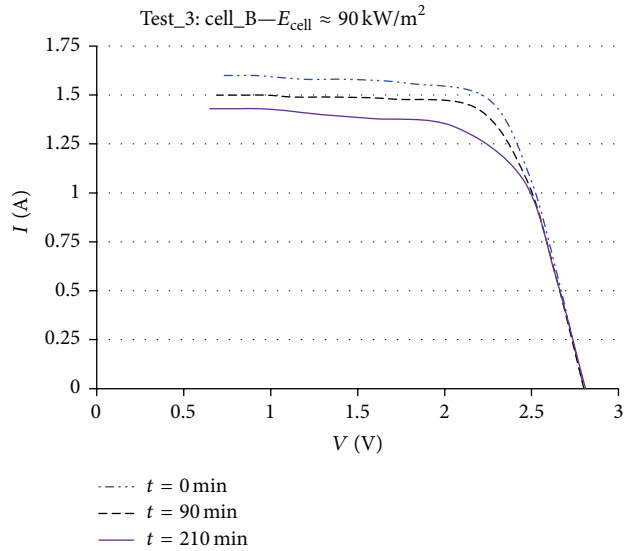


Figure 7: $V$-$I$ curves acquired during Test_3, at the beginning and after 1 hour and 30 min and 3 hours and 30 min of exposure.

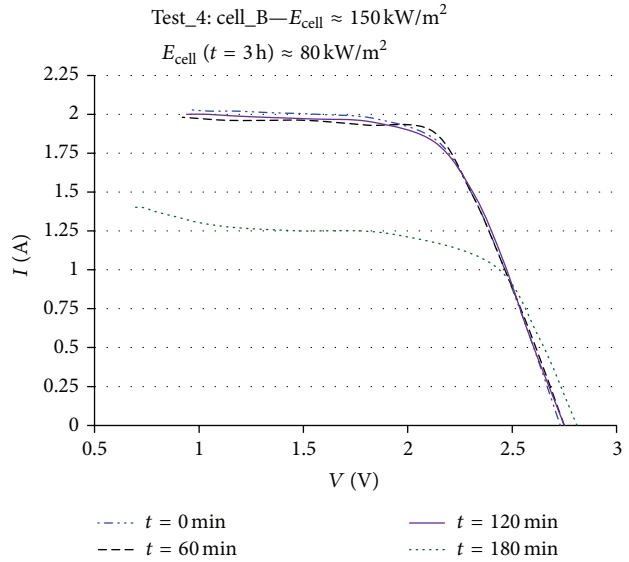


Figure 8: $V$-$I$ curves acquired during Test_4, at the beginning and after 1, 2, and 3 hours of exposure.

Table 2: Parameters characterizing Test_2.

| $t$ (min) | 0 | 60 | 120 |
|---|---|---|---|
| $E_{cell}$ (kW/m$^2$) | 157.1 | 157.7 | 152.6 |
| $P_{cell}$ (W) | 15.71 | 15.77 | 15.26 |
| $T_{cell}$ (°C) | 52 | 54 | 57 |
| $V_{OC}$ (Volt) | 2.16 | 2.10 | 2.30 |
| $P_{out}$ (W) | 1.86 | 1.68 | 1.70 |
| $\eta$ ($P_{out}/P_{cell}$) | 11.8% | 10.7% | 11.1% |

performance of Cell_A, with an improper $V$-$I$ curve and low extracted power, suggests a possible damage of the sample. A visual examination of Cell_A has confirmed the presence of damages.

Table 3: Parameters characterizing Test_3.

| $t$ (min) | 0 | 90 | 210 |
|---|---|---|---|
| $E_{cell}$ (kW/m$^2$) | 93.9 | 90.2 | 83.8 |
| $P_{cell}$ (W) | 9.39 | 9.02 | 8.38 |
| $T_{cell}$ (°C) | 45 | 45 | 42 |
| $V_{OC}$ (Volt) | 2.80 | 2.80 | 2.81 |
| $P_{out}$ (W) | 3.33 | 3.13 | 2.75 |
| $\eta$ ($P_{out}/P_{cell}$) | 35.5% | 34.7% | 32.8% |

Table 4: Parameters characterizing Test_4.

| $t$ (min) | 0 | 60 | 120 | 180 |
|---|---|---|---|---|
| $E_{cell}$ (kW/m$^2$) | 152.6 | 147.7 | 148.3 | 81.6 |
| $P_{cell}$ (W) | 15.26 | 14.77 | 14.83 | 8.16 |
| $T_{cell}$ (°C) | 52 | 53 | 55 | 33 |
| $V_{OC}$ (Volt) | 2.73 | 2.75 | 2.75 | 2.81 |
| $P_{out}$ (W) | 3.92 | 4.01 | 3.88 | 2.48 |
| $\eta$ ($P_{out}/P_{cell}$) | 25.7% | 27.1% | 26.2% | 30.4% |

Table 5: Parameters characterizing Test_5.

| $T_{cell}$ (°C) | 38 | 44 | 56 | 65 |
|---|---|---|---|---|
| $E_{cell}$ (kW/m$^2$) | 89.1 | 89.1 | 89.1 | 89.1 |
| $P_{cell}$ (W) | 8.91 | 8.91 | 8.91 | 8.91 |
| $V_{OC}$ (Volt) | 2.17 | 2.15 | 2.12 | 2.11 |
| $P_{out}$ (W) | 0.72 | 0.70 | 0.68 | 0.70 |
| $\eta$ ($P_{out}/P_{cell}$) | 8.08% | 7.86% | 7.63% | 7.86% |

The quantitative evaluation of the PV cell performance is given by the efficiency $\eta$ calculated in Tables 1–5 as the ratio $P_{out}/P_{cell}$. The efficiency of Cell_B (26–36) is satisfactory while the efficiency for Cell_A (9-10) does not reach the expected $\eta$ value, confirming once again the malfunctioning of Cell_A. However Cell_B presents an unexpected behavior for the efficiency: the $\eta$ value (26–30) for higher concentration, at $D = 430$ mm, is lower than for $D = 420$ mm ($\eta = 33$–$36$), with inferior concentration. Analyzing the value of cell temperature $T_{Cell}$, it can be noted that even if the Peltier module is still active the temperature rises ten degrees in case of higher concentration. This effect can indicate that the efficiency of these cells is very sensitive to the cell temperature. Another aspect that could affect the cell efficiency is the fact, proved in laboratory, that for $D = 420$ mm the uniformity of the light beam is better than at distance $D = 430$ mm. However the main dependence seems to be on temperature, as column 4 of Table 4 demonstrates: at $D = 430$ mm, when the sun power decreases, reducing $T_{Cell}$, the efficiency improves.

*6.3. Results Varying the Cell Temperature.* A series of measurements is carried out in order to control the effects of the variation of the cell temperature, excluding the Peltier module and so allowing the temperature to rise. It is performed at the shorter lens-cell distance $D$, which corresponds to a lower concentration, in order to allow the measurement of the temperature. At $D = 430$ mm the temperature variation would be too fast.

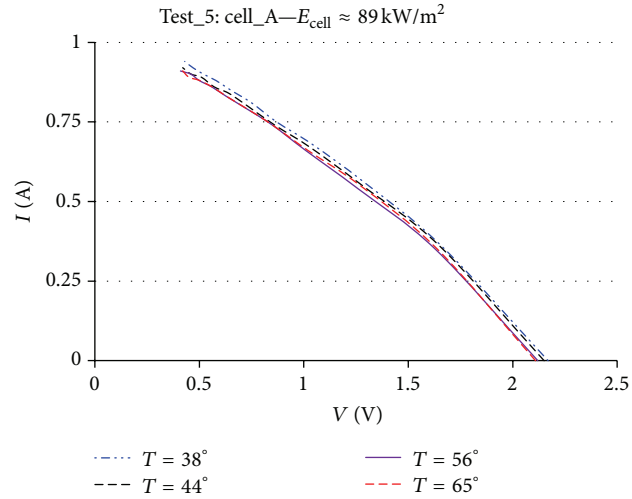


Figure 9: $V$-$I$ curves acquired during Test_5, at different temperatures of the cell.

*Test_5.* Specifications are as follows: distance lens-cell: 420 mm; duration of exposure: 15 minutes; other parameters: variation of the cell temperature; sample: Cell_A.

The temperature of the cell $T_{Cell}$ is a very important quantity. During the basic exposure tests at $D = 420$ mm (*Test_1* and *Test_3*) the range of $T_{Cell}$ is 38–43°C for Cell_A and 42–45°C for Cell_B. Higher temperatures are reached in the basic exposure tests at $D = 430$ mm (*Test_2* and *Test_4*): the $T_{Cell}$ range is 52–57°C for Cell_A and 52–55°C for Cell_B (except for $t = 3$ h when $T_{Cell} = 33$°C). A dedicated test (*Test_5*), reported in Figure 9 and Table 5, examines the system behavior varying the cell temperature from 38°C to 65°C: the power density incident on the cell remains constant; the open-circuit voltage and the maximum electrical power extracted show only small fluctuations towards inferior values when $T_{Cell}$ increases.

## 7. Conclusion

Experimentation with direct exposure to sunlight is essential to evaluate the behavior of solar components in situations very similar to operative solar plants. In particular optoelectronic components for concentrating photovoltaic systems require an optical concentrator and a solar tracker to be examined in outdoor tests. When photocells are studied it is evident that the external measurements are useful because they can help to assess performance, functioning characteristics, and limitations of use. However some preliminary measurements in laboratory are suitable for choosing the geometric parameters appropriate for the outdoor tests.

The proposed methodology has the advantage of reproducing the real working conditions and the sun trackers allow to mount a custom optical systems (collector with possible secondary optics) to focus sunlight on the photocell, while solar simulators have their own optical system that focuses artificial light on the cell. The laboratory experimentation, using a solar divergence collimator [11], permits a more

precise evaluation of the optical characteristics of the components, while solar simulators often have a divergence much larger than the solar rays, being aimed to reproduce the solar intensity.

The principal aim of this solar test is to characterize the photocells measuring voltage ($V$) and current ($I$) across the cell: the $V$-$I$ curves indicate the behavior of the optoelectronic component.

Characterization curves and test parameters are compared for two exemplificative solar cells showing a completely different behavior. They are samples of the same type of photovoltaic cell and they are indicated as Cell_A and Cell_B. The cells are tested exposing them to concentrated solar light, focused by a large Fresnel lens. The experimentation is carried out for various exposure times $t$ and at different lens-cell distances $D$, selected in order to have the required concentration of sunlight.

Analogously to the parameters controls made in laboratory, during the field measurements it is interesting and practically useful to monitor the ambient and working conditions. These physical quantities represent the functioning parameters of the sample under test and the environmental state of the whole device for solar collection.

Comparing the results of the different exposure tests, it appears evident that Cell_B shows a correct behavior and an improved efficiency with respect to Cell_A. The $V$-$I$ curves for Cell_B have a trend similar to the theoretical one for a photocell, while the $V$-$I$ curves for Cell_A deviate much from this trend. Also the performance of Cell_B is definitely better, in terms of both open-circuit voltage and electrical power extracted, with the same power density on the cell. The reason is that Cell_A is damaged.

In conclusion, at a distance of 420 mm from the Fresnel lens Cell_B reaches the maximum efficiency with values between 33 and 36 and the most uniform illumination of the cell is obtained. At a lens-cell distance of 430 mm Cell_B furnishes the maximum value of electrical power extracted, which is 4 W.

For what concerns the behavior in time, the curves do not undergo significant changes for an exposure of 2-3 hours.

In the only test carried out by varying the temperature of the PV cell, the temperature increase does not produce changes on the $V$-$I$ curves or alteration of the parameters, in the regime of temperatures examined (38–65°C).

This research is under development and further studies can investigate the behavior of other photovoltaic cells under different conditions of solar concentration.

## Conflict of Interests

The authors declare that there is no conflict of interests regarding the publication of this paper.

## References

[1] D. Hirsch, P. V. Zedtwitz, T. Osinga, J. Kinamore, and A. Steinfeld, "A new 75 kW high-flux solar simulator for high-temperature thermal and thermochemical research," *Journal of Solar Energy Engineering*, vol. 125, no. 1, pp. 117–120, 2003.

[2] K. R. Krueger, J. H. Davidson, and W. Lipiński, "Design of a new 45 kWe high-flux solar simulator for high-temperature solar thermal and thermochemical research," *Journal of Solar Energy Engineering—Transactions of the ASME*, vol. 133, no. 1, Article ID 011013, 2011.

[3] D. S. Codd, A. Carlson, J. Rees, and A. H. Slocum, "A low cost high flux solar simulator," *Solar Energy*, vol. 84, no. 12, pp. 2202–2212, 2010.

[4] C. Domínguez, I. Antón, and G. Sala, "Solar simulator for concentrator photovoltaic systems," *Optics Express*, vol. 16, no. 26, pp. 14894–14901, 2008.

[5] J. Petrasch, P. Coray, A. Meier et al., "A novel 50 kW 11,000 suns high-flux solar simulator based on an array of xenon arc lamps," *Journal of Solar Energy Engineering, Transactions of the ASME*, vol. 129, no. 4, pp. 405–411, 2007.

[6] S. H. Jang and M. W. Shin, "Fabrication and thermal optimization of LED solar cell simulator," *Current Applied Physics*, vol. 10, no. 3, supplement, pp. S537–S539, 2010.

[7] U. C. Pernisz, "Development of a standard test method for measuring photovoltaic cell performance," *Solar Cells*, vol. 7, no. 1-2, pp. 203–208, 1982.

[8] M. Bliss, T. R. Betts, and R. Gottschalg, "Advantages in using LEDs as the main light source in solar simulators for measuring PV device characteristics," in *Reliability of Photovoltaic Cells, Modules, Components, and Systems*, vol. 7048 of *Proceedings of SPIE*, Neelkanth G. Dhere, San Diego, Calif, USA, August 2008.

[9] S. Kohraku and K. Kurokawa, "New methods for solar cells measurement by LED solar simulator," in *Proceddings of the 3rd World Conference on Photovoltaic Energy Conversion*, vol. 2, pp. 1977–1980, May 2003.

[10] D. Fontani, P. Sansoni, F. Francini, D. Jafrancesco, L. Mercatelli, and E. Sani, "Pointing sensors and sun tracking techniques," *International Journal of Photoenergy*, vol. 2011, Article ID 806518, 9 pages, 2011.

[11] D. Fontani, P. Sansoni, E. Sani, S. Coraggia, D. Jafrancesco, and L. Mercatelli, "Solar divergence collimators for optical characterisation of solar components," *International Journal of Photoenergy*, vol. 2013, Article ID 610173, 10 pages, 2013.

[12] S. Kohraku and K. Kurokawa, "A fundamental experiment for discrete-wavelength LED solar simulator," *Solar Energy Materials & Solar Cells*, vol. 90, no. 18-19, pp. 3364–3370, 2006.

[13] S. H. Jang and M. W. Shin, "Fabrication and thermal optimization of LED solar cell simulator," *Current Applied Physics*, vol. 10, no. 3, pp. S537–S539, 2010.

[14] D. Kolberg, F. Schubert, N. Lontke, A. Zwigart, and D. M. Spinner, "Development of tunable close match LED solar simulator with extended spectral range to UV and IR," *Energy Procedia*, vol. 8, pp. 100–105, 2011.

[15] W. Wang and B. Laumert, "Simulate a 'sun' for solar research: a literature review of solar simulator technology," KTH Literature Review 2014, Department of Energy Technology, Division of Heat and Power Technology, Royal Institute of Technology, Stockholm, Sweden, 2014.

[16] T. K. Mallick, "Indoor experimental characterisation of a three trough 50° effective acceptance half-angle line-axis concentrating asymmetric compound parabolic photovoltaic concentrator using a continuous solar simulator," in *Optics and Heat Transfer for Asymmetric Compound Parabolic Photovoltaic Concentrators for Building Integrated Photovoltaics*, chapter 5 of PhD Thesis, Faculty of Engineering, Ulster University, Coleraine, UK, 2003.

[17] C. Domínguez, I. Antón, and G. Sala, "Solar simulator for concentrator photovoltaic systems," *Optics Express*, vol. 16, no. 19, pp. 14894–14901, 2008.

[18] I. Antón, R. Solar, G. Sala, and D. Pachón, "IV testing of concentration modules and cells with non-uniform light patterns," in *Proceedings of the the 17th European Photovoltaic Solar Energy Conference and Exhibition*, pp. 611–614, 2001.

[19] W. Keogh and A. Cuevas, "Simple flashlamp I-V testing of solar cells," in *Proceedings of the IEEE 26th Photovoltaic Specialists Conference*, pp. 199–202, October 1997.

[20] R. Winston, J. C. Mińano, and P. Benítez, *Nonimaging Optics*, Elsevier Academic Press, Amsterdam, The Netherlands, 2005.

[21] J. C. Chaves, *Introduction to Nonimaging Optics*, CRC Press, Boca Raton, Fla, USA, 2008.

[22] A. Davis and F. Kühnlenz, "Optical design using fresnel lenses," *Optik & Photonik*, vol. 2, no. 4, pp. 52–55, 2007.

[23] W. B. Stine and M. Geyer, *Power from the Sun*, 2001, http://www.powerfromthesun.net/book.html.

Hindawi Publishing Corporation
International Journal of Photoenergy
Volume 2015, Article ID 718316, 7 pages
http://dx.doi.org/10.1155/2015/718316

*Research Article*

# Glazed PVT Collector with Polysiloxane Encapsulation of PV Cells: Performance and Economic Analysis

**Tomas Matuska,[1] Borivoj Sourek,[2] Vladimir Jirka,[2] and Nikola Pokorny[2]**

[1] *Faculty of Mechanical Engineering, Czech Technical University, Technicka 4, 166 07 Prague, Czech Republic*
[2] *University Centre of Energy Efficient Buildings, Czech Technical University, Trinecka 1024, 273 43 Bustehrad, Czech Republic*

Correspondence should be addressed to Tomas Matuska; tomas.matuska@fs.cvut.cz

Received 4 September 2015; Accepted 11 October 2015

Academic Editor: Xudong Zhao



Development of a new concept of glazed PVT collector based on temperature resistant polysiloxane encapsulation material is presented together with the results from experimental testing and modelling. Performance and economic analysis in 4 different European climates has been done to derive the competitive price of the PVT collector concepts with main focus on the glazed PVT collector under development. Results have shown that specific market price 400 to 500 EUR/m$^2$ for the glazed PVT collector should not be exceeded in order to become competitive with conventional combination of photothermal and photovoltaic collectors.

## 1. Introduction

Solar photovoltaic-thermal (PVT) liquid collectors represent a new technology on the market which combines the electricity and heat generation from the same receiving surface in one device. The hybrid PVT collectors provide both heat and electricity, while the heat generation is several times higher than the electricity. Through the solar electricity and heat cogeneration, the total energy output per unit collector area can be higher than the outputs of conventional photovoltaic (PV) module and photothermal (PT) collector placed and operated separately with the equal total area [1, 2]. Such feature could be effectively used in the building applications with high and constant use of thermal energy during the year but with the limited roof area, for example, DHW in the multifamily buildings and block of flats, or in the solar active houses with high solar fraction, for example, self-sufficient houses with a seasonal storage.

Because of the mature and cheap PV manufacturing process, the PVT collectors available on the market are based on standard PV laminates from ethylene-vinyl-acetate (EVA) compound. The hybrid PVT collectors based on EVA encapsulant are mainly offered as the unglazed ones so far with a poor thermal performance for usual solar thermal applications in buildings. Despite this fact, the market price of unglazed hybrid PVT liquid collectors achieves high level in comparison with standard glazed solar thermal collectors and PV modules. To improve the thermal performance the glazed PVT collector design has been developed [3] based on high performance components (fractal absorber, antireflection coatings, etc.). Stagnation temperature in glazed PVT solar collectors could reach 120 to 180°C and this fact reveals the main drawback of EVA copolymer application as an encapsulant of PV cells. Application of EVA laminate restricts the permanent exposition of PVT absorber to temperatures above 90°C because of its corrosiveness under high temperature exposition [4]. It has been proved that the long-term thermal load at such temperature levels results in decomposition of EVA to acetic acid which causes the corrosion of PV cells contacts, delamination, and also degradation of the encapsulation layer transparency [5–7].

High stagnation temperature of the glazed PVT collector leads to searching in the new materials for encapsulation of the strings of PV cells. A novel glazed PVT collector concept based on PV laminate with polysiloxane gel has been developed at Czech Technical University in Prague. Polysiloxane gel instead of EVA lamination compound offers several important advantages, mainly the high temperature resistance and high transparency. A developed glazed PVT collector is described, and results of testing are presented

and used for the performance-economic analysis to give an answer to basic questions concerning the possible competitiveness of glazed PVT collector. The maximum market price for the PVT liquid collector concepts has been determined for combined solar heat and power supply for multifamily building in order to be competitive when compared with conventional separate PV and PT collectors installation at given boundary conditions (building heat and electricity load, energy prices, and prices of conventional solar collectors) in different climates of Europe.

## 2. Glazed PVT Collector Concept with Polysiloxane Encapsulation

Silicone polymers (polysiloxanes) are more suitable candidates for application as PV encapsulant for glazed PVT collectors than the EVA material. Polysiloxane gel offers several important advantages like large range of operation temperature (from −60 to +250°C), high transparency for solar radiation (even higher compared to EVA in solar wavelength region), compensation of thermal dilatation stresses due to low modulus of elasticity (permanent gel), high physical adhesion to semiconductors, glass, and most other materials without use of sublayers, and good heat transfer from PV cells to heat exchanger due to higher thermal conductivity [7–9]. Polysiloxane laminate thus opens the application potential especially for the glazed PVT collectors development. Silicone gel encapsulation machine available at University Centre for Energy Efficient Buildings (Czech Technical University, CTU) enables fabricating the solar PVT collector prototypes. The encapsulation technology is based on low vacuum dosing of the gel into the gap between glass pane and flat heat exchanger with immersed strings of PV cells. The encapsulation process is carried out at room temperature. This fact brings a clear advantage for future production.

Strong accent has been put also on simplicity of the glazed PVT collector design and fabrication by means of reduced number of elements to compose the collector. A new concept of solar glazed PVT collectors has been introduced. Double glazing with a gap between glass panes 20 mm filled with argon has been used for encapsulation of PV cells with the iron heat exchanger by polysiloxane gel (see Figure 1). Two designs have been tested so far. Nonselective glazed PVT collector has been fabricated from double glazing with uncoated solar glass panes and double glazing with a low emissivity coating has been used for the spectrally selective PVT collector. Today low-e coatings have high transparency for visible range but unfortunately significantly reduced transmittance for near infrared region of solar radiation spectrum. The presented glazed selective PVT collector has been made with commercially widely available low-e coating with no optimization of the emissivity and transparency. Fully wetted heat exchanger has been used for both PVT collectors. Aperture area of the glazed PVT collectors was 0.67 $m^2$. In total only 4 × 6 polycrystalline PV cells at size 156 × 156 mm have been used due to given size of absorber. Aperture area has been covered to 87% by PV cells (packing factor). Absorber has been insulated by 40 mm of mineral wool on the back and 10 mm of EPDM foam at the edge side and put into wooden frame.

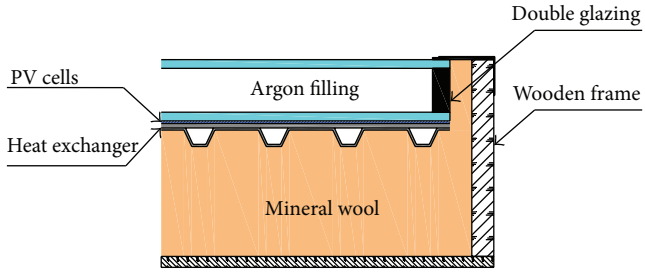


Figure 1: Layout of the investigated glazed PVT collectors.

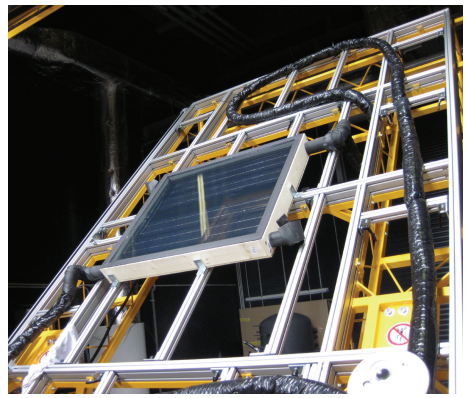

Figure 2: Glazed nonselective PVT collector at indoor test stand.

Glazed solar PVT collector prototypes have been tested under conditions of artificial sun at University Centre for Energy Efficient Buildings in Bustehrad (see Figure 2). Tests have been performed in accordance with EN 12975 for the open circuit mode and under MPPT electric load conditions.

Figure 3 shows the comparison of thermal performance characteristics for glazed PVT prototypes with siloxane gel lamination (selective, nonselective) and state-of-the-art solar photothermal (PT) selective collector. All characteristics resulted from the experimental testing. Comparison has confirmed the excellent properties of polysiloxane gel encapsulation. High zero-loss efficiency for nonselective alternative of PVT prototype indicates the good heat transfer from PV absorber into heat transfer liquid and high transparency of the polysiloxane layer. On the other side, the high radiative heat loss reduces the thermal performance of the nonselective PVT collector at high temperatures. Results for selective PVT collector prototype have confirmed the assumption of the high reflection losses in the near infrared radiation region due to the low-e coating applied to absorber laminate glass. In any case, the results revealed the field for further improvements of the glazed PVT collector. Main effort should be concentrated on optimized low-e coating with high solar transmittance but low emissivity for near infrared region. Such coatings with transmittance 86% and emissivity 30% are already in the market and will be used further for the final glazed PVT concept [10]. Thermal efficiency for the new glazed selective

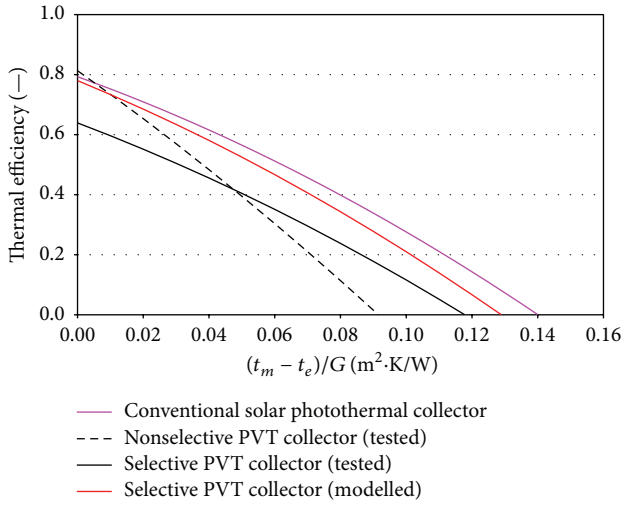


Figure 3: Comparison of thermal efficiency characteristics for glazed PVT collectors (open circuit) under development and state-of-the-art photothermal collector.

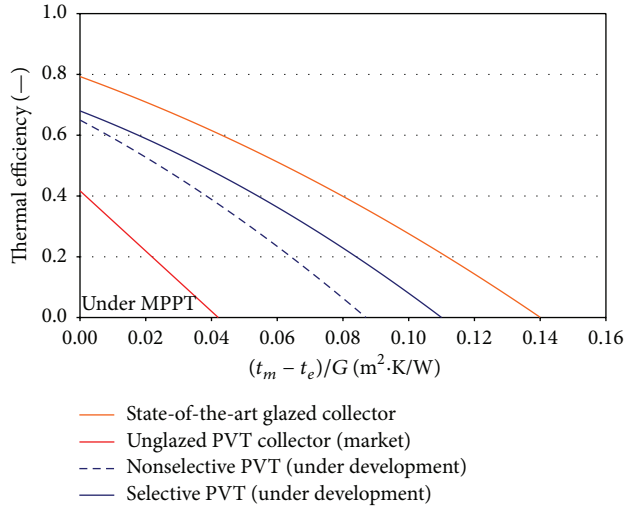


Figure 4: Thermal efficiency characteristics of PVT collectors used in analysis (under MPPT electric load).

PVT collector has been modelled with a detailed glazed PVT model [11]. Results for open electric circuit mode are added into graph in Figure 3. The characteristics are shown in dependency on the difference between the mean fluid temperature $t_m$ and ambient temperature $t_e$ reduced by solar irradiance $G$ [W/m$^2$].

## 3. Performance-Economic Analysis of PVT Application for Multifamily Building

Today research and development of solar energy products have to focus on competitive solutions. It is quite problematic to develop the components which are sophisticated and efficient on the one side but with the payback time beyond the lifetime. The development and commercialization of the PVT collector design requires the performance and economic information to analyse the competitiveness at the potential market. The maximum competitive price of the PVT collector and realistic production costs can indicate if the glazed PVT concept is viable or not or at which boundary conditions (e.g., energy prices). Therefore, the target of the performance and economic analysis presented here was to find the competitive specific price range for given concepts of solar hybrid PVT collectors. The investigated alternatives of solar hybrid PVT collectors are

(i) unglazed PVT collector in the quality available on the market,

(ii) glazed nonselective PVT collector with the siloxane gel encapsulation,

(iii) glazed selective PVT collector with the siloxane gel encapsulation.

Thermal performance of the analysed hybrid PVT collector concepts is represented by thermal efficiency characteristics in MPPT (maximum power point tracking) operation; see Figure 4. The characteristics have been derived from the testing and modelling of given PVT concepts assuming uniform use of polycrystalline PV cells with efficiency 15% (standard testing conditions) and power temperature coefficient 0.45%/K. The same PV cells have been considered also for conventional PV module performance modelling. Figure 4 shows also the thermal efficiency characteristic for state-of-the-art solar thermal collector with spectrally selective surface used for modelling of conventional glazed solar photothermal collector applied in the performance analysis.

The analysis has been performed for combined solar heat and power system for multifamily residential building. The performance and economic analyses are based on the solar energy system with the combined heat and electricity production for a residential building with 45 flats and 100 occupants. Solar heat is used for DHW preparation, and solar electricity is used for the building appliances load. Heat demand for hot water use in the building is 96 MWh/a. Electricity demand for the building is 113 MWh/a. Analyses have been performed for four different climate zones in Europe with different annual solar irradiation sum: Prague (1096 kWh/m$^2$·a), Stockholm (1206 kWh/m$^2$·a), Milan (1367 kWh/m$^2$·a), and Marseille (1760 kWh/m$^2$·a).

The solar system with hybrid PVT liquid collectors of different design concepts has been compared with conventional solar heat and power system combining the state-of-the-art solar photothermal collectors and photovoltaic modules with identical polycrystalline cells as used in hybrid PVT collectors. Available solar collector field area 100 m$^2$ on the building roof is the total collector area for all systems in the analyses. Conventional solar PV and PT system is considered in 5 alternatives differing in the percentage ratio of PV and PT solar collector area applied. The alternatives are

(i) 100% PV (100 m$^2$ of PV collector, 0 m$^2$ of PT collector),

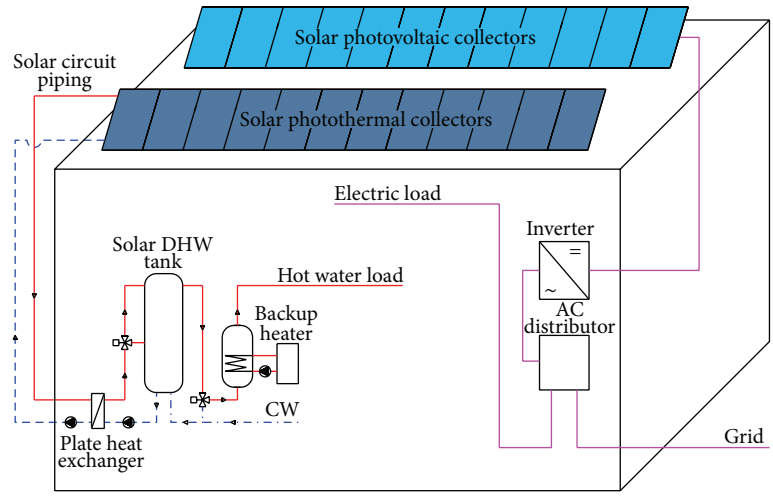


Figure 5: Simplified scheme of the considered solar energy system for block of flats.

(ii) 75% PV-25% PT (75 $m^2$ of PV collector, 25 $m^2$ of PT collector),

(iii) 50% PV-50% PT (50 $m^2$ of PV collector, 50 $m^2$ of PT collector),

(iv) 25% PV-75% PT (25 $m^2$ of PV collector, 75 $m^2$ of PT collector),

(v) 100% PT (0 $m^2$ of PV collector, 100 $m^2$ of PT collector).

Solar heat and power systems have been modeled in TRNSYS environment with use of the available models for unglazed PVT collector [12] and glazed PVT collector [11]. Simplified scheme of the solar energy system is shown in Figure 5. Solar thermal part of the investigated system variants consists of several main components: solar collectors with slope 45° and orientation to south, insulated pipes of collector circuit, heat exchanger, and insulated solar DHW storage tank. Parameters of the main components for the solar thermal systems alternatives are considered dependent on collector field area considered in the different variants. Dimension of the collector circuit pipes is based on specific mass flow rate 15 kg/h·$m^2$ of collector area (low flow solar system). Pipes length of solar collector circuit in outdoor environment is 130 m, and length of pipes inside the building is 30 m. Solar tank volume has been determined from specific value 50 L/$m^2$ of collector area. Solar plate heat exchanger has the efficiency 85%. PV power system is a conventional grid-on system with DC/AC inverter. Total system losses are considered 10%. Whole PV electricity production is assumed to be consumed for the building appliances load.

Results of TRNSYS simulations for individual alternatives for Prague climate (moderate climate) and Marseille (warm climate) are compared in Figure 6. Comparison shows the general advantage of the glazed hybrid PVT collectors in energy yields. Despite the lower effectivity for heat production compared to conventional solar thermal collector and lower effectivity for electricity production compared to conventional PV modules, the glazed selective PVT collector results in higher combined energy gains when compared with separate PV and PT combination with different ratio between the technologies. Nonselective PVT collector shows heat production lower than conventional state-of-the-art solar photothermal collector in the conditions of Prague; however, the significant portion of energy produced is the electricity with better usability compared to heat. Marseille conditions are better and total energy production of nonselective glazed PVT collector is even higher than for conventional thermal collector. Unglazed PVT collector shows a low thermal performance in the domestic hot water application especially in the moderate climate of Prague.

To define the competitive price for investigated PVT collectors on the market, the following economic conditions have been set. Inputs for the economic calculations are the heat and electricity price and costs for solar PT and PV collectors and the system costs. Electricity price for households in Europe varies between 8 eurocents/kWh and 30 eurocents/kWh depending on the region [13]. Similarly, the range of heat price is quite wide between 4 eurocents/kWh and 16 eurocents/kWh dependent on the fuel and technology used for heat production and local legislation, for example, specific taxes on fossil fuels [14]. Electricity price of 16 eurocents/kWh and heat price of 8 eurocents/kWh common in Germany with the largest solar systems market in Europe have been used for the economic analysis.

Costs for solar energy systems are given by solar thermal collectors costs, solar PV modules costs, and the costs for the rest of the system (piping, storage, control, cables, invertor, support constructions, etc.). Simplification has been used in the idea that solar collectors are always considered representing the 50% of total system costs in both PV and PT systems. Solar collector costs are considered 120 EUR/$m^2$ for photovoltaic polycrystalline modules and 350 EUR/$m^2$ for the state-of-the-art spectrally selective solar thermal collectors. The same costs have been considered as the costs for the rest of the system.

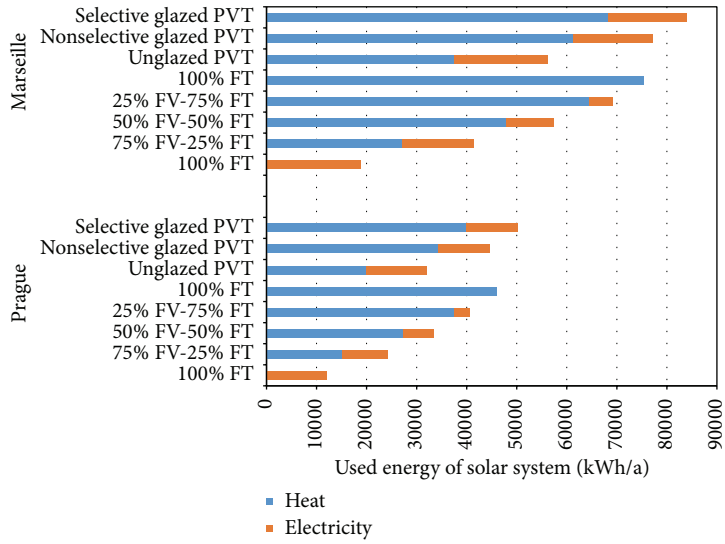


Figure 6: Comparison of energy gains for different PVT collector designs and conventional combination.

The competitive specific price for given hybrid PVT collector alternative has been derived from the balance of investment costs and operation costs for 20 years lifetime period for conventional PV/PT system and the hybrid PVT system. The specific collector price is derived from the conditions that total lifetime costs of hybrid PVT system and combined conventional PV and PT system are equal. Interest rate is considered equal to energy price increase, assuming that both are at 5% level. Competitive specific price (EUR/m$^2$) for hybrid PVT collectors has been calculated from the results of performance analyses (energy savings) and the economic inputs presented above. Each solar hybrid PVT system has been economically compared with 5 different conventional PV and PT system alternatives (ratio between PV and PT collector area). Results are shown in Figures 7–9 for investigated alternatives of PVT collectors.

Graph in Figure 7 shows the competitive specific price for unglazed PVT collectors available at today European market. While market price for unglazed PVT collector ranges today between 300 and 500 EUR/m$^2$, competitive price level is much lower and thus the unglazed PVT collectors are not competitive with conventional combination of photothermal and photovoltaic collectors even in southern Europe. Only the cheapest unglazed collector systems could compete with photovoltaic only or photothermal only systems. Unglazed PVT collectors are out of the competitive range for central and northern Europe due to the poor thermal performance. It could be stated that unglazed PVT collectors are not economically applicable for solar DHW systems and have a very limited application potential with their market price today.

The situation is better for the glazed PVT collectors. In the case of nonselective collectors the range of the competitive price is 300 to 500 EUR/m$^2$ for southern Europe but significantly lower for central and northern Europe (see Figure 8). The target technology of the glazed selective PVT

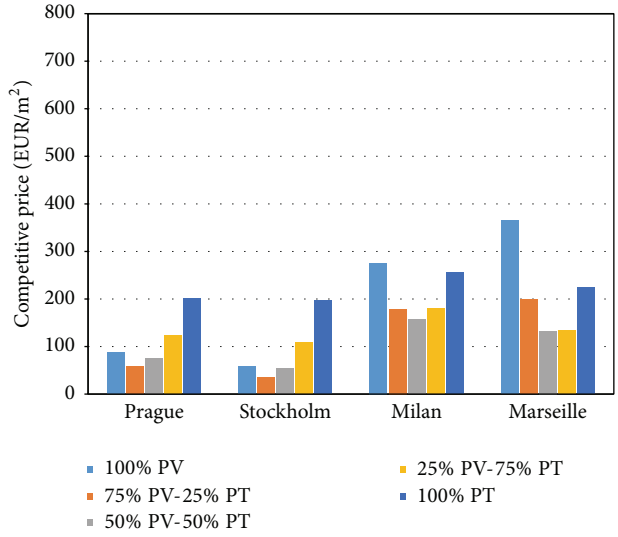


Figure 7: Competitive specific price of unglazed hybrid PVT collector.

collectors ranges between 300 and 400 EUR/m$^2$ for central and northern Europe and between 400 and 600 EUR/m$^2$ for southern Europe (see Figure 9). These figures are much more optimistic with respect to conservative inputs for economic analysis (low increase of energy prices and high interest rate for residential application) and show the glazed selective PVT collector as a viable concept.

## 4. Conclusion

The new concept of glazed solar PVT collector with polysiloxane gel encapsulation of PV cells has been developed and prototypes were tested and evaluated. Experimental work has confirmed the excellent optical and thermal performance

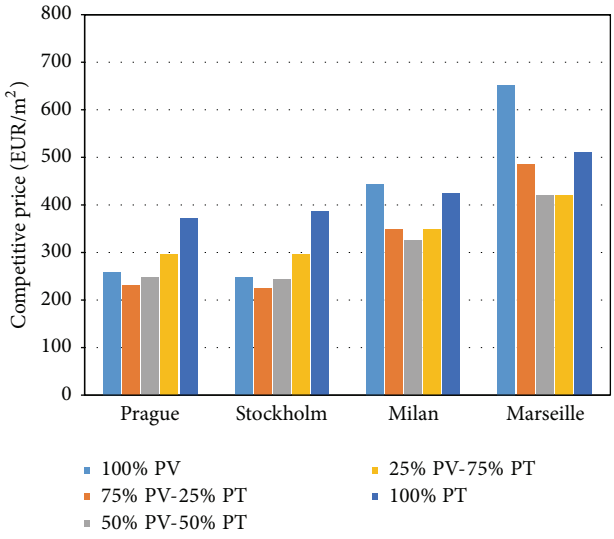


Figure 8: Competitive specific price of glazed nonselective hybrid PVT collector.

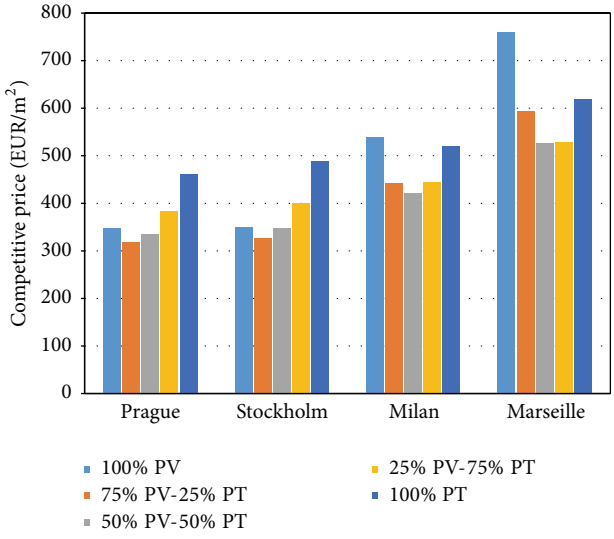


Figure 9: Competitive specific price of glazed selective hybrid PVT collector.

features of polysiloxane laminate application for solar PVT absorbers. Further improvements will be done in glazed PVT collector design using the advanced highly transparent low-e glazing. To evaluate the commercial potential of the different PVT collector concepts, the competitive market price has been subjected to performance and economic analysis for combined solar heat and power system for given residential building. It has been shown that unglazed PVT collectors in the field of common solar DHW applications cannot be competitive with the conventional solar thermal collector and photovoltaic modules combination. The resulted competitive price figures for the presented glazed selective PVT collector which is under development have proved the viability of the new concept.

## Conflict of Interests

The authors declare that there is no conflict of interests regarding the publication of this paper.

## Acknowledgments

The research leading to these results has received funding from the European Union's Seventh Framework Programme FP7/2007–2011 under Grant Agreement no. 282825, Acronym MacSheep. The paper has been supported by European Union project OP VaVpI no. CZ.1.05/2.1.00/03.0091, University Centre for Energy Efficient Buildings.

## References

[1] H. A. Zondag, D. W. de Vries, W. G. J. van Helden, R. J. C. van Zolingen, and A. A. van Steenhoven, "The yield of different combined PV-thermal collector designs," *Solar Energy*, vol. 74, no. 3, pp. 253–269, 2003.

[2] T. T. Chow, G. Pei, K. F. Fong, Z. Lin, A. L. S. Chan, and J. Ji, "Energy and exergy analysis of photovoltaic-thermal collector with and without glass cover," *Applied Energy*, vol. 86, no. 3, pp. 310–316, 2009.

[3] P. Dupeyrat, C. Ménézo, M. Rommel, and H.-M. Henning, "Efficient single glazed flat plate photovoltaic–thermal hybrid collector for domestic hot water system," *Solar Energy*, vol. 85, no. 7, pp. 1457–1468, 2011.

[4] A. Parretta, M. Bombace, G. Graditi, and R. Schioppo, "Optical degradation of long-term, field-aged c-Si photovoltaic modules," *Solar Energy Materials & Solar Cells*, vol. 86, no. 3, pp. 349–364, 2005.

[5] H. A. Zondag and W. G. J. van Helden, "Stagnation temperature in PVT collectors," in *Proceedings of the PV in Europe—From PV Technology to Energy Solutions Conference and Exhibition*, Rome, Italy, October 2002.

[6] H. A. Zondag, "Flat-plate PV-Thermal collectors and systems: a review," *Renewable and Sustainable Energy Reviews*, vol. 12, no. 4, pp. 891–959, 2008.

[7] V. Poulek, D. S. Strebkov, I. S. Persic, and M. Libra, "Towards 50 years lifetime of PV panels laminated with silicone gel technology," *Solar Energy*, vol. 86, no. 10, pp. 3103–3108, 2012.

[8] V. Poulek, M. Libra, V. Jirka, and I. Persic, *Polysiloxane Gel Lamination Technology for Solar Panels and Rastered Glazing*, ILSA, Praha, Slovakia, 2013.

[9] T. Matuska, V. Jirka, and V. Poulek, "Use of polysiloxane gel as laminate for solar PVT collectors," in *Proceedings of the International Conference on Solar Energy and Buildings (EuroSun '14)*, Aix-les-Bains, France, September 2014.

[10] F. GIovanneti, S. Föste, N. Ehrmann, and G. Rockendorf, "High transmittance, low emissivity glass covers for flat plate collectors: applications and performance," *Energy Procedia*, vol. 30, pp. 106–115, 2012.

[11] N. Pokorny, T. Matuska, and B. Sourek, "Modelling of glazed liquid PV-T collector with use of detail model," in *Proceedings of the Building Simulation International Conference (BS '15)*, Hyderabad, India, 2015.

[12] M. Stegmann, E. Bertram, G. Rockendorf, and S. Janßen, "Model of an unglazed photovoltaic thermal collector based

on standard test procedures," in *Proceedings of the 30th ISES Biennial Solar World Congress (SWC '11)*, pp. 2639–2647, Kassel, Germany, September 2011.

[13] Eurostat Electricity prices for household consumers, 2014, http://epp.eurostat.ec.europa.eu.

[14] Euroheat & Power District heating and cooling statistics—country by country survey, 2014, http://www.euroheat.org/.

Hindawi Publishing Corporation
International Journal of Photoenergy
Volume 2015, Article ID 787280, 7 pages
http://dx.doi.org/10.1155/2015/787280

*Research Article*

# Study on Concentrating Characteristics of a Solar Parabolic Dish Concentrator within High Radiation Flux

**Qianjun Mao,[1] Liya Zhang,[1] and Hongjun Wu[2]**

[1]*School of Civil Engineering, Northeast Petroleum University, Daqing 163318, China*
[2]*Provincial Key Laboratory of Oil & Gas Chemical Technology, College of Chemistry & Chemical Engineering, Northeast Petroleum University, Daqing 163318, China*

Correspondence should be addressed to Qianjun Mao; maoqianjun@163.com and Hongjun Wu; hjwu@nepu.edu.cn

Received 29 June 2015; Revised 25 August 2015; Accepted 30 August 2015

Academic Editor: Xudong Zhao



Concentrating characteristics of the sunlight have an important effect on the optical-thermal conversion efficiency of solar concentrator and the application of the receiver. In this paper, radiation flux in the focal plane and the receiver with three focal lengths has been investigated based on Monte Carlo ray-tracing method. At the same time, based on the equal area-height and equal area-diameter methods to design four different shape receivers and numerical simulation of radiation flux distribution characteristics have also been investigated. The results show that the radiation flux in the focal plane increases with decreasing of the focal length and the diameter of the light spot increases with increasing of the focal length. The function of the position with a maximum of radiation flux has been obtained according to the numerical results. The results also show that the radiation flux distribution of cylindrical receiver has the best performance in all four receivers. The results can provide a reference for future design and application of concentrating solar power.

## 1. Introduction

With the rapid development of global economy, the challenges for environment and energy are more and more important to the human. Concentrating solar power (CSP) is regarded as an effective way to solve energy problem [1, 2]. The main idea of CSP is that the sunlight hits the surface of the earth and concentrates on the receiver, where the fluid is heated from the energy [3–6]. A large number of CSP projects have currently been developed or proposed in many countries, particularly in China, Spain, and USA. As we know, the concentrating characteristics of the sunlight in CSP plant have very huge effect on the efficiency and cost of the power. The concentrating types of CSP plant often have four contributions: solar power tower, solar parabolic dish, parabolic tough collector, and linear Fresnel reflector. Solar parabolic dish system has the best concentration ratio in all four types and the radiation flux has maximum. Therefore, the investigation of concentrating characteristics of a solar parabolic concentrator with a high radiation flux is very necessary and can provide a reference to the state-of-the-art design of CSP plant.

A large number of advancements have taken place in recent years in an effort to make radiation flux of the receiver more uniformly and effectively. As for the CSP system, there are some researches that focus on the solar radiation, conversion efficiency, and storage tank [7–9]. Ji et al. have experimentally investigated the application and the efficiency in solar optical-thermal and PV fields, that is, solar heating water and heat pump, and have obtained some important results [10–14]. Shuai et al. have applied the Monte Carlo ray-tracing method and coupled with optical property to simulate the performance of a solar parabolic dish system. They have proposed an upside-down pear cavity receiver based on the concept of equivalent radiation flux. The results show that uniformity performance of the wall flux is compared with five traditional geometries [15]. Clausing has presented an analytical model to calculate convective loss for a receiver. The analytical results and experimental evidence in the research have indicated that the convective

loss for the receiver is appreciable [16, 17]. Nithyanandam and Pitchumani have integrated the cost and performance model of an encapsulated phase change materials thermal energy storage and latent heat to study the dynamic thermal energy system performance [18]. Emes et al. have assessed the influence on the levelized cost of electricity of the design wind speed [19]. Desai and Bandyopadhyay have reported extensive energy and economic analysis of CSP plant [20].

In the above literatures, these researches focus on the energy conversion efficiency and the concentrating types, but the effect of the local length of parabolic dish and geometrical configuration of the receiver on the radiation flux and the system's efficiency is limited. In this paper, the concentrating ways of sunlight firstly have been established based on Monte Carlo ray-tracing method. After that, the effect of the local length on the radiation flux in the local plane and the receiver has been investigated. Finally, the effect of the geometrical configuration of the receiver on the radiation flux distribution has been simulated. The present study can provide a reference for the future design and application of CSP plant.

## 2. Monte Carlo Ray-Tracing Method

The Monte Carlo ray-tracing method, referred to as MCRT, is a popular tool with high accuracy in this field [21, 22]. Therefore, MCRT method has been employed for calculating radiation performance for all cases in present study. As we have known, the idea of this method is that the transfer process of the solar radiation is divided into four subprocesses, that is, emission, reflection, absorption, and scattering, and every subprocess has an occurrence probability [23–27]. The object of the study is divided into many surface units and mathematical functions can stand for them. The MCRT method used in this paper is to assume every surface emits a certain quantity of light rays, after which each ray is tracked and judged based on whether it is absorbed by the material, interface, or escapes from the system. In the numerical simulation, each sunlight ray carries the same amount of energy and has a specific direction determined from the appropriate probability function. What happens to each of these sunlight rays depends on the physical parameters of the materials of the system, which is described by a set of statistical relationships. The computer code for MCRT method has been written in FORTRAN language in-house. The detailed description of this model can be inferred from the literature [3]. The outer surface of the receiver is considered to be adiabatic. The receiver is located at the focal plane of the parabolic dish system.

## 3. Results and Discussions

*3.1. Effect of the Local Length on the Radiation Flux Distribution.* In this study, the radiation flux distributions of the local plane and receiver within three local lengths, that is, 2500 mm, 3250 mm, and 4000 mm, have been obtained. In simulation process, the basic parameters are as follows: incident solar irradiation in the air is 1100 W/m$^2$, system error is 0 mrad, radius of the parabolic dish concentrator is 2600 mm, height of the parabolic dish concentrator is 520 mm, reflectivity of the parabolic dish concentrator is 0.9, radius of the cylindrical receiver is 100 mm, and height of the cylindrical receiver is 260 mm.

Light spot performance of the local plane in different local lengths has been simulated and shown in Figure 1. It can be seen from the figure that the light spot is circle and radius of light spot increases with increasing of local length. The results show that the diameter of light spot is about 22.4 mm and radiation flux of light spot is about 30.46 MW/m$^2$ when the local length is 2500 mm. Meanwhile, the results show that the diameter of light spot is about 30.0 mm and radiation flux of light spot is about 21.80 MW/m$^2$ when the local length is 3250 mm. The results also show that the diameter of light spot is about 37.0 mm and radiation flux of light spot is about 18.58 MW/m$^2$ when the local length is 4000 mm.

3D radiation flux distribution of the receiver in different local lengths has been simulated and shown in Figure 2. It is very obvious that the positions with the maximum flux are about 60 mm, 127 mm, and 160 mm when the local lengths are 2500 mm, 3250 mm, and 4000 mm, respectively. It also can be found that the position with the maximum flux increases with increasing of local length. This distribution has indicated that local length has important effect on the concentrating characteristic of sunlight. When sunlight hits the wall of the receiver, almost all sunlight rays can be absorbed by the receiver.

Figure 3 shows the curve of the position along the wall, the diameter of light spot, and the radiation flux of light spot in different local lengths. It can be obtained from the figure that the optimal design is essential for the system. When the radius of the receiver is more than the radius of light spot, the sunlight can enter into the receiver. However, when the radius of the receiver is less than the radius of light spot, part of sunlight rays cannot enter into the receiver, which produces optical heat loss. According to the above results, the function of the position along the wall and the local length with an error of 5% can be proposed and given as follows:

$$\tan\theta = 10.10 - 5.05 \times 10^{-3} \times p + 0.67022 \times 10^{-6} \times p^2, \quad (1)$$

where $\theta$ is an angle of the axis direction of the receiver and inlet direction of the sunlight and $p$ is local length with unit of mm. For this equation, it can only be used for the same concentrating system and the cylindrical receiver. Also, when the parameters of the concentrating system change, the results can accordingly be obtained from the computer code for MCRT method.

*3.2. Effect of Geometrical Configuration on the Radiation Flux Distribution.* To investigate the effects of the geometrical configurations on the radiation flux distribution, four receivers (i.e., frustum, inverted frustum, cylindrical, and conical receivers) shown in Figure 4 have been designed and simulated. The parameters of the receiver are given based on the equal area-height and area-radius method and shown in Tables 1 and 2, respectively.

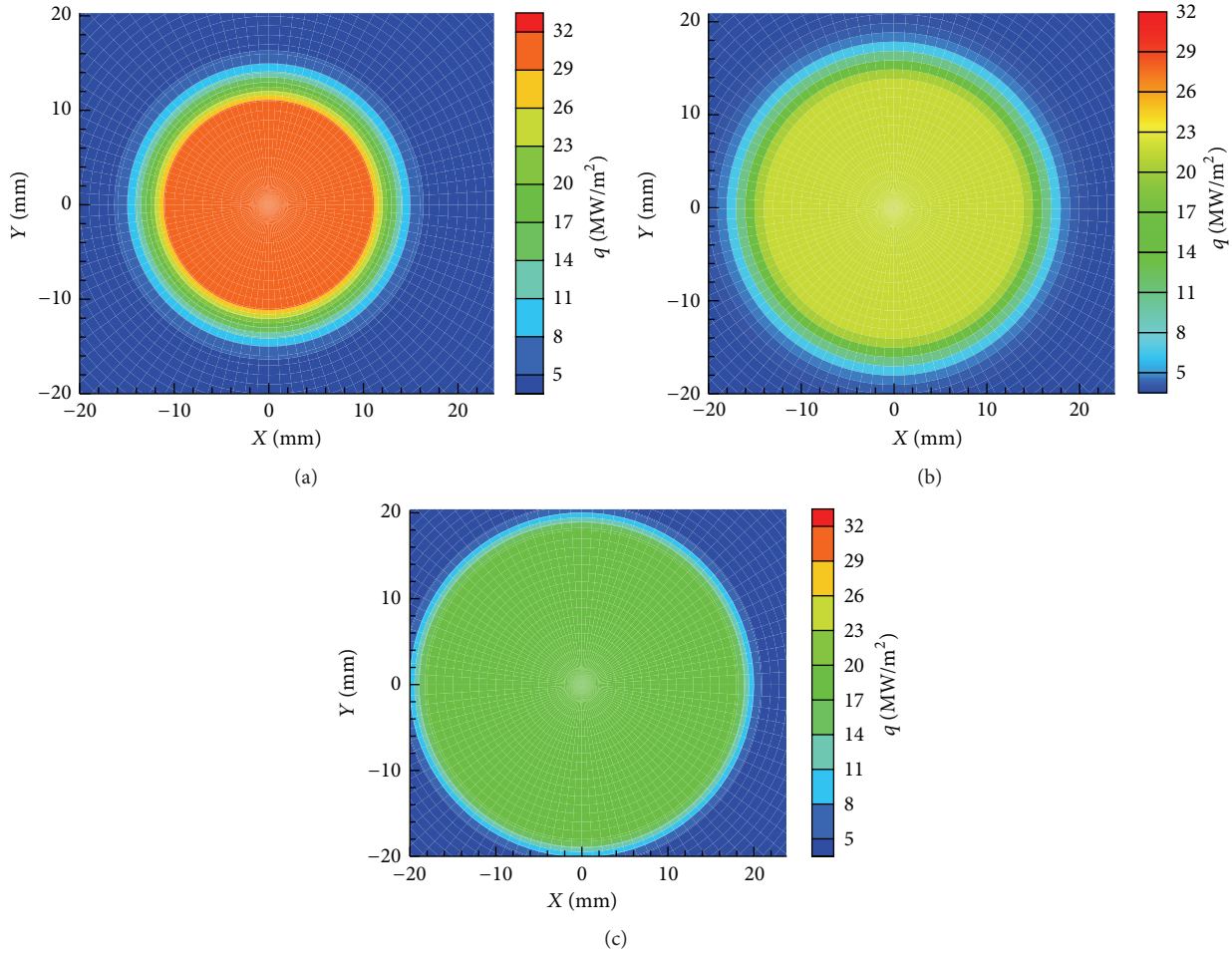


Figure 1: Radiation flux distribution in focal plane with different focal lengths: (a) 2500 mm; (b) 3250 mm; (c) 4000 mm.

Table 1: Design parameters of the receiver based on equal area-height method.

| Shapes | Height (mm) | Radius in the bottom (mm) | Radius in the top (mm) |
|---|---|---|---|
| Frustum | 260 | 120 | 78 |
| Inverted frustum | 260 | 78 | 120 |
| Cylindrical | 260 | 100 | 100 |
| Conical | 260 | 168 | 0 |

Table 2: Design parameters of the receiver based on equal area-radius method.

| Shapes | Height (mm) | Radius in the bottom (mm) | Radius in the top (mm) |
|---|---|---|---|
| Frustum | 235 | 100 | 120 |
| Inverted frustum | 285 | 100 | 80 |
| Cylindrical | 260 | 100 | 100 |
| Conical | 510 | 100 | 0 |

Figure 5 shows the radiation flux distribution of the receiver based on equal area-height method. It can be seen from the figure that (1) the radiation flux is symmetrical along the circumferential direction; (2) the performance for the radiation flux distribution in the conical receiver is the worst; (3) the characteristics of the radiation flux distribution in the cylindrical receiver are similar to frustum and inverted frustum receiver.

Figure 6 shows the radiation flux distribution of the receiver based on equal area-radius method. It also can be seen from the figure that (1) the radiation flux is also symmetrical along the circumferential direction; (2) the performance for the radiation flux distribution in the conical receiver is the worst. All radiation flux almost focuses on the middle of the receiver and a little radiation flux in the top and bottom of the receiver; (3) the radiation flux distribution in the cylindrical receiver obviously priors to other receivers. For getting the higher efficiency of the system, the higher radiation flux is necessary for the receiver.

## 4. Conclusions

In this paper, radiation flux in the focal plane and the receiver with three focal lengths has been investigated based on

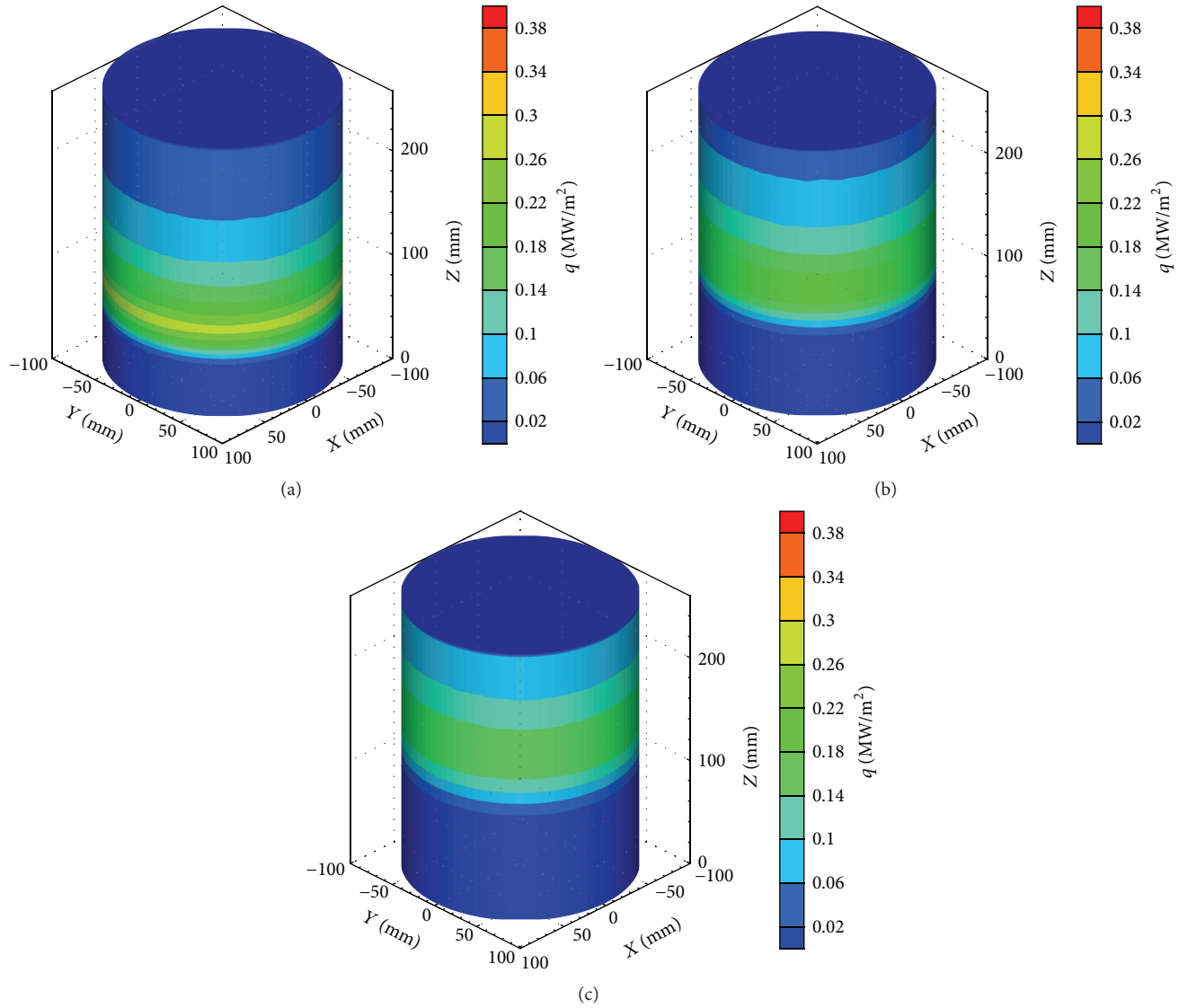


Figure 2: Radiation flux distribution in the receiver with different focal lengths: (a) 2500 mm; (b) 3250 mm; (c) 4000 mm.

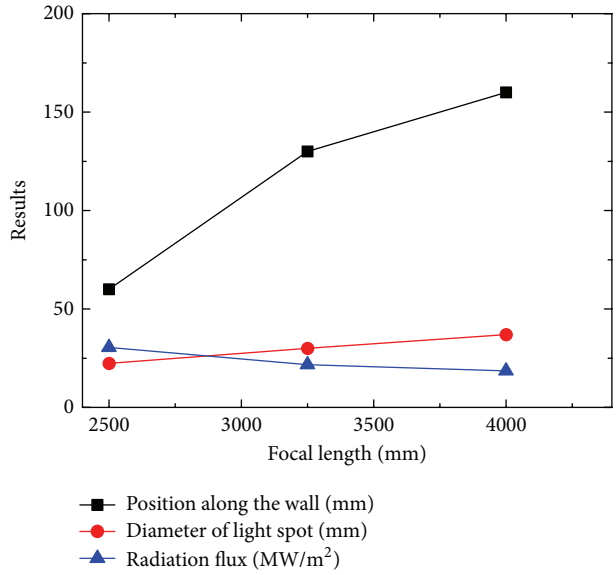


Figure 3: Effect of the focal length on the performance of concentrating characteristics.

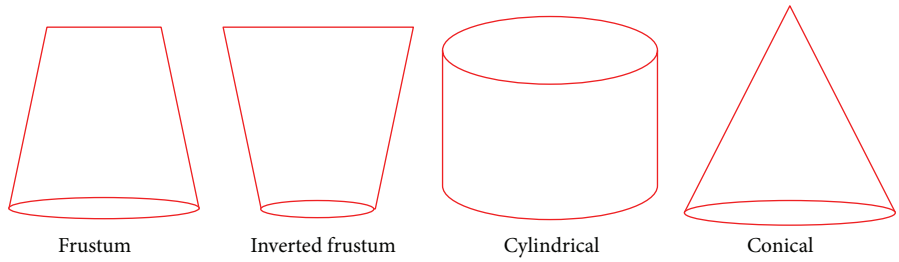


Figure 4: Four types of the receiver.

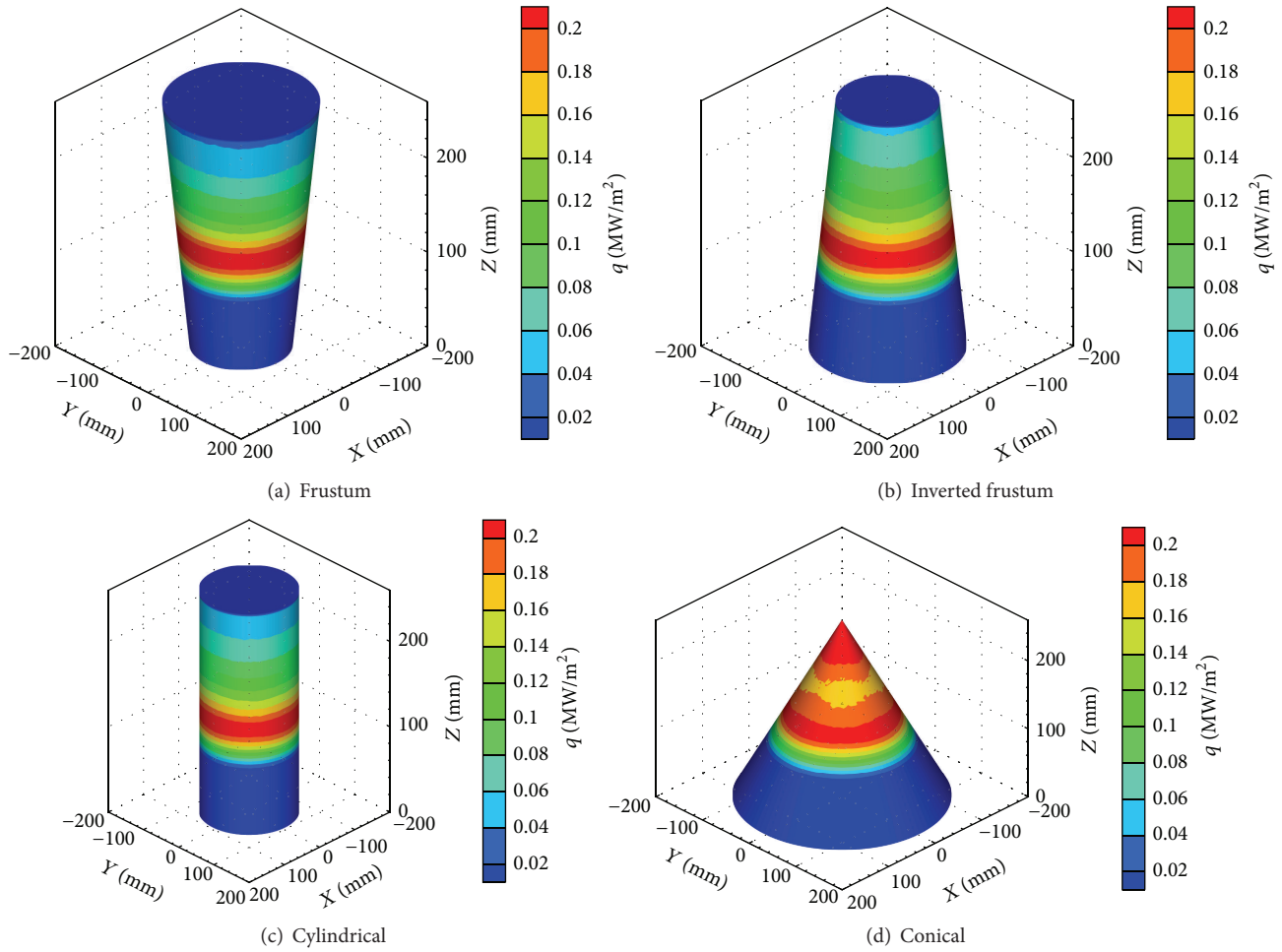


Figure 5: Radiation flux distribution based on equal area-height method.

MCRT method. Also, four different shape receivers have been designed and simulated based on the equal area-height and equal area-diameter methods. The main conclusions can be given as follows:

(1) The radiation flux in the focal plane increases with decreasing of the focal length and the diameter of the light spot increases with increasing of the focal length.

(2) The positions with the maximum flux are about 60 mm, 127 mm, and 160 mm when the local lengths are 2500 mm, 3250 mm, and 4000 mm, respectively. The function of the position with a maximum of radiation flux has been obtained according to the simulation results in this paper.

(3) The results show that the radiation flux distribution of cylindrical receiver has the best performance in all four receivers, which will result in a higher efficiency of the system.

This paper aims to know the characteristic of radiation flux distribution for the receiver in different focal lengths

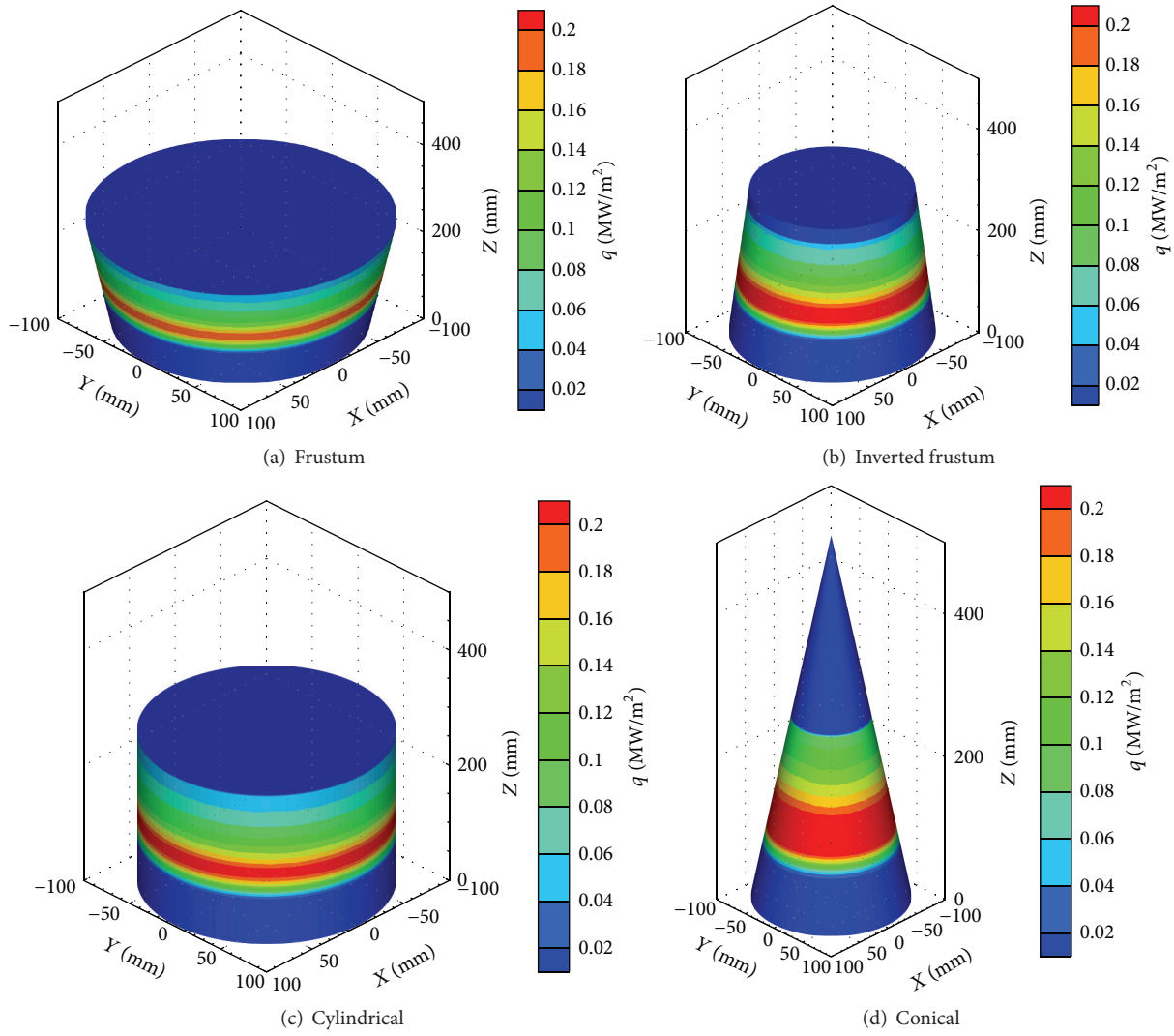


Figure 6: Radiation flux distribution based on equal area-radius method.

and geometrical configurations and make a starting point to motivate future investigation in this field.

## Conflict of Interests

The authors declare that there is no conflict of interests regarding the publication of this paper.

## Acknowledgments

This work is supported by the National Natural Science Foundation of China (nos. 51406033 and 21306022), University Nursing Program for Young Scholars with Creative Talents in Heilongjiang Province (no. UNPYSCT-2015075), and the Natural Science Foundation of Heilongjiang Province (no. LC2012C35). Besides, a very special acknowledgement is made to the editors and referees who made important comments to improve this paper.

## References

[1] J. T. Liu, M. Li, Q. F. Yu, and D. L. Ling, "A novel parabolic trough concentrating solar heating for cut tobacco drying system," *International Journal of Photoenergy*, vol. 2014, Article ID 209028, 10 pages, 2014.

[2] F. Al-Amri and T. K. Mallick, "Effects of nonuniform incident illumination on the thermal performance of a concentrating triple junction solar cell," *International Journal of Photoenergy*, vol. 2014, Article ID 642819, 12 pages, 2014.

[3] Q. Mao, Y. Shuai, and Y. Yuan, "Study on radiation flux of the receiver with a parabolic solar concentrator system," *Energy Conversion and Management*, vol. 84, pp. 1–6, 2014.

[4] Q. Mao, Y. Yuan, and Y. Shuai, "Effects of atmospheric aerosol on the direct normal irradiance on the earth's surface," *International Journal of Hydrogen Energy*, vol. 39, no. 12, pp. 6364–6370, 2014.

[5] M. Qianjun, X. Ming, S. Yong, and Y. Yuan, "Study on solar photo-thermal conversion efficiency of a solar parabolic dish

system," *Environmental Progress and Sustainable Energy*, vol. 33, no. 4, pp. 1438–1444, 2014.

[6] Q. Mao, M. Xie, and H. Tan, "Effects of material selection on the radiation flux of a tube receiver in a dish solar system," *Heat Transfer Research*, vol. 45, no. 4, pp. 339–347, 2014.

[7] K. S. Reddy and G. Veershetty, "Viability analysis of solar parabolic dish stand-alone power plant for Indian conditions," *Applied Energy*, vol. 102, pp. 908–922, 2013.

[8] Z. Li, D. Tang, J. Du, and T. Li, "Study on the radiation flux and temperature distributions of the concentrator-receiver system in a solar dish/Stirling power facility," *Applied Thermal Engineering*, vol. 31, no. 10, pp. 1780–1789, 2011.

[9] H. Singh and P. C. Eames, "A review of natural convective heat transfer correlations in rectangular cross-section cavities and their potential applications to compound parabolic concentrating (CPC) solar collector cavities," *Applied Thermal Engineering*, vol. 31, no. 14-15, pp. 2186–2196, 2011.

[10] J. Ji, C. Guo, W. Sun, W. He, Y. Wang, and G. Li, "Experimental investigation of tri-functional photovoltaic/thermal solar collector," *Energy Conversion and Management*, vol. 88, pp. 650–656, 2014.

[11] J. Ji, Y. Wang, W. Yuan, W. Sun, W. He, and C. Guo, "Experimental comparison of two PV direct-coupled solar water heating systems with the traditional system," *Applied Energy*, vol. 136, pp. 110–118, 2014.

[12] J. Jie, J. Cai, W. Huang, and Y. Feng, "Experimental study on the performance of solar-assisted multi-functional heat pump based on enthalpy difference lab with solar simulator," *Renewable Energy*, vol. 75, pp. 381–388, 2015.

[13] L. Guiqiang, P. Gang, S. Yuehong, J. Jie, and S. B. Riffat, "Experiment and simulation study on the flux distribution of lens-walled compound parabolic concentrator compared with mirror compound parabolic concentrator," *Energy*, vol. 58, pp. 398–403, 2013.

[14] G. Li, G. Pei, J. Ji, and Y. Su, "Outdoor overall performance of a novel air-gap-lens-walled compound parabolic concentrator (ALCPC) incorporated with photovoltaic/thermal system," *Applied Energy*, vol. 144, pp. 214–223, 2015.

[15] Y. Shuai, X. Xia, and H. Tan, "Radiation performance of dish solar concentrator/cavity receiver systems," *Solar Energy*, vol. 82, no. 1, pp. 13–21, 2008.

[16] A. M. Clausing, "An analysis of convective losses from cavity solar central receivers," *Solar Energy*, vol. 27, no. 4, pp. 295–300, 1981.

[17] A. M. Clausing, "Convective losses from cavity solar receivers–comparisons between analytical predictions and experimental results," *Journal of Solar Energy Engineering, Transactions of the ASME*, vol. 105, no. 1, pp. 29–33, 1983.

[18] K. Nithyanandam and R. Pitchumani, "Cost and performance analysis of concentrating solar power systems with integrated latent thermal energy storage," *Energy*, vol. 64, pp. 793–810, 2014.

[19] M. J. Emes, M. Arjomandi, and G. J. Nathan, "Effect of heliostat design wind speed on the levelised cost of electricity from concentrating solar thermal power tower plants," *Solar Energy*, vol. 115, pp. 441–451, 2015.

[20] N. B. Desai and S. Bandyopadhyay, "Optimization of concentrating solar thermal power plant based on parabolic trough collector," *Journal of Cleaner Production*, vol. 89, pp. 262–271, 2014.

[21] Z. Cheng, Y. He, and F. Cui, "Studies on concentrating solar collectors with a new modelling method and unified MCRT code," *Chinese Science Bulletin*, vol. 57, no. 22, pp. 2127–2136, 2012 (Chinese).

[22] J. B. Fang, J. J. Wei, X. W. Dong, and Y. S. Wang, "Thermal performance simulation of a solar cavity receiver under windy conditions," *Solar Energy*, vol. 85, no. 1, pp. 126–138, 2011.

[23] T. H. Ping and M. Lallemand, "Transient radiative-conductive heat transfer in flat glasses submitted to temperature, flux and mixed boundary conditions," *International Journal of Heat and Mass Transfer*, vol. 32, no. 5, pp. 795–810, 1989.

[24] T. Heping, B. Maestre, and M. Lallemand, "Transient and steady-state combined heat transfer in semi-transparent materials subjected to a pulse or a step irradiation," *Journal of Heat Transfer*, vol. 113, no. 1, pp. 166–173, 1991.

[25] F. Wang, Y. Shuai, H. Tan, and C. Yu, "Thermal performance analysis of porous media receiver with concentrated solar irradiation," *International Journal of Heat and Mass Transfer*, vol. 62, no. 1, pp. 247–254, 2013.

[26] F. Wang, R. Lin, B. Liu, H. Tan, and Y. Shuai, "Optical efficiency analysis of cylindrical cavity receiver with bottom surface convex," *Solar Energy*, vol. 90, pp. 195–204, 2013.

[27] F. Wang, Y. Shuai, H. Tan, and L. Gong, "Proposal of the shape layout of trapezoidal cavity receiver to improve the optical efficiency," *Heat Transfer Research*, vol. 46, no. 5, pp. 429–446, 2015.

Hindawi Publishing Corporation
International Journal of Photoenergy
Volume 2015, Article ID 786246, 6 pages
http://dx.doi.org/10.1155/2015/786246

*Research Article*

# Application of a Noncarboxylated Dye Compound in a Dye-Sensitized Solar Cell Containing a Cyclodextrin Layer

**Tatsuya Takeshita, Takao Umeda, Noriaki Oonishi, and Michihiro Hara**

*Department of Environmental and Food Sciences, Fukui University of Technology, 3-6-1 Gakuen, Fukui 910-8505, Japan*

Correspondence should be addressed to Michihiro Hara; hara@fukui-ut.ac.jp

Received 16 April 2015; Accepted 28 May 2015

Academic Editor: Xudong Zhao



We report the fabrication and characterization of a dye-sensitized solar cell containing a carboxymethyl-$\beta$-cyclodextrin sodium salt (CM-$\beta$-CD) layer and a noncarboxylated dye compound (tris(2,2′-bipyridyl)ruthenium(II)dichloride hexahydrate (Ru-dye)). The values of the incident photon-to-current conversion efficiency (IPCE) of the Ru-dye/CM-$\beta$-CD-containing device measured under 450 and 490 nm light irradiation were, respectively, 2.35% and 3.33%. The IPCE was due to the absorption of Ru-dye in ethanol solution. In contrast, the IPCE of the device that was prepared without the CM-$\beta$-CD layer measured under 450 nm irradiation was approximately three times smaller. Accordingly, the current findings demonstrate the application of a noncarboxylated dye compound in DSSCs incorporating a CM-$\beta$-CD layer.

## 1. Introduction

Dye-sensitized solar cells (DSSCs) have attracted much attention owing to their colorful appearance, low manufacturing cost, and application as a clean energy conversion device. Recently, various types of highly efficient DSSCs, such as organic thin film devices, flexible, and perovskite-based devices, have been produced at low cost [1–9]. The photoelectric conversion mechanism of DSSCs involves the following processes: (1) injection of electrons by the photoexcited chemically adsorbed dye molecule into the titanium oxide ($TiO_2$) layer and (2) reduction of the oxidized dye by a redox couple ($I/I_3^-$) present in the electrolyte. The maximum conversion efficiency of DSSCs reported to date is ~10% [10]; however, the conversion efficiency values remain to date significantly lower than the expected theoretical values [11] for inorganic solar cells. To address this issue, various parameters of the DSSC have been examined such as the photoanode, the counter electrode, and the optical properties of the dye and the electrolyte [12–19]. To improve cell performance, studies on the inclusion of a cyclodextrin- (CD-) based layer in the photoanode of DSSCs, though rare, have been reported, as exemplified. The inclusion of complexes of $\beta$-cyclodextrin and 4-methyl-1-cyclohexane carboxylic acid has been reported to inhibit electron recombination of the injected electrons and redox couples near the surface of the bare $TiO_2$ particles (employed as part of the photoanode) [20]. Additionally, the inclusion of [2]rotaxane formed by $\beta$-cyclodextrin and terpyridyl ruthenium complex achieved a cell conversion efficiency of 0.523% [21]. In contrast, the introduction of a dye molecule into DSSCs containing a CD layer via the inclusion effect of CD and the resulting cell performance have not been reported.

Presently, it is known that specific substituents, that is, carboxyl groups, are necessary for the chemical adsorption of the dye onto semiconductor $TiO_2$. However, such a requirement limits the choice of the dye compound for application in DSSCs that could potentially limit progress in the performance of DSSCs. It is known that CD molecules have cavities of which the sizes are dependent on the number of glucose units ($\alpha$-CD: 6 units; $\beta$-CD: 7 units; $\gamma$-CD: 8 units). The cavities can include various types of organic compounds by hydrophobic interaction in aqueous media. Thus, the incorporation of a CD layer in the device for the inclusion of dye molecules, not requiring specific (carboxylate) adsorptive groups, is expected to broaden the selection of dye

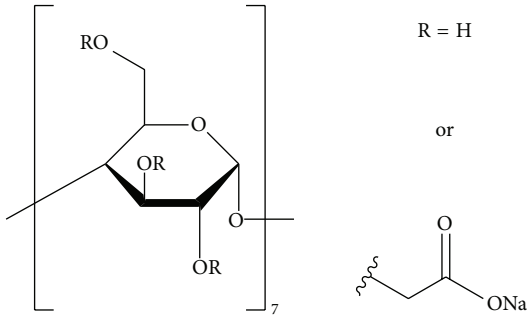


Figure 1: Molecular structure of carboxymethyl-$\beta$-cyclodextrin sodium salt (CM-$\beta$-CD).

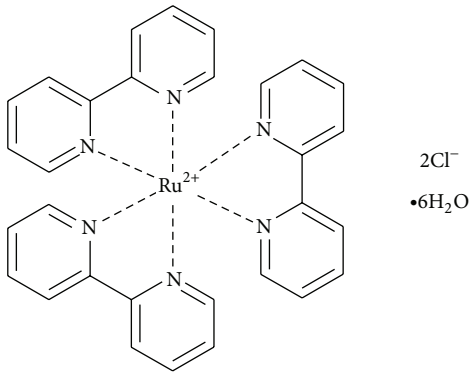


Figure 2: Molecular structure of tris(2,2′-bipyridyl)ruthenium(II) dichloride hexahydrate (Ru-dye).

molecules for application in DSSCs. Thus, offering a new strategy for the development of DSSCs with improved performance. Herein, we examined the fabrication and characterization of DSSCs featuring a CD (carboxymethyl-$\beta$-cyclodextrin sodium salt (CM-$\beta$-CD; Figure 1)) layer and the application of a noncarboxylated dye compound (tris-(2,2′-bipyridyl)ruthenium(II)dichloride hexahydrate (Ru-dye; Figure 2)) in DSSCs.

## 2. Experimental

*2.1. Materials.* The $TiO_2$ paste was prepared by mixing $TiO_2$ particles (6.0 g, Nippon Aerosil, Tokyo, Japan), polyethylene glycol (0.3 g, Nacalai Tesque), acetylacetonate (0.15 mL, WAKO), and Triton X-100 (0.3 mL, Nacalai Tesque). Ru-dye was purchased from Tokyo Kasei (Japan). The electrolyte solution was purchased from Solaronix. CM-$\beta$-CD was purchased from Sigma-Aldrich (Japan). The fluorine-doped tin oxide- (FTO-) coated glass with a sheet resistance of 9.3 $\Omega/cm^2$ was purchased from Asahi Glass Co., Ltd. Titanium tetrachloride ($TiCl_4$), benzene (spectrophotometric grade), and ethanol (spectrophotometric grade) were purchased from WAKO. All materials were used as received.

*2.2. Device Fabrication.* FTO-coated glass substrates were cleaned by successive washing in acetone (Nacalai Tesque, Kyoto, Japan), assisted with sonication and acetone vapor. Then, the FTO-coated glass substrates were irradiated with ultraviolet light (Senjyu UV lamp VX-200HK002) for 20 min. The $TiO_2$ paste was transferred to a bottle, and churning was performed for 10 min using a churning deaerator (THINKY, AR-100). Then, the $TiO_2$ paste was applied onto the FTO-coated glass substrates by a squeegee method and sintered for 1 h at 500°C. The temperature was set to rise from room temperature to 500°C for 20 min. The FTO-coated glass substrates were then immersed in 0.1 M $TiCl_4$ aqueous solution for 18 h. After immersion, the substrates were dried with warm air, and sintered at 500°C for 1 h. Two devices were fabricated in the absence and presence of a CM-$\beta$-CD layer (referred to as Ru-dye-containing and Ru-dye/CM-$\beta$-CD-containing devices, resp.). Adsorption of CM-$\beta$-CD onto the $TiO_2$-based DSSCs was performed by immersing the device in $2.9 \times 10^{-2}$ g/mL CM-$\beta$-CD aqueous solution for 24 h. Following immersion, the device was immersed in $3.0 \times 10^{-2}$ M ethanol solution for 24 h. Any residual dye solution was rinsed off with benzene. The counter electrode was fabricated by Pt sputtering the FTO-coated glass in Ar atmosphere.

*2.3. Measurements.* The current ($I$)-voltage ($V$) profiles of the devices under light irradiation (light source comprised 500 W Xe lamp, USHIO UXL-500SX, and MT10-T monochromator; Bunkoukeiki Co., Ltd.) were recorded on an Advantest R6243 power source meter. A condenser lens was also used. The light intensity was measured using a power meter (Broadband Power/Energy Meter, 13PEM 001, Melles Griot). For the $I$-$V$ and light intensity measurements, an aperture mask of 0.28 $cm^2$ was set on the device and power meter. The $I$-$V$ measurements were performed on an open cell. The short-circuit current density ($I_{sc}$), open-circuit voltage ($V_{oc}$), fill factor (FF), and incident photon-to-current conversion efficiency (IPCE) were evaluated from the $I$-$V$ profiles. The absorption and fluorescence spectra of Ru-dye in ethanol solution, and the Ru-dye-containing and Ru-dye/CM-$\beta$-CD-containing devices were recorded on a spectrophotometer (Hitachi, U-3310) and a fluorescence spectrophotometer (PerkinElmer, LS55), respectively.

## 3. Results and Discussion

*3.1. Steady-State Absorption and Fluorescence Spectra.* Figure 3 shows the steady-state absorption spectrum (black line) of Ru-dye in ethanol solution. A maximum absorption peak was observed at ~450 nm in the visible light region. A maximum fluorescence peak (red line) was observed at ~606 nm using a 450-nm light irradiation. The color (yellow) of the solution was consistent with a solution molar concentration in the order of $10^{-5}$ M.

*3.2. Structure of the Ru-Dye/CM-$\beta$-CD Complex.* The most stable minimum-energy structure obtained from the inclusion of Ru-dye into CM-$\beta$-CD, as calculated by MM2, is shown in Figure 4. The length and width of Ru-dye along the long and short axes were, respectively, 11.7 Å and 9.6 Å.

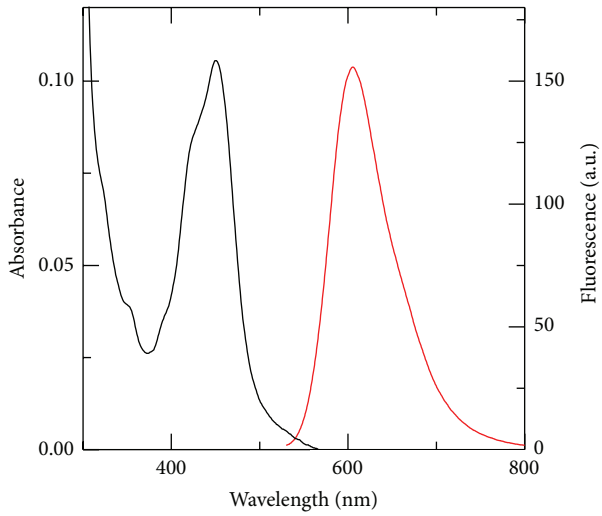


Figure 3: Absorption (black) and fluorescence (red) spectra of Ru-dye ($1.1 \times 10^{-5}$ M) in ethanol.

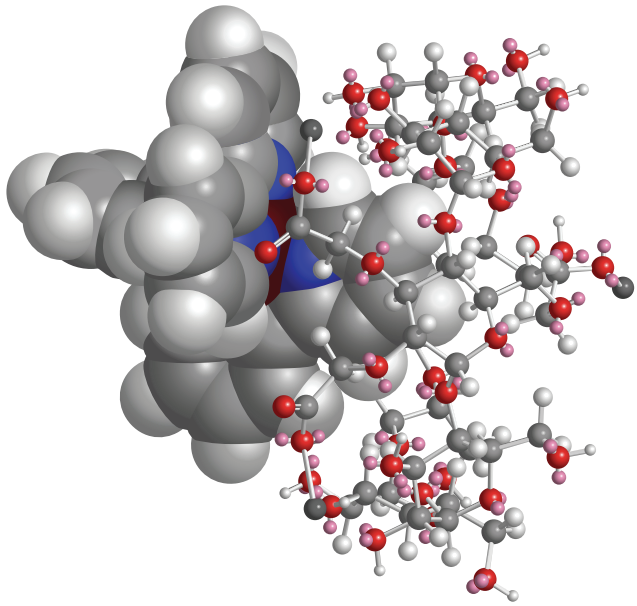

Figure 4: Minimum energy structure of the Ru-dye/CM-$\beta$-CD complex as calculated by MM2. The Ru-dye/CM-$\beta$-CD complex was modeled and subjected to geometry optimization to the most energetically stable structure using CS Chem3D.

The calculations indicated that only one of the pyridine rings of Ru-dye was incorporated into CM-$\beta$-CD while the two bipyridine units of Ru-dye protruded into the solution.

The photoelectrode surface of the device changed from white to yellow following immersion in the Ru-dye solution. The color of the photoelectrode surface was consistent with the color of Ru-dye in ethanol ($1.1 \times 10^{-5}$ M). The adsorption of Ru-dye onto the $TiO_2$ surface is expected to occur via

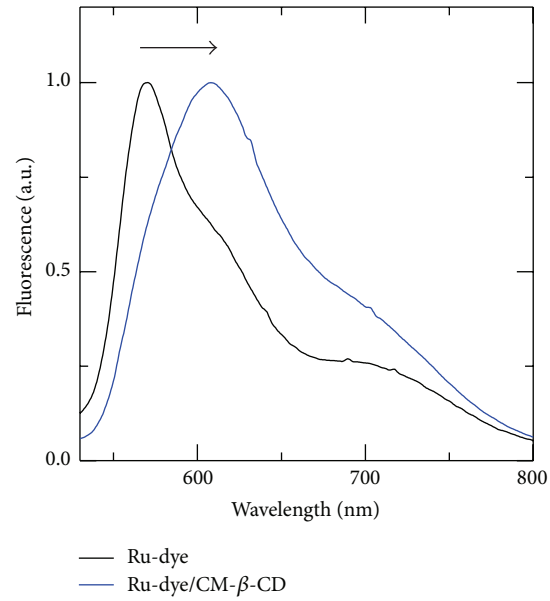


Figure 5: Fluorescence spectra of the Ru-dye-containing and Ru-dye/CM-$\beta$-CD-containing devices following excitation with 450 nm light irradiation.

chemical bonds between $TiO_2$ and hexahydrate Ru-dye. The fluorescence maximum peaks of the Ru-dye-containing and Ru-dye/CM-$\beta$-CD-containing devices were observed at ~570 and ~608 nm, using 450 nm light irradiation, respectively (Figure 5). In addition to the shift in the fluorescence maximum peak, the Ru-dye/CM-$\beta$-CD-containing device featured a broader fluorescence spectrum. For the Ru-dye-noncontaining and Ru-dye/CM-$\beta$-CD-noncontaining, fluorescence characteristics pertaining to $TiO_2$ were not observed using an excitation wavelength of 450 nm. This result indicated that Ru-dye was incorporated into the cavities of CM-$\beta$-CD. Therefore, the result suggested the occurrence of adsorption of the carboxylic acid sodium salt group of CM-$\beta$-CD onto $TiO_2$ and inclusion of Ru-dye into the cavities of CM-$\beta$-CD (in addition to the direct adsorption of Ru-dye onto $TiO_2$).

*3.3. Photovoltaic Performance of the DSSCs.* The *I-V* characteristics of the Ru-dye-containing and Ru-dye/CM-$\beta$-CD-containing devices were measured under 450 nm light irradiation (Figure 6). The irradiation wavelength was selected according to the absorption peak of Ru-dye in ethanol solution. As observed, the Ru-dye-containing and Ru-dye/CM-$\beta$-CD-containing devices featured *I-V* properties. Here, *I-V* characteristics were not affected by temperature from 15 to 25°C (i.e., at room temperature).

In contrast, the $TiO_2$ DSSC prepared in the absence of a dye sensitizing layer (i.e., Ru-dye or Ru-dye/CM-$\beta$-CD) did not display any *I-V* characteristics under 450 nm light irradiation. This confirms the onset of photoabsorption of

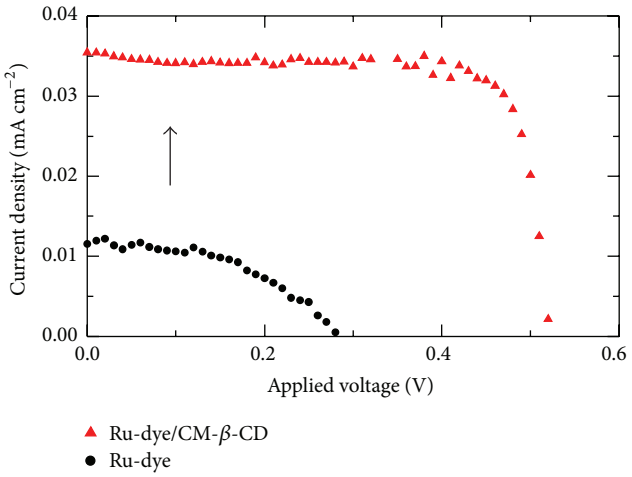


Figure 6: *I-V* profiles of the Ru-dye-containing and Ru-dye/CM-$\beta$-CD-containing devices measured under 450 nm light irradiation.

Ru-dye and Ru-dye/CM-$\beta$-CD for photoelectric conversion to occur (expressions (1) and (2)).

$$S_0 + h\nu \ (\lambda = 450\ \text{nm}:\ 2.8\ \text{eV}) \longrightarrow S_1\ (2.2\ \text{eV}) \longrightarrow \text{photoelectric conversion (Ru-dye)} \quad (1)$$

$$S_0 + h\nu \ (\lambda = 450\ \text{nm}:\ 2.8\ \text{eV}) \longrightarrow S_1\ (2.0\ \text{eV}) \longrightarrow \text{photoelectric conversion (Ru-dye/CM-}\beta\text{-CD)} \quad (2)$$

The singlet excitation energy ($S_1$) values of the Ru-dye-containing and Ru-dye/CM-$\beta$-CD-containing devices were calculated as 2.2 and 2.0 eV from the respective fluorescence spectra. The $S_1$ values of the Ru-dye-containing and Ru-dye/CM-$\beta$-CD-containing devices are smaller than the photon energy associated with 450 nm light irradiation (i.e., 2.8 eV), thereby implying the onset of photoelectric conversion (Figure 7).

The calculated IPCE values (under 450 nm light irradiation) of the Ru-dye-containing and Ru-dye/CM-$\beta$-CD-containing devices were 0.77% and 2.35%, respectively (Table 1). The higher IPCE of the Ru-dye/CM-$\beta$-CD-containing device was attributed to the increase in the concentration of Ru-dye in the device as a result of the CM-$\beta$-CD inclusion effect discussed earlier. Additionally, higher $V_{oc}$ and FF values were observed for the Ru-dye/CM-$\beta$-CD-containing device when compared with those of the Ru-dye-containing device. Improvements in the $V_{oc}$ and FF were attributed to the reduced electron recombination processes with $I_3^-$ in the electrolyte and electrons of the bare surface of the $TiO_2$ particles in the presence of the Ru-dye/CM-$\beta$-CD layer [20].

To confirm the photoabsorption of the Ru-dye/CM-$\beta$-CD-containing device in the visible light region, the *I-V* profiles of the device and associated IPCE values were calculated in the visible light region at intervals of 10 nm. The *I-V* profile of the device measured under 580 nm light irradiation is also included (Figure 8, black markers). Maximum IPCE of the Ru-dye/CM-$\beta$-CD-containing device was obtained under

Table 1: Photovoltaic performance of devices prepared in the absence and presence of a CM-$\beta$-CD layer.

| Device | $\lambda$ (nm) | FF | $V_{oc}$ (V) | $I_{sc}$ (mA/cm$^2$) | IPCE (%) |
|---|---|---|---|---|---|
| Ru-dye | 450 | 0.49 | 0.28 | 0.012 | 0.77 |
| Ru-dye/CM-$\beta$-CD | 450 | 0.78 | 0.52 | 0.035 | 2.35 |
| | 490 | 0.81 | 0.54 | 0.062 | 3.33 |

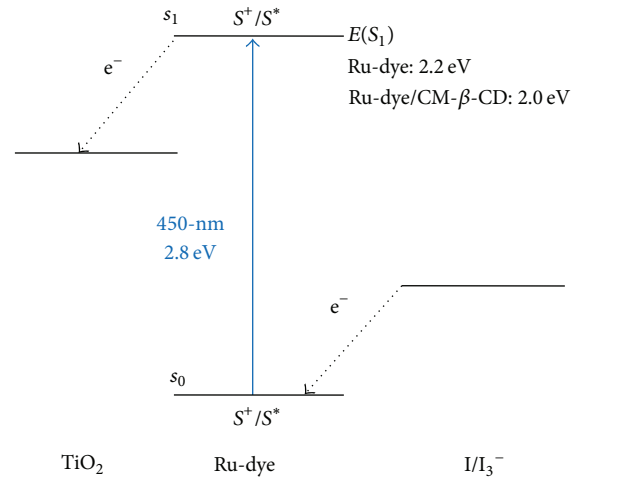


Figure 7: Energy diagrams of the Ru-dye-containing and Ru-dye/CM-$\beta$-CD-containing devices showing the ground and excited states of the devices.

490 nm light irradiation (Figure 8, blue markers). The $I_{sc}$, $V_{oc}$, and FF values obtained under 490 nm light irradiation are also listed in Table 1. The absorption spectrum of Ru-dye in ethanol and the IPCE spectrum of the Ru-dye/CM-$\beta$-CD-containing device were compared (Figure 9). As observed, the IPCE plot of the Ru-dye/CM-$\beta$-CD-containing device and absorption spectrum of Ru-dye in ethanol were comparable, which indicates that photoconversion efficiency is due to the photoabsorption of Ru-dye. However, the maximum IPCE peak was shifted by 40 nm relative to the absorption peak of Ru-dye in ethanol. This result suggests that Ru-dye is stabilized by polarity of the ethanol solution. Therefore, Ru-dye/CM-$\beta$-CD was photoabsorbed and acted as a sensitizing dye (Scheme 1).

## 4. Conclusion

We demonstrated the fabrication and characterization of a noncarboxylated Ru-dye-based DSSC incorporating a CM-$\beta$-CD layer. The formation of the Ru-dye/CM-$\beta$-CD inclusion complex was investigated by fluorescence spectroscopy. The fluorescence maximum peaks of the Ru-dye-containing and Ru-dye/CM-$\beta$-CD-containing devices were observed at ~570 and ~608 nm using an excitation wavelength of 450 nm. The shift in the maximum fluorescence peak of the CM-$\beta$-CD layer-containing device indicated that Ru-dye was incorporated into the CM-$\beta$-CD layer. The *I-V* characteristics of the Ru-dye/CM-$\beta$-CD-containing device measured under

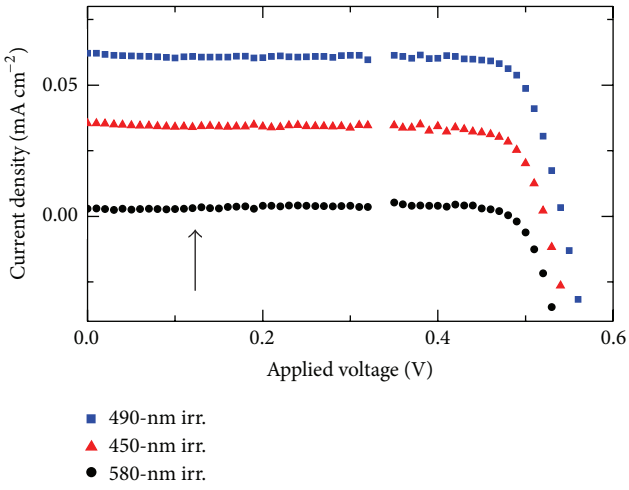


FIGURE 8: $I$-$V$ profiles of the Ru-dye/CM-$\beta$-CD-containing device measured under 580, 490, and 450 nm light irradiation.

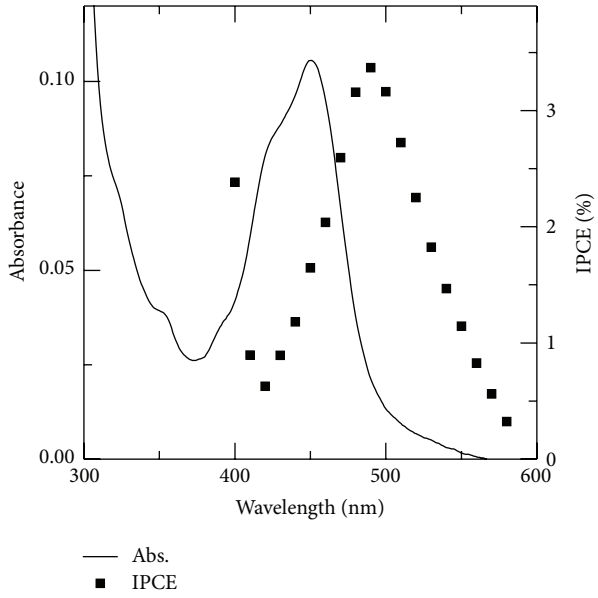


FIGURE 9: Plots of IPCE versus wavelength of Ru-dye/CM-$\beta$-CD-containing device and absorption spectrum of Ru-dye ($1.1 \times 10^{-5}$ M) in ethanol.

450 nm light irradiation confirmed the photoabsorption of Ru-dye/CM-$\beta$-CD relative to the $I$-$V$ results of device fabricated in the absence of Ru-dye ($TiO_2$ only), whereby photoabsorption was not observed. The IPCE was due to the absorption of Ru-dye. And the IPCE plot obtained at varying irradiation wavelengths nearly overlapped with the absorption spectrum of Ru-dye in ethanol measured at the same irradiation wavelengths. Additionally, the Ru-dye/CM-$\beta$-CD-based device featured improved photovoltaic performance.

In summary, the inclusion of the CM-$\beta$-CD layer improved the photovoltaic performance of the cell containing a noncarboxylated dye compound. The findings present

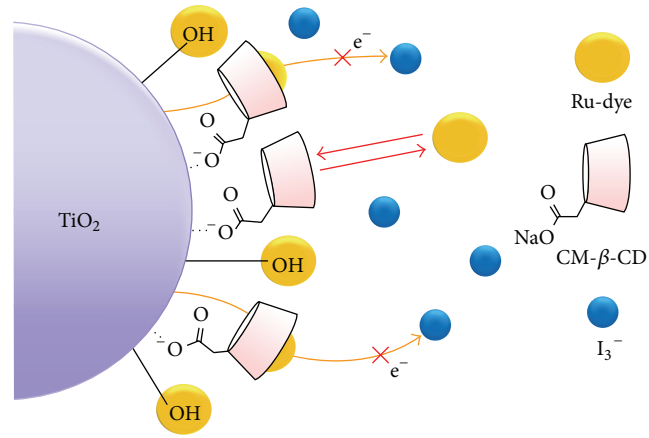


SCHEME 1: Model of the adsorption of Ru-dye/CM-$\beta$-CD complex onto $TiO_2$.

a gateway to future studies involving the optimization of devices incorporating a CM-$\beta$-CD layer and investigation of a wider selection of noncarboxylated compounds to achieve high photovoltaic efficiencies. Additionally, CM-$\beta$-CD-based DSSCs offer potential for IPCE control and enhancement of performance in the absence of external stimulus response molecules.

## Conflict of Interests

The authors report that there is no conflict of interests.

## Acknowledgment

This research was supported by the Ministry of Education, Culture, Sports, Science and Technology Program for the Strategic Research Foundation at Private Universities (2011–2016).

## References

[1] M.-D. Zhang, H.-X. Xie, X.-H. Ju et al., "D-D-$\pi$-A organic dyes containing 4,4′-di(2-thienyl)triphenylamine moiety for efficient dye-sensitized solar cells," *Physical Chemistry Chemical Physics*, vol. 15, no. 2, pp. 634–641, 2013.

[2] L. Kranz, C. Gretener, J. Perrenoud et al., "Doping of polycrystalline CdTe for high-efficiency solar cells on flexible metal foil," *Nature Communications*, vol. 4, article 2306, 2013.

[3] H.-M. Lee, S.-B. Kang, K.-B. Chung, and H.-K. Kim, "Transparent and flexible amorphous In-Si-O films for flexible organic solar cells," *Applied Physics Letters*, vol. 102, no. 2, Article ID 021914, 2013.

[4] G. J. Hedley, A. J. Ward, A. Alekseev et al., "Determining the optimum morphology in high-performance polymer-fullerene organic photovoltaic cells," *Nature Communications*, vol. 4, article 2867, 2013.

[5] J. Chang, Z. Ming Kam, Z. Lin, C. Zhu, J. Zhang, and J. Wu, "$TiO_x$/Al bilayer as cathode buffer layer for inverted organic solar cell," *Applied Physics Letters*, vol. 103, no. 17, Article ID 173303, 2013.

[6] J. Zhao, X. Yang, M. Cheng, S. Li, and L. Sun, "New organic dyes with a phenanthrenequinone derivative as the $\pi$-conjugated bridge for dye-sensitized solar cells," *The Journal of Physical Chemistry C*, vol. 117, no. 25, pp. 12936–12941, 2013.

[7] Q. Feng, X. Jia, G. Zhou, and Z.-S. Wang, "Embedding an electron donor or acceptor into naphtho[2,1-b:3,4-b′] dithiophene based organic sensitizers for dye-sensitized solar cells," *Chemical Communications*, vol. 49, no. 67, pp. 7445–7447, 2013.

[8] O. Malinkiewicz, A. Yella, Y. H. Lee et al., "Perovskite solar cells employing organic charge-transport layers," *Nature Photonics*, vol. 8, no. 2, pp. 128–132, 2014.

[9] D. Liu and T. L. Kelly, "Perovskite solar cells with a planar heterojunction structure prepared using room-temperature solution processing techniques," *Nature Photonics*, vol. 8, no. 2, pp. 133–138, 2014.

[10] B. O'Regan and M. Graetzel, "A low-cost, high-efficiency solar cell based on dye-sensitized colloidal $TiO_2$ films," *Nature*, vol. 353, no. 6346, p. 737, 1991.

[11] Z. Yue, H. Shen, Y. Jiang et al., "Large-scale black multicrystalline silicon solar cell with conversion efficiency over 18 %," *Applied Physics A*, vol. 116, no. 2, pp. 683–688, 2014.

[12] Y.-S. Chien, P.-Y. Yang, I.-C. Lee et al., "Enhanced efficiency of the dye-sensitized solar cells by excimer laser irradiated carbon nanotube network counter electrode," *Applied Physics Letters*, vol. 104, no. 5, Article ID 051114, 2014.

[13] S. G. Shin, K. H. Kim, C. W. Bark, and H. W. Choi, "Improving the performance of dye-sensitized solar cells by using the conversion luminescence of a phosphor," *Journal of the Korean Physical Society*, vol. 65, no. 10, pp. 1682–1686, 2014.

[14] S. G. Shin, C. W. Bark, and H. W. Choi, "The effect of phosphor-$TiO_2$ layer on the performance of dye-sensitized solar cells," *Molecular Crystals and Liquid Crystals*, vol. 600, no. 1, pp. 47–55, 2014.

[15] S.-J. Kim, H.-S. Ko, G.-H. Jeong, K.-H. Park, J.-J. Yun, and E.-M. Han, "Fabrication and characterization of reduced graphene oxide counter electrode for dye-sensitized solar cells," *Molecular Crystals and Liquid Crystals*, vol. 598, no. 1, pp. 1–5, 2014.

[16] D. Maheswari and P. Venkatachalam, "Enhanced efficiency and improved photocatalytic activity of 1 : 1 composite mixture of $TiO_2$ nanoparticles and nanotubes in dye-sensitized solar cell," *Bulletin of Materials Science*, vol. 37, no. 6, pp. 1489–1496, 2014.

[17] M. Imperiyka, A. Ahmad, S. A. Hanifah, A. A. Umar, N. S. Mohamed, and M. Y. Rahman, "Photo-polymerization of methacrylate based polymer electrolyte for dye-sensitized solar cell," *Journal of Polymer Engineering*, vol. 34, no. 8, pp. 695–702, 2014.

[18] F. Gu, W. Huang, S. Wang, X. Cheng, Y. Hu, and P. S. Lee, "Open-circuit voltage improvement in tantalum-doped $TiO_2$ nanocrystals ," *Physical Chemistry Chemical Physics*, vol. 16, no. 47, pp. 25679–25683, 2014.

[19] M. Z. Razali, H. Abdullah, S. Shaari, and M. R. Taha, "Preparation of photoelectrode CNT/$TiO_2$ doped ZnO nanocomposite by sol-gel method for dye-sensitized solar cell," *Optoelectronics and Advanced Materials, Rapid Communications*, vol. 8, no. 5-6, pp. 451–456, 2014.

[20] S. Park, H. Kim, S. Jang, and J. Won, "Effects of cyclodextrin complexes acting as barriers on $TiO_2$ nanoparticles in DSSCs," *Journal of Photochemistry and Photobiology A: Chemistry*, vol. 283, pp. 17–21, 2014.

[21] Y. Ou, G. Chen, J. Yin, G.-A. Yu, and S. H. Liu, "Rotaxane based on terpyridyl bimetal ruthenium complexes and $\beta$-cyclodextrin as organic sensitizer for dye-sensitized solar cells," *Journal of Coordination Chemistry*, vol. 64, no. 17, pp. 3062–3067, 2011.

Hindawi Publishing Corporation
International Journal of Photoenergy
Volume 2015, Article ID 151874, 7 pages
http://dx.doi.org/10.1155/2015/151874

*Research Article*

# Sensitive Analysis for the Efficiency of a Parabolic Trough Solar Collector Based on Orthogonal Experiment

**Xiaoyan Liu,[1,2] Jing Huang,[3] and Qianjun Mao[1]**

[1]*School of Civil Engineering, Northeast Petroleum University, Daqing 163318, China*
[2]*The Higher Educational Key Laboratory for Disaster Prevention, Mitigation and Protection Engineering of Heilongjiang Province, Northeast Petroleum University, Daqing 163318, China*
[3]*Installation Company, Daqing Oilfield Construction Company Ltd., Daqing 163300, China*

Correspondence should be addressed to Xiaoyan Liu; liu_xydq@163.com and Qianjun Mao; maoqianjun@163.com

Received 10 July 2015; Accepted 24 August 2015

Academic Editor: Xudong Zhao



A multitude of the researches focus on the factors of the thermal efficiency of a parabolic trough solar collector, that is, the optical-thermal efficiency. However, it is limited to a single or double factors for available system. The aim of this paper is to investigate the multifactors effect on the system's efficiency in cold climate region. Taking climatic performance into account, an average outlet temperature of LS-2 collector has been simulated successfully by coupling SolTrace software with CFD software. Effects of different factors on instantaneous efficiency have been determined by orthogonal experiment and single factor experiment. After that, the influence degree of different factors on the collector instantaneous efficiency is obtained clearly. The results show that the order of effect extent for average maximal deviation of each factor is inlet temperature, solar radiation intensity, diameter, flow rate, condensation area, pipe length, and ambient temperature. The encouraging results will provide a reference for the exploitation and utilization of parabolic trough solar collector in cold climate region.

## 1. Introduction

Recently, with the increasing attention of the international community about energy problem, solar energy and the other renewable energies rise gradually on large-scale application [1]. Under this background, the solar energy converting technology, especially concentrating light technology, has a broad prospect. There are several common concentrating collectors, such as trough type, dish type, and tower type. Compared with the other two collectors, the trough solar energy collector has been widely used. The most mature technologies are its convenient installation, simple construction, and the low cost [2–4]. Based on the above characteristics, a multitude of the researches focus on the factors of the thermal efficiency of a parabolic trough collector from a view of the optical and thermal properties.

Gao et al. [5, 6] have carried out the simulation on the performance of parabolic trough solar collector according to 30 $m^2$ experimental devices. The relationship of efficiency with the solar flux, the heat transfer fluid flow rate, the wind speed, and the diameter of the receivers has been found. Lüpfert et al. [7] have proposed methods for measuring receiver heat losses including field measurement and laboratory setups both based on energy balances from the hot inside of the receiver tube to the ambient air. Zhang et al. [8, 9] have presented an experimental study of the heat losses of a double glazing vacuum U-type solar receiver mounted in a parabolic trough collector natural circulation system for generating medium-temperature steam. Kalogirou [10] has a survey of the various types of solar thermal collector and application. The results of the paper show that solar energy collectors can be used in a wide variety of systems, can provide significant environmental and financial benefits, and will be used whenever possible. Xiao et al. [11] have simulated the heat flux distribution on the outer surface of absorber tube of a parabolic solar collector receiver based on Monte Carlo Ray-Trace method. Nonlinear heat flux distribution was considered as complex boundary condition used in FVM to simulate the coupled heat transfer problem. The results show that the angle span of reducing area becomes larger

Table 1: The basic parameters of the LS-2 collector.

| Pipe length (m) | Opening width (m) | Focal length (m) | Metal tube diameter (m) | Glass tube diameter (m) |
|---|---|---|---|---|
| 7.8 | 5 | 1.49 | 0.067 (inner)/0.075 (outer) | 0.115 |

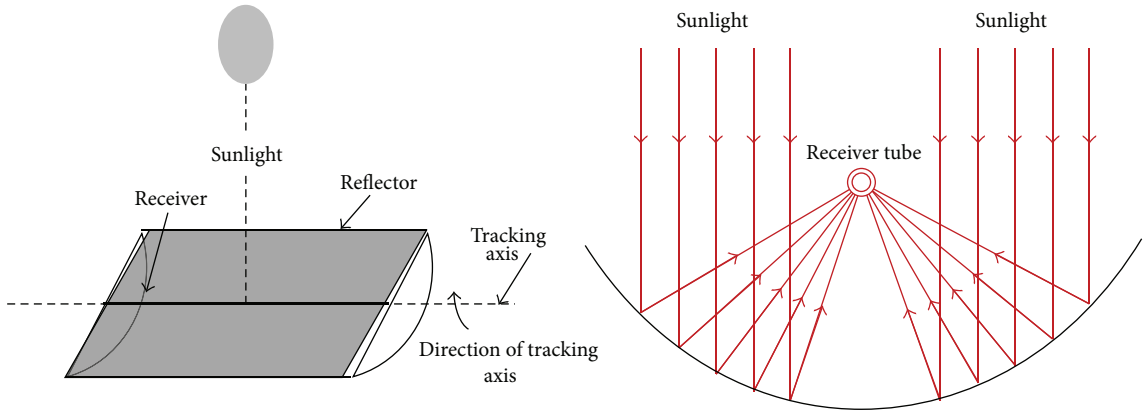


Figure 1: The main view and the axial diagram of the collector.

with increasing geometric concentration ratios. Naeeni and Yaghoubi [12] have investigated a two-dimensional numerical simulation of turbulent flow around parabolic tough collectors of the 250 kW solar power plants in Shiraz, Iran.

It is important to study the parabolic trough solar collector according to the above literature summaries. However, it is limited to single or double factors for available system. The aim of this paper is to investigate the multifactors effect on the system's efficiency in cold climate region. Therefore, effects of different factors on instantaneous efficiency have been determined by orthogonal experiment and simulated for each group of experiments. After that, the influence degree of different factors on the collector instantaneous efficiency is obtained clearly.

## 2. Model

*2.1. Physical Model.* In order to analyze the efficiency conveniently, LS-2 experiment trough solar collector has been selected for this study designed by Dudley et al. [13]. The basic parameters of the collector are listed in Table 1. The main view and axial diagram of the collector are shown in Figure 1.

The main principles of the model shown in Figure 1 are the following: the incident sunlights on the earth's surface deriving from the sun through the atmosphere hit the parabolic trough reflector and remain as perpendicular to the incident angle as possible through the solar tracking device; then the energy received by the reflector is reflected to the receiver. Therefore the receiver has received the high heat flux density of solar radiation, and the working fluid inside the pipe is heated to provide thermal power for the electric production.

*2.2. Mathematical Model.* The calculation of wall heat flux in collector's tube is numerically simulated using SolTrace software. Simulation conditions are as follows: the collector of the reflector plate is selected to aluminum with the reflectivity of 0.76, refractive index of 1, shape error of 3 mrad, and specular reflection error of 0.5 mrad; also, the reflectivity of metal collector tube is of 0.1, refractive index of 0, shape error of 0.0001 mrad, and specular reflection error of 0.0001 mrad. It is simulated by the ray-tracing method after the optical geometric parameters have been set. It is shown that the calculation accuracy is higher and the degree of operation is less when the ray quantities are $10^6$ and the most inputting lights are $10^8$. According to the simulated heat flux, the optical efficiency is calculated as follows:

$$\eta_{\text{opt}} = \frac{q_u \pi D_2 L}{I A_m}. \tag{1}$$

The instantaneous efficiency of the collector can be calculated by CFD software. The model of receiver tube and the 2D mesh has been obtained by Gambit tool. The division of grid adopts tetrahedral mesh; the grid size of fluid part is 1 mm, the grid size of the metal part is 2 mm, and grid needs to refine for both inner and outer surface of metal wall. The boundary condition of inlet section is velocity inlet whereas it is pressure outlet for the outlet. According to the simulation results, the instantaneous efficiency is calculated as follows:

$$\eta = \frac{Q_u}{A_m I} = \frac{C_p m \left(t_{\text{out}} - t_{\text{in}}\right)}{A_m I}, \tag{2}$$

where $\eta_{\text{opt}}$ is the optical efficiency of collector; $A_m$ is the opening area of parabolic mirror, $m^2$; $I$ is solar radiation intensity, $W/m^2$; $Q_u$ is the available energy of working fluid in the heating metal tube, W; $q_u$ is the surface heat flux of receiver, $W/m^2$; $D_2$ is the external diameter of receiver tube, mm; $L$ is the length of vacuum tube, m; $t_{\text{in}}$ is the temperature

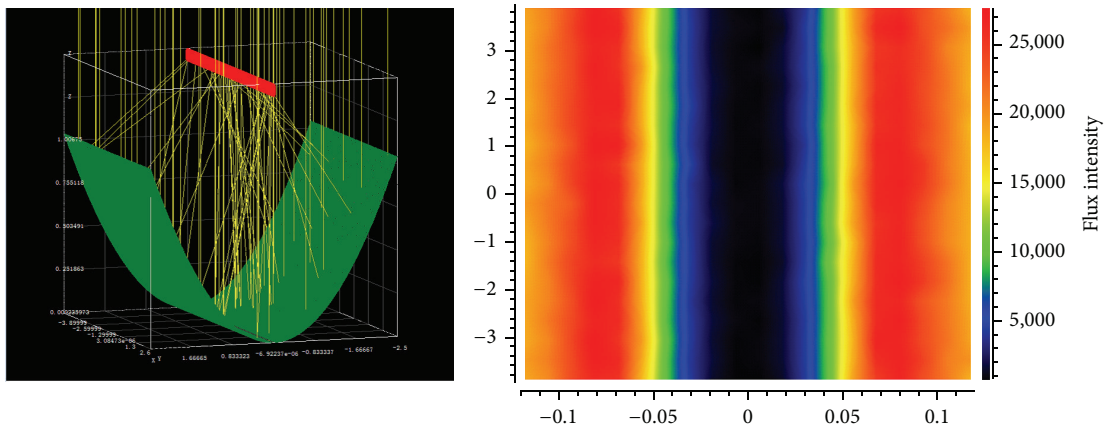


Figure 2: The simulation model and the heat density distribution of the LS-2 collector.

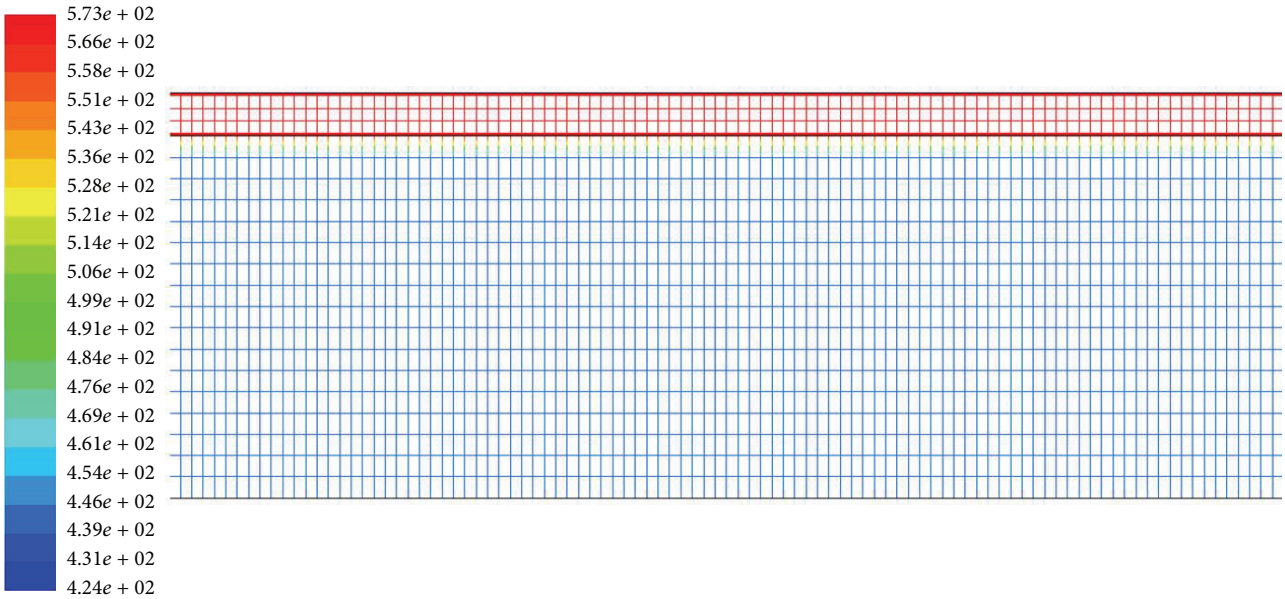


Figure 3: The temperature cloud of the receiver tube.

of fluid inlet, °C; $t_{out}$ is the average temperature of fluid outlet, °C; $m$ is the mass flow of fluid, kg/s. $C_p$ is specific heat J/(kg·K).

## 3. Results and Discussions

### 3.1. Verification of Simulation Results

*3.1.1. Model Validation of Optical Efficiency.* Simulation model and heat density distribution with the direct normal irradiance of 968.2 W/m$^2$ were shown in Figure 2. According to 1–50 rays, the result of average heat flux density of the collector is 15306 W/m$^2$. After that, the optical efficiency of 74.5% can be obtained by (1). Reference [13] shows that experimental results of the optical efficiency are 73.7%. Therefore, there is a good agreement of 1.07% between the simulation and experiment results.

*3.1.2. Model Validation of Instantaneous Efficiency.* To obtain the average outer temperature and the efficiency, the concrete parameter conditions are as follows: wind speed is 3.7 m/s, the ambient temperature is 22.4°C, the inlet flow rate is 0.24 m/s, and the inlet temperature of collector is 151°C. According to the average heat flux of metal tube surface simulated by SolTrace software, the average temperature of the fluid outlet has been simulated with the second boundary condition. Figure 3 shows the temperature cloud picture of the receiver tube. By monitoring on the average temperature of outlet, it is found that the temperature is 170.3°C when the iteration has been converged, which has an error of 0.4% with the previous experiment results of 171.3°C [13]. The instantaneous efficiency of collector is 62.2%.

*3.2. Sensitive Analysis of a Parabolic Trough Collector in Cold Climate.* It can be seen from the above section that the model is correct. In this section, water is used as the heat transfer

Table 2: The factors and levels graph.

| Level | Factors | | | | | | |
|---|---|---|---|---|---|---|---|
| | Pipe length (m) | Condensation area (m) | Diameter (mm) | Solar radiation intensity ($W/m^2$) | Ambient temperature (°C) | Flow rate (m/s) | Inlet temperature (°C) |
| 1 | 0.1 | 2 | 55 | 200 | −20 | 0.1 | 30 |
| 2 | 2 | 4.5 | 70 | 600 | 0 | 0.2 | 150 |
| 3 | 7 | 6.5 | 100 | 800 | 20 | 0.3 | 300 |

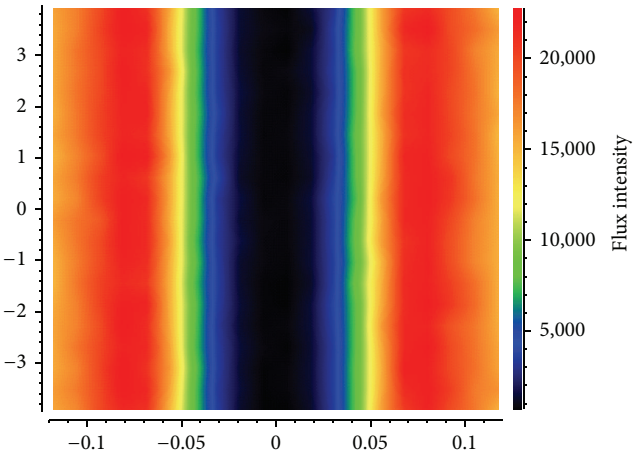


Figure 4: The heat density distribution of the collector.

medium and ambient parameters of the coldest month in Daqing city are regarded as meteorological parameters. The main parameters are the following: fluid inlet temperature is 30°C, flow rate is 0.2 m/s, solar radiation intensity is 800 $W/m^2$, and the ambient temperature is −18.5°C. Firstly, the average heat flux density of receiver is 12884.4 $W/m^2$, which is numerically simulated using SolTrace software and the instantaneous efficiency is 75.86% calculated by (1); secondly, outlet average temperature is 36.8°C, which is numerically simulated using CFD software which is a popular tool in solar radiation and application fields [14–17], and the instantaneous efficiency is 63.87% calculated by (2). Figures 4 and 5 are the picture of heat density distribution and the temperature cloud picture of the receiver tube in cold climate region.

*3.3. Influence Factor Analysis of Instantaneous Efficiency.* There are many parameters which can affect the collector efficiency, so the analysis of the influence factors can provide theoretical support and technical reserves for promotion and application of solar energy heat utilization technology. The main parameters in this paper are as follows: diameter, pipe length, condensation area, solar radiation intensity, flow rate, inlet temperature, and ambient temperature. Special points from different influencing factors, 7 factors and 3 level orthogonal tables for the orthogonal experiment, choosing L18 ($3^7$) orthogonal tables, the factors, and mathematical method have been used for the test arrangement scheme. Finally, by calculating and analyzing the test results, levels graphs are shown in Table 2.

As shown in Table 2, it needs 18 experimental results to simulate for each condition and then calculate the instantaneous efficiency. The experimental program and the simulation results are shown in Tables 3 and 4, respectively.

According to the results of Table 4, calculating the average values of factors index of *k1*, *k2*, and *k3* and average maximal deviation *R* at the same level and analyzing the primary and secondary factors, the results are shown in Table 5. It can be seen from the table that average maximal deviation *R* represents the influence degree of instantaneous efficiency of collector, and the greater average maximal deviation stands for the greater influence degree. Therefore, the results show that the order of effect extent for average maximal deviation of each factor is inlet temperature, solar radiation intensity, diameter, flow rate, condensation area, pipe length, and ambient temperature. According to the results, the effects of the three main factors on instantaneous efficiency determined by single factor experiment are shown in Figures 6–8.

It can be seen from Figure 6 that with the increasing inlet temperature the efficiency of collector decreases and the decreasing extent is gradually strong. The reason is that the temperature of the metal and glass tube increases with the increasing inlet temperature, the temperature difference between metal wall and outside glass tube gradually increases, and the radiative heat loss increases. In another view, the temperature outside glass tube increases with increasing radiative heat loss between metal pipe and glass tube. Meanwhile the thermal radiation loss and convective heat loss outside the surface of the glass tube to the atmosphere have also an increase. It can be seen from the figure that the efficiency almost goes to more than 60% with the inlet temperature less than 150°C. In Figure 7, the increasing of solar radiation intensity causes the instantaneous efficiency going higher with about 56.36~64.62%. Also, it can be found that the trend becomes rapid in 200–600 $W/m^2$; however, it slows down after the solar radiation of 600 $W/m^2$.

Figure 8 shows that with the increasing diameter of collector tube the collector efficiency increases at the beginning period and becomes slow after the diameter reaches up to 75 mm. Also, the efficiency decreases with increasing diameter when the diameter is more than 75 mm. The main reason is that with the increasing diameter of the metal pipe the area of collector increases, and the absorbed solar energy increases accordingly, which results in the increasing efficiency. On the

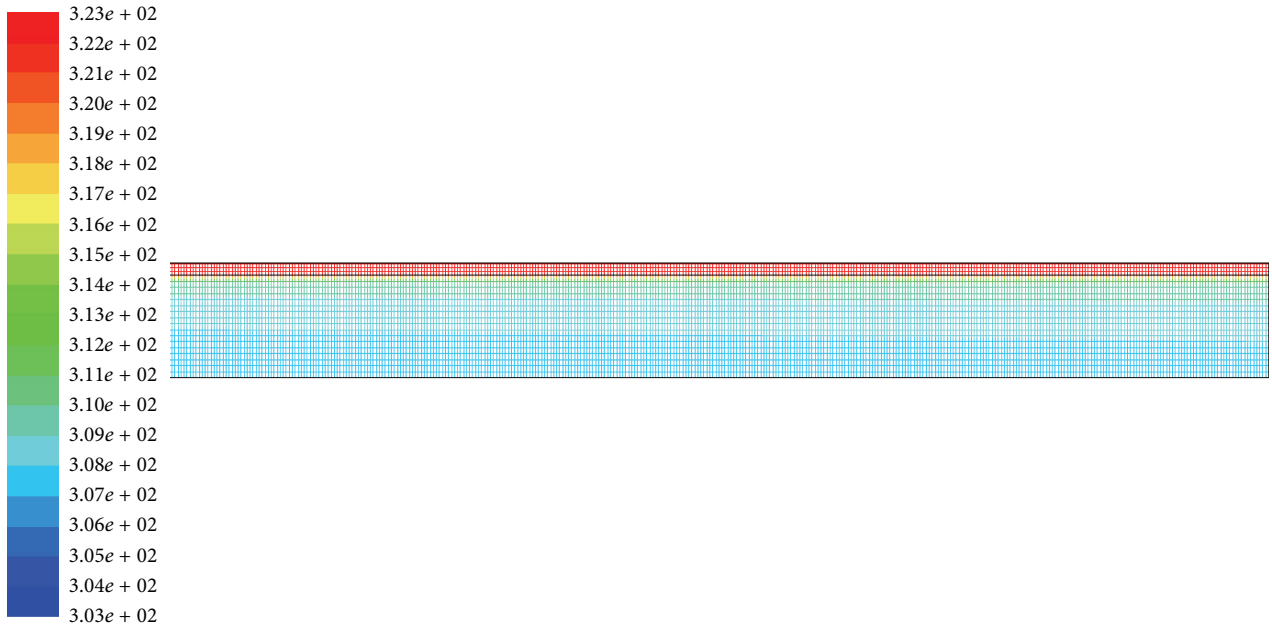


Figure 5: The temperature cloud of the receiver tube.

Table 3: Experimental program.

| Number | Pipe length (m) | Condensation area (m) | Diameter (mm) | Solar radiation intensity ($W/m^2$) | Ambient temperature (°C) | Flow rate (m/s) | Inlet temperature (°C) |
|---|---|---|---|---|---|---|---|
| 1 | 1 | 1 | 1 | 1 | 1 | 1 | 1 |
| 2 | 1 | 2 | 2 | 2 | 2 | 2 | 2 |
| 3 | 1 | 3 | 3 | 3 | 3 | 3 | 3 |
| 4 | 2 | 1 | 1 | 2 | 2 | 3 | 3 |
| 5 | 2 | 2 | 2 | 3 | 3 | 1 | 1 |
| 6 | 2 | 3 | 3 | 1 | 1 | 2 | 2 |
| 7 | 3 | 1 | 2 | 1 | 3 | 2 | 3 |
| 8 | 3 | 2 | 3 | 2 | 1 | 3 | 1 |
| 9 | 3 | 3 | 1 | 3 | 2 | 1 | 2 |
| 10 | 1 | 1 | 3 | 3 | 2 | 2 | 1 |
| 11 | 1 | 2 | 1 | 1 | 3 | 3 | 2 |
| 12 | 1 | 3 | 2 | 2 | 1 | 1 | 3 |
| 13 | 2 | 1 | 2 | 3 | 1 | 3 | 2 |
| 14 | 2 | 2 | 3 | 1 | 2 | 1 | 3 |
| 15 | 2 | 3 | 1 | 2 | 3 | 2 | 1 |
| 16 | 3 | 1 | 3 | 2 | 3 | 1 | 2 |
| 17 | 3 | 2 | 1 | 3 | 1 | 2 | 3 |
| 18 | 3 | 3 | 2 | 1 | 2 | 3 | 1 |

other hand, the efficiency of the collector decreases with heat loss increasing caused by increasing the surface area of the collector. In the meantime, with the increasing diameter of collector tube, the flow velocity obviously decreases because the flow rate is kept at a constant, and the efficiency must decrease because of the decreasing convective heat transfer rate between the inner wall of metal tube and the fluid. Based on the above analysis, there is a critical value of the diameter for this condition. When the diameter is less than the critical value, the efficiency increases with increasing the diameter, whereas it decreases with increasing the diameter when the diameter is more than the critical value.

Table 4: The experimental results of instantaneous efficiency.

| Serial number | Instantaneous efficiency (%) | Serial number | Instantaneous efficiency (%) | Serial number | Instantaneous efficiency (%) |
|---|---|---|---|---|---|
| 1 | 53.15 | 7 | 51.09 | 13 | 63.77 |
| 2 | 63.65 | 8 | 60.93 | 14 | 45.26 |
| 3 | 54.83 | 9 | 58.79 | 15 | 62.09 |
| 4 | 54.04 | 10 | 64.20 | 16 | 53.15 |
| 5 | 64.10 | 11 | 50.29 | 17 | 63.65 |
| 6 | 59.02 | 12 | 52.18 | 18 | 54.83 |

Table 5: Instantaneous efficiency factors analysis of parabolic trough collector (%).

| | Pipe length | Condensation area | Diameter | Solar radiation intensity | Ambient temperature | Flow rate | Inlet temperature |
|---|---|---|---|---|---|---|---|
| $k1$ | 56.38 | 58.38 | 55.38 | 52.51 | 57.17 | 56.25 | 60.12 |
| $k2$ | 58.05 | 56.36 | 58.50 | 59.49 | 57.03 | 59.00 | 59.93 |
| $k3$ | 57.50 | 57.19 | 58.05 | 59.94 | 57.74 | 56.68 | 51.89 |
| $R$ | 1.664 | 2.020 | 3.120 | 7.431 | 0.712 | 2.745 | 8.227 |

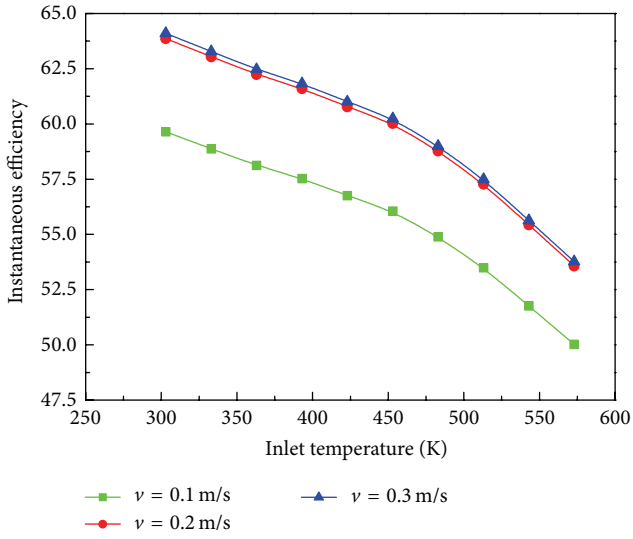


Figure 6: The influence of inlet temperature on the instantaneous efficiency.

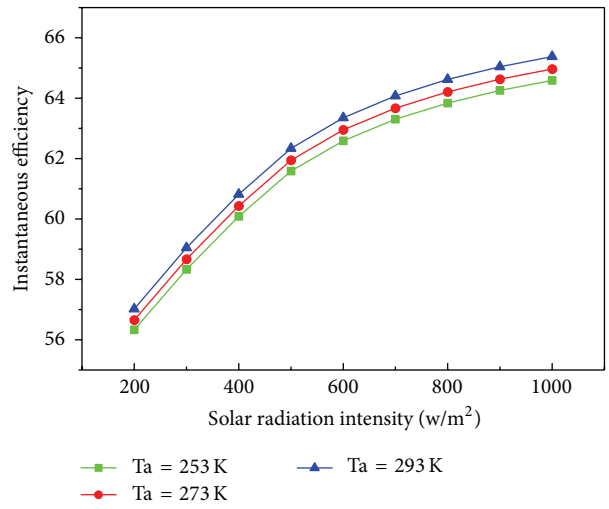


Figure 7: The influence of solar radiation intensity on the instantaneous efficiency.

## 4. Conclusions

Taking climatic performance into account, effects of different factors on instantaneous efficiency have been determined by orthogonal experiment and single factor experiment. The main conclusions are as follows:

(1) The results show that the order of effect extent for average maximal deviation of each factor is inlet temperature, solar radiation intensity, diameter, flow rate, condensation area, pipe length, and ambient temperature.

(2) The inlet temperature is the uppermost factor. The efficiency of collector is lower and lower, and the decrease extent is gradually strong with the increasing inlet temperature.

(3) The ambient temperature has a minimum effect on the efficiency. The instantaneous efficiency of collector has a slight increasing of about 1% when the ambient temperature increases.

(4) In this model, there is an optimal outer diameter of 75 mm for the collector. Also, the instantaneous efficiency of collector has a maximum in this case.

The results can provide a reference for the exploitation and utilization of this collector in cold climate region.

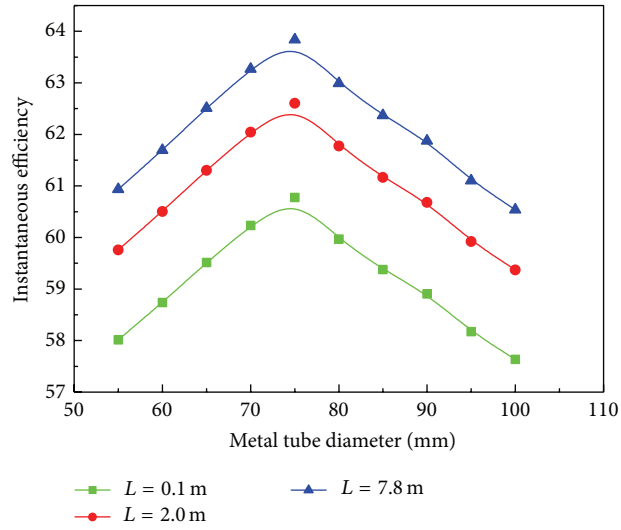


FIGURE 8: The influence of metal tube diameter on the instantaneous efficiency.

## Conflict of Interests

The authors declare that there is no conflict of interests regarding the publication of this paper.

## Acknowledgments

This work is supported by the National Natural Science Foundation of China (nos. 51176024 and 51406033) and University Nursing Program for Young Scholars with Creative Talents in Heilongjiang Province (no. UNPYSCT-2015075). Besides, a very special acknowledgement is made to the editors and referees who made important comments to improve this paper.

## References

[1] N. Nallusamy, S. Sampath, and R. Velraj, "Experimental investigation on a combined sensible and latent heat storage system integrated with constant/varying (solar) heat sources," *Renewable Energy*, vol. 32, no. 7, pp. 1206–1227, 2007.

[2] D. Mills, "Advances in solar thermal electricity technology," *Solar Energy*, vol. 76, no. 1–3, pp. 19–31, 2004.

[3] M. Thirugnanasambandam, S. Iniyan, and R. Goic, "A review of solar thermal technologies," *Renewable and Sustainable Energy Reviews*, vol. 14, no. 1, pp. 312–322, 2010.

[4] H. Price, E. Lüpfert, D. Kearney et al., "Advances in parabolic trough solar power technology," *Journal of Solar Energy Engineering, Transactions of the ASME*, vol. 124, no. 2, pp. 109–125, 2002.

[5] Z.-C. Gao, J. Sui, Q.-B. Liu et al., "Simulation on the performance of a 30 m2 parabolic trough collector," *Journal of Engineering Thermophysics*, vol. 31, no. 4, pp. 541–544, 2010 (Chinese).

[6] Q. Liu, Y. Wang, Z. Gao, J. Sui, H. Jin, and H. Li, "Experimental investigation on a parabolic trough solar collector for thermal power generation," *Science China Technological Sciences*, vol. 53, no. 1, pp. 52–56, 2010.

[7] E. Lüpfert, K.-J. Riffelmann, H. Price, F. Burkholder, and T. Moss, "Experimental analysis of overall thermal properties of parabolic trough receivers," *Journal of Solar Energy Engineering, Transactions of the ASME*, vol. 130, no. 2, Article ID 021007, 5 pages, 2008.

[8] L. Zhang, Z. Yu, L. Fan et al., "An experimental investigation of the heat losses of a U-type solar heat pipe receiver of a parabolic trough collector-based natural circulation steam generation system," *Renewable Energy*, vol. 57, pp. 262–268, 2013.

[9] L. Zhang, W. Wang, Z. Yu et al., "An experimental investigation of a natural circulation heat pipe system applied to a parabolic trough solar collector steam generation system," *Solar Energy*, vol. 86, no. 3, pp. 911–919, 2012.

[10] S. A. Kalogirou, "Solar thermal collectors and applications," *Progress in Energy and Combustion Science*, vol. 30, no. 3, pp. 231–295, 2004.

[11] J. Xiao, Y.-L. He, Z.-D. Cheng, Y.-B. Tao, and R.-J. Xu, "Performance analysis of parabolic trough solar collector," *Journal of Engineering Thermophysics*, vol. 30, no. 5, pp. 729–733, 2009 (Chinese).

[12] N. Naeeni and M. Yaghoubi, "Analysis of wind flow around a parabolic collector (1) fluid flow," *Renewable Energy*, vol. 32, no. 11, pp. 1898–1916, 2007.

[13] V. Dudley, G. Kolb, M. Sloan et al., "SEGS LS2 solar collector-test results," Tech. Rep. SANDIA94-1884, Sandia National Laboratories, Albuquerque, NM, USA, 1994.

[14] F. Wang, Y. Shuai, H. Tan, and C. Yu, "Thermal performance analysis of porous media receiver with concentrated solar irradiation," *International Journal of Heat and Mass Transfer*, vol. 62, no. 1, pp. 247–254, 2013.

[15] F. Wang, J. Tan, and Z. Wang, "Heat transfer analysis of porous media receiver with different transport and thermophysical models using mixture as feeding gas," *Energy Conversion and Management*, vol. 83, pp. 159–166, 2014.

[16] Q. Mao, Y. Yuan, and Y. Shuai, "Effects of atmospheric aerosol on the direct normal irradiance on the earth's surface," *International Journal of Hydrogen Energy*, vol. 39, no. 12, pp. 6364–6370, 2014.

[17] Q. Mao, Y. Shuai, and Y. Yuan, "Study on radiation flux of the receiver with a parabolic solar concentrator system," *Energy Conversion and Management*, vol. 84, pp. 1–6, 2014.

Hindawi Publishing Corporation
International Journal of Photoenergy
Volume 2015, Article ID 163808, 12 pages
http://dx.doi.org/10.1155/2015/163808

*Research Article*

# Solar Thermal System Evaluation in China

**Xinyu Zhang,[1] Wei Xu,[1] Tao He,[1] Shijun You,[2] Yan Gao,[3] Min Wang,[1] and Bojia Li[1]**

[1]*National Center for Quality Supervision and Testing of Solar Heating Systems (Beijing), China Academy of Building Research, Beijing 100013, China*
[2]*School of Environmental Science and Engineering, Tianjin University, Tianjin 30072, China*
[3]*Beijing Key Laboratory of Green Building and Energy Efficient Technology, Beijing University of Civil Engineering and Architecture, Beijing 10044, China*

Correspondence should be addressed to Xinyu Zhang; zxyhit@163.com

Received 30 July 2015; Accepted 7 September 2015

Academic Editor: Xudong Zhao



More than 581 solar thermal systems (STSs), 98 counties, and 47 renewable application demonstration cites in China need to be inspected by the end of 2015. In this study, the baseline for performance and economic evaluation of STSs are presented based on the site test data and related references. An index used to evaluate STSs was selected, and methods to acquire the parameters used to calculate the related index were set. The requirements for sensors for testing were specified. The evaluation method was applied to three systems and the result shows that the evaluation method is suitable for the evaluation of STSs in China.

## 1. Introduction

Buildings are responsible for most of the primary energy use in many countries and regions. In China, about 43% of primary energy is consumed in buildings [1], in the USA 41% [2], and in the EU about 40% [3]. The use of fossil energy will increase the greenhouse gas emissions and cause global climate change [4]. But, fortunately, we have abundant renewable energy. Many countries have introduced policies to encourage the application of renewable energy, especially solar energy, to reduce the consumption of primary energy [5–9]. From 2007 to 2010, in China, 581 projects, 98 counties, and 47 cities have got national financial support for the application of renewable energy in buildings. Solar thermal systems (STSs) are widely used in most of these projects, especially solar water heating systems. Solar energy can generate heat and produce power [10]. According to the statistical data from the International Energy Agency, space heating and domestic hot water consume 46% of the total energy used in residential buildings and 45% in commercial buildings [11]. The required temperature for heating and domestic hot water ranges from 30°C to 100°C, and in this condition solar thermal systems have a dominant advantage for their higher energy conversion efficiency, compared with solar photovoltaic (PV) systems. Solar water heating systems (SWHS) are widely applied in many countries [12–16]. Solar heating and cooling systems are also applied in some special regions and for certain buildings [17–24].

The aim in using solar energy is to reduce the consumption of fossil energy. Can this be achieved in reality? Halawa et al. [15] compared the thermal performance evaluation of SWHS in Austria, Taiwan, and Japan and found that robust methods to assess the SWHS thermal performance in the three regions are required. This similar work is also necessary for any other regions and countries.

Many researchers have undertaken evaluations based on optimal designs and simulations. Juanicó [25] presented a new design for a roof integrated water solar collector for domestic heating and cooling in Argentina. Marcos et al. [20] designed an experimental solar energy facility to meet as much of the heating demand in a typical Spanish dwelling as possible. The system was observed to meet 65.3% of the space heating demand and 46% of the cooling demand. Hobbi and Siddiqui [26] performed an optimal design of a forced circulation solar water heating system for a residential unit in the cold Canadian climate using TRNSYS, and the fraction of solar energy for the entire system was used as the optimization parameter. Allouhi et al. [7] assessed the

technical feasibility of a solar water heating system under Moroccan conditions using simulations. The results showed a higher solar energy fraction can be achieved in these regions when using an evacuated tube solar collector. The evaluation work by Yue and Huang [27] showed that the application of solar water heaters can cover all the energy consumption for hot water in Taiwan. Kalogirou [28, 29] analyzed the environmental benefits of domestic solar energy systems, to show that the energy spent on the manufacture and installation of a SWHS is recouped in about 1.2 years with respect to a life cycle assessment. The payback time varied from a few months to 9.5 years according to fuel costs and the particular pollutant considered with respect to the emissions produced.

Ozyogurtcu et al. [30] compared a ventilation system assisted with exhaust air heat recovery, an electric heater, and solar energy from a technoeconomic view. The results showed that the payback period of the suggested system was 5 years and 8 months. Similar work was performed by Tsoutsos et al. [31]. Al-Salaymeh et al. [32] undertook an economic investigation of an integrated boiler-solar energy saving system in Jordan. The investigation showed that using a SWHS to heat space and domestic water is cost-effective, and the payback time can be as low as 3 years under the Jordanian oil price of 2006–2008. Zhai et al. [33] proposed an energy and exergy analysis on a novel hybrid solar heating, cooling, and power generation system for a remote area in northwestern China. The case study showed that the system had a higher conversion efficiency than the conventional solar thermal power generation system alone, but the payback time was about 18 years under the conventional energy price of the year studied. Ozgener and Hepbasli [34, 35] performed a parametric study on the energy and exergy assessment of a solar assisted ground source heat pump system used for heating a greenhouse in Turkey, in which the peak system heat coefficient of performance (COP) was up to 2.79 on a typical hot day in Izmir, and the best exergy efficiency was 75.6%.

Researchers have evaluated case studies in many countries. Michaelides and Eleftheriou [36] performed an experimental investigation on the thermal performance of a SWHS in Cyprus. The results showed that its thermal performance was relatively insensitive to solar radiation fluctuations ranging from 800 to 1000 W/m$^2$. Ayompe and Duffy [16] evaluated a solar water heating system with a heat pipe evacuated tube solar collector in Ireland based on a year of testing data from a field trial. The results showed that more attention should be paid to the heat loss from the supply pipe to improve the solar energy fraction and collector efficiency. Sekret and Turski [37] studied a solar adsorption cooling system in Poland. The real value of the cooling efficiency of the COP coefficient for the adsorption ice water generator, and real global efficiency of the adsorption system, was 0.27 and 0.23, respectively. Ferreira Leite et al. [23] investigated a central air-conditioning system based on adsorption and solar energy in Brazil, under the mean value of the total daily solar radiation in João Pessoa. The regenerated heat supplied by solar energy was up to 75%, and the COP of the adsorption chillers was found to be around 0.6. Xu et al. [38] reported on a demonstration greenhouse with a solar seasonal heat storage system in Shanghai. The interior air temperature was 15°C while the ambient value was −3°C without any auxiliary heating equipment installed. Esen and Yuksel [39] studied applying biogas, solar, and ground source heat pump system for heating a greenhouse in Turkey and no serious defects were found in the (2009/2010) heating season, which proved the system could be used to supply the energy demand for greenhouses in the East and Southeast regions of Turkey.

It is importance to present a baseline to evaluate solar thermal system performance. Based on previous research results on STS evaluation and the STS application situation in China, the method is presented in this paper. The technical and economic aspects are considered in the method. The evaluation index and the test method for acquiring the parameters to calculate the evaluation index are also considered. The application of the method in three solar thermal systems in buildings shows that the evaluation method is suitable and can be used to evaluate the performance of a STS. The output of this research is part of the Chinese National Standard on evaluation methods for renewable energy systems applied in buildings.

## 2. Scope and Evaluation Index

*2.1. Scope.* The solar thermal systems referred to in this study include solar water heating, solar space heating, and solar air-conditioning systems. Thirty-seven solar thermal systems were tested by the Quality Supervision and Testing of Solar Heating Systems (Beijing) in 2009, of which 32 were solar water heating systems. Therefore, the index for evaluation is mainly based on solar water heating systems, because of their wide application in China. For solar space heating and solar air-conditioning systems, specific indices are considered. The main aim of the evaluation is to verify conformity in the system design. All of the evaluation indices should meet the design requirements. If there are no requirements during design, the evaluation index should meet related national standard requirements.

*2.2. Evaluation Index*

*2.2.1. Technical Evaluation Index.* The collection of solar thermal energy and ability to cope with the load should be considered during the evaluation process. Based on the test results and related references [13, 16, 17, 27, 40–42], the solar energy fraction, efficiency of the solar collecting system, and heat loss coefficient of the storage tank were selected to evaluate the thermal performance of the solar collecting system. The solar energy fraction is also related to the total energy consumption. If the solar energy fraction, efficiency of the solar collecting system, and heat loss of the storage tank are not identified during the design, the solar energy fraction should meet the requirements in Table 1, and the efficiency of the solar collecting system should meet the requirements in Table 2. The heat loss coefficient of the storage tank should be less than 30 W/(m$^3$·K).

For the SWHS, the supply water temperature is taken into account and should be less than 50°C as required in the Chinese standard for hot water supply. For solar space heating

Table 1: Requirement for the solar energy fraction in different solar energy resource regions.

| Solar energy resource region | Solar water heating system | Solar space heating system | Solar air-conditioning system |
|---|---|---|---|
| Extremely rich | $f \geq 60$ | $f \geq 50$ | $f \geq 40$ |
| Abundant | $f \geq 50$ | $f \geq 40$ | $f \geq 30$ |
| Richer | $f \geq 40$ | $f \geq 30$ | $f \geq 20$ |
| Normal | $f \geq 30$ | $f \geq 20$ | $f \geq 10$ |

Note: the solar energy resource region in Tables 1, 5, 6, and 7 is divided by the annual solar hours and annual solar irradiation on the horizontals, detailed in the appendix of the Chinese national standard for solar heating system (GB 50495-2009).

Table 2: Requirement for the efficiency of a solar collecting system.

| Solar water heating system | Solar space heating system | Solar air-conditioning system |
|---|---|---|
| $\eta \geq 42$ | $\eta \geq 35$ | $\eta \geq 30$ |

and solar air-conditioning systems, the indoor temperature is introduced. According to previous research results [17, 19, 21, 24, 43], the thermal COP is introduced to evaluate the performance of solar air-condition systems, which is the product of the efficiency of the solar collecting system and the COP of the chiller. The thermal COP indicates the ability of the solar air-conditioning system to convert solar energy to cooling capacity. To obtain a general performance of the solar air-conditioning system, the thermal COP should be given during the evaluation.

*2.2.2. Economic Evaluation Index.* When considering using renewable energy systems to meet the heating and cooling requirements of a building, the cost of the system is critical and can lead to an increase in the initial investment. A renewable energy system should be based on economic rationality and technical feasibility. The reasonable design of a solar thermal system should compensate the increased investment by a specific operating year during the lifetime of the system. The cost to benefit of the system is put forward. This index indicates the cost to obtain 1 kWh energy saved during the system lifetime. It is the ratio of the increment in the system costs to the total energy saved over the whole lifetime of the system. To establish the viability of the system quickly, a simple payback period is selected. For a solar water heating system, the simple payback period should be less than 5 years, and for a solar space heating system, it should be less than 10 years. During the evaluation, the simple payback period for the solar air-conditioning system and its cost-benefit should be given.

*2.2.3. Environmental Evaluation Index.* The aim in using renewable energy is to reduce the consumption of fossil energy. For the alternative standard, coal is selected, with which the reduction in greenhouse gas emission can be assessed. The reductions of $CO_2$, $SO_2$, and dust are the indices for environmental evaluation. These indices should be presented during the evaluation.

## 3. Parameters and Requirements for the Test

*3.1. Parameters.* To asses all the STSs, the efficiency of the solar collecting system, the total energy consumption, the heat gain of the collecting system, and the heat loss of the storage tank should be got. For the solar water heating system, the supply water temperature should be given to evaluate the energy quality of the system. For the solar space heating and solar air-conditioning systems, the indoor temperature should be recorded. The heating energy consumed and cooling energy supplied by the chiller only apply to the solar air-conditioning systems.

*3.2. System Sampling Method.* To improve the testing efficiency and reduce test cost, it is necessary to select the typical system to be evaluated.

Solar water heating systems must have the same type of solar collector, scope for solar energy collection and hot water supply, system operating mode, heat transfer media, location of the auxiliary heat source installation, and system startup mode. The difference between the gross solar collector area and storage tank must be limited to 10%. Overall the system should be treated as the same type. The number of systems to be evaluated should be 2% of the same types of systems or at least one.

Solar space heating and air-conditioning systems should have the same type of solar collector, operating mode for solar energy collection, storage capacity for heating (cooling), type of chiller, and energy delivery system. The difference between the gross solar collector area, rated cooling capacity of the chiller, and heated (cooled) building area should be limited to 10% and should be treated as the same type. The number of systems evaluated should be 5% of the same type of system or at least one.

*3.3. Requirements for Meteorological Conditions*

*3.3.1. System Monitoring for the Long Term.* Long term monitoring of a solar water heating system should be greater than 120 successive days, the middle day of which should be the Spring or Autumn Equinox in a year.

The solar space heating system should be monitored for the whole heating season, and for the solar air-conditioning system, the monitoring time should cover the whole cooling season.

The average load during long term monitoring should be greater than 30% of the load under the design conditions.

*3.3.2. Short Term Test.* Short term monitoring should be over at least 4 days and performed continuously. The operating conditions should be as close to the design operating conditions as possible. The average load for a short term test should be greater than 50% of the load under the design conditions. The indoor temperature should be recorded when the building is in heat transfer equilibrium.

Table 3: Accuracy and precision of instruments for temperature measurement.

| Parameter | Instrument accuracy | Instrument precision |
|---|---|---|
| Temperature, ambient air | ±0.5°C | ±0.2°C |
| Temperature, water | ±0.2°C | ±0.1°C |

The ambient temperature for the solar water heating system should be the annual average surrounding temperature ±10°C. For the solar space heating system, it should be greater than the surrounding temperature for heating load calculations and less than 12°C. For the solar air-conditioning system, it should be greater than 25°C and less than the dry bulb surrounding temperature for the cooling load calculations.

Results should be obtained for at least four different days with the specified solar irradiation as follows. The difference between the recorded and specified values should be ±0.5 MJ/(m$^2$·d):

(1) Daily solar irradiation less than 8 MJ/(m$^2$·d).

(2) Daily solar irradiation equal to or greater than 8 MJ/(m$^2$·d) and less than 12 MJ/(m$^2$·d).

(3) Daily solar irradiation equal to or greater than 12 MJ/(m$^2$·d) and less than 16 MJ/(m$^2$·d).

(4) Daily solar irradiation equal to or greater than 16 MJ/(m$^2$·d).

During the test procedure, the range for recording the solar irradiation can be adjusted based on the real situation, but an even spread is required for the solar irradiation.

*3.4. Requirements for Sensors.* Solar irradiation should be recorded by a pyranometer, which should meet Chinese national standard for a pyranometer (GB/T 19565).

The ambient air temperature should be measured using a shaded aspirated sampling device approximately 1 m above the ground, not closer than 1.5 m to the collector and system components and not further than 10 m from the system. The field-of-view of the air temperature sensor should not include chimneys, cooling towers, or hot exhaust. The sensor for measuring the water temperature should be submerged in the water. The temperate sensors and related data recorders should have a time constant of 10 s or less and have an accuracy and precision equal to or better than the requirements in Table 3.

The accuracy of the liquid flow rate measurement should be equal to ±1.0%.

Mass measurement should be accurate to ±1.0%.

Elapsed time measurement should be accurate to ±0.2%.

Analog and digital recorders used should have an accuracy equal to or better than ±0.5% of the full scale reading and have a time constant of 1 second or less. Digital techniques and electronic integrators used should have accuracy equal to or better than 1.0% of the measured value. The input impedance of recorders should be greater than 1000 times the impedance of the sensors or 10 MΩ, whichever is the higher. In no case should the smallest scale division of the instrument or instrument exceed twice the specified precision.

Length measurement should be made with an accuracy of ±1.0%.

The accuracy for the heat meter should be class 2 according to the Chinese construction industry standard for heat meters (CJ128).

## 4. Method to Determine the Parameters

*4.1. Efficiency of Solar Collecting System.* For the short term test, the daily test starts at 8 am, and when the accumulated solar irradiation meets the requirement of the specified value, the circulation is stopped. The efficiency of solar collecting system can be expressed by

$$\eta = \frac{Q_j}{AH}, \tag{1}$$

where $\eta$ is the efficiency of the solar collecting system, $A$ the solar collector's area in m$^2$, $H$ the solar irradiation on the aperture area of the solar collector in MJ/m$^2$, and $Q_j$ the useful energy gained in units of MJ, which can be expressed by

$$Q_j = \sum_{i=1}^{n} m_{ji}\rho_w c_{pw}\left(t_{dji} - t_{bji}\right)\Delta T_{ji} \times 10^{-6}, \tag{2}$$

where $m_{ji}$ is the average flow rate of solar collecting system in m$^3$/s, $c_{pw}$ is the constant specific heat of the heat transfer media in J/kg·°C, $\rho_w$ is the density of the heat transfer media in kg/m$^3$, $t_{dji}$ is the inlet temperature of the solar collecting in the efficiency of the solar collecting system in °C, $t_{bji}$ is the outlet temperature of the solar collecting in the efficiency of the solar collecting system in °C, $\Delta T_{ji}$ is the recorded time interval in seconds and $\Delta T_{ji}$ should be less than 600 s, and $n$ is the total number of recorded data. The useful energy gained can be acquired by testing the flow rate, the inlet and outlet temperature of the solar collecting system or by using a heat meter.

*4.2. Total Energy Consumption.* For short term monitoring, the duration for total energy consumption ranges between 8:00 and 8:00 the next morning.

The total energy consumption can be acquired using the flow rate and two temperatures or using a heat meter. It can be expressed as

$$Q_z = \sum_{i=1}^{n} m_{zi}\rho_w c_{pw}\left(t_{dzi} - t_{bzi}\right)\Delta T_{zi} \times 10^{-6}, \tag{3}$$

where $Q_z$ is the total energy consumption in units of MJ, $m_{zi}$ the average flow rate of the system in m$^3$/s, $t_{dzi}$ the hot water temperature supplied by the solar water heating system or the supply water temperature for the solar space heating system or the return water temperature for the solar air-condition system supply water temperature in °C, $t_{bzi}$ the cold water temperature for the solar water heating system or

the return water temperature for the solar space heating system or the supply water temperature for the solar air-conditioning system in ˚C, and $\Delta T_{zi}$ the recording time interval in seconds which should be less than 600 s.

During the test for total energy consumption, the hot water supplied by the solar water heating system, and the indoor temperatures for the solar heating and solar air-conditioning systems, should be recorded at the same time each day. The hot water temperature and indoor temperature should be the arithmetic average of the recorded data.

*4.3. Heating Energy Consumed and Cooling Energy Supplied by the Chiller.* For short term monitoring, the duration for the heating energy consumed and cooling energy supplied by the chiller ranges between 8:00 and 8:00 the next morning, and before recording the test data, the chiller should operate stably for an hour.

The heating energy consumed and cooling energy supplied by the chiller can be acquired from the flow rate and the two temperatures or using the heat meter. The heating energy consumed by the chiller can be expressed by

$$q_r = \frac{\sum_{i=1}^{n} m_{ri}\rho_w c_{pw}\left(t_{dri} - t_{bri}\right)\Delta T_{ri} \times 10^{-3}}{\Delta T}, \quad (4)$$

where $q_r$ is the heating energy consumed by the chiller in units of kW, $m_{ri}$ the average flow rate system in $m^3/s$, $t_{dri}$ the supply water temperature to the chiller in ˚C, $t_{bri}$ the return water temperature from the chiller in ˚C, $\Delta T_{ri}$ the recording time interval in seconds, which should be less than 600 s, and $\Delta T_t$ the total recording time in seconds.

The cooling energy supplied by the chiller should be

$$q_l = \frac{\sum_{i=1}^{n} m_{li}\rho_w c_{pw}\left(t_{dli} - t_{bli}\right)\Delta T_{li} \times 10^{-3}}{\Delta T_t}, \quad (5)$$

where $q_l$ is the cooling energy supplied by the chiller in units of kW, $m_{li}$ the average flow rate system in $m^3/s$, $t_{dli}$ the return water temperature to the chiller in ˚C, $t_{bli}$ the supply water temperature from the chiller in ˚C, and $\Delta T_{li}$ the recording time interval in seconds which should be less than 600 s.

*4.4. Heat Loss Coefficient of Storage Tank.* The test for the heat loss coefficient of the storage tank lasts from 20:00 to 6:00 the next morning. During the test, no cold water should enter the tank and no hot water should leave the tank. The start temperature for the test should be higher than 50˚C, and the temperature difference between the temperature in the tank and surrounding air temperature should be greater than 20 K.

The heat loss coefficient of the storage tank can be expressed as

$$U_{\mathrm{SL}} = \frac{\rho_w c_{pw} \ln\left[\left(t_i - t_{\mathrm{as(av)}}\right) / \left(t_f - t_{\mathrm{as(av)}}\right)\right]}{\Delta\tau}, \quad (6)$$

where $U_{\mathrm{SL}}$ is the heat loss coefficient of the storage tank in $W/(m^3{\cdot}K)$, $\Delta\tau$ the duration of the heat loss test in seconds, $t_i$ the initial temperature in the tank at the beginning of the test in ˚C, $t_f$ the final temperature in the tank after the heal loss test in ˚C, and $t_{\mathrm{as(av)}}$ the average surrounding air temperature during the heat loss test in ˚C.

## 5. Evaluation

*5.1. Technical Evaluation.* Initially, the hot water temperature and the indoor temperature should meet the related standard requirements, and then the evaluation can proceed. The heat loss coefficient of the storage tank should be less than $30\ W/(m^3{\cdot}K)$.

*5.1.1. Solar Energy Fraction.* The solar energy fraction is expressed as

$$f = \frac{Q_j}{Q_z}. \quad (7)$$

For long duration system monitoring, the solar energy fraction should be the average value. For the short term test, expressed as

$$f = \frac{\left(x_1 f_1 + x_2 f_2 + x_3 f_3 + x_4 f_4\right)}{\left(x_1 + x_2 + x_3 + x_4\right)}, \quad (8)$$

where $f_1$, $f_2$, $f_3$, and $f_4$ are the solar energy fractions for the four tested solar irradiations and $x_1$, $x_2$, $x_3$, and $x_4$ the numbers of days that have one of the four specified solar irradiations in a year.

*5.1.2. Efficiency of Solar Collecting System.* For long duration system monitoring, the efficiency of the solar collecting system should be the average value. For the short term test, expressed as

$$\eta = \frac{\left(x_1\eta_1 + x_2\eta_2 + x_3\eta_3 + x_4\eta_4\right)}{\left(x_1 + x_2 + x_3 + x_4\right)}, \quad (9)$$

where $\eta_1, \eta_2, \eta_3$, and $\eta_4$ are the efficiency of the solar collecting system for the four tested solar irradiations determined by (1).

*5.1.3. Thermal COP for Solar Air-Conditioning System.* Thermal COP for the solar air-conditioning system is expressed by

$$\mathrm{COP}_r = \eta\left(\frac{q_l}{q_r}\right), \quad (10)$$

where $\mathrm{COP}_r$ is the thermal COP for the solar air-conditioning system.

*5.2. Economic Evaluation*

*5.2.1. Cost-Benefit for the System.* The cost-benefit for the system is related to the amount of energy saved in the lifetime of the system and the investment, expressed as

$$\mathrm{CBR}_r = 3.6 \times \frac{C_{zr}}{\left(Q_{tr} q N\right)}, \quad (11)$$

Table 4: Operating efficiency of a heating resource using conventional energy.

| Conventional energy | Domestic water | Space heating | Thermal driven cooling |
|---|---|---|---|
| Electricity | 0.31 | / | / |
| Coal | / | 0.70 | 0.70 |
| Natural gas | 0.84 | 0.80 | 0.80 |

where $CBR_r$ is the cost-benefit for the system in ¥RMB/kWh, $C_{zr}$ the added investment for the use of STS in ¥RMB, $q$ the heat value of standard coal (in China this value is 29.307 MJ/(kgce)), $N$ the lifetime of the system (normally it should be 15 years), and $Q_{tr}$ the amount of alternative energy in kgce, expressed as

$$Q_{tr} = \frac{Q_{nj}}{q\eta_t}, \tag{12}$$

where $\eta_t$ is the operating efficiency of the heat resource with conventional energy (if not given in related files, it can be decided in Table 4) and $Q_{nj}$ the useful heat gain yearly in MJ. For the long term monitoring, it should be the accumulated value during the monitoring, and for the short test, it is expressed as

$$Q_{nj} = x_1 Q_{j1} + x_2 Q_{j2} + x_3 Q_{j3} + x_4 Q_{j4}, \tag{13}$$

where $Q_{j1}$, $Q_{j2}$, $Q_{j3}$, and $Q_{j4}$ are the useful energy gained from the four tested solar irradiations determined by (2) in MJ.

*5.2.2. Simple Payback Year.* The simple payback period can be expressed as

$$N_h = \frac{C_{zr}}{C_{sr}}, \tag{14}$$

where $C_{sr}$ is saved cost in ¥RMB and can be expressed by

$$C_{sr} = PQ_{tr}\frac{q}{3.6} - M_r, \tag{15}$$

where $P$ is the price of conventional energy in ¥RMB/kWh and $M_r$ is the cost for system maintenance in ¥RMB.

*5.3. Environmental Evaluation*

*5.3.1. Reduction Emission of $CO_2$.* The reduction emission of $CO_2$ can be expressed by

$$E_{r\mathrm{co}_2} = Q_{tr}V_{\mathrm{co}_2}, \tag{16}$$

where $E_{r\mathrm{co}_2}$ is the reduction emission of $CO_2$ in kg and $V_{\mathrm{co}_2}$ the emission factor of $CO_2$ in kg/kgce (it is 2.47 kg/kgce).

*5.3.2. Reduction Emission of $SO_2$.* The reduction emission of $SO_2$ is expressed by

$$E_{r\mathrm{so}_2} = Q_{tr}V_{\mathrm{so}_2}, \tag{17}$$

where $E_{r\mathrm{so}_2}$ is the reduction emission of $SO_2$ in kg and $V_{\mathrm{so}_2}$ the emission factor of $SO_2$ in kg/kgce (it is 0.02 kg/kgce).

Table 5: Rank of the solar energy fraction for a solar water heating system in different solar energy resource regions.

| Solar energy resource region | Rank 1 | Rank 2 | Rank 3 |
|---|---|---|---|
| Extremely rich | $f \geq 80$ | $80 > f \geq 70$ | $70 > f \geq 60$ |
| Abundant | $f \geq 70$ | $70 > f \geq 60$ | $60 > f \geq 50$ |
| Richer | $f \geq 60$ | $60 > f \geq 50$ | $50 > f \geq 40$ |
| Normal | $f \geq 50$ | $50 > f \geq 40$ | $40 > f \geq 30$ |

Table 6: Rank of the solar energy fraction for a solar space heating system in different solar energy resource regions.

| Solar energy resource region | Rank 1 | Rank 2 | Rank 3 |
|---|---|---|---|
| Extremely rich | $f \geq 70$ | $70 > f \geq 60$ | $60 > f \geq 50$ |
| Abundant | $f \geq 60$ | $60 > f \geq 50$ | $50 > f \geq 40$ |
| Richer | $f \geq 50$ | $50 > f \geq 40$ | $40 > f \geq 30$ |
| Normal | $f \geq 40$ | $40 > f \geq 30$ | $30 > f \geq 20$ |

Table 7: Rank of the solar energy fraction for a solar air-conditioning system in different solar energy resource regions.

| Solar energy resource region | Rank 1 | Rank 2 | Rank 3 |
|---|---|---|---|
| Extremely rich | $f \geq 60$ | $60 > f \geq 50$ | $50 > f \geq 40$ |
| Abundant | $f \geq 50$ | $50 > f \geq 40$ | $40 > f \geq 30$ |
| Richer | $f \geq 40$ | $40 > f \geq 30$ | $30 > f \geq 20$ |
| Normal | $f \geq 30$ | $30 > f \geq 20$ | $20 > f \geq 10$ |

*5.3.3. Reduction Emission of Dust.* The reduction emission of dust can be expressed by

$$E_{rfc} = Q_{tr}V_{fc}, \tag{18}$$

where $E_{rfc}$ is the reduction emission of dust in kg and $V_{fc}$ is the emission factor of dust in kg/kgce (it is 0.01 kg/kgce).

## 6. Assessment and Rank for STS

Each index should meet the requirements in Section 2.2, at which point the assessment result is passed. If one index performs poorly, the assessment cannot be passed. If the solar energy fraction and efficiency of the solar collecting system are equal to or greater than the values in Tables 1 and 2, the performance of the STS can be ranked. There are 3 levels of rank for the solar energy fraction, with rank 1 being the highest. The type of STS and solar energy resource considered during the ranking are detailed in Tables 5–7. There are also 3 levels of rank for the efficiency of the solar collecting system, with rank 1 being the highest. The type of STS considered during the ranking is detailed in Table 8. The rank for solar energy fraction and the efficiency of the solar collecting system are the same, as is the final rank for STS. If

Table 8: Rank of the efficiency for a solar collecting system.

| Rank | Solar water heating system | Solar space heating system | Solar air-conditioning system |
|---|---|---|---|
| Rank 1 | $\eta \geq 65$ | $\eta \geq 60$ | $\eta \geq 55$ |
| Rank 2 | $65 > \eta \geq 50$ | $60 > \eta \geq 45$ | $55 > \eta \geq 40$ |
| Rank 3 | $50 > \eta \geq 42$ | $45 > \eta \geq 35$ | $40 > \eta \geq 30$ |

Figure 1: Flat plate solar collectors for solar water heating system in Shenzhen.

the ranks for the solar energy fraction and the efficiency of the solar collecting system are different, the rank for the STS is the lower. For instance, if the rank for the solar energy fraction is rank 1, the rank for the efficiency of the solar collecting system is rank 3, and the final rank for STS will be 3.

## 7. Application of the Evaluation System with Short Term Test Data

### *7.1. Solar Water Heating System for an Apartment in Shenzhen*

*7.1.1. Description of Solar Water Heating Systems.* For the systems located in Baoan, Shenzhen city, the design requirement is that the system can supply each resident 60 L hot water with the temperature of 55°C. A 490 $m^2$ flat plate solar collector was used and installed on the roof (Figure 1), and an electricity heater was used as a backup heat resource.

*7.1.2. Test Results.* Detailed test results are given in Table 9. Based on (8), the yearly solar energy fraction was 73%. The solar collecting system was 44% efficient.

The test result for the heat loss coefficient of the storage tank was 14 W/($m^3$ · °C). The average temperature of the supplied hot water was 55.6°C during the test.

The cost-benefit of the system was 0.15 ¥RMB/kWh, less than the electricity price in Shenzhen, which was 0.70 ¥RMB/kWh, implying the solar water heating system can save electricity in domestic water heating.

The simple payback period was 2.8 years. The yearly reductions in emission of $CO_2$, $SO_2$, and dust were 63138 kg, 511 kg, and 256 kg, respectively.

Figure 2: Flat plate solar collectors integrated with slope roof for solar space heating system in Beijing.

*7.1.3. Evaluation and Rank.* Shenzhen is located in a richer solar energy resource region. Comparing the test results with the data in Tables 1 and 2, the solar energy fraction and efficiency of the solar collecting system were greater than requirements. Therefore, the system passed the final evaluation. According to Table 5, the rank for the system should be rank 1. According to Table 8, the rank for the system should be rank 3, so the final rank for the system was rank 3.

During the ranking procedure, it was found that the solar energy fraction for the system was greater than the requirement, but the efficiency of the solar collecting system was relatively lower compared with other systems. This led to an increase in initial investment and the operating temperature of the solar collecting system was at a higher level. It is possible that the solar water heating system can perform better and at a lower cost in the present situation.

### *7.2. Solar Space Heating System for a Rural Residential Building in Beijing*

*7.2.1. Description of the Solar Water Heating Systems.* The systems are located in Pinggu, Beijing, and were part of a demonstration project for a rural area in Beijing to save energy and improve indoor air quality. The building was a typical rural house in the south of China with a floor area of 160 $m^2$. A flat plate solar collector was used and integrated with the slope of the roof (Figure 2). The aperture area was 24.21 $m^2$. The system supplied energy for space heating and domestic water. Two tanks were used in the system, one tank of 1500 L to store heat and another of 100 L for hot water. The small scale boiler with higher efficiency was used as backup energy. The fuel for the boiler was coal.

*7.2.2. Test Results.* The test was performed during the hot season. Detailed test results are given in Table 10.

Based on (8), the solar energy fraction for heating was 41%, and the average indoor temperature during the test was 16.9°C, as detailed in Table 11. The test result for the solar energy fraction during the season without a heating requirement was 91%.

For the efficiency of the solar collecting system during heating, the test result was 51%. The solar collecting system

Table 9: Test results for a solar water heating system.

| Number | Ambient temperature °C | Solar irradiation MJ/m$^2$ | Useful heat gain MJ | Total energy consumption MJ | Efficiency of solar collecting system | Solar energy fraction | Consumed hot water m$^3$ |
|---|---|---|---|---|---|---|---|
| 1 | 25.9 | 7.82 | 239.4 | 697.2 | 0.33 | 0.34 | 7.81 |
| 2 | 27.3 | 12.74 | 474.1 | 977.3 | 0.40 | 0.49 | 7.54 |
| 3 | 28.4 | 20.48 | 942.3 | 941.6 | 0.50 | 1.00 | 7.93 |
| 4 | 30.2 | 17.96 | 839.4 | 838.6 | 0.51 | 1.00 | 8.05 |

Table 10: Test results for a solar space heating system during heating conditions.

| Number | Solar irradiation | Useful heat gain | Energy consumed for space heating | Energy consumption for domestic water | Energy consumed of conventional energy | Efficiency of solar collecting system | Solar energy fraction |
|---|---|---|---|---|---|---|---|
| | MJ/m$^2$ | MJ | MJ | MJ | MJ | | |
| 1 | 17.0 | 233.7 | 379.7 | 20.6 | 216.9 | 0.57 | 0.52 |
| 2 | 12.6 | 173.9 | 361.1 | 15.9 | 247.3 | 0.57 | 0.41 |
| 3 | 7.0 | 38.16 | 180.4 | 0.7 | 184.3 | 0.23 | 0.17 |
| 4 | 22.1 | 288.3 | 360.0 | 5.8 | 157.7 | 0.54 | 0.65 |

Table 11: Indoor air temperature test results during heating conditions.

| Number | 2nd living room °C | 1st living room °C | 2nd bed room with south window °C | Outside airspeed M·s$^{-1}$ |
|---|---|---|---|---|
| 1 | 16.5 | 17.8 | 16.3 | 1.11 |
| 2 | 15.9 | 18.0 | 14.6 | 0.85 |
| 3 | 14.7 | 18.2 | 14.1 | 0.65 |
| 4 | 19.3 | 19.8 | 17.7 | 0.72 |

Figure 3: Evacuated tube solar collector for solar air-conditioning system in Beijing.

was often overheating which was an abnormal condition during the season without any heating requirements.

The test result for the heat loss coefficient of both tanks was 15 W/(m$^3$ · °C).

The cost-benefit of the system was 0.66 ¥RMB/kWh, which was higher than the electricity price in Beijing, at 0.52 ¥RMB/kWh. This implied the cost of a solar space heating system for water heating was too high, so the simple payback period was up to 13.5 years, if one considered the interest on money and investment requirement that the cost should be paid back during the lifetime of the system.

The yearly reductions in the emission of $CO_2$, $SO_2$, and dust were 3058 kg, 25 kg, and 13 kg, respectively.

*7.2.3. Evaluation and Rank.* Beijing is located in a richer solar energy resource region, and comparing the test results with the data in Tables 1 and 2, the solar energy fraction and efficiency of the solar collecting system were greater than the requirements. Therefore the system passed its final evaluation. According to Tables 6 and 8, the system should be at rank 2, so the final rank for the system was rank 2.

The rank of the solar space heating system in this project seemed good, but from an economic view, the result is not acceptable. The test was performed during the first year. As time passes, the performance of a solar collector can deteriorate, which was proved by Zhang et al. [44]. This problem should be considered in further applications of solar heating systems.

### 7.3. Solar Air-Conditioning System for an Office in Beijing

*7.3.1. Description of Solar Air-Conditioning Systems.* This system was located in Beijing and supplied cooling energy in summer and heat in winter. The floor area for this office was 1850 m$^2$ over two floors. The U type evacuated tube solar collector was used with an aperture area of 457 m$^2$ and installed on the flat roof of the building (Figure 3). To make full use of the solar energy in summer, the slope of the solar collector frame was 25°. The total investment in the heating and air-conditioning system was 1.39 M ¥RMB,

Table 12: Equipment for a solar air-conditioning system.

| | | |
|---|---|---|
| Solar collecting system | Type | Indirect, forced circulation |
| | Solar collector | U type evacuated tube solar collector |
| | Heat transfer media | Water |
| | Number of storage tanks | 1 |
| | Tank volume | 15 $m^3$ |
| | Insulation material and thickness | 50 mm polyurethane |
| Refrigeration system | Type of refrigerator | WFC-SC50 |
| | Cooling capacity of refrigerator | Cooling capacity 176 kW |
| | Manufacture | Yazaki |
| | Number of storage tanks | 1 |
| | Tank volume | 8 $m^3$ |
| Backup | Type | Biomass boiler |

and the investment in the solar air-conditioning system was 0.45 M ¥RMB. The details of the equipment in the system are given in Table 11.

*7.3.2. Test Results.* The tests were performed in both hot and cold seasons. Details of the test results for the cold season are in Table 12.

The test result for the solar energy fraction for cooling was 83%, the efficiency of the solar collecting system 50%, the thermal COP 0.41, and the average indoor temperature 25.6°C. The test result for the heat loss coefficient of the heat storage tank is 3 W/($m^3 \cdot$ °C).

The cost saved during the cooling season was 42 k ¥RMB, the cost-benefit of the system during cooling season was 0.15 ¥RMB/kWh, and the simple payback period was 10.7 years. The reductions in emissions of $CO_2$, $SO_2$, and dust during the cooling season were 593,000 kg, 480 kg, and 240 kg, respectively.

Details for the test results for the cold season are given in Table 13.

The test result for the solar energy fraction for heating was 72%, the efficiency of the solar collecting system was 43%, and the average indoor temperature was 22.0°C. The cost saved during the hot season was 15 k ¥RMB. Details for the test results for heat season are given in Table 14.

Considering all the results of the cold and hot seasons, the cost-benefit for the system was 0.09 ¥RMB/kWh, and the simple payback period was 7.9 years. The reductions in emissions of $CO_2$, $SO_2$, and dust were 960,000 kg, 779 kg, and 389 kg, respectively.

*7.3.3. Evaluation and Rank.* Beijing is located in a richer solar energy resource region, and comparing the test results with the data in Tables 1 and 2, the solar energy fraction and efficiency of the solar collecting system were greater than the requirements. Therefore the system passed its final evaluation. Based on the test results for the cooling season, according to Table 7, the rank for the solar air-conditioning system should be rank 1. According to Table 8, the rank for the solar air-conditioning system should be rank 2, so the final rank for the solar air-conditioning system was rank 2.

From the evaluation, the solar air-conditioning system was able to match the load requirements for different seasons.

## 8. Conclusions

Through the research, an evaluation method for solar thermal systems was presented. It has provided a baseline for the evaluation of many systems in China. The output of the research is part of Chinese national standard (GB/T 50801). The evaluation method was applied to three systems and the result showed that the evaluation method was suitable for the acceptance inspection of STSs.

During the application of the standard, some improvements were found. More index should be added for comprehensive evaluations of systems. The solar energy fraction can be changed to be expressed with different parameters that can be closer to the real situation. The payback period should be considered with more factors, and saving energy not taken into account, depending on the type of backup energy used.

## Nomenclature

$A$: Aperture area of solar collector, $m^2$
$c_{pw}$: Constant specific heat, kJ/(kg·°C)
$CBR_r$: Cost-benefit for system, RMB¥/kWh
$C_{zr}$: Added investment for the use of STS, RMB¥
$C_{sr}$: Saved cost, RMB¥
$E_{rco_2}$: Reduction emission of $CO_2$, kg/kgce
$E_{rfc}$: Reduction emission of dust, kg/kgce
$E_{rso_2}$: Reduction emission of $SO_2$, kg/kgce
$H$: Solar irradiation on the aperture of solar collector, MJ/$m^2$
$m_{ji}$: Average flow rate of solar collecting system, $m^3$/s
$m_{li}$: Average flow rate of cooling water from the chiller, $m^3$/s
$m_{ri}$: Average flow rate of heating water to the chiller, $m^3$/s
$m_{zi}$: Average flow rate of the system, $m^3$/s
$n$: Total numbers of recorded data
$N$: Lifetime of the system
$N_h$: Simple payback year
$q$: Heat value of standard coal, MJ/(kgce)
$q_l$: Cooling energy supplied by the chiller, kW
$q_r$: Heating energy consumed by the chiller, kW
$Q_{nj}$: Useful heat gain yearly, MJ
$Q_j$: Useful energy gained by solar collecting system, MJ
$Q_{tr}$: Amount of alternative energy, kgce
$Q_z$: Total energy consumption, MJ
$P$: Price of conventional energy, RMB¥/kWh
$M_r$: Cost for system maintenance, RMB¥

Table 13: Test results for a solar air-conditioning system during cooling conditions.

| Number | Ambient temperature ˚C | Solar irradiation MJ/m$^2$ | Useful heat gain MJ | Efficiency of solar collecting system | Solar energy fraction | COP of absorption chiller |
|---|---|---|---|---|---|---|
| 1 | 36.0 | 25.6 | 6551.6 | 0.56 | 1.00 | 0.81 |
| 2 | 30.7 | 16.3 | 3948.0 | 0.53 | 1.00 | 0.82 |
| 3 | 32.7 | 11.5 | 1944.5 | 0.37 | 0.57 | 0.70 |
| 4 | 27.4 | 6.1 | 1115.1 | 0.40 | 0.09 | 0.65 |

Table 14: Test results for a solar air-conditioning system during heating conditions.

| Number | Ambient temperature ˚C | Solar irradiation MJ/m$^2$ | Useful heat gain MJ | Efficiency of solar collecting system | Total energy consumption | Solar energy fraction |
|---|---|---|---|---|---|---|
| 1 | −4.2 | 7.34 | 1261.2 | 0.38 | 3596.1 | 0.35 |
| 2 | −3.4 | 14.43 | 3027.2 | 0.46 | 3763.5 | 0.80 |
| 3 | 2.2 | 11.49 | 2237.4 | 0.43 | 2935.7 | 0.76 |
| 4 | 0.7 | 16.66 | 3524.1 | 0.46 | 3976.1 | 0.89 |

$t_{as(av)}$: Average surrounding air temperature during the heat loss test, ˚C
$t_{bji}$: Outlet temperature of solar collecting system, ˚C
$t_{bli}$: Supply water temperature from the chiller, ˚C
$t_{bri}$: Return water temperature from the chiller, ˚C
$t_{bzi}$: Cold water temperature for solar water heating system or return water temperature for solar space heating system or supply water temperature for solar air-conditioning system, ˚C
$t_{dji}$: Outlet temperature of solar collecting system, ˚C
$t_{dli}$: Return water temperature to the chiller, ˚C
$t_{dri}$: Supply water temperature to the chiller, ˚C
$t_{dzi}$: Hot water temperature supplied by solar water heating system or the supply water temperature for solar water heating system or the return water temperature for solar air-conditioning system, ˚C
$t_f$: Final temperature in the tank after the heal loss test, ˚C
$t_i$: Initial temperature in the tank at the beginning of the heat loss test, ˚C
$U_{SL}$: Heat loss coefficient of the storage tank, W/(m$^3$·K)
$V_{co_2}$: Emission factor of $CO_2$, kg/kgce
$V_{fc}$: Emission factor of dust, kg/kgce
$V_{so_2}$: Emission factor of $SO_2$, kg/kgce.

*Greek Symbols*

$\rho_w$: Density of heat transfer media, kg/m$^3$
$\eta$: Efficiency of solar collecting system, %
$\eta_t$: Operating efficiency of heat resource with conventional energy
$\Delta T_{(j,z,r,l)i}$: Recording time interval, s
$\Delta T_t$: Total recording time, s
$\Delta\tau$: The duration of the heat loss test, s.

*Abbreviations*

COP: Coefficient of performance
STS: Solar thermal systems in buildings
GB: Chinese national standard.

## Conflict of Interests

The authors declare that there is no conflict of interests regarding the publication of this paper.

## Acknowledgments

This work was funded by the Chinese National Scientific Program (2014BAJ01B03) and Applied Foundation of the China Academy of Building Research (20140109330730039). The contribution of the Beijing Collaborative Innovation Center of Energy-Saving and Emission-Reduction and the help from the people who contributed to GB/T 50801 are acknowledged.

## References

[1] Y. Hang, M. Qu Ming, and F. Zhao, "Economical and environmental assessment of an optimized solar cooling system for a medium-sized benchmark office building in Los Angeles, California," *Renewable Energy*, vol. 36, no. 2, pp. 648–658, 2011.

[2] B. Lin and H. Liu, "China's building energy efficiency and urbanization," *Energy and Buildings*, vol. 86, pp. 356–365, 2015.

[3] European Commission (EC), *Green-Paper—Towards a European Strategy for the Security of Energy Supply*, COM 769, Commission of the European Communities, Brussels, Belgium, 2000.

[4] IPCC, *Climate Change 2013: The Physical Science Basis*, Cambridge University Press, Cambridge, UK, 2013.

[5] K. H. Solangi, M. R. Islam, R. Saidur, N. A. Rahim, and H. Fayaz, "A review on global solar energy policy," *Renewable and Sustainable Energy Reviews*, vol. 15, no. 4, pp. 2149–2163, 2011.

[6] T. Kousksou, A. Allouhi, M. Belattar et al., "Renewable energy potential and national policy directions for sustainable development in Morocco," *Renewable and Sustainable Energy Reviews*, vol. 47, pp. 46–57, 2015.

[7] A. Allouhi, A. Jamil, T. Kousksou, T. El Rhafiki, Y. Mourad, and Y. Zeraouli, "Solar domestic heating water systems in Morocco: an energy analysis," *Energy Conversion and Management*, vol. 92, pp. 105–113, 2015.

[8] H. Xie, C. Zhang, B. Hao, S. Liu, and K. Zou, "Review of solar obligations in China," *Renewable and Sustainable Energy Reviews*, vol. 16, no. 1, pp. 113–122, 2012.

[9] S. Mekhilef, A. Safari, W. E. S. Mustaffa, R. Saidur, R. Omar, and M. A. A. Younis, "Solar energy in Malaysia: current state and prospects," *Renewable and Sustainable Energy Reviews*, vol. 16, no. 1, pp. 386–396, 2012.

[10] S. Mekhilef, R. Saidur, and A. Safari, "A review on solar energy use in industries," *Renewable and Sustainable Energy Reviews*, vol. 15, no. 4, pp. 1777–1790, 2011.

[11] D. Ürge-Vorsatz, L. F. Cabeza, S. Serrano, C. Barreneche, and K. Petrichenko, "Heating and cooling energy trends and drivers in buildings," *Renewable and Sustainable Energy Reviews*, vol. 41, pp. 85–98, 2014.

[12] U. Stritih, E. Osterman, H. Evliya, V. Butala, and H. Paksoy, "Exploiting solar energy potential through thermal energy storage in Slovenia and Turkey," *Renewable and Sustainable Energy Reviews*, vol. 25, pp. 442–461, 2013.

[13] M. S. Mohsen and B. A. Akash, "Evaluation of domestic solar water heating system in Jordan using analytic hierarchy process," *Energy Conversion and Management*, vol. 38, no. 18, pp. 1815–1822, 1997.

[14] R. Zheng, T. He, X. Zhang, Z. Huang, and Y. Deng, "Developing situation and energy saving effects for solar heating and cooling in China," *Energy Procedia*, vol. 30, pp. 723–729, 2012.

[15] E. Halawa, K. C. Chang, and M. Yoshinaga, "Thermal performance evaluation of solar water heating systems in Australia, Taiwan and Japan—A comparative review," *Renewable Energy*, vol. 83, pp. 1279–1286, 2015.

[16] L. M. Ayompe and A. Duffy, "Thermal performance analysis of a solar water heating system with heat pipe evacuated tube collector using data from a field trial," *Solar Energy*, vol. 90, pp. 17–28, 2013.

[17] M. Qu, H. Yin, and D. H. Archer, "A solar thermal cooling and heating system for a building: experimental and model based performance analysis and design," *Solar Energy*, vol. 84, no. 2, pp. 166–182, 2010.

[18] A. M. Papadopoulos, S. Oxizidis, and N. Kyriakis, "Perspectives of solar cooling in view of the developments in the air-conditioning sector," *Renewable and Sustainable Energy Reviews*, vol. 7, no. 5, pp. 419–438, 2003.

[19] M. Mazloumi, M. Naghashzadegan, and K. Javaherdeh, "Simulation of solar lithium bromide-water absorption cooling system with parabolic trough collector," *Energy Conversion and Management*, vol. 49, no. 10, pp. 2820–2832, 2008.

[20] J. D. Marcos, M. Izquierdo, and D. Parra, "Solar space heating and cooling for Spanish housing: potential energy savings and emissions reduction," *Solar Energy*, vol. 85, no. 11, pp. 2622–2641, 2011.

[21] G. A. Florides, S. A. Kalogirou, S. A. Tassou, and L. C. Wrobel, "Modelling and simulation of an absorption solar cooling system for Cyprus," *Solar Energy*, vol. 72, no. 1, pp. 43–51, 2002.

[22] X. Q. Zhai and R. Z. Wang, "A review for absorbtion and adsorbtion solar cooling systems in China," *Renewable and Sustainable Energy Reviews*, vol. 13, no. 6-7, pp. 1523–1531, 2009.

[23] A. P. Ferreira Leite, F. A. Belo, M. M. Martins, and D. B. Riffel, "Central air conditioning based on adsorption and solar energy," *Applied Thermal Engineering*, vol. 31, no. 1, pp. 50–58, 2011.

[24] K. F. Fong, T. T. Chow, C. K. Lee, Z. Lin, and L. S. Chan, "Comparative study of different solar cooling systems for buildings in subtropical city," *Solar Energy*, vol. 84, no. 2, pp. 227–244, 2010.

[25] L. Juanicó, "A new design of roof-integrated water solar collector for domestic heating and cooling," *Solar Energy*, vol. 82, no. 6, pp. 481–492, 2008.

[26] A. Hobbi and K. Siddiqui, "Optimal design of a forced circulation solar water heating system for a residential unit in cold climate using TRNSYS," *Solar Energy*, vol. 83, no. 5, pp. 700–714, 2009.

[27] C.-D. Yue and G.-R. Huang, "An evaluation of domestic solar energy potential in Taiwan incorporating land use analysis," *Energy Policy*, vol. 39, no. 12, pp. 7988–8002, 2011.

[28] S. A. Kalogirou, "Environmental benefits of domestic solar energy systems," *Energy Conversion and Management*, vol. 45, no. 18-19, pp. 3075–3092, 2004.

[29] S. A. Kalogirou, "Solar thermal collectors and applications," *Progress in Energy and Combustion Science*, vol. 30, no. 3, pp. 231–295, 2004.

[30] G. Ozyogurtcu, M. Mobedi, and B. Ozerdem, "Techno-economic evaluation of a ventilation system assisted with exhaust air heat recovery, electrical heater and solar energy," *Energy and Buildings*, vol. 72, pp. 17–23, 2014.

[31] T. Tsoutsos, N. Frantzeskaki, and V. Gekas, "Environmental impacts from the solar energy technologies," *Energy Policy*, vol. 33, no. 3, pp. 289–296, 2005.

[32] A. Al-Salaymeh, I. Al-Rawabdeh, and S. Emran, "Economical investigation of an integrated boiler—solar energy saving system in Jordan," *Energy Conversion and Management*, vol. 51, no. 8, pp. 1621–1628, 2010.

[33] H. Zhai, Y. J. Dai, J. Y. Wu, and R. Z. Wang, "Energy and exergy analyses on a novel hybrid solar heating, cooling and power generation system for remote areas," *Applied Energy*, vol. 86, no. 9, pp. 1395–1404, 2009.

[34] O. Ozgener and A. Hepbasli, "A parametrical study on the energetic and exergetic assessment of a solar-assisted vertical ground-source heat pump system used for heating a greenhouse," *Building and Environment*, vol. 42, no. 1, pp. 11–24, 2007.

[35] O. Ozgener and A. Hepbasli, "Experimental performance analysis of a solar assisted ground-source heat pump greenhouse heating system," *Energy and Buildings*, vol. 37, no. 1, pp. 101–110, 2005.

[36] I. M. Michaelides and P. C. Eleftheriou, "An experimental investigation of the performance boundaries of a solar water heating system," *Experimental Thermal and Fluid Science*, vol. 35, no. 6, pp. 1002–1009, 2011.

[37] R. Sekret and M. Turski, "Research on an adsorption cooling system supplied by solar energy," *Energy and Buildings*, vol. 51, pp. 15–20, 2012.

[38] D. Xu, Q. Liu, J. Lei, and H. Jin, "Performance of a combined cooling heating and power system with mid-and-low temperature solar thermal energy and methanol decomposition integration," *Energy Conversion and Management*, vol. 102, pp. 17–25, 2015.

[39] M. Esen and T. Yuksel, "Experimental evaluation of using various renewable energy sources for heating a greenhouse," *Energy and Buildings*, vol. 65, pp. 340–351, 2013.

[40] M. M. Kablan, "Techno-economic analysis of the Jordanian solar water heating system," *Energy*, vol. 29, no. 7, pp. 1069–1079, 2004.

[41] J. Yoo, "Evaluation of solar hot water heating system applications to high-rise multi-family housing complex based on three years of system operation," *Energy and Buildings*, vol. 101, pp. 54–63, 2015.

[42] T.-T. Chow, Z. Dong, L.-S. Chan, K.-F. Fong, and Y. Bai, "Performance evaluation of evacuated tube solar domestic hot water systems in Hong Kong," *Energy and Buildings*, vol. 43, no. 12, pp. 3467–3474, 2011.

[43] U. Desideri, S. Proietti, and P. Sdringola, "Solar-powered cooling systems: technical and economic analysis on industrial refrigeration and air-conditioning applications," *Applied Energy*, vol. 86, no. 9, pp. 1376–1386, 2009.

[44] X. Zhang, S. You, W. Xu et al., "Test result analysis of the stagnation effect on the thermal performance of solar collector," *Energy Procedia*, vol. 30, pp. 824–828, 2012.